

**SYNTHESIS AND STUDIES ON SUPERPARAMAGNETIC  
IRON OXIDE NANOPARTICLES**

**A THESIS**

*Submitted To The*

**UNIVERSITY OF PUNE**

*For The Degree Of*

**DOCTOR OF PHILOSOPHY**

**(IN CHEMISTRY)**

*By*

**V. SREEJA**

*Under The Guidance Of*

**Dr. P. A. JOY**

PHYSICAL AND MATERIALS CHEMISTRY DIVISION

NATIONAL CHEMICAL LABORATORY

PUNE 411008, INDIA

**FEBRUARY 2011**

## **DECLARATION**

I declare that the thesis entitled “**Synthesis and Studies on Superparamagnetic Iron Oxide Nanoparticles**”, submitted for the Degree of Doctor of Philosophy in Chemistry, to the University of Pune, have been carried out by me at Physical and Materials Chemistry Division, National Chemical Laboratory, Pune under the guidance of Dr. P. A. Joy. The work is original and has not been submitted in part or full by me, for any degree or diploma to this or to any other University.

Date:

**Mrs. V. Sreeja**

Place : Pune

*Dedicated to*

*My husband, Mr. Renjith Lakshmanan*

*He is the symbol of love and friendship. He is the one who is the  
backbone of my success.*

*∫*

*My Parents, Mr. Devarajan and Mrs. Vijayamma*

*They have taught me much more than science and given me the most  
important gift of all, love.*

## *Acknowledgement*

*The tree which filleth the arms grew from the tiniest sprout; the tower of nine storey's rose from a little mound of earth, the journey of a thousand miles began with a single step*

*-Lao Tzu*

*The voyage through the sea of knowledge ends in the shore of destiny which passes through different obstacles, people and stages of life. Words cannot tell it, the beautiful moment beyond victory, which melted away like tears of joy, when I stand near the bank of this memorable achievement.*

*My deepest sense of gratitude and sincere thanks are due to my Research Supervisor, Dr. P. A. Joy, for his constant encouragement, guidance and support throughout my Ph. D. I am especially indebted to him for providing me enormous freedom to pursue research. I am also thankful to him for teaching me the elements of modesty and concern for others. He has the rarest combination of humanity, professional skills and scientific knowledge. I always admire his excellent ability to locate the best quality in every student and adaptability to people of varying attitudes and temperament. This feat would have been definitely impossible without his vibrant guidance and moral support.*

*I owe a special dept of thanks to Dr. H.S. Potdar, Dr. Raja Mohanan. and Dr. Ajith kumar for their fruitful scientific supports.*

*I would like to thank Dr. Saurav Pal, (Director, NCL), for providing me all the infrastructural facilities. I would extend my sincere thanks to Dr. Anil Kumar (Head, Physical Chemistry Division) for his persistent encouragement and support. Also, I am grateful to Dr. Vijayamohanan, Dr. I. S. Mulla, Dr. B. L. V. Prasad and Dr. S. D. Prasad for their encouragement. Thanks are also due to our divisional staff, Shri. Dipak Jori and Shri. S. F. Punekar for their willing cooperation.*

*I also acknowledge Dr. C. S. Gopinath, Dr. Nandini Devi, and Dr. Kala Raj (Catalysis division), for the inspiration and encouragement throughout my research.*

*Innumerable thanks go to Dr.Surendran, Deepak, Vinod, Sanyo and Smitha, the five fingers of my hand, for their friendship and worthwhile supports for my research especially for the NMR work,*

*My special thanks to my friends especially Shelva, Khaja, Mangesh and Pankaj from the core of my heart, for being delighted with my achievements and for sharing the hard time. The wonderful memories of the precious times shared with each of them will be cherished forever...Also it gives immense pleasure to thank my labmates ; Ganga, Dr.Sasanka Deka, Dr.Shekhar Bhame, Dr.Seema Verma, Khaja, Mangesh, Pankaj, Lenin, Bindu, Govind, Anjali and Jaya for providing me with an excellent working ambience during my research work. I owe deeply to my ever loving friends in NCL; Leena, Sadiq, Venugopal, Rahul, Regi, Sowmya, Jima, Aany, Jijil, Rajesh, Shoey, Anish, Renny and Nagendra Gupsae. I always cherish my memorable moments with Sony Chechi's smile, Mahima Chechi's inspirational words, Shapoo's acting, Manasi's dance, Anjali's coffee and all host elites in NCL.*

*I find no words to express the love of my appa, amma, jayakuttan and sreekuttan, who have always given me the best of everything. They are the crystals of my every successful moment in life.*

*Behind my efforts is one person whose day-to-day patience and encouragement were essential: my soul, Renjith, who has shared the happiness and tough times during my work. These few words are only a small fraction of my enormous sense of love, appreciation, and thanks.*

*I acknowledge CSIR, India for granting research fellowship.*

*Above all, I thank God; the almighty for this most amazing moment, for the leaping greenly spirits of trees, for the blue dream of sky and for everything .....*

- Sreeja .V

1	INTRODUCTION	1
1.1	Material Science	1
1.2	Nanomaterials	1
1.3	Magnetic Nanomaterials	2
	1.3.1 Classification of Magnetic Nanomaterials	3
1.4	Overview of Magnetism	4
	1.4.1 Diamagnetism	4
	1.4.2 Paramagnetism	4
	1.4.3 Ferromagnetism	5
	1.4.4 Antiferromagnetism	6
	1.4.5 Ferrimagnetism	7
	1.4.6 Magnetic Anisotropy	7
	1.4.7 Magnetic Domains	9
	1.4.8 Magnetic Hysteresis	12
1.5	Magnetism in Nanoparticles	13
	1.5.1 Finite Size effect	14
	1.5.2 Surface Effects	20
	1.5.3 Interparticle Interactions in Magnetic Nanoparticles	23
1.6	Materials Related to the Present Work	25
	1.6.1 Structure of spinels	25
	1.6.2 Magnesium Aluminate	26
	1.6.3 Zinc Aluminate	27
	1.6.4 Magnetite	28
1.7	Magnetism of Iron Oxides	28
1.8	Synthesis of Iron Oxides Nanoparticles	31
1.9	Stabilisation of Iron Oxides Nanoparticles	33
1.10	Application of Iron Oxides Nanoparticles	35
	1.10.1 Biomedical Applications	35
	1.10.2 Information storage	45
	1.10.3 Other Applications	46
1.11	Objectives of the present work	47
1.12	Organization of the thesis	48

2	<b>SYNTHESIS METHODS AND CHARACTERISATION</b>	60
2.1	Introduction	60
2.2	Synthesis	60
2.2.1	Coprecipitation method	60
2.2.2	Glycine-Nitrate autocombustion method	61
2.2.3	Surface coating of nanoparticles	63
2.3	Characterization and Measurement Techniques	63
2.3.1	Powder X-Ray diffraction	63
2.3.2	Transmission electron microscopy	65
2.3.3	Photon correlation spectroscopy	66
2.3.4	Infrared spectroscopy	67
2.3.5	Thermogravimetric analysis	68
2.3.6	UV-Visible Spectroscopy	69
2.3.7	Magnetic measurements	69
2.3.8	Nuclear Magnetic Resonance Spectroscopy	71
	2.3.8.1 Magic angle spinning	72
	2.3.8.2 Multiple Quantum Magic-Angle Spinning	73
3	<b>SYNTHESIS AND MAGNETIC PROPERTIES OF IRON OXIDE NANOPARTICLES</b>	
3.1	Introduction	79
3.2	Synthesis of Magnetite Nanoparticles	84
3.2.1	Addition of Fe stock solution by a burette	84
	3.2.1.1 PXRD Analysis	86
	3.2.1.2 TEM Analysis	87
	3.2.1.3 Magnetic Measurement	88
3.2.2	Addition of Fe stock solution by a separating funnel	91
	3.2.2.1 PXRD Analysis	92
	3.2.2.2 TEM Analysis	93
	3.2.2.3 Magnetic Measurement	93
3.2.3	Direct addition of Fe stock solution	95
	3.2.3.1 PXRD Analysis	96
	3.2.3.2 TEM Analysis	98
	3.2.3.3 Magnetic Measurement	99

3.3.	Comparison of magnetic properties of magnetite nanoparticles with different particle size	102
3.3.1	Field and temperature dependence	102
3.4	Conclusions	106
4	<b>SURFACE MODIFICATION OF MAGNETITE NANOPARTICLES AND THEIR CHARACTERIZATION</b>	
4.1	Introduction	112
4.2	Synthesis and magnetic properties of dextran coated magnetite nanoparticles	113
4.2.1	Synthesis	115
4.2.2	Powder XRD Analysis	116
4.2.3	TEM Analysis	118
4.2.4	DLS Analysis	119
4.2.5	FTIR Studies	121
4.2.6	Thermal Analysis	122
4.2.7	Magnetic Measurements	124
4.3	Synthesis and magnetic properties of l-ascorbic acid coated magnetite nanoparticles	132
4.3.1	Synthesis	132
4.3.2	Powder XRD Analysis	133
4.3.3	TEM Analysis	134
4.3.4	DLS Analysis	136
4.3.5	FTIR Studies	137
4.3.6	Thermal Analysis	138
4.3.7	Reduction studies	139
4.3.8	Magnetic Measurements	142
4.3.9	T <sub>1</sub> and T <sub>2</sub> measurements	148
4.4	Conclusions	150

5	COMPARISON OF THE MAGNETIC PROPERTIES OF BARE AND SURFACE COATED MAGNETITE NANOPARTICLES	
5.1	Introduction	154
5.2	Comparison of the magnetic properties before and after coating with dextran	155
5.3	Comparison of the Magnetic Behavior dextran coated powder and fluid samples	165
5.4	Comparison of the magnetic properties before and after coating with ascorbic acid	169
5.5	Conclusions	170
6	SOLID STATE NMR STUDIES ON NANOCRYSTALLINE ALUMINATE SPINELS	
6.1	Introduction	173
6.2	Solid State NMR Studies on $MgAl_2O_4$ Nanoparticles	175
6.2.1	Synthesis	175
6.2.2	Powder XRD Analysis	177
6.2.3	TEM Analysis	179
6.2.4	Solid state NMR studies	179
6.3	Solid State NMR Study on $ZnAl_2O_4$ Nanoparticles	193
6.3.1	Synthesis	193
6.3.2	Powder XRD Analysis	194
6.3.3	TEM Analysis	195
6.3.4	Solid state NMR studies	196
6.4	Conclusions	202
7	CONCLUSIONS AND FUTURE PROSPECTS	208

## LIST OF PUBLICATIONS

## LIST OF TABLES

3.1	Comparison of the properties of iron oxide nanoparticles reported in the literature. LT – low temperature, RT – room temperature	82
3.2	Sample codes and mode of addition	86
3.3	Sample codes and crystallite size of sample synthesized by burette addition	87
3.4	Sample codes and crystallite size of synthesized samples by separating funnel addition	92
3.5	Sample codes crystallite size, particle size and lattice parameter of samples by direct addition.	96
3.6	Magnetic data of samples with different particle sizes	105
4.1	Particle size obtained from TEM, XRD and DLS of uncoated and dextran coated magnetite nanoparticles	117
4.2	Sample codes and weight loss of dextran coated magnetite obtained from TGA	123
4.3	Magnetic data of uncoated and dextran coated magnetite nanoparticles	131
4.4	Sample code and weight loss of ascorbic acid obtained from TGA	139
4.5	Magnetic data of uncoated and ascorbic acid coated magnetite nanoparticles	146
6.1	Sample codes, annealing Temperatures, and the particle sizes obtained from XRD and TEM of magnesium aluminate nanoparticles	176
6.2	NMR Parameters of magnesium aluminate nanoparticles obtained from the $^{27}\text{Al}$ MAS Experiments, Using the DMFIT Program	189
6.3	Sample codes, annealing temperatures, and the particle sizes obtained from XRD and TEM	194
6.4	NMR Parameters Obtained from the $^{27}\text{Al}$ MAS Experiments, Using the DMFIT Program	201

## LIST OF FIGURES

1.1	Schematic representation of the different types of magnetic nanostructures [21]	3
1.2	(a) Alignment of magnetic moments in different magnetic materials and (b) variation of the inverse susceptibility with temperature of para-, antiferro, ferro- and ferri-magnetic materials.	5
1.3	Magnetisation curves for magnetite along hard and easy directions [30]	8
1.4	Schematic illustration of the breakup of magnetisation into domains (a) single domain, (b) two domains, (c) four domains and (d) closure domains.	10
1.5	Schematic representation of a 180° domain wall.	11
1.6	Magnetization process in ferromagnetic materials.	12
1.7	In nanometer scale, parameters such as size, shape, composition, and magnetocrystalline anisotropy strongly affect the magnetism of nanoparticles [17].	13
1.8	Variation of the coercivity of magnetic particles with particle diameter, and comparison of magnetization curves of typical ferro, ferri and superparamagnetic substances.	15
1.9	Figure 1.9. Size dependent saturation magnetisation value of magnetite nanoparticles and pictorial illustration of surface spin canting effect of nanoparticles [17].	16
1.10	Energy diagram of magnetic nanoparticles	17
1.11	Variation of blocking temperature with respect to particle size in cobalt nanoparticles [45].	18
1.12	Magnetisation vs temperature of magnesium ferrite and cobalt ferrite nanoparticles [46].	19
1.13	Magnetization curves of superparamagnetic iron oxide nanoparticles above and below $T_B$	20

1.14	The different magnetic effects occurring in magnetic nanoparticles [59].	22
1.15	Structure of Spinel	27
1.16	Different types of interactions for different types of lattice sites in spinels [36].	30
1.17	Surface modification strategies for designing MNP probes with high colloidal stability [102].	35
1.18	Tailored MNPs for molecular and cellular magnetic resonance imaging (MRI). a) Controlling the magnetism of the nanoparticles core, b) tailoring the surface ligands of the nanoparticle shell, c) the molecular targeting capability of biomolecule-conjugated nanoparticles. d) High performance utilizations of nanoparticles for molecular and cellular MRI [102].	36
1.19	The structure of MRI contrast agent based on nanoparticles [126].	37
1.20	MR contrast effects of MNPs [102].	38
1.21	Nanoscale size effect of magnetite nanoparticles on magnetism and MR contrast effects [129].	39
1.22	Dopant dependent effect on magnetisation values and effect on MR contrast [17].	39
1.23	Schematic representation of drug delivery using magnetic nanoparticles [102].	44
2.1	Schematic diagram of the VSM components [26].	70
2.2	Typical memory experiments following (a) FC protocol and (b) ZFC protocol.	71
2.3	A) Effects of the second-order frequency shifts $\Delta 2(\phi, \theta)$ on the central transition spectrum arising from a static powder. (B) Orientation dependence of the two Legendre polynomials $\{Pl(\cos\chi)\}_{l=2,4}$ that define the line broadening of central transition quadrupolar patterns [30].	74
2.4	Pulse sequence and coherence diagram used	76
3.1	Powder XRD patterns of a) Fe1a, b) Fe1b, and c) Fe1c. The	87

	simulated pattern of Fe <sub>3</sub> O <sub>4</sub> is shown at the bottom and indexed.	
3.2	TEM micrograph of Fe1c sample and TEM histogram of the particle size distribution	88
3.3	Field dependence of magnetisation of Fe1a and Fe1c samples, at room temperature.	89
3.4	ZFC curve of Fe1a and Fe1b samples.	90
3.5	Temperature dependent magnetisation curve of Fe1a and Fe1c samples,	91
3.6	XRD pattern of a) Fe2a, b) Fe2b. The simulated pattern of Fe <sub>3</sub> O <sub>4</sub> is shown at the bottom and indexed.	92
3.7	TEM micrograph of Fe2a sample (left) and TEM histogram of the particle size distribution	93
3.8	Field dependence of magnetisation of Fe2a and Fe2b samples	94
3.9	Temperature dependent magnetisation curves of a) Fe2a and b) Fe2b samples	95
3.10	XRD pattern of a)Fe3a, b)Fe3b, c) Fe3c and d) Fe3d. The simulated pattern of Fe <sub>3</sub> O <sub>4</sub> is shown at the bottom and indexed.	97
3.11	a) Change in the crystallite size with synthesis temperature b) Arrhenius plot of ln(D) against 1/T for the samples synthesised at different temperatures.	97
3.12	TEM micrographs of a)Fe3c and b) Fe3d and TEM histogram of the particle size distribution.	99
3.13	Field dependent magnetisation curves of a) Fe3a, b) Fe3b, c) Fe3c and d) Fe3d.	100
3.14	Temperature dependent magnetisation curve of a) Fe3a, b) Fe3b, c) Fe3c and d) Fe3d.	101
3.15	Room temperature magnetisation of (a) Fe1c, (b) Fe2a, (c) Fe3c (d) Fe3d.	103
3.16	Temperature dependent magnetisation of (a) Fe1c, (b) Fe2a, (c) Fe3c (d) Fe3d.	104
3.17	Variation of blocking temperature and crystalline anisotropy with particle volume of magnetite nanoparticles.	106
4.1	Structure of dextran molecule	114

4.2	XRD patterns of (a) Fe1, (b) Fedx1, (c) Fedx2, and (d) Fedx3. The simulated pattern of Fe <sub>3</sub> O <sub>4</sub> is shown and indexed at the bottom.	117
4.3	Transmission electron micrographs (left) and the corresponding particle size distribution (right) of a) Fe1 b) Fedx1 c) Fedx2	118
4.4	DLS particle size distribution of a) Fedx1 b) Fedx2 c) Fedx3	120
4.5	Infrared spectra of (a) Fe1, (b) Pure dextran, (c) Fedx3, (d) Fedx2, and e) Fedx1	122
4.6	Thermograms of Fe1, Fedx1, Fedx2, and Fedx3.	123
4.7	Room temperature magnetic measurements of (a) Fe1, (b) Fedx1, (c) Fedx2, (d) Fedx3	124
4.8	M-H Curves of (a) Fe1, (b) Fedx1, (c) Fedx2, and (d) Fedx3 based on weight loss of dextran (per gram of Fe <sub>3</sub> O <sub>4</sub> )	125
4.9	Normalised Curve of uncoated (Fe1) and dextran coated sample (Fedx1)	126
4.10	Variation of saturation magnetisation with particle size of uncoated and dextran coated magnetite nanoparticles	127
4.11	ZFC and FC magnetization curves of a) Fe1, b) Fedx1, c) Fedx2, and d) Fedx3	129
4.12	XRD pattern (a) Fe1 (b) FeAc1 (c) FeAc2. The simulated pattern of Fe <sub>3</sub> O <sub>4</sub> is shown and indexed at the bottom.	134
4.13	Transmission electron micrographs (left) and the corresponding particle size distribution (right) of a) Fe1 b) FeAc1 c) FeAc2	135
4.14	DLS particle size distribution of FeAc2 and FeAc1 samples	136
4.15	Structure of ascorbic acid molecule	137
4.16	FTIR spectra (a) pure ascorbic acid, (b) Fe1, (c) FeAc2, (d) FeAc1	138
4.17	Thermograms of pure ascorbic acid, Fe1, FeAc1 and FeAc2.	139
4.18	UV-Vis spectra of ascorbic acid and methylene blue before and after reduction with ascorbic acid coated magnetite nanoparticles.	141
4.19	FTIR spectra of FeAc1 a) after reduction, b) before reduction	142

4.20	Room temperature magnetisation curves of a) Fe1, b) FeAc1, c) FeAc2 samples.	143
4.21	M-H Curve of (a) Fe1, (b) FeAc1, (c) FeAc2 based on weight loss of dextran (calculated per gram of Fe <sub>3</sub> O <sub>4</sub> )	144
4.22	Normalised Curve of uncoated and ascorbic acid coated (Fe Ac1) samples	145
4.23	Temperature variation of magnetisation of a) Fe1, b) FeAc1 and c) FeAc2 samples	147
4.24	Plots of inverse relaxation times (a) 1/T <sub>1</sub> and (b) 1/T <sub>2</sub> as a function of iron concentration.	149
5.1	ZFC and FC magnetization curves of a) Fe1 and b) Fedx1	156
5.2	Magnetisation curves of Fe1 at different temperatures	157
5.3	Magnetisation curves of Fedx1 at different temperatures.	158
5.4	Normalized magnetization curves of Fe1 and Fedx1 at 12 K.	159
5.5	Temperature variation of coercivity of coated and uncoated magnetite nanoparticles.	159
5.6	FC memory experiments of the un-coated Fe <sub>3</sub> O <sub>4</sub> nanoparticles Fe1c (left) and Fe3c (right) samples (see chapter 3). Original FC curve (red); Cooling curve with magnetic field switched off at a constant temperature (black); Heating curve in the same magnetic field while the field is on (green)	161
5.7	Memory effect studies on the dextran coated magnetite sample Fedx1	164
5.8	Field dependence of magnetisation of dextran coated magnetite samples (Fedx2) in the form of powder and fluid.	166
5.9	ZFC and FC magnetization curves of dextran coated magnetite samples (Fedx2) in the form of powder and fluid in water.	167
5.10	Memory effect studies on the dextran coated magnetite sample in the fluid form Fedx2.	167
5.11	Magnetization as a function of magnetic field for the dextran coated magnetite nanoparticles (Fedx2), measured at different low temperatures, a) in the powder form and b) as fluid.	168

5.12	FC memory experiments of Fe1c (top) and FeAc2 (bottom) samples. Original FC curve (red); Cooling curve with magnetic field switched off at a constant temperature (black); Heating curve in the same magnetic field while the field is on (green)	169
6.1	Power XRD patterns of MgAl <sub>2</sub> O <sub>4</sub> nanoparticles annealed at different temperatures, MA1 – 400 °C, MA2 – 600 °C, MA3 – 800 °C, MA4 – 1000 °C, MA5 – 1200 °C, MA6 – 1400 °C. The simulated pattern of MgAl <sub>2</sub> O <sub>4</sub> (MA) is shown and indexed for comparison.	178
6.2	Transmission electron micrograph of the sample annealed at 400 °C (MA1) and 600 °C (MA2). The inset shows the corresponding electron diffraction pattern.	179
6.3	<sup>27</sup> Al MAS NMR spectra of MgAl <sub>2</sub> O <sub>4</sub> of different particle sizes, recorded on AV300 spectrometer at a sample spinning speed of 12.5 kHz.	181
6.4	<sup>27</sup> Al MAS NMR spectra of MgAl <sub>2</sub> O <sub>4</sub> of different particle sizes, recorded on AV500 spectrometer at a sample spinning speed of 34.1 kHz.	182
6.5	Experimental and calculated <sup>27</sup> Al MAS NMR spectra for the samples (a) MA1 (b) MA2, (c) MA3, d) MA4, (e) MA5 and (f) MA6. The bottom traces show the separate components for the different aluminum coordinations.	185
6.6	Cation distribution in MgAl <sub>2</sub> O <sub>4</sub> nanoparticles obtained from fitting the <sup>27</sup> Al MAS NMR spectra, plotted as a function of particle size. Note that the <i>x</i> -axis is not to scale.	190
6.7	Normalized AV300 <sup>27</sup> Al MAS NMR spectra of the MgAl <sub>2</sub> O <sub>4</sub> samples MA1, MA2, and MA3. The intensities are normalized with respect to the (a) Al <sub>VI</sub> as well as the (b) Al <sub>IV</sub> peaks.	191
6.8	MQMAS NMR of MA2 (600 °C heated sample)	192

6.9	Power XRD patterns of $\text{ZnAl}_2\text{O}_4$ nanoparticles annealed at different temperatures, ZA1 – 400 °C, ZA2 – 450 °C, ZA3 – 500 °C, ZA4 – 600 °C, ZA5 – 800 °C, ZA6 – 1000 °C. The simulated pattern of $\text{ZnAl}_2\text{O}_4$ (ZA) is shown and indexed for comparison.	195
6.10	Transmission electron micrographs of the samples annealed at 400 °C (ZA1) and 500°C (ZA3). The inset shows the corresponding electron diffraction pattern.	196
6.11	$^{27}\text{Al}$ MAS NMR spectra of $\text{ZnAl}_2\text{O}_4$ of different particle sizes, recorded on AV300 spectrometer at a sample spinning speed of 12.5 kHz	197
6.12	$^{27}\text{Al}$ MAS NMR spectra of $\text{ZnAl}_2\text{O}_4$ of different particle sizes, recorded on AV500 spectrometer at a sample spinning speed of 34.1 kHz	198
6.13	Experimental and calculated $^{27}\text{Al}$ MAS NMR spectra for the samples ZA1 and ZA3. The bottom traces in both cases show the separate components for the different aluminum coordinations.	199
6.14	Cation distribution in $\text{ZnAl}_2\text{O}_4$ nanoparticles obtained from fitting the $^{27}\text{Al}$ MAS NMR spectra, plotted as a function of particle size. Note that the $x$ -axis is not to scale.	200

---

**CHAPTER 1****1 INTRODUCTION****1.1 Material Science**

The Science of Materials is a modern introduction to the structures and properties of solids. Materials science [1,2] is the multidisciplinary field related to the studies on different aspects of materials. Materials science in a primitive form is one of the oldest forms of engineering and applied science. It is closely related to applied physics, chemistry and chemical engineering, biology and bioengineering, electrical engineering, civil engineering and mechanical engineering. In other terms, materials science is defined as the one which is concerned with the relation of composition, structure, and processing of materials to their properties. With significant media attention to nanoscience and nanotechnology in the recent years, materials science has been propelled to the forefront of research activities. We have just begun to see the impact of the materials revolution. Materials science involves the preparation and characterization of materials to ensure that they have the properties required for a particular application. The central concept of materials science is relating the microstructure of a material to the properties one wants it to have. By working with the microstructure, one can tailor the central properties of that material. Materials scientists are generally employed by industry or in laboratories where the focus is on developing product-related technologies. Classes of materials include plastics, glass, ceramics, metals, and semiconductors. Key properties of materials include their mechanical behavior, electrical, magnetic optical and thermal characteristics, chemical stability and other physical properties such as density and grain structure. Other applications of materials science include studies of superconducting materials [3], graphite materials [4], integrated-circuit chips [5], and fuel cells [6].

**1.2 Nanomaterials**

Good things come in small packages. A nanomaterial is one such thing. During the past decade, nanomaterials have attracted enormous interest of the research community worldwide. These materials, notable for their extremely small size, have the potential for wide-ranging industrial, biomedical and technological applications. Nanomaterials [7,8] can be metals, ceramics, polymeric materials or

composite materials. Their defining characteristic is a very small feature size in the range of 1-100 nanometers (nm). Nanoscience has become the focus of modern materials science because of the potential technological importance, which stems from the unique physical properties of nanomaterials [9]. At the nano level, some material properties are affected by the laws of atomic physics, rather than behaving as traditional bulk material properties. Because of the small dimensions, the nanomaterials possess exotic electronic, magnetic and optical properties, high chemical reactivity, extremely high surface/volume ratio. The spectrum of nanomaterial ranges from inorganic or organic, crystalline or amorphous particles, which can be found single particles, aggregates, powders or dispersed in a matrix, over colloids, suspensions and emulsions, nanolayers and films, up to the class of fullerenes and their derivatives. Also supramolecular structures such as dendrimers, micelles or liposomes belong to the field of nanomaterials.

Nanomaterials have recently become one of the most active research fields in the areas of material science. The study of nanomaterials is one field with the earliest starting that obtained rich achievements in nanoscience and nanotechnology. Nanomaterials play a very important supporting role for applications of nanoscience and nanotechnology in the field of fabrication, such as information storage and technology, energy sources, environment, health and medical treatments.

### **1.3 Magnetic Nanomaterials**

The unique properties of magnetic nanomaterials and structures on the nanometer scale have sparked the attention of materials developers [10,11]. Nanomagnetic materials [12] are made of particles with sizes going from a few nanometers to a few hundred nanometers. Nanosized magnetic materials offer potential applications including information storage [13], color imaging, bioprocessing [14], magnetic refrigeration [15] and ferrofluids [16]. Many migratory animals and some microbes possess magnetic nanoparticles in their body that are utilized as a natural biomagnetic compass [17]. For example, salmon fish have a series of magnetic nanoparticles in the nasal capsules of their forehead, which are believed to respond to the geomagnetic field of the earth and help them reach their homes after journeys that can last tens of thousands of kilometres for three to four

years. Researchers have developed artificial magnetic nanoparticles through soft chemical routes [18].

### 1.3.1 Classification of Magnetic Nanomaterials

Magnetic nanomaterials can be categorized into various types [19]. A broad classification of nanomagnetic materials may be made as particulate nanomagnets, geometrical nanomagnets and layered nanomagnets.

- Particulate nanomagnets: granular solids where one or more phases are magnetic nanograined layers grown on columnar films; quasi granular film made by heat treating multi layers of immiscible solids
- Geometrical nanomagnets: columnar films or nanowires ; needle shaped particles in a matrix.
- Layered nanomagnets: multilayers with metallic and/or other nanometer- thick films on a supporting substrate.

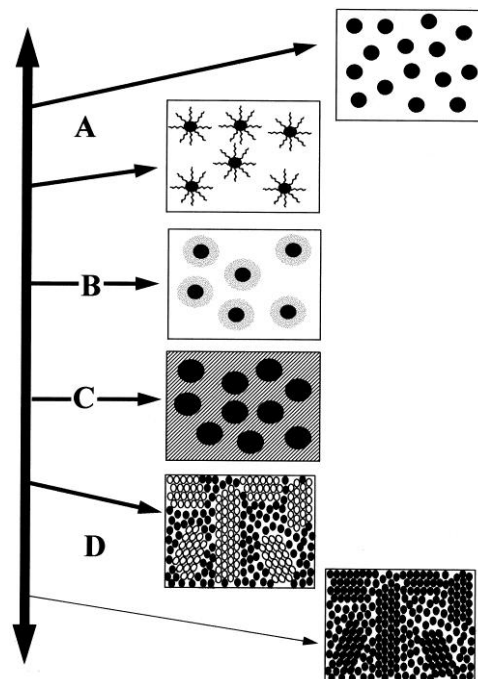


Figure 1.1. Schematic representation of the different types of magnetic nanostructures. Type-A materials include the ideal ultrafine particle system, with interparticle spacing large enough to approximate the particles as noninteracting. Type-B materials are ultrafine particles with a core-shell morphology. Type-C nanocomposites are composed of small magnetic particles embedded in a nonmagnetic matrix. Type-D materials consist of small crystallites dispersed in a noncrystalline matrix [21].

D. Givord [20] explicates that magnetic nanomaterials fall in to two categories (a) Systems with nanometric dimensions (b) Systems with macroscopic dimensions, but made up of crystallites with nanometric dimensions. Again Pelecky et.al [21] defines a classification designed to emphasize the physical mechanisms responsible for the magnetic behavior as shown in Figure 1.1.

## **1.4 Overview of Magnetism**

Magnetism [22] has been studied since the sixth century BC [23]. When the Greek philosopher Thales of Miletus noted the attraction of iron to lodestone; it is also at the vanguard of modern innovations in nanotechnology. The real birth of modern magnetism is in 1819 when Hans Christian Oersted discovered that an electric current produces a magnetic field. In magnetic materials [24], the most important sources of magnetization are the electron's orbital angular motion around the nucleus and the electron's intrinsic magnetic moment. Five basic types of magnetism [25,26] have been observed, and classified on the basis of the magnetic behavior of materials in response to magnetic fields at different temperatures. These types of magnetism [27] are: paramagnetism diamagnetism, ferromagnetism, ferrimagnetism and antiferromagnetism.

### **1.4.1 Diamagnetism**

Diamagnetism results from the fundamental principle of electromagnetism, known as Lenz's law, which states that when a conducting loop is acted upon by an applied magnetic field, a current is induced in the loop that counteracts the change in the field. Diamagnetism can be modeled as if the orbits of the electrons were the current loop. The induced moment is small and opposite to the field when such a material experiences an applied field. A diamagnetic material has the magnetic susceptibility  $< 0$ , with typical values of the order of  $10^{-5}$  to  $10^{-6}$ .

### **1.4.2 Paramagnetism**

Paramagnetism is a form of magnetism which occurs only in the presence of an externally applied magnetic field. Paramagnetic materials are attracted to magnetic fields; hence have a relative magnetic susceptibility of  $> 0$ . In 1895, the French

Physicist Pierre Curie first reported about the variation of paramagnetic susceptibilities with temperature. He stated that, mass susceptibility of a paramagnetic substance varies inversely with the absolute temperature and this is mathematically given by

$$\chi = \frac{C}{T} \quad (1.1)$$

This equation is known as Curie's law, where  $C$  is the Curie constant. In this theory, it is assumed that individual magnetic moments do not interact with each other, but acted only by the applied magnetic field and thermal agitation.

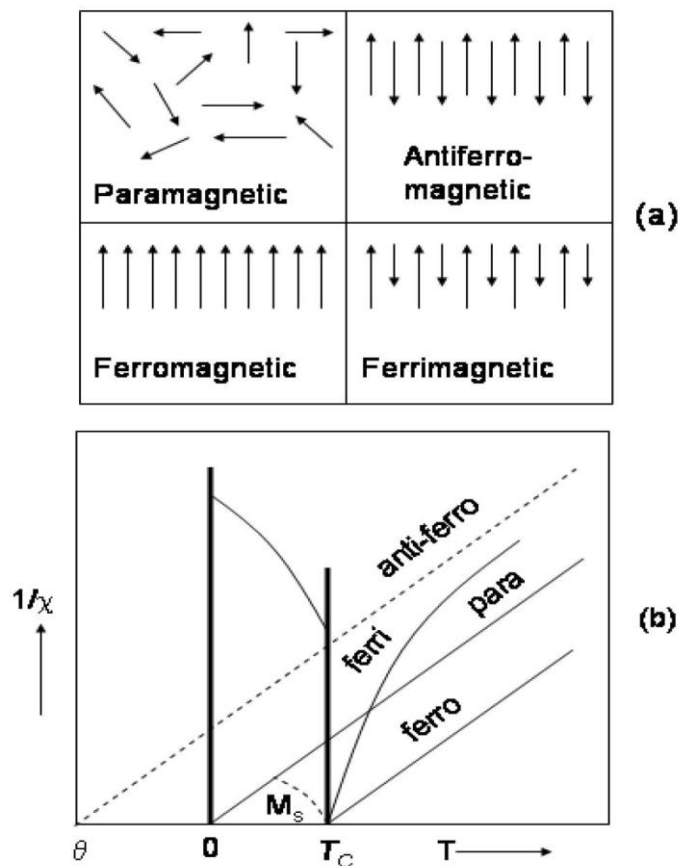


Figure 1.2. (a) Alignment of magnetic moments in different magnetic materials and (b) variation of the inverse susceptibility with temperature of para-, antiferro-, ferro- and ferri-magnetic materials.

### 1.4.3 Ferromagnetism

Ferromagnetic materials exhibit a long-range ordering phenomenon at the atomic level which causes the adjacent magnetic moments to line up parallel with

each other in a region called a domain [28]. Within the domain, the magnetic field is intense, but in a bulk sample the material will usually be unmagnetized because the many domains will themselves be randomly oriented with respect to one another. Ferromagnetism is exhibited by certain metals, alloys, and compounds of the transition metal ions, rare earth elements in which, below a certain temperature called the Curie temperature,  $T_C$ , the magnetic moments prefer to align in a common direction. Ferromagnetic materials behave like paramagnets above the  $T_C$ . In Curie's law, it is assumed that individual magnetic moments do not interact with each other, but acted only by the applied magnetic field and thermal agitation. In 1907, Weiss modified this law by employing the idea of a molecular field ' $H_m$ '. This term is the internal field inside a material and acted in addition to the applied field  $H$ . Thus

$$H_m = \gamma M \quad (1.2)$$

where  $\gamma$  is the molecular field constant. Therefore, the total field in the material

$$H_t = H + H_m \quad (1.3)$$

Solving these equations and Curie's law, Weiss postulated that

$$\chi = \frac{M}{\rho H} = \frac{C}{T - \rho C \gamma} = \frac{C}{T - \theta} \quad (1.4)$$

This equation is known as the Curie-Weiss law, where  $\theta$  is a measure of the strength of the magnetic interactions. For substances obeying Curie's law,  $\theta = \gamma = 0$ . The alignment of magnetic moments and the variation of the ferromagnetic susceptibility with temperature are shown in Figure 1.2.

#### 1.4.4 Antiferromagnetism

In antiferromagnetic materials the magnetic moments on the adjacent atoms align in opposite directions to each other, thereby leading to a net zero magnetic moment associated with the bulk material. They have small positive susceptibility at all temperatures, but their susceptibilities vary in a peculiar way with temperature. The theory of antiferromagnetism was developed by Neel [29]. Below a characteristic temperature, called as Neel temperature,  $T_N$ , the two sublattices undergo spontaneous magnetic ordering as in case of ferromagnetic materials, but the net magnetization is

zero because of the opposing directions of the sublattices magnetizations. Under the influence of an externally applied magnetic field, a small net magnetization can be detected. Above the Neel temperature, antiferromagnetic materials behave like paramagnets. The alignment of the magnetic moments and the temperature variation of susceptibility of an antiferromagnetic material are shown in Figure 1.2.

#### 1.4.5 Ferrimagnetism

Ferrimagnetism is a phenomenon in which there is partial cancellation of the adjacent magnetic moments. Ferrimagnetism is also called as uncompensated antiferromagnetism. Ferrimagnetic materials behave like paramagnetic materials above  $T_C$  and can retain spontaneous magnetization below the Curie temperature like ferromagnetic materials. The general theory of ferrimagnetism was developed by Neel. The uncompensated sublattice magnetization give way to have ferrimagnetic materials with different magnetic characteristics. The temperature dependencies of magnetic moments on the two sublattices are different. So, the magnetization may even change sign with changing temperature. The temperature, at which the sublattice magnetizations just cancel, is called  $T_{\text{comp}}$

#### 1.4.6 Magnetic Anisotropy

The magnetic properties of materials are strongly affected by one important property, called as magnetic anisotropy. This term simply means that the magnetic properties depend on the directions in which they are measured. There are several kinds of magnetic anisotropy such as, crystal anisotropy, shape anisotropy, stress anisotropy and exchange anisotropy. Anisotropy can also be induced by magnetic annealing, plastic deformation etc. Of these, the crystal anisotropy is intrinsic to the material. In crystalline materials the preferred directions of magnetization are called as magnetic easy axis or preferred axis. Because the applied magnetic field must do work against the anisotropy force to turn the magnetization away from the easy direction, there must be an energy stored in any crystal in the magnetization points in a non-easy direction. The anisotropy energy is defined as the amount of energy required to rotate the magnetization from a preferred or "easy" direction to a so called "hard" direction. In other words, crystal anisotropy can be regarded as a force which tends to bind the magnetization to directions of certain forms in the crystal [30]. In a

cubic crystal, if magnetization,  $M_s$ , makes angles  $a, b, c$  with the crystal axes, and  $\alpha_1, \alpha_2$  and  $\alpha_3$  be the cosines of these angles then, the anisotropy energy  $E$ , is given by,

$$E = K_0 + K_1(\alpha_1^2\alpha_2^2 + \alpha_2^2\alpha_3^2 + \alpha_3^2\alpha_1^2) + K_2(\alpha_1^2\alpha_2^2\alpha_3^2) + \dots \quad (1.5)$$

where  $K_0, K_1, K_2, \dots$  are constants for a particular material and are expressed in  $\text{erg/cm}^3$ . For example, here are magnetization curves for magnetite.

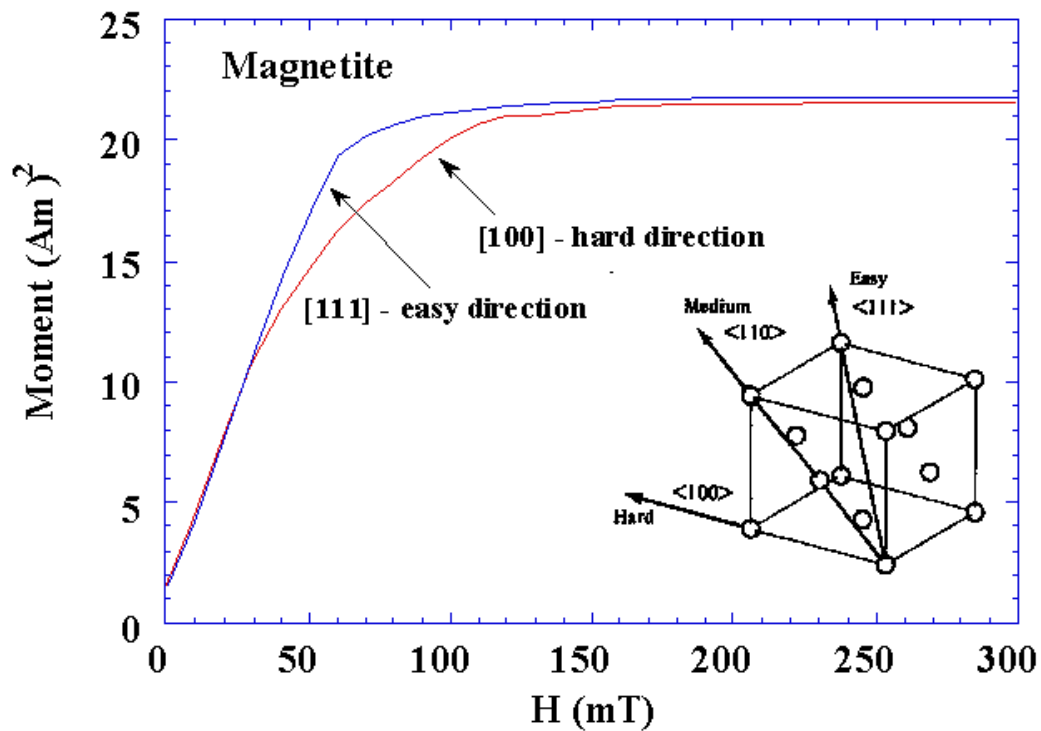


Figure 1.3. Magnetisation curves for magnetite along hard and easy directions [30]

Depending on the crystallographic orientation of the sample in the magnetic field, the magnetization reaches saturation in different fields.

In magnetite, above 130 K,

$\langle 111 \rangle$  is the easy direction of magnetization

$\langle 100 \rangle$  is the hard direction of magnetization

$\langle 110 \rangle$  is the intermediate direction of magnetization.

For a sphere of magnetite, there will be six easy directions of magnetization corresponding to the three [111] axes. Magnetocrystalline anisotropy is the energy necessary to deflect the magnetic moment in a single crystal from the easy to the hard direction. The easy and hard directions arise from the interaction of the spin magnetic moment with the crystal lattice (spin-orbit coupling). In cubic crystals, like magnetite, the magnetocrystalline anisotropy energy is given by a series expansion in terms of the angles between the direction of magnetization and the cube axes. It is sufficient to represent the anisotropy energy in an arbitrary direction by just the first two terms in the series expansion. These two terms each have an empirical constant associated with them called the first- and second order anisotropy constants, or  $K_1$  and  $K_2$ , respectively. At 300 K,  $K_1 = -1.35 \times 10^5$  ergs/cm<sup>3</sup>  $K_2 = -0.44 \times 10^5$  ergs/cm<sup>3</sup>. Magnetic anisotropy strongly affects the shape of hysteresis loops and controls the coercivity and remanence. Anisotropy is also of considerable practical importance because it is exploited in the design of most magnetic materials of commercial importance.

#### 1.4.7 Magnetic Domains

In order to explain the fact that ferromagnetic materials with spontaneous magnetisation could exist in the demagnetised state Weiss proposed the concept of magnetic domains. Weiss built the theory based on the earlier work carried out by Ampère, Weber and Ewing suggesting the existence of domains. The findings of this work revealed that within a domain large numbers of atomic moments are aligned, typically  $10^{12}$ - $10^{18}$ , over a much larger volume than was previously suspected. The magnetisation within the domain is saturated and will always lie in the easy direction of magnetisation when there is no externally applied field. The direction of the domain alignment across a large volume of material is more or less random and hence the magnetisation of a specimen can be zero.

Magnetic domains [31,32] exist in order to reduce the energy of the system. A uniformly magnetised specimen as shown in Figure 1.4(a) has a large magnetostatic energy associated with it. This is the result of the presence of magnetic free poles at the surface of the specimen generating a demagnetising field,  $H_d$ . From the convention adopted for the definition of the magnetic moment for a magnetic dipole, the magnetisation within the specimen points from the South Pole to the north pole, while the direction of the magnetic field points from north to south. Therefore, the

demagnetising field is in opposition to the magnetisation of the specimen. The magnitude of  $H_d$  is dependent on the geometry and magnetisation of the specimen. In general, if the sample has a high length to diameter ratio (and is magnetised in the long axis) then the demagnetising field and the magnetostatic energy will be low.

The breakup of the magnetisation into two domains as illustrated in Figure 1.4 (b) reduces the magnetostatic energy by half. In fact if the magnet breaks down into  $N$  domains then the magnetostatic energy is reduced by a factor of  $1/N$ , hence Figure 1.4 (c) has a quarter of the magnetostatic energy of Figure 1.4(a). Figure 1.4 (d) shows a closed domain structure where the magnetostatic energy is zero, however, this is only possible for materials that do not have a strong uniaxial anisotropy, and the neighbouring domains do not have to be at  $180^\circ$  to each other.

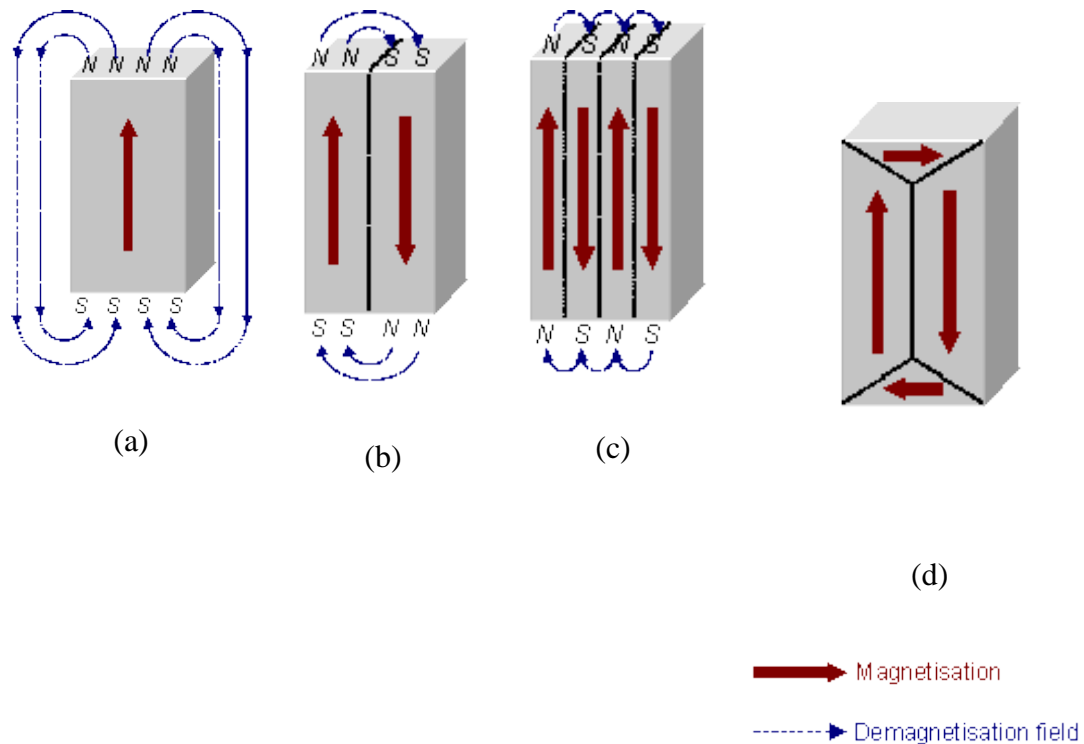


Figure 1.4. Schematic illustration of the breakup of magnetisation into domains (a) single domain, (b) two domains, (c) four domains and (d) closure domains.

The introduction of a domain raises the overall energy of the system, therefore the division into domains only continues while the reduction in magnetostatic energy is greater than the energy required to form the domain wall. The energy associated a domain wall is proportional to its area. The schematic representation of the domain

wall, shown in Figure 1.5, illustrates that the dipole moments of the atoms within the wall are not pointing in the easy direction of magnetisation and hence are in a higher energy state. In addition, the atomic dipoles within the wall are not at  $180^\circ$  to each other and so the exchange energy is also raised within the wall. Therefore, the domain wall energy is an intrinsic property of a material depending on the degree of magnetocrystalline anisotropy and the strength of the exchange interaction between neighbouring atoms. The thickness of the wall will also vary in relation to these parameters, as strong magnetocrystalline anisotropy will favour a narrow wall, whereas a strong exchange interaction will favour a wider wall.

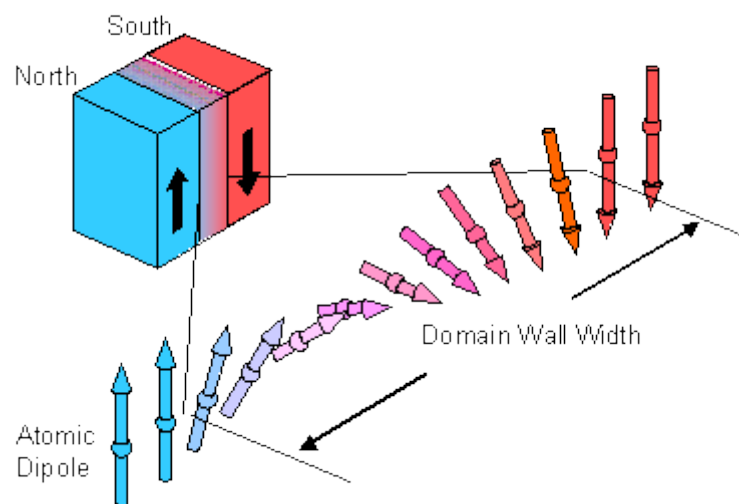


Figure 1.5. Schematic representation of a  $180^\circ$  domain wall.

A minimum energy can therefore be achieved with a specific number of domains within a specimen. This number of domains will depend on the size and shape of the sample (which will affect the magnetostatic energy) and the intrinsic magnetic properties of the material (which will affect the magnetostatic energy and the domain wall energy). There are many ways to observe magnetic domains. Each method has a different application because not all domains are the same. In condensed matter, domains can be circular, square, irregular, elongated, and striped, all of which have varied sizes and dimensions. Previous reviews and overviews on domain observation techniques can be found in the literature [33,34,35].

### 1.4.8 Magnetic Hysteresis

Understanding magnetic hysteresis is vitally important to the development of the science of magnetism as a whole and to the advancement of practical magnetic device applications. The basic magnetization process in ferromagnetic materials is shown in Figure 1.6. For a ferromagnetic material, the field dependence of magnetization is nonlinear and at large values of  $H$ , the magnetization  $M$  becomes constant and reaches a saturation value called as  $M_s$ . However, once saturated, the reversal of magnetic field to zero does not bring the magnetization  $M$ , to zero. It still possesses a finite magnetization called as remnant magnetization ( $M_R$ ). In order to bring the remnant magnetization to zero, a reverse field is required. The magnitude of this field is called coercivity ( $H_c$ ). The  $M$ - $H$  curve in the case of ferro/ferrimagnetic materials is called as hysteresis loop. The value of  $M_s$ ,  $M_R$  and  $H_c$  determine the magnetic nature of the material. The hysteresis loop represents the energy loss during the process of magnetization and demagnetization. During one complete cycle, this amount of energy (the hysteresis loss) is proportional to the area inside the loop.

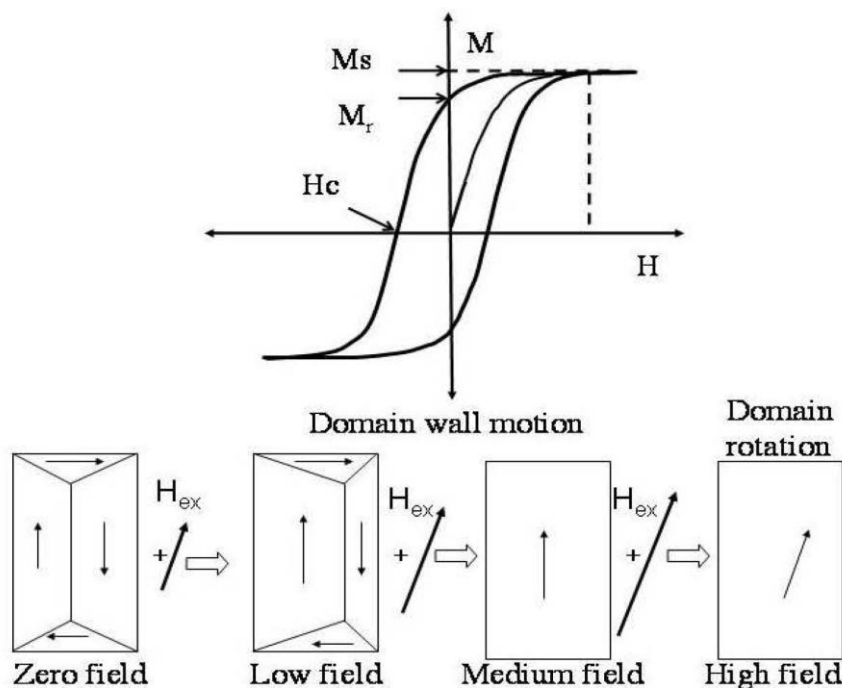


Figure 1.6. Magnetization process in ferromagnetic materials.

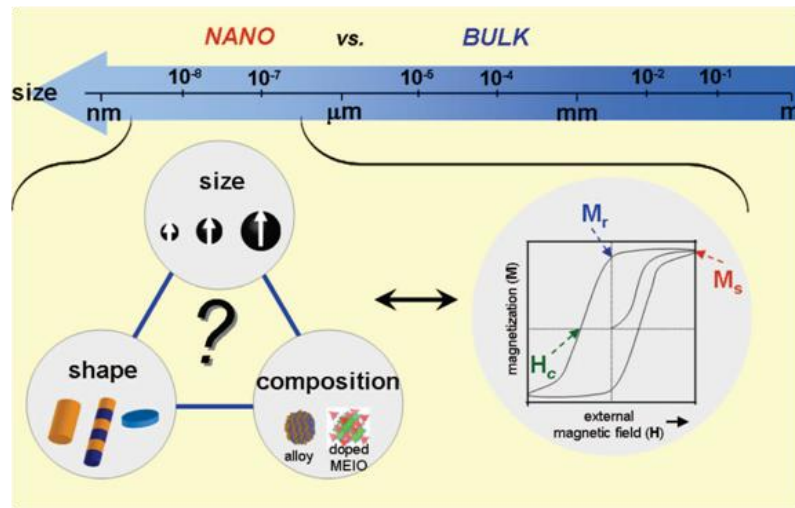


Figure 1.7. In nanometer scale, parameters such as size, shape, composition, and magnetocrystalline anisotropy strongly affect the magnetism (e.g., coercivity, saturation magnetization, remanence) of nanoparticles [17].

## 1.5 Magnetism in Nanoparticles

Many new interesting phenomena were observed in magnetic nanoparticles from their bulk counterparts. The fundamental magnetic properties such as coercivity ( $H_c$ ) and susceptibility ( $\chi$ ) are no longer permanent material characteristics and are susceptible to variations in their size, shape, and composition are shown in Figure 1.7. When the particle size of a magnetic material is reduced below a critical size limit, the thermal energy is not sufficient to overcome the coupling forces between the atoms, but is sufficient to change the direction of magnetization of the entire particle. This results in a fluctuating magnetization causing the magnetic moments to average to zero. Thus the material behaves in a similar manner to paramagnetism, except that instead of each individual atom being independently influenced by an external magnetic field, the moment of the entire particle is aligned with the field. These particles are called superparamagnetic particles. Superparamagnetism occurs when the particle size is generally in between 1-10 nm. Two key issues dominate the magnetic properties of nanoparticles, i.e., finite-size effects and surface effects. Finite-size effects result from the quantum confinement of the electrons, whereas typical surface effects are related to the symmetry breaking of the crystal structure at the boundary of each particle.

### 1.5.1 Finite Size effect

The two most studied finite-size effects in nanoparticles are the single domain limit and the superparamagnetic limit. Large magnetic particles are composed of multidomain [21,36], where regions of uniform magnetization are separated by domain walls in order to reduce the magnetostatic energy. The formation of the domain walls is a process driven by the balance between the magnetostatic energy ( $\Delta E_{MS}$ ) which increases proportionally to the volume of the materials and the domain-wall energy ( $E_{dw}$ ), which increases proportionally to the interfacial area between domains. If the sample size is reduced, there is a critical volume below which it costs more energy to create a domain wall than to support the external magnetostatic energy of the single-domain state. This critical diameter typically lies in the range of a few tens of nanometers and depends on the material. It is influenced by the contribution from various anisotropy energy terms. The critical diameter of a spherical particle,  $D_c$ , below which it exists in a single-domain state is reached when  $\Delta E_{MS} = E_{dw}$ , which implies

$$D_c \approx 18 \frac{\sqrt{AK_{eff}}}{\mu_o M^2} \quad (1.6)$$

where,  $A$  is the exchange constant,  $K_{eff}$  is anisotropy constant,  $\mu_o$  is the vacuum permeability, and  $M$  is the saturation magnetization. Typical values of  $D_c$  for some important spherical magnetic nanoparticles are reported by Xavier Batlle [37].

A single-domain particle is a uniformly magnetized region with all the moments aligned in the same direction. The magnetization will be reversed by spin rotation since there are no domain walls to move. This is the reason for the very high coercivity observed in small nanoparticles [38]. The dependence of coercivity on particle size shows behaviour similar to that schematically illustrated in Figure 1.8.

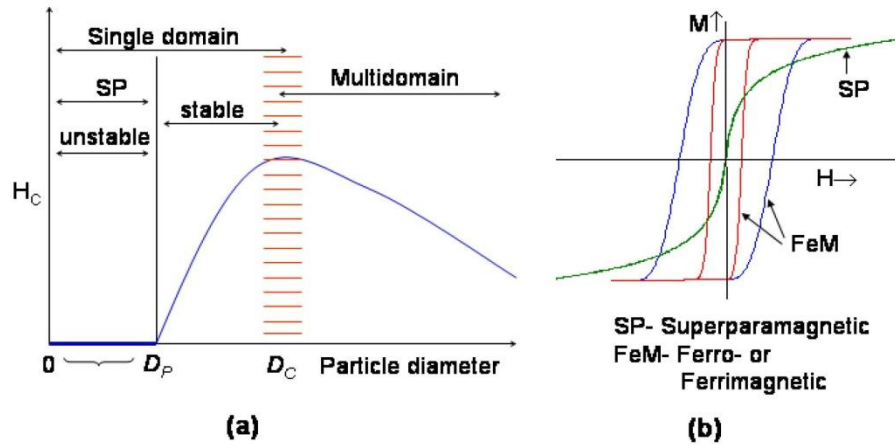


Figure 1.8. Variation of the coercivity of magnetic particles with particle diameter, and comparison of magnetization curves of typical ferro, ferri and superparamagnetic substances.

In this single-domain regime, the magnetic coercivity increases as the size of the nanoparticle increases with the relationship [39]

$$H_c = \frac{2K_u}{M_s} \left[ 1 - 5 \left( \frac{kT}{K_u V^2} \right) \right] \quad (1.7)$$

where  $M_s$  is the saturation magnetization,  $K_u$  is the anisotropy constant and  $V$  is the volume of the particles. Above the critical size ( $D > D_c$ ), multidomain magnetism begins in which a smaller reversal magnetic field is required to make the net magnetization zero. Another source for the high coercivity in a system of small particles is the shape anisotropy.

Saturation magnetization of nanoparticles is also strongly dependent on their size. Magnetic materials possess magnetically disordered spin glass [40] like layers near the surface due to the reduced spin–spin exchange coupling energy at the surface are schematically shown in Figure 1.9. In bulk material, the disordered surface layer is minimum as compared to the total volume of the material, such surface spin canting effects are negligible in case of bulk magnetic materials. For magnetic nanomaterial the surface canting effects play marked role in the saturation magnetization value ( $M_s$ ), depicted as

$$M_s = M_s(\text{bulk}) \left[ \frac{(r-d)}{r} \right]^3 \quad (1.8)$$

where  $r$  is the size,  $M_s(\text{bulk})$  is the saturation magnetization of bulk materials, and  $d$  is the thickness of disordered surface layer [41,42]. For very small nanoparticles less than  $\sim 5$  nm, such size effect on  $M_s$  is more noticeable, since internal spins of the nanoparticle also start to be canted as well as the surface spins due to increased interactions between the surface and internal spins [43]. Such size effects on magnetization have been well demonstrated in the case of magnetism-engineered iron oxide,  $\text{Fe}_3\text{O}_4$ , nanoparticles. As the size of magnetically engineered iron oxide nanoparticles increases from 4 to 6, 9, and 12 nm, the mass magnetization values change from 25 to 43, 80, and 101 emu/(g Fe), respectively as pointed out in Figure 1.9. This result shows a linear relationship upon the plotting of  $M_s^{1/3}$  vs  $r^{-1}$  as predicted in equation 1.8

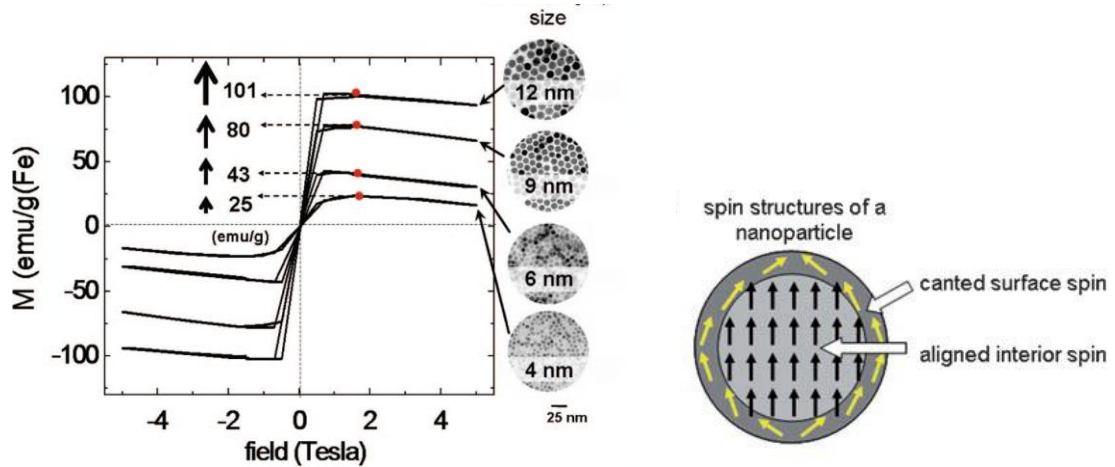


Figure 1.9. Size dependent saturation magnetisation value of magnetite nanoparticles and pictorial illustration of surface spin canting effect of nanoparticles [17].

The second important phenomenon is superparamagnetic limit which takes place in magnetic nanoparticles. The superparamagnetism can be understood by considering the behaviour of a well-isolated single-domain particle. The magnetic anisotropy energy per particle which is responsible for holding the magnetic moments along a certain direction can be expressed as follows

$$E(\theta) = K_{\text{eff}} V \sin^2 \theta \quad (1.9)$$

where  $V$  is the particle volume,  $K_{\text{eff}}$  anisotropy constant and  $\theta$  is the angle between the magnetization and the easy axis. The energy barrier  $K_{\text{eff}}V$  separates the two energetically equivalent easy directions of magnetization. With decreasing particle

size, the thermal energy,  $kT$ , exceeds the energy barrier  $K_{\text{eff}}V$  and the magnetization is easily flipped and is schematically shown in Figure 1.10.

For  $kT > K_{\text{eff}}V$  the system behaves like a paramagnet, instead of atomic magnetic moments, there is now a giant magnetic moment inside each particle. This system is named as superparamagnet. Such a system has no hysteresis and the data of different temperatures superimpose onto a universal curve of  $M$  versus  $H/T$ .

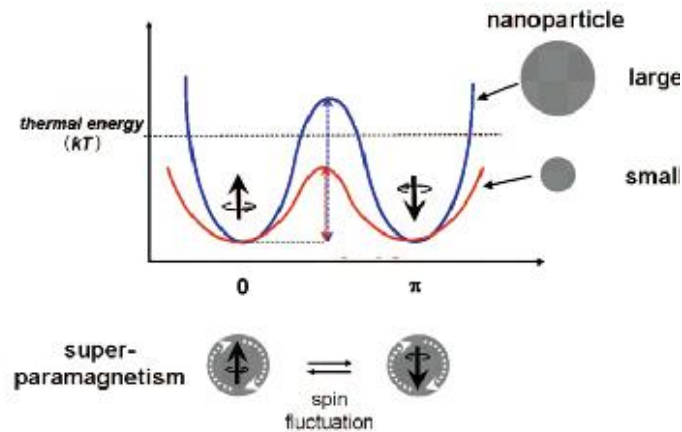


Figure 1.10. Energy diagram of magnetic nanoparticles

Cooling of a superparamagnetic particle reduces the energy of thermal fluctuations, and, at a certain temperature, the free movement of magnetization becomes blocked by anisotropy. The temperature of the transition from the superparamagnetic to the ferromagnetic state is called the blocking temperature ( $T_B$ ). The blocking temperature is related to the particle volume and the anisotropy constant. The latter can be calculated as

$$T_B = \frac{K_{\text{eff}}V}{25 k_B} \quad (1.10)$$

The blocking temperature depends on the effective anisotropy constant, the size of the particles, the applied magnetic field, and the experimental measuring time. Such size-dependent magnetism changes has been observed in  $\gamma\text{-Fe}_2\text{O}_3$  [44] and cobalt nanoparticles [45].  $\gamma\text{-Fe}_2\text{O}_3$  nanoparticles of 55 nm exhibit ferrimagnetic behavior with a coercivity of 52 Oe at 300 K, but smaller 12 nm sized  $\gamma\text{-Fe}_2\text{O}_3$  nanoparticles show superparamagnetism with no hysteresis behavior. For cobalt nanoparticles, ferromagnetic to superparamagnetic transitions occur at much lower

temperatures of 10, 20, 100, 180, and 370 K for nanoparticles with sizes of 2, 4, 6, 8, and 13 nm, respectively, in comparison to 1394 K for bulk cobalt and is pointed out in Figure 1.11. A simple and rapid way to estimate the blocking temperature is provided by dc magnetic measurements, in which zero-field-cooled and field-cooled procedures are employed. The sample is cooled from room temperature in zero magnetic field (ZFC) and in a magnetic field (FC). Then a small magnetic field is applied (about 50 Oe) and the magnetization is recorded on warming. As temperature increases, the thermal energy disturbs the system and more moments acquire the energy to be aligned with the external field direction. The number of unblocked, aligned moments reaches a maximum at  $T_B$ . Above the blocking temperature the thermal energy is strong enough to randomize the magnetic moments leading to a decrease in magnetization. A distribution of the particle sizes results in a distribution of the blocking temperatures. The same trend has been observed in oxide nanoparticles and by Zhang and co-workers [46] as shown in Figure 1.12

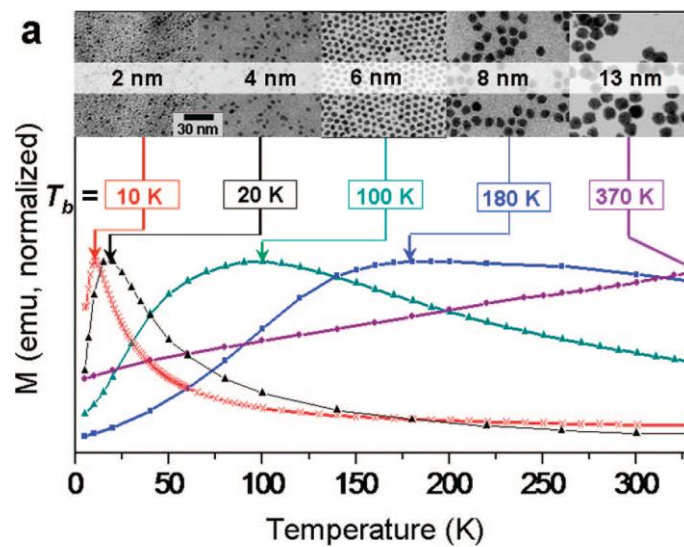


Figure 1.11. Variation of blocking temperature with respect to particle size in cobalt nanoparticles [45].

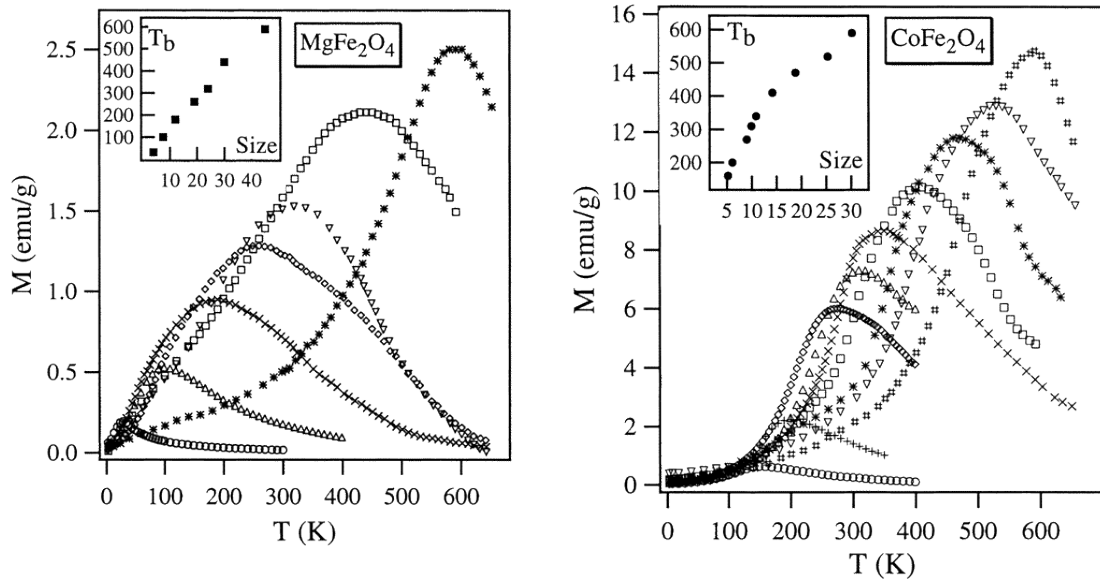


Figure 1.12. Magnetisation vs temperature of magnesium ferrite and cobalt ferrite nanoparticles [46].

As shown in Figure 1.13, the curve at room temperature ( $T > T_B$ ) shows typical superparamagnetic behavior. But below a certain temperature i.e. blocking temperature ( $T_B$ ), the particles do not have enough thermal energy to compete thermal equilibrium with the applied field during the time required for the measurement, and magnetic hysteresis appears. When small particles are cooled to a particular temperature, hysteresis will appear and superparamagnetism disappears, as shown for the curve for  $T < T_B$ . Below blocking temperature magnetization will be stable.

For superparamagnetic particles, no magnetic hysteresis is observed and a reasonable approximation is to regard these as individual spins and the Langevin equation [23] may be applied, which is given by,

$$\frac{M}{M_s} = L(\alpha) = \coth\alpha - \frac{1}{\alpha} \quad (1.11)$$

where  $\alpha = \frac{\mu H}{kT}$  and  $\mu$  is the magnetic moment of the particle and  $H$ , the applied magnetic field.

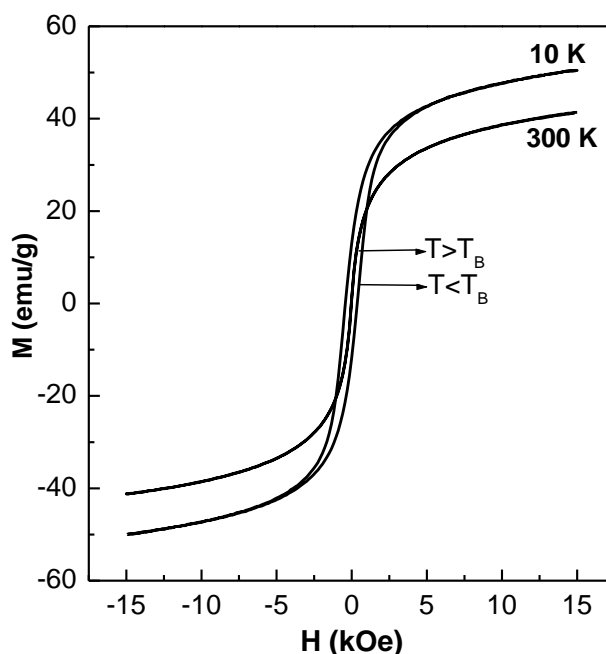


Figure 1.13. Magnetization curves of superparamagnetic iron oxide nanoparticles above and below  $T_B$

### 1.5.2 Surface Effects

As the particles size decreases, the surface area is increasing so that a large percentage of atoms are exposed to the surface in nanoparticles. Owing to this large surface atoms/bulk atoms ratio, the surface spins make an important contribution to the magnetization. This local breaking of the symmetry might lead to changes in the band structure, lattice constant and atom coordination. Under these conditions, some surface and/ or interface related effects occur, such as surface anisotropy and, under certain conditions, core–surface exchange anisotropy can occur.

Surface effects can lead to a decrease of the magnetization of small particles with respect to the bulk value. This reduction has been associated with different mechanisms, such as the existence of a magnetically dead layer on the particles surface, the existence of canted spins, or the existence of a spin-glass-like behavior of the surface spins. Recently, Ghosh et al [47] synthesized CoO nanoparticles, which shows enhanced magnetic properties with decreasing particle size. Rao et al. [48,49] pointed out that magnetism may be a universal character of all inorganic oxide

nanoparticles with a high surface-to-volume ratio, although, without more detailed explanation.

Another surface-driven effect is the enhancement of the magnetic anisotropy [50,51],  $K_{eff}$ , with decreasing particle size. This anisotropy value can exceed the value obtained from the crystalline and shape anisotropy and is assumed to originate from the surface anisotropy. In a very simple approximation, the anisotropy energy of a spherical particle with diameter  $D$ , surface area  $S$ , and volume  $V$ , may be described by one contribution from the bulk and another from the surface:

$$K_{eff} = K_v + \frac{6}{D} K_s \quad (1.12)$$

where  $K_v$  and  $K_s$  are the bulk and surface anisotropy energy constants, respectively. Bødker et al. [52] have shown that  $K_{eff}$  changes when the surfaces are modified or adsorb different molecules, which explains very well the contribution of the surface anisotropy to  $K_{eff}$ . For uncoated antiferromagnetic nanoparticles, weak ferromagnetism can occur at low temperatures (Figure 1.14f), which has been attributed to the existence of uncompensated surface spins of the antiferromagnet. Since this situation effectively corresponds to the presence of a ferromagnet in close proximity to an antiferromagnet, additional effects, such as exchange bias [53], can result. Hormes et al. [54] discussed the influence of various coatings (e.g., Cu, Au) on the magnetic properties of cobalt nanoparticles, and came to the conclusion that a complex interplay between particle core and coating determines the properties, and tuning may therefore be difficult. Organic ligands [55,56], used to stabilize the magnetic nanoparticles [57], also have an influence on their magnetic properties, that is, ligands can modify the anisotropy and magnetic moment of the metal atoms located at the surface of the particles. A magnetic coating [58] on a magnetic nanoparticle usually has a dramatic influence on the magnetic properties. The combination of two different magnetic phases will lead to new magnetic nanocomposites, with many possible applications. The most striking feature which takes place when two magnetic phases are in close contact is the exchange bias effect. A recent review of exchange bias in nanostructured systems is given by Nogus et al [53]. The exchange coupling across the interface between a ferromagnetic core and an antiferromagnetic shell or vice versa causes this effect. Exchange bias is the shift of

the hysteresis loop along the field axis in systems with ferromagnetic (FM)–antiferromagnetic (AFM) interfaces (Figure 1.14e). This shift is induced by a unidirectional exchange anisotropy created when the system is cooled below the Neel temperature of the antiferromagnet. This exchange coupling can provide an extra source of anisotropy leading to magnetization stabilization. The exchange bias effect was measured for the first time in cobalt nanoparticles surrounded by an antiferromagnetic CoO layer. There are numerous systems where the exchange bias has been observed, and some of the most investigated systems are: ferromagnetic nanoparticles coated with their antiferromagnetic oxides (e. g., Co/CoO, Ni/NiO), nitrides (Fe–Fe<sub>2</sub>N), and sulfides (Fe–FeS), ferrimagnetic–antiferromagnetic (Fe<sub>3</sub>O<sub>4</sub>–CoO), or ferrimagnetic–ferromagnetic (TbCo–Fe<sub>20</sub>Ni<sub>80</sub>) nanoparticles. Exchange biased nanostructures have found applications in many fields, such as permanent magnets, recording media, and spintronics.

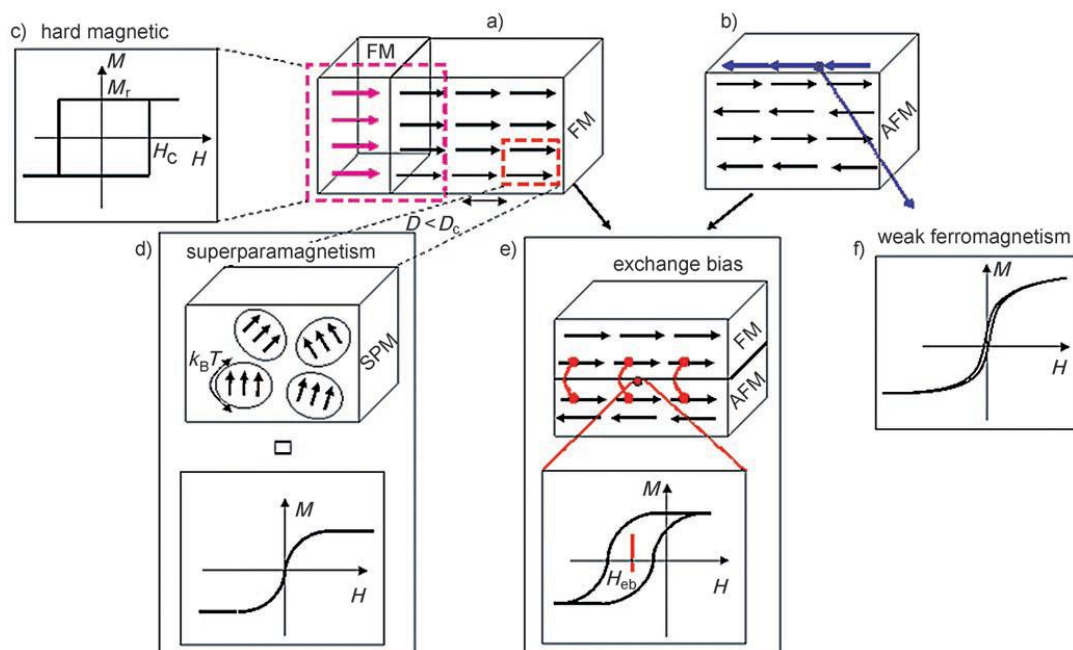


Figure 1.14. The different magnetic effects occurring in magnetic nanoparticles. The spin arrangement in a) a ferromagnet (FM) and b) an antiferromagnet (AFM);  $D$ =diameter,  $D_c$ =critical diameter. c) A combination of two different ferromagnetic phases (magenta arrows and black arrows in (a)) d) An illustration of the magnetic moments in a superparamagnet (SPM). e) The interaction (exchange coupling; linked red dots) at the interface between a ferromagnet and an antiferromagnet produces the exchange bias effect. f) Pure antiferromagnetic arises net magnetization from uncompensated surface spins (blue arrows in (b)). This Figure, is a rather simplistic view of some phenomena present in small magnetic particles [59].

### 1.5.3 Interparticle Interactions in Magnetic Nanoparticles

The magnetic properties of samples of nanoparticles are often strongly influenced by interparticle interactions. In particular, interactions can have a significant influence on the superparamagnetic relaxation.

The superparamagnetic relaxation time of a particle,  $\tau$ , is given by the Néel-Brown expression

$$\tau = \tau_0 \exp\left(\frac{K_{eff}V}{k_B T}\right) \quad (1.13)$$

where  $k_B$  is the Boltzmann's constant, and  $\tau_0 \approx 10^{-9}$  s. In some cases, the interactions result in faster relaxation and, in other cases, they result in some suppression of the relaxation.

The main types of magnetic interactions which can be present in a system of small particles are: a) dipole–dipole interactions, b) direct exchange interactions for touching particles, c) superexchange interactions for metal particles in an insulating matrix, d) RKKY (Ruderman-Kittel-Kasuya-Yosida) interactions for metallic particles embedded in a metallic matrix.

Depending on the strength of the interaction between the particles, such magnetic nanoparticles are known to change their superparamagnetic nature to spin glass-like nature [60]. Since these nanoparticles behave as if they are single domains, each particle can be considered to possess a huge, single spin called superspin [61, 62]. The strongly interacting superspins are often known as super spin glasses [63] whereas weak interaction of superspins results in superparamagnetism [64]. It is important in the applications of these materials that these superspins are noninteracting or only weakly interacting. There are many recent reports available in the literature [65] which deals with the studies on interaction behaviour [66,67] of magnetic nanoparticles [68,69]. Similar to the dispersed magnetic nanoparticles, are the magnetic nanoclusters, which also behave individually like single domains or superspins. These superspins may again interact with one another and the interaction may be of dipolar nature or any other magnetic exchange types such as superexchange

or antisymmetric Dzyaloshinskii-Moriya interaction [70,71]. Besides, the interaction between superspins depend on the size, density and nature of the cluster.

The physical concepts used for explaining the conventional spin glasses can be extended in the case of superspin glasses, due to the similarity of their response to magnetic field and relaxation behavior. Spin glasses are magnetic systems exhibiting both quenched disorder and frustration [72]. Such a behavior is observed below a temperature called spin-glass transition temperature ( $T_g$ ) or freezing temperature ( $T_f$ ). The spin glass phenomenon was first discovered in the magnetism of dilute alloys such as AuFe where RKKY interactions between the spins of magnetic atoms and conducting electrons play a major role. It is believed that in spin glasses, a localized pair of moments (spins) has equal probability of having a ferromagnetic or an antiferromagnetic interaction which results in frustration. The experimental and theoretical features of spin glasses have been discussed in detail Mydosh [73], and some important physical concepts about spin glasses are briefly explained as follows.

The spin glasses are characterized by a remarkable thermomagnetic irreversibility and relaxation properties. Several theoretical models have been developed in order to explain the unusual behavior of these materials. The Sherrington-Kirkpatrick model suggests a mean field approach and considers an infinite range of coupling between the Ising spins to form infinite energy states [74]. Whereas, the droplet model by Fisher and Huse claims that the real, short-range systems, behave quite differently and the glassy phase being described by only two pure states, related by a global inversion of the spins, and no phase transition occurring in a magnetic field [75,76].

The dynamic properties of a spin glass system are often experimentally studied by the aging, memory and chaos effects [77,78]. The relaxation of a spin glass material is logarithmically slow, and it depends on the time spent at low temperature which is otherwise known as *aging*. Aging at a temperature,  $T$ , is fully reinitialized by heating the sample above the  $T_g$ . It corresponds to the slow evolution of the system towards equilibrium, starting at the time of the quench below  $T_g$ . The peculiarities of aging and related magnetic effects in spin glasses are observed during the small temperature cycles within the temperature range of existence of spin glass features. It is important to note that aging at a higher temperature barely contributes to aging at a

lower temperature. Or in other words, the state formed at a higher temperature does not normally affect the aging at a lower temperature. This is explained by the *chaotic* aspect of the spin glass phase. Also, interesting memory effects are observed during a reverse thermal cycle. Or in other words, when the sample is heated back to the temperatures at which it has been previously aged, it *remembers* the state formed during aging. There have been various approaches derived from Parisi's solution of Sherrington-Kirkpatrick model. Here, the aging is described in terms of a random walk in the space of metastable states, and the memory and chaos (rejuvenation) effects in terms of a hierarchical organization of these metastable states, as a function of temperature. The physical picture is of the existence of a large number of nearly degenerate states at lower temperatures, these states merge again when the temperature is raised back. A droplet picture as mentioned previously, is also used to explain the aging, chaos and memory effects found in spin glasses in which at each temperature, the equilibrium spin glass state is considered to consist of a thermally activated droplet excitation of various sizes.

The existence of glassy dynamics and memory effects are also observed in some ferroelectric materials, magnetic nanoparticles and dense, frozen ferrofluids [79, 80]. They also show aging, chaos and memory effects similar to the spin glasses, but the effects are weaker in nanoparticles. The glassy nature is thought to be due to the interacting nature of magnetic nanoparticles.

## **1.6 Materials Related to the Present Work**

This thesis deals with the studies on spinel type oxides such as Magnetite, Magnesium Aluminate and Zinc Aluminate. The structural and magnetic aspects of these materials are discussed in the following sections.

### **1.6.1 Structure of spinels**

Spinel [36] are a class of chemically and thermally stable materials suitable for a wide variety of applications. The spinel lattice is composed of a close-packed oxygen arrangement in which 32 oxygen ions form a unit cell that is the smallest repeating unit in the crystal network. Between the layers of oxygen ions, there are interstices that may accommodate the metal ions. Now, the interstices are not all the

same; some which we will call A sites are surrounded by or coordinated with 4 nearest neighbouring oxygen ions whose lines connecting their centers form a tetrahedron. Thus, A sites are called tetrahedral sites. The other type of site (B sites) is coordinated by 6 nearest neighbour oxygen ions whose center connecting lines describe an octahedron. The B sites are called octahedral sites. In the unit cell of 32 oxygen ions, there are 64 tetrahedral sites and 32 octahedral sites. If all of these were filled with metal ions, of either +2 or +3 valence, the positive charge would be very much greater than the negative charge and so the structure would not be electrically neutral. It turns out that of the 64 tetrahedral sites, only 8 are occupied and out of 32 octahedral sites, only 16 are occupied. If, as in the mineral, spinel, the tetrahedral sites are occupied by divalent ions and the octahedral sites are occupied by the trivalent ions. Spinel-type oxides have the general formula  $AB_2O_4$  where A and B are two different cations of comparable ionic sizes. However, the occupation of these two sites in the spinel-type oxides is decided by various factors, such as ionic size, cationic charge, electron distribution, electronic state, etc., so that no simple rule can predict the actual ionic distribution [81]. The degree of distribution or the relative distributions of A and B ions in the two sites, is determined by the competition between many of these factors. Therefore, spinels are of different types such as (i) normal spinel, where the A and B cations are distributed in the tetrahedral and octahedral sites, respectively; (ii) inverse spinel, where the A cations are in the octahedral sites and one-half of the B cations are pushed to the tetrahedral sites, and (iii) mixed spinel, where both the A and B cations are randomly distributed in both the sites [82]. Considering the distribution of cations in the two different sites, spinels are represented by the general formula  $(A_{1-x}B_x)[A_xB_{2-x}]O_4$ . In this formula, the brackets ( ) and [ ] represent the tetrahedral and octahedral sites, respectively, and  $x$  denotes the inversion parameter or the degree of inversion. The variables  $x = 0$  and  $x = 1$  are for normal and inverse spinels, respectively [83].

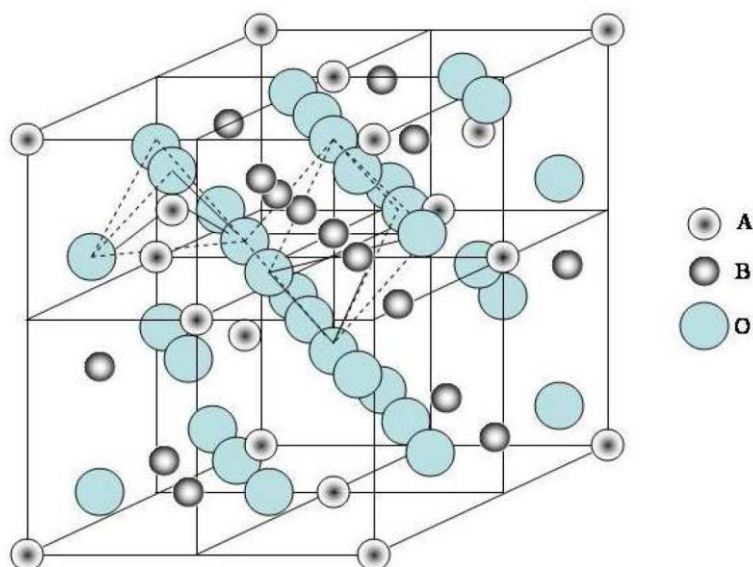


Figure 1.15. Structure of Spinel

### 1.6.2 Magnesium Aluminate

Magnesium aluminate comes under the category of normal spinels. In the original spinel,  $\text{MgAl}_2\text{O}_4$ , under equilibrium conditions, the A ion, Mg, is occupied in the tetrahedral sites and the B ion, Al, is occupied in the octahedral sites. Previous studies showed that  $\text{MgAl}_2\text{O}_4$  has partially inverse spinel structure [84,85]. The disordered behavior of bulk  $\text{MgAl}_2\text{O}_4$  and the deviation of the structural parameters as a function of temperature have been studied by solid-state NMR [86], X-ray diffraction [87], neutron diffraction [88], ESR [89], and electrical conductivity measurements [90]. A recent  $^{27}\text{Al}$  MAS NMR study, on  $\text{MgAl}_2\text{O}_4$  precursor powders of very high specific surface area synthesized at low temperatures, has reported the presence of a five-coordinated Al site apart from the octahedral and tetrahedral Al coordinated sites [91].

### 1.6.3 Zinc Aluminate

Zinc aluminate is also considered as a normal spinel where the tetrahedral site is occupied by Zn ion and octahedral sites are occupied by Al ion. Previously it has been reported that bulk  $\text{ZnAl}_2\text{O}_4$  has very small amount of inversion and its dielectrical, thermo physical, elastic and structural properties have been studied [92].

### 1.6.4 Magnetite

Magnetite [93,94] is the black ferrimagnetic material having the chemical formula  $\text{Fe}_3\text{O}_4$  containing both  $\text{Fe}^{2+}$  and  $\text{Fe}^{3+}$ . It has the inverse spinel structure. They reflect the diversity of research for the past decades. Magnetite differ from most other iron oxides is that it contains both divalent and trivalent ions. The structure is that of an inverse spinel has the general formulae  $\text{B}[\text{AB}]\text{O}_4$  where  $\text{A}=\text{Fe}^{2+}$ ,  $\text{B}=\text{Fe}^{3+}$  and the bracket denotes octahedral sites. Magnetite has a face centered cubic unit cell based on oxygen arrangement in which 32 oxygen ions form a unit cell that is the smallest repeating unit in the crystal network. The structure consists of octahedral and mixed tetrahedral/octahedral sites. Eight tetrahedral sites are distributed between  $\text{Fe}^{2+}$  and  $\text{Fe}^{3+}$  ie, trivalent ions occupy both tetrahedral and octahedral sites. There are 8 formula units per unit cell and the unit cell edge length is 0.839 nm.

### 1.7 Magnetism of Iron Oxides

Iron oxides are ferrimagnetic at room temperature. The exchange forces between the metal ions in a ferrimagnetic material will act through the oxygen ions by means of the indirect exchange mechanism, which is best known as the superexchange interaction. If there are  $n$  identical magnetic ions per unit volume, with a fraction  $x$  located on A site and a fraction  $y = (1-x)$  on B site with  $\mu_A$  and  $\mu_B$  as the average moments of A and B ions, respectively, in the the direction of the field at temperature  $T$  ( $\mu_A \neq \mu_B$ , being different sites), then the total magnetization on the two sublattices is

$$M = M_A + M_B = xM_a + yM_b \quad (1.14)$$

The molecular field acting on the sublattice A is

$$H_m A = -\gamma_{AB}M_B + \gamma_{AA}M_A \quad (1.15)$$

and molecular field acting on the sublattice B is

$$H_m B = -\gamma_{AB}M_A + \gamma_{BB}M_B \quad (1.16)$$

where  $M_A$  and  $M_B$  are the magnetization of the A and B sublattices, respectively.  $\gamma_{AA}$  and  $\gamma_{BB}$  define the strength of the A-A and B-B interactions and  $\gamma_{AB}$  defines that of the A-B interaction. In the equations 1.14 and 1.15, the molecular field coefficients  $\gamma$  are regarded as positive quantities and the negative sign corresponds to the antiparallel interaction between A and B ions, whereas the positive sign corresponds to the parallel interaction between the same site ions. The magnetization of each sublattice obeys the Curie law,

$$M_A = \frac{C_A}{T} (H + H_{mA}) \quad (1.17)$$

$$M_B = \frac{C_B}{T} (H + H_{mB}) \quad (1.18)$$

Since the Curie constants  $C_A$  and  $C_B$  are not identical for the two different sites, the above equations are modified by introducing the term density of ferrimagnetic materials on the right hand sides and now putting the values of  $H_{mA}$  and  $H_{mB}$  in equations 1.16 and 1.17, the magnetization on the two different sites are obtained as

$$M_A = \frac{\rho C_A}{T} (H + \gamma_{AA} M_A - \gamma_{AB} M_B) \quad (1.19)$$

and

$$M_B = \frac{\rho C_B}{T} (H + \gamma_{BB} M_B - \gamma_{AB} M_A) \quad (1.20)$$

After solving this two equations, the mass susceptibility,  $\chi$ , of a ferrimagnetic material is obtained as

$$\chi = \frac{M}{\rho H} = \frac{T}{C} + \frac{1}{\chi_0} - \frac{K}{T-\theta} \quad (1.21)$$

where  $C = C_A + C_B$  and  $K$  is a constant. Although  $\theta$  has the dimension of temperature, it has no physical significance above the Curie temperature. Therefore,

$$\chi = \frac{C}{T-\theta} \quad (1.22)$$

Thus, from equation 1.20, it is concluded that above the Curie temperature ferrimagnetic materials obey the Curie-Weiss law [95,96].

Magnetization in ferrites occurs from the uncompensated antiferromagnetism, so the magnitude of magnetization depends on composition, cation distribution and the relative strength of the possible interactions. Since cation-cation distances are large in ferrites due to their crystal structure, direct exchange interactions are negligible. The major interaction occurs in ferrites is the superexchange interaction between octahedral and tetrahedral cations or A-O-B interactions. The next acceptable interaction is B-O-B superexchange. However A-O-A interaction [97] is not coming into picture, as it is very weak. The types of interactions in ferrite and the angle between them are shown in Figure 1.16 schematically. The strength of exchange interactions control the saturation magnetization and the Curie temperature of the ferrites and this exchange interaction is controlled by cation distribution.

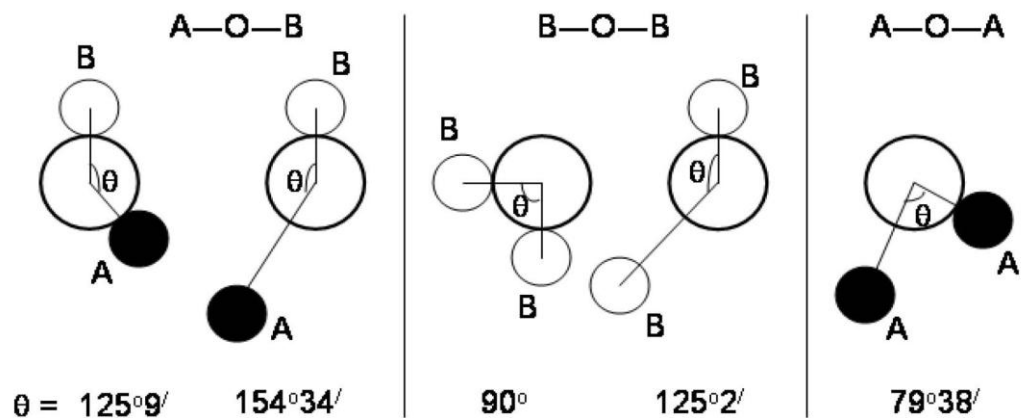


Figure 1.16. Different types of interactions for different types of lattice sites in spinels [36].

Magnetite is ferrimagnetic at room temperature and has a Curie temperature of 850 K. The two different cation sites in the structure, tetrahedral (A) occupied by  $\text{Fe}^{3+}$  and octahedral occupied by  $\text{Fe}^{3+}$  and  $\text{Fe}^{2+}$  as explained in the previous section. These sites form the basis for two interpreting magnetic sublattices. Below  $T_c$ , the spin on the A and B sites are antiparallel and in addition, the magnitude of two types of spin are unequal. This results the ferrimagnetism. The main type of interaction is antiferromagnetic coupling via the  $127^\circ \text{Fe}_A\text{-O-Fe}_B$  linkage and is stronger coupling on octahedral sites. On the latter sites the electrons are thermally delocalised over the

$\text{Fe}^{2+}$  and  $\text{Fe}^{3+}$  ions and it is this localisation that is responsible for the high conductivity of magnetite. The exchange constants are -28, -18, 3 J(K) for  $J_{AB}$ ,  $J_{AA}$ , and  $J_{BB}$ , respectively [94]. At 118 K ( the Verwey transition temperature), an ordered arrangement of  $\text{Fe}^{2+}$  and  $\text{Fe}^{3+}$  ions on the B sites exist and this inhibits electron delocalisation. The preferred direction of magnetisation is along the 8[111] cube diagonals. Magnetite nanoparticles behave as superparamagnetic at room temperature.

The distribution of the sizes, shapes, surface defects, and phase purity are only a few of the parameters influencing the magnetic properties, which makes the investigation of the magnetism in small particles very complicated.

## 1.8 Synthesis of Iron Oxides Nanoparticles

Iron oxide nanoparticles [98,99] with well-defined morphology have attracted considerable attention for their structural characteristics that endow them for a wide range of potential applications [100,101] However, it is a great challenge to develop simple and reliable synthetic methods for the synthesis [102] of magnetic materials with designed chemical components and controlled morphologies, which strongly affect the properties of magnetic materials. The first main challenge of the synthesis consists of defining experimental conditions, leading to a monodisperse population of magnetic nanoparticles of suitable size. The second critical point is to select a reproducible process that can be industrialized without any complex purification procedure. Numerous chemical methods can be used to synthesize magnetic nanoparticles such as microemulsions [103], sonochemical reactions [104], hydrothermal reactions [105], polymeric precursor method [106], and electrochemical synthesis [107]. These methods have been used to prepare particles with homogeneous composition and narrow size distribution. It is well known short burst of nucleation followed by slow controlled growth is critical to produce monodispersed nanoparticles. However, the most common method for the production of iron oxide nanoparticles is the chemical coprecipitation method by using iron salts [108].

The first controlled preparation of superparamagnetic iron oxide particles using alkaline precipitation of  $\text{FeCl}_3$  and  $\text{FeCl}_2$  was performed by Massart [109]. In the original synthesis, magnetite ( $\text{Fe}_3\text{O}_4$ ) particles were roughly spherical, and their diameter measured by XRD was 12 nm. The disadvantage of these aqueous based

syntheses is that the pH value of the reaction mixture has to be adjusted in both the synthesis and purification steps, and the process toward smaller monodisperse nanoparticles has only very limited success. It is well known that a short burst of nucleation and subsequent slow controlled growth is crucial to produce monodisperse particles. Controlling these processes is therefore the key in the production of monodisperse iron oxide magnetic nanoparticles. However, the synthesis of monodisperse magnetic oxide nanocrystals has recently been reported

Recently Zhao [110] and co-workers synthesised magnetite nanoparticles of different morphology by polyol process. In this process, a precursor compound is suspended in a liquid polyol which act as a reducing agent as well as a stabilizer. The suspension is stirred and heated to a given temperature that can reach the boiling point of the polyol. By adjusting the concentration of KOH in polyol and iron source, Lijun Zhao and co-workers synthesised magnetite nanoparticles of various morphologies, which exhibit excellent magnetic properties.

The synthesis of monodisperse, spherical particles with anisotropic superparamagnetic susceptibility and homogeneous biphasic geometry was done by Yuet and group [111], which shows promising applications ranging from fundamental studies on self-assembly to the development of photonic crystals and drug delivery systems. By considering Janus particles, the two functionalities in the same particle like the god in the roman religion represented with two heads placed back to back so that he might look in two directions at the same time. This Janus type superparamagnetic hydrogel was synthesised by microfluidic pathway.

At the beginning of the last century, the controlled self assembly of iron oxide nanoparticles has become an area of increasing interest. Xinlei Huang [112] and his team explored the templated self-assembly of brome mosaic virus (BMV) capsids around negatively charged iron oxide NPs leading to hybrid magnetic virus-like particles. The used phospholipid micelle approach is to obtain a magnetic nanoparticle template able to promote self-assembly of a protein cage and result in a virus like nanoparticles. He demonstrates a convenient and powerful way and the concept can be generalized to many types of nanoparticle assembly, such as colloidal crystallization, nanoparticle superlattices, and various types of interfacial mediation using nanoparticles.

The synthesis of magnetic nanoparticles, covering a wide range of compositions and tuneable sizes, has made substantial progress, especially over the past decade. Different kinds of monodisperse spherical nanocrystals with controllable particle sizes and compositions have been synthesized by a wide range of chemical synthetic procedures. However, mechanisms of nucleation and growth during particle formation are still challenges to be faced in the coming years. An unavoidable problem associated with nanoparticles is their intrinsic instability over long periods of time. Such small particles tend to form agglomerates to reduce the energy associated with the high surface area/volume ratio of the nanosized particles. Consequently, it is crucial to develop coating strategies to chemically improve the stability of the magnetic nanoparticles.

### **1.9 Stabilisation of Iron Oxides Nanoparticles**

The stabilization of the iron oxide particles is crucial to obtain magnetic colloidal ferrofluids that are stable against aggregation in both a biological medium and a magnetic field. The stability of a magnetic colloidal suspension results from the equilibrium between attractive and repulsive forces. Theoretically, four kinds of forces can contribute to the interparticle potential in the system. (a) van der Waals forces induce strong short-range isotropic attractions. (b) The electrostatic repulsive forces can be partially screened by adding salt to the suspension. The theoretical description of these two forces is known as the Derjaguin-Landau-Verwey-Overbeek (DLVO) theory [113]. For magnetic suspensions, magnetic dipolar forces between two particles must be added. These forces induce anisotropic interactions, which are found to be globally attractive if the anisotropic interparticle potential is integrated over all directions. Finally, steric repulsion forces have to be taken into account for coated particles [114]. Stabilization of magnetic particles can be achieved by playing on one or both of the two repulsive forces: electrostatic and steric repulsion. Controlling the strength of these forces is a key parameter to elaborate particles with good stability. The steric force is difficult to predict and quantify. It is quite well-described theoretically for polymers. It depends, among other parameters, upon the molecular weight of the polymer and its density [115]. The electrostatic repulsion can be followed through the knowledge of the diffusion potential that may be very close to the zeta potential [116] and the Debye-Huckel length that mainly depends upon the

ionic strength and pH of the solution. A way to test electrostatic stability is to follow the aggregation kinetics of colloidal suspensions by varying the salt concentration. This can be achieved through the stability factor ( $W$ ) that measures the effectiveness of the potential barrier in preventing the particles from aggregation.  $W$  is defined as the ratio of the number of collisions between particles and the number of collisions resulting in aggregation. It can therefore be expressed as  $W = \frac{K_{fast}}{K}$ , where  $K_{fast}$  is the rate constant describing rapid aggregation (every collision leads to an aggregation) and  $K$  is the aggregation rate constant at the salt concentration used. This stability factor can be achieved through light scattering (static or dynamic) or turbidimetric measurements [117,118]. The stability factor as a function of added salt gives access to the critical concentration of coagulation. At this concentration, the double electrostatic layer is entirely suppressed and  $K = K_{fast}$  becomes independent of the salt concentration.

In iron oxide, the surface iron atoms act as Lewis acids and coordinate with molecules that donate lone-pair electrons. Therefore, in aqueous solutions, the Fe atoms coordinate with water, which dissociates readily to leave the iron oxide surface hydroxyl functionalized. These hydroxyl groups are amphoteric and may react with acids or bases [119]. Dependent upon the pH of the solution, the surface of the magnetite will be positive or negative. The isoelectric point is observed at pH 6.8. Around this point [point of zero charge (PZC)], the surface charge density ( $\Sigma$ ) is too small and the particles are no longer stable in water and flocculate. Playing on both electrostatic and steric stabilization is then necessary to obtain stable iron oxide nanoparticles. The surface of iron oxide nanoparticles can be stabilised by using functional groups including carboxyates, phosphates, amines and sulphates [120] which binds to the surface through OH groups adsorbed on the surface. So many reports are available in the literature for the surface modification [121,122] of iron oxide nanoparticles [123,124].

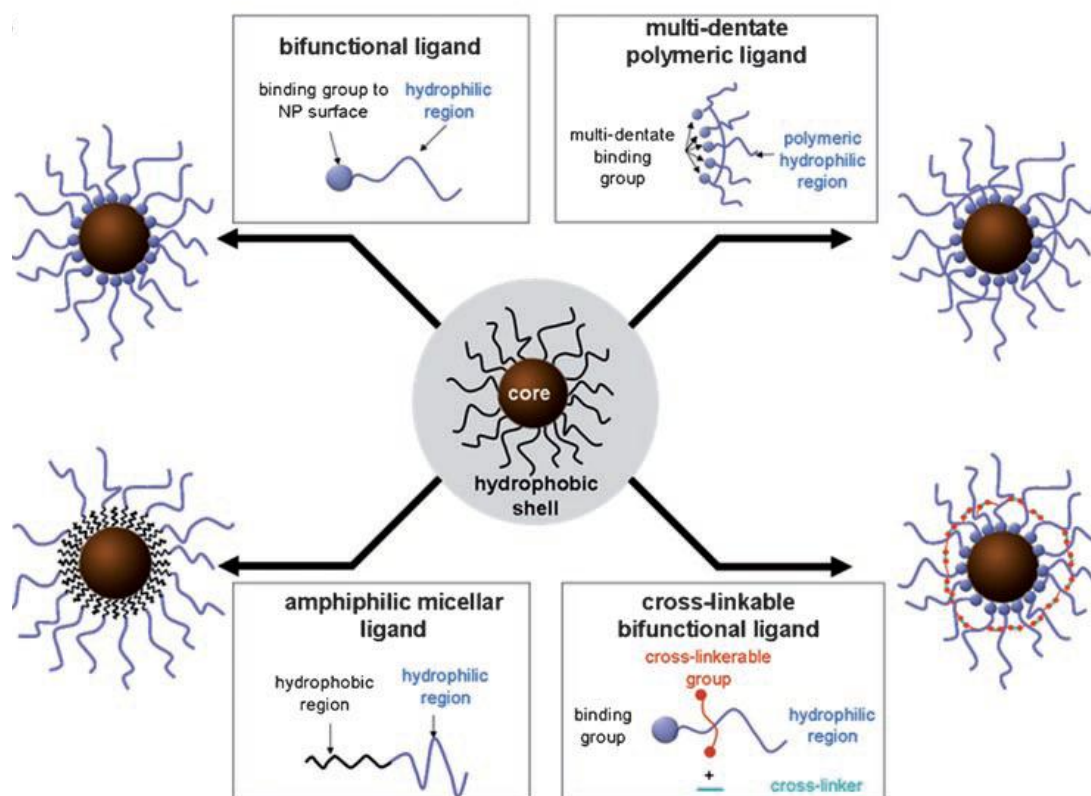


Figure 1.17. Surface modification strategies for designing MNP probes with high colloidal stability [102].

## 1.10 Application of Iron Oxides Nanoparticles

### 1.10.1 Biomedical Applications

Magnetic nanoparticles (MNPs) can be used in a wide variety of biomedical applications [125], ranging from contrast agents for magnetic resonance imaging to the deterioration of cancer cells via hyperthermia treatment ensemble in Figure 1.18. Most of these promising applications require well-defined and controllable interactions between the MNPs and living cells. A novel and straightforward coating method was recently developed, enabling stable particle functionalization. Furthermore, this functionalization method allows the introduction of a tunable coating that can be specifically adapted according to the application, thereby ensuring more controllable cellular interactions, and paving the way to a bright future in medicine. Superparamagnetism is particularly useful in applications such as externally guided drug delivery, hyperthermia, etc.

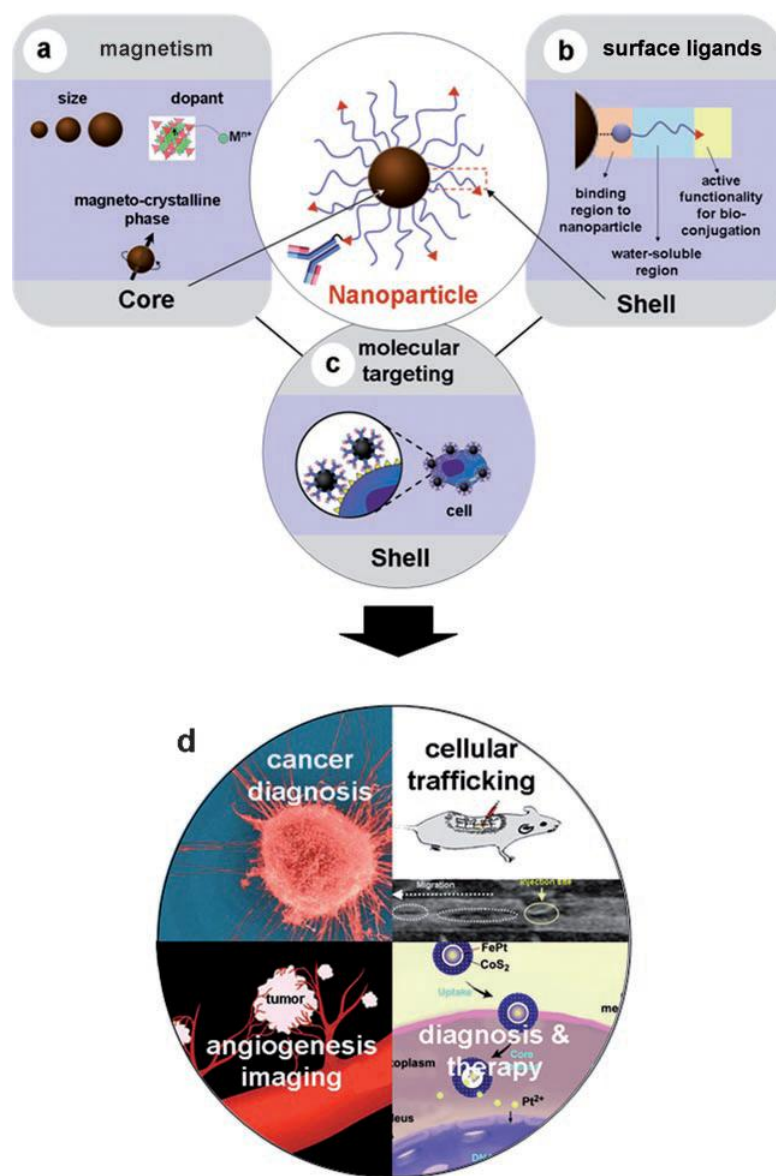


Figure 1.18. Tailored MNPs for molecular and cellular magnetic resonance imaging (MRI). a) Controlling the magnetism of the nanoparticles core, b) tailoring the surface ligands of the nanoparticle shell, c) the molecular targeting capability of biomolecule-conjugated nanoparticles. d) High performance utilizations of nanoparticles for molecular and cellular MRI [102].

### 1.10.1.1 Iron oxide nanoparticles for MRI

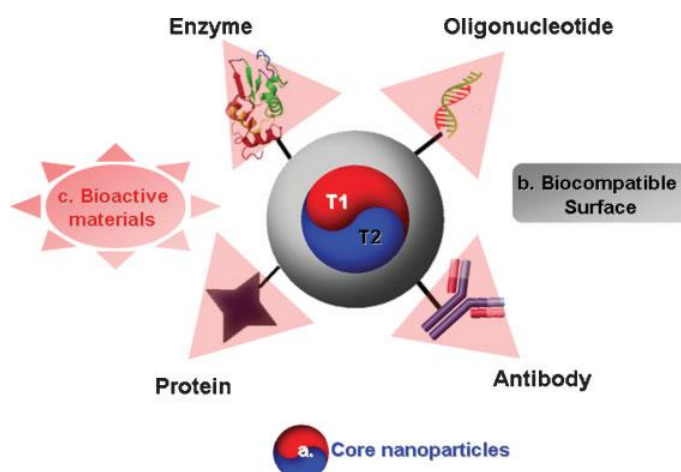


Figure 1.19. The structure of MRI contrast agent based on nanoparticles [126].

The contrast mechanism is more complicated for MRI [127], where the contrast enhancement occurs as a result of the interaction between the contrast agents and neighbouring water protons, which can be affected by many intrinsic and extrinsic factors such as proton density and MRI pulse sequences. The basic principle of MRI [128,129] is based on nuclear magnetic resonance (NMR) together with the relaxation of proton spins in a magnetic field. When the nuclei of protons are exposed to a strong magnetic field, their spins align either parallel or antiparallel to the magnetic field. During their alignment, the spins precess under a specified frequency, known as the Larmor frequency. When a resonance frequency in the radio-frequency (RF) range is introduced to the nuclei, the protons absorb energy and are excited to the antiparallel state. After the disappearance of the RF pulse, the excited nuclei relax to their initial, lower-energy state. There are two different relaxation pathways.

- Longitudinal or  $T_1$  relaxation
- Transverse or  $T_2$  relaxation

Longitudinal relaxation is due to energy exchange between the spins and surrounding lattice (spin-lattice relaxation), re-establishing thermal equilibrium. As spins go from a high energy state back to a low energy state, RF energy is released back into the surrounding lattice. Transverse or  $T_1$  relaxation, involves the decreased net magnetization ( $M_z$ ) recovering to the initial state. Under an applied magnetic field

( $B_0$ ), a magnetic dipole moment  $m$  is induced in superparamagnetic nanoparticles. When water molecules diffuse into the periphery (outer sphere) of the induced dipole moment, the magnetic relaxation processes of the water protons are perturbed and the spin–spin relaxation time ( $T_2$ ) is shortened. Such changes result in the darkening of the corresponding area in  $T_2$ - weighted MR images (Figure 1.20). The degree of the  $T_2$  contrast effect is typically represented by the spin–spin relaxivity  $R_2$  ( $R_2=1/T_2$ ), where higher values of  $R_2$  result in a greater contrast effect.

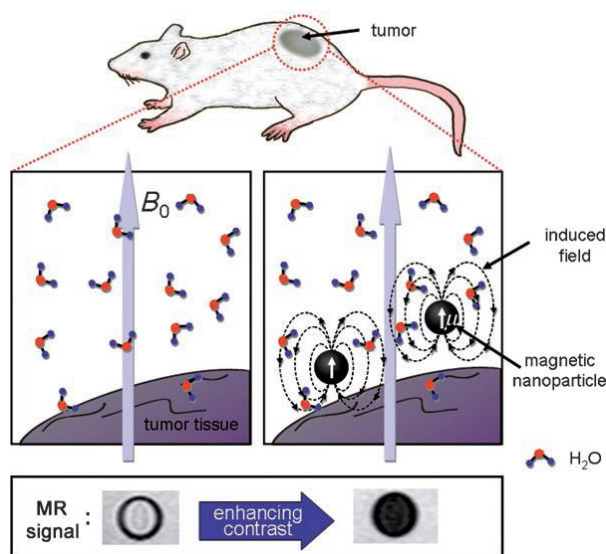


Figure 1.20. MR contrast effects of MNPs. Under an external field ( $H_0$ ), MNPs are magnetized with a magnetic moment of  $m$  and generate an induced magnetic field which perturbs the nuclear spin relaxation processes of the water protons. This perturbation leads to MR contrast enhancement which appears as a darkening of the corresponding section of the image [102].

One important parameter for the MR contrast-enhancement effect of MNPs is their size. In the ideal case, all of the magnetic spins in a bulk magnetic material are aligned parallel to the external magnetic field. However, in the nanoscale regime, surface spins tend to be slightly tilted to form a magnetically disordered spin-glass-like surface layer (Figure 1.9) [40]. Such surface spin-canting effects of MNPs have a significant influence on their magnetic moments and MR contrast-enhancement effects. This effect is size dependent and is well demonstrated in the case of magnetism-engineered iron oxide (MEIO,  $Fe_3O_4$ ) nanoparticles, where the variation of their size from 4 nm, 6 nm, 9 nm, and 12 nm results in mass magnetization values of 25, 43, 80, and 101 emu per gram Fe, respectively (Figure 1.21) [130]. As the nanoparticle size decreases, the surface effect becomes more pronounced and is

reflected in the reduced net magnetic moment. Such size dependent magnetism directly influences the MR enhancement effect. The relaxivity coefficient ( $r_2$ ) gradually increases for 4 nm, 6 nm, 9 nm, and 12 nm sized nanoparticles, respectively, which is shown by the MR contrast changing from light gray to black.

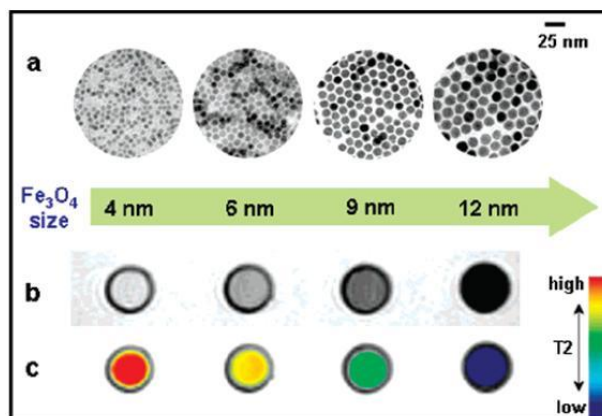


Figure 1.21. Nanoscale size effect of magnetite nanoparticles on magnetism and MR contrast effects [129].

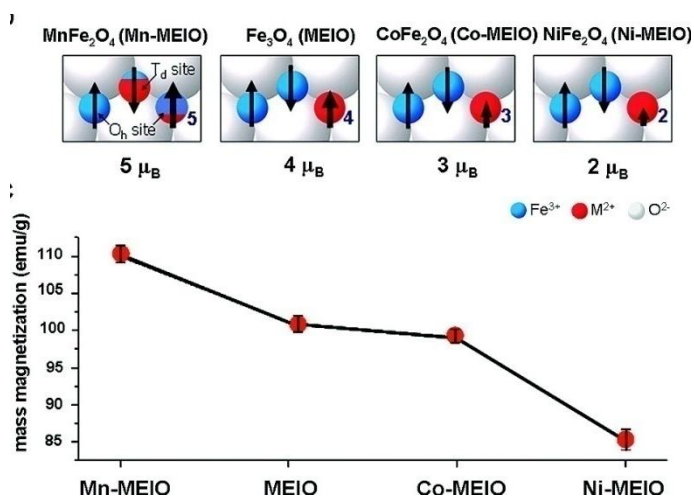


Figure 1.22. Dopant dependent effect on magnetisation values and effect on MR contrast [17].

The magnetism of nanoparticles can be greatly influenced by doping with magnetically susceptible elements. This is demonstrated for  $MFe_2O_4$  nanoparticles in which  $Fe^{2+}$  ions are replaced by other transition-metal dopants  $M^{2+}$  where  $M = Mn, Ni, Co$ . These metal-doped MEIO nanoparticles can induce significant MR contrast-enhancement effects. Under T2-weighted MR scans,  $MnFe_2O_4$  (MnMEIO) shows the

strongest MR contrast effect than other ferrite nanoparticles was reported by Lee and co-workers [131] and is pointed out in Figure 1.22.

### **1.10.1.2 Iron oxide nanoparticles for Magnetic fluid hyperthermia**

Magnetic fluid hyperthermia (MFH) cancer treatment involves injecting a fluid containing magnetic nanoparticles directly into tumors. When placed in an alternating magnetic field with frequencies similar to FM radio signals, the nanoparticles generate heat and destroy the tumours. This minimally invasive procedure, unlike laser, microwave, and ultrasound hyperthermia, prevents unnecessary heating in healthy tissues because only the magnetic nanoparticles absorb the magnetic field. The use of hyperthermia to treat cancer has been a recent topic of research. Magnetic fluid hyperthermia offers particularly promising capabilities for treating several types of cancer.

The body maintains a normal temperature of 37°C. Healthy cells, however, can survive temperatures up to 42°C. According to the National Cancer Institute, hyperthermia cancer treatment kills cancerous cells by elevating their temperatures to the therapeutic temperature range, 42-45°C. This approach can destroy tumors with minimal damage to healthy tissues and, therefore, limit negative side effects. Currently, oncologists often use hyperthermia cancer treatment in combination with radiotherapy and chemotherapy. In addition to eliminating many cancerous cells, hyperthermia can make resistant cells more vulnerable to other treatments.

Gilchrist [132] and others proposed the use of magnetic materials in hyperthermia in 1957. The particles used in hyperthermia exhibit ferro- or ferrimagnetic properties. Ferro- and ferrimagnetic particles display magnetism even in the absence of an applied magnetic field. Pankhurst and others [133] also describe heating in magnetic nanoparticles. Particles with diameters of 10 nanometers or less typically demonstrate superparamagnetic properties. The magnetic moments of superparamagnetic nanoparticles are randomly reoriented by the thermal energy of their environment and do not display magnetism in the absence of a magnetic field. Unlike ferro- and ferrimagnetic materials, they do not aggregate after exposure to a magnetic field [134]. Aggregation can hinder the body's efforts to remove the nanoparticles. Therefore, superparamagnetic nanoparticles are ideal candidates for

hyperthermia cancer treatment. Magnetic fluids generally consist of magnetic nanoparticles dispersed in water or a hydrocarbon fluid. For medical applications, the biocompatibility of both the fluid and nanoparticles must be considered. The fluid must have a neutral pH and physiological salinity. The particles should remain evenly dispersed throughout the fluid, and must therefore be small enough to avoid precipitation due to gravitational forces. In addition, the magnetic material should not be toxic. The established biocompatibility of magnetite ( $\text{Fe}_3\text{O}_4$ ) makes it a common choice. Magnetic fluid hyperthermia cancer treatments must maintain therapeutic temperatures in diseased tissues for approximately 30 minutes [132]. Excessive heating, however, can cause unwanted charring. Nanoparticles with low-Curie temperatures – defined as the temperature when the material loses its magnetic moment – heat until they reach the Curie temperature and then remain ineffective unless their temperature falls below the Curie temperature. Nanoparticles with Curie temperatures near the therapeutic range can efficiently maintain temperatures between 42 and 45°C and therefore enhance magnetic fluid hyperthermia. These self-regulating nanoparticles ensure diseased tissues reach the necessary temperatures while preventing excessive heating and damage to surrounding healthy tissues. Now a days, increased heating rates of magnetic fluids are an important challenge in order to minimize dosages of magnetic fluids needed to reach therapeutic temperatures in magnetic fluid hyperthermia (MFH) [135,136]. Possible approaches to increase heating rates of super- paramagnetic particles for MFH would be to increase the anisotropy of the nanoparticles (shape or magnetocrystalline) or increasing the field strength used for treatment. Lot of enchanting research articles are found in the literature regarding the use of iron oxide nanoparticles for magnetic fluid hyperthermia [137,138].

### **1.10.1.3 Iron oxide nanoparticles for the treatment of Osteoporosis**

Bone diseases (including osteoporosis, osteoarthritis and bone cancer) are of great concern to the medical world. These bone diseases has been studied for a number of years, no current effective prevention and treatment methods exist for this disease. There are several major barriers that exist for the use of any pharmaceutical agents to stimulate new bone formation. First, the agents can cause non-specific bone formation in areas not desirable. This is because these agents are often delivered in

non-specific ways (such as through the mouth, directly into the blood stream, etc.). Second, if delivered locally to the tissue around the area of low bone density, they rapidly diffuse to adjacent tissues which limit their potential to promote prolonged bone formation in targeted areas of weak osteoporotic bone. For these reasons, researchers developed novel drug-carrying systems that will specifically attach to osteoporotic (not healthy) bone. Moreover, some of these novel drug carrying systems will then distribute pharmaceutical agents locally to quickly increase bone mass.

In order to be used effectively in fighting diseases, specific surface chemistry of the nanoparticles need to be tailored for their desired biomedical applications. Magnetic nanoparticles [139,140] are also of interest and the main interest for the use of magnetic nanoparticles in biomedical applications is that an inhomogeneous external magnetic field exerts a force on them, and thus they can be manipulated or transported to a specific diseased tissue by a magnetic field gradient. They also have controllable sizes, so that their dimensions can match either that of a virus (20–500 nm), of a protein (5–50 nm) or of a gene (2nm wide and 10–100 nm long). In addition, magnetic particles are of interest because they do not retain any magnetism after removal of the magnetic field.

Recently Thomas Webster and his group [141] successfully synthesised iron oxide nanoparticles functionalised by calcium phosphate and found that these nanoparticles are suitable candidate for orthopaedic applications. Specifically in this study, efforts will focus on the prolonged release of bioactive agents to efficiently regenerate enough bone for a patient to return to a normal active lifestyle. One potential advantage of formulating CP magnetic nanoparticles is that as the magnetic particles accumulate, e.g., in bone tissue, they can play an important role in detection through MRI to locate, monitor and control drug activities.

#### **1.10.1.4. Iron oxide for Drug targeting**

Drug targeting has emerged as one of the modern technologies for drug delivery. Superparamagnetic iron oxide nanoparticles in combination with an external magnetic field allow delivering particles to the desired target area and fixing them at the local site while the medication is released and acts locally (Magnetic drug

targeting). The mentioned new technologies using SPION allow the minimization of systemic side effects.

Drug targeting [142] involves passive, active or physical targeting. In passive targeting the distribution of the drugs within the body occurs through drug and carrier properties that are unchanged. Active targeting is achieved with mechanisms that allow direct targeting of drugs and/or carriers to specific cells, tissues or organ systems through specific recognition mechanisms. Physical targeting allows distribution of drugs and carrier systems through external influences, such as magnets in the case of SPIONs.

The use of colloidal systems, where substances with a very fine distribution and particle size between 5 and 300 nm are used as carrier systems, changes the distribution pattern of drugs within the body. Apart from nanoparticles, also microparticles [143], microemulsions [144], liposomes [145], niosomes [146] and pharmacosomes [147] belong to this group. A complete characterization of the particulate system is necessary to make a decision whether the use of a nanocarrier system is appropriate for a specific *in vivo* application. Nanoparticles can be described with the following physicochemical properties depending upon vital factors for their distribution within the body system: size of particles, toxicity, surface charge, capacity for protein adsorption, surface hydrophobicity, rate of loading, release kinetics, stability resp. degeneration of carrier system, hydration behavior, electrophoretic mobility, porosity, specific surface characteristics, density, crystallinity, contact angle and molecular weight. Size of particles, toxicity, surface charge and protein adsorption capacity are the most important features for use *in vivo* drug targeting.

The size of particles usually refers to the total diameter of the particles including the iron core and the coating. Since the smallest diameter of capillaries in the body is 4  $\mu\text{m}$ , larger particles will be mainly captured and withheld in the lungs results in causing emboli within the capillary bed of the lungs. Depending on particle size, uptake may be subdivided in phagocytosis (all sizes) or pinocytosis (particles <150 nm). Large particles will be only removed by cells capable of phagocytosis, whereas smaller particles can be removed by all types of cells through pinocytosis (all cells are capable of pinocytosis). If suspensions containing nanoparticles are used in

vivo, they should be hydrophilic and their pH should be close to 7.4. In addition, they should be degraded and eliminated by the body system without residues, otherwise they may accumulate in certain cell compartments, such as liposomes, or tissues from the phagocytosis system.

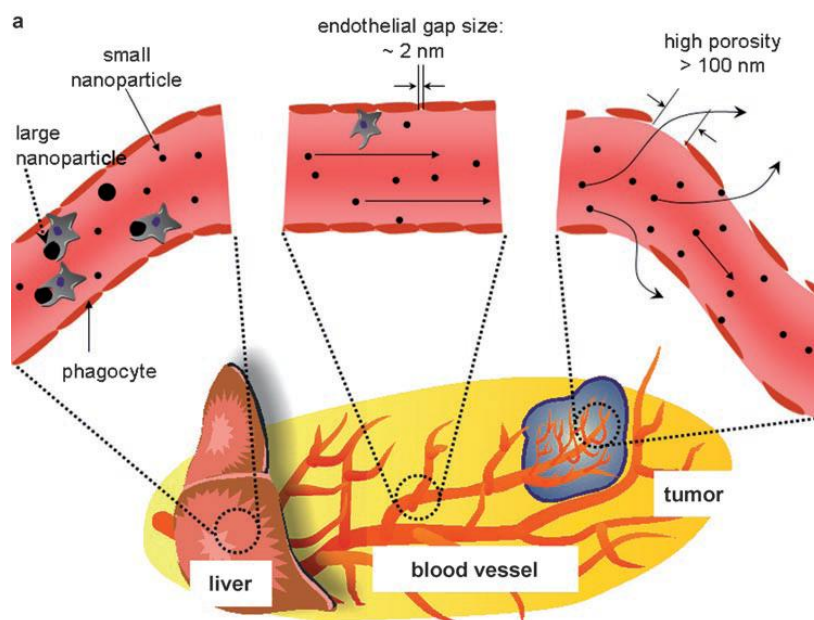


Figure 1.23. Schematic representation of drug delivery using magnetic nanoparticles [102].

Now a day's these type of research is moving into animal testing, involves injecting nanoparticles made of iron oxide into the body, where they flow through the bloodstream and enter tumors. Solid tumors must form new blood vessels to grow. But because this growth is so rapid in cancerous tumors, there are gaps in the endothelial cells that line the inside of the blood vessels which is pictorially shown in Figure 1.23. The nanoparticles can slip through these gaps to enter the tumors. Once inside the tumor, the nanoparticles can be triggered to group together by a mechanism designed by the MIT engineers [148,149]. Specifically, certain enzymes, or proteases, inside the tumors cause the nanoparticles to self-assemble or stick together. The resulting nanoparticle clumps are too big to get back out of the gaps. Further, the clumps have a stronger magnetic signal than do individual nanoparticles, allowing detection by MRI.

The mechanism relies to inject nanoparticles that will self-assemble when they are exposed to proteases inside of invasive tumors, as reported by S. N. Bhatia [148]. When these nanoparticles assemble they should get stuck inside the tumor and be more visible on an MRI. This might allow for noninvasive imaging of fast-growing cancer 'hot spots' in tumors. The technique initially is being used to study breast tumors. Bhatia added that it eventually may be applied to many different types of cancers and to study the "triggers" that turn a benign mass in the body into a cancerous tumor. Nanoparticles also hold the promise of carrying medicines that could kill cancer cells, replacing radiation or chemotherapy treatments that cause negative side effects such as hair loss or nausea.

### **1.10.2 Information storage**

Advances in information storage technologies since the 1950s have led to tremendous progress in the preparation of magnetic nanoparticles with defined properties. These magnetic materials are employed in both the information storage media and in the 'write' and 'read' heads. At present, nanostructured materials dominate in both media and heads. In the future, it is likely that virtually all media and heads will be composed of nanostructured materials. Magnetic recording essentially involves detecting changes in the direction of magnetization in the storage medium. In order to store the magnetization transitions at high densities, several constraints are imposed on the storage media [150] and on the write and read heads. With a high storage density [151,152], the distance between magnetization reversals becomes very small. This produces strong demagnetizing fields on the stored 'bit'. For stable storage, the coercive force,  $H_c$ , must be high enough to withstand these demagnetizing fields. Another media consideration is a high remanence to ensure sufficient stray field for detection of the transition. This would suggest a high saturation magnetization,  $M_s$ , for the media; however, high  $M_s$  increases the demagnetizing field [153]. Thus, a storage medium with both high  $H_c$  and  $M_s$  would seem to be required. These media requirements must be matched by the head properties. The higher the  $H_c$ , the stronger the field needed from the write head to produce a transition. High permeability (for low write currents) and high data rates ( $> 100$  MHz) place additional constraints on the write head materials. All these constraints on media and heads are met by nano-sized structures. There are two types

of storage medium: particulate (e.g. tapes), and thin films (e.g. disks). In both these configurations, the basic magnetic entities are single magnetic domains, i.e. regions in which the magnetization is essentially uniform.

In recent past Bachman [154] and co-workers synthesized well-defined, tunable, ordered Fe<sub>3</sub>O<sub>4</sub> nanotubes by atomic layer deposition techniques and enabled us to observe a strong size dependence in the magnetism of Fe<sub>3</sub>O<sub>4</sub> nanotubes. They proposed that these arrays of pseudo-one-dimensional ferromagnetic nanostructure can be used in high-density data storage devices.

### 1.10.3 Other Applications

Magnetic nanoparticles have emerged as alternative soluble matrixes for supporting homogeneous organic reactions. This is because when the size of the support materials is decreased to the nanometer scale, the surface area of nanoparticles will increase dramatically. As a consequence, nanoparticle supports could have higher catalyst loading capacity than many conventional support matrixes, leading to the improved catalytic activity of the nanoparticle-supported catalysts. In addition, catalysts are usually immobilized on the surface of nanoclusters. Reactants in solution have easy access to the active sites on the surface of nanoparticles, avoiding the problems encountered in many heterogeneous support matrixes where a great portion of catalysts are present deep inside the matrix backbones and reactants have the limited access to the catalytic sites.

Superparamagnetic nanoparticles [155,156] are a new type of soluble matrix that potentially can address the isolation and recycling problems for immobilization of homogeneous catalysts. These magnetic nanoparticles [157] usually have a core/shell structure consisting of a magnetic iron oxide core surrounded by a layer of lightly cross-linked polymeric shell wall. The organic polymer shells stabilize nanoparticles by preventing aggregation of inorganic cores and offer a platform for immobilization of catalysts. These Iron oxide cores will respond to a magnetic field but retain no magnetization properties when the field is removed. The lack of magnetic remanence prevents nanoparticles from forming magnetized clumps in the reaction media. In addition, unusually high magnetization moments of “super”paramagnetic materials allow the use of low-field magnets to efficiently concentrate magnetic nanoparticles.

Iron/iron oxide core–shell nanoparticles ( $\text{Fe@Fe}_x\text{O}_y$ ) are a versatile support for immobilizing catalytic metals was introduced by Veinot [158] and his group. He highlighted that  $\text{Fe@Fe}_x\text{O}_y$  decorated with Pd ( $\text{Fe@Fe}_x\text{O}_y/\text{Pd}$ ) exhibits high catalytic activity toward Suzuki–Miyaura cross-coupling reactions in aqueous solution at room temperature.

In this account we have discussed the aspects of magnetism and reviewed about the synthesis of magnetic nanoparticles, properties and their applications as demonstrated in biological and in electronics. However, there are a number of unsolved issues that remain to be addressed before these nanoparticles could reach industrial applications. For example in synthetic point of view, there are several research areas such as developing new chemical routes to achieve monodisperse magnetic nanoparticles directly without any size selection process. Most of these applications require monodispersed magnetic nanoparticles. All though the current understanding about magnetic properties of nanoparticles are limited, more studies and experimental exploration in this area can lead to significant advances in various fields of next generation applications.

### 1.11 Objectives of the present work

For all the proposed applications of the magnetic nanoparticles, detailed information on their magnetic behavior such as information on the magnetic exchange and dipolar interactions between the particles, magnitude of magnetization, superparamagnetism and superparamagnetic blocking temperature, etc. are very essential. Below the blocking temperature, the nanoparticles show magnetic hysteresis and therefore they are not useful for many applications. All these parameters vary when a single particle is coated with surfactants or made in to the form of fluids and also the properties will vary depending on the size and shape of the particles, dispersion, type of surfactant used and the properties of the medium of suspension in the case of ferrofluids.

The objectives of the present work are:

- ◆ Synthesis of magnetic nanoparticles of  $\text{Fe}_3\text{O}_4$  by coprecipitation method and structural characterization by using XRD, IR, TEM, HRTEM, etc.

- ◆ Optimization of synthesis parameters to achieve smallest nanoparticles, with narrow size distribution and reproducibility, from the application point of view
- ◆ Coating studies of these nanoparticles by using biocompatible molecules and detailed characterization
- ◆ Detailed study of the dispersion and stability of these nanoparticles in aqueous media.
- ◆ Studies on the interaction behavior of these nanoparticles by magnetic measurements.
- ◆ Synthesis of non-magnetic materials having the same structure as that of the magnetic particles to understand the local structural changes taking place on particle surface.
- ◆ Detailed characterization of these nanoparticles by solid state NMR.

## 1.12 Organization of the thesis

In this thesis we have focused on two areas in which chemistry and magnetism are inextricably linked: the synthesis of magnetic nanoparticles and fabrication of biocompatible magnetic nanomaterials and ferrofluids. Moreover, we studied the physical aspects of the interaction behavior of these nanoparticles to differentiate and understand the superparamagnetic and superspin glass properties exhibited by the same material under different conditions. All these studies involve different kinds of magnetic measurements such as field dependence of magnetization, zero field cooled and field cooled magnetization, relaxation studies, etc. Solid state NMR studies have been made on nanoparticles of non-magnetic materials having the same structure as that of the magnetic particles to understand the local structural changes taking place on the surface of the particles when their sizes are reduced to few nanometers.

The **first chapter** (this chapter) introduces the concept of nano science and various types of magnetic nanomaterials that have been synthesized for various applications. Also, a detailed discussion of the synthesis methods, magnetic properties and applications of magnetic nanomaterials is presented.

The experimental methods and characterization techniques used in the present work are briefly discussed in the **second chapter**.

The **third chapter** describes the synthesis and magnetic properties of iron oxide nanoparticles.  $\text{Fe}_3\text{O}_4$  nanoparticles have been synthesized by the reverse co-precipitation method. The main advantage of the co-precipitation process is that a large amount of nanoparticles can be synthesized in a single batch. However, the control of particle size distribution is limited, because only kinetic factors are controlling the growth of the crystal. The mode of addition of Fe stock solutions to the base during the synthesis was found to be decisive in controlling the crystallite and particle size as well as distribution of the produced  $\text{Fe}_3\text{O}_4$  nanoparticles. Lower temperature and higher degree of agitation were the favorable conditions for producing smaller particles with narrow distribution. The synthesis conditions for obtaining reproducible results were optimized by XRD and magnetic measurements.

**Fourth chapter** of the thesis describes the synthesis and functionalization of  $\text{Fe}_3\text{O}_4$  nanoparticles by dextran and ascorbic acid. The work is focused on detailed studies on the magnetic properties of coated as well as uncoated magnetic nanoparticles. In the generation of magnetic nanoparticles for biological applications, the control over synthetic parameters influencing the particles' physicochemical properties are of great interest due to the strong influence of particle size and surface properties on biological applications. We have synthesized dextran and ascorbic acid coated iron oxide nanoparticles and systematically evaluated synthetic parameters that may influence the properties of these nanoparticles. In the present investigation, the structural and the magnetic properties of the nanoparticles were investigated. The influence of the non-magnetic shell on the magnetic dipole–dipole interactions between the neighboring particles was determined by low temperature magnetic measurements. Colloidal suspensions of magnetic nanoparticles, with biomedical application as contrast agents in magnetic resonance imaging, in mind, have been prepared by coating iron oxide nanoparticles with ascorbic acid. The  $T_1$  and  $T_2$  relaxation times are recorded by an NMR instrument using inversion recovery pulse sequence.

**Chapter five** of the thesis deals with the comparison of the magnetic properties and the interaction behavior of coated and uncoated iron oxide nanoparticles. The magnetic properties of uncoated particles changes after coating with ascorbic acid and dextran. This was confirmed by zero field cooling, field cooling and memory experiments. The studies suggest the interacting and non-interacting behavior of

uncoated and coated nanoparticles, respectively, giving rise to superspin glass and superparamagnetic characteristics..

**Chapter six** highlights the studies on non-magnetic spinel type oxide nanoparticles by solid state NMR, to understand the coordination and distribution behavior of the different metal ions in these nanoparticles. For magnetic nanoparticles, the exchange interactions at the surface of a particle will be different from those inside due to changes in the coordination behavior at the surface when the size of the particles is reduced to nanodimensions. Therefore, studying and understanding the coordination and distribution behavior of the different metal ions in the nanoparticles of spinel-type oxides is very important to understand the changes in the magnetic properties with size. Solid state NMR is a useful and important technique to obtain information on local structural variations. The degree of the distribution of the  $\text{Al}^{3+}$  ions in the tetrahedral and octahedral sites in the nanoparticles and changes in the coordination behavior with particle size of the nonmagnetic spinel  $\text{MgAl}_2\text{O}_4$  and  $\text{ZnAl}_2\text{O}_4$  having different particle sizes has been determined by  $^{27}\text{Al}$  magic-angle spinning (MAS) NMR spectroscopy. It has been observed that the inversion parameter decreases with increasing particle size. Apart from the usual tetrahedral and octahedral coordinations present in the bulk material, the presence of five coordinated Al sites has been observed in nanoparticles and a second octahedral coordination is observed for nanoparticles of larger sizes.

**Chapter seven** is an overall conclusion from the present studies on magnetic and non-magnetic spinel type oxide nanoparticles. The present results and future perspectives are discussed in this chapter.

---

**References**

- 1 Mercier, J.; Zambelli, G.; Kurz, W. *Introduction to materials science*, Elsevier, Paris, **2002**
- 2 Askeland, D. R.; Fulay, P.P. *Essentials of Materials Science and Engineering: Second Edition*, Ceneage learning, New York, **2009**
- 3 Hott, R.; Kleiner, R.; Wolf, T.; Zwicknag, G. *Frontiers in Superconducting Material*, Springer Verlag, Berlin, **2004**
- 4 Krüger, A. *Carbon Materials and Nanotechnology*, Wiley-Interscience Publication, Weinheim, **2010**
- 5 Widmann, D.; Mader, H.; Friedrich, H.; Hans Friedrich, *Technology of integrated circuits*, Springer, Berlin Heidelberg, **2000**
- 6 Basu, S.; *Recent trends in fuel cell science and technology*, Springer, New York, **2007**
- 7 Caruta, B. M. *Nanomaterials: new research*, Nova Science publishers, New York, **2005**
- 8 Hosono, H.; *Nanomaterials: from research to applications*, Elsevier, The Netherlands, **2006**
- 9 Linkov, I.; Steevens, J.; *Nanomaterials: Risks and Benefits*, Springer, The Netherlands, **2009**
- 10 Bader, S. D. *Rev. Mod. Phys.* **2006**, 78, 1.
- 11 Skomski, R. *J. Phys.: Condens. Matter*, 2003, 15, R841.
- 12 Ratner, M.; Ratner, D. *Nanotechnology: a gentle introduction to the next big idea*, Prentice Hall, New Jersey, **2002**
- 13 Fernández, L.; Corso, M.; Schiller, F.; Ilyn, M.; Holder, M.; Ortega, J. E. *Appl. Phys. Lett.* **2010**, 96, 013107
- 14 Gonzalez, A. E.; Marti´nez-Herna´ndez, A. L.; Angeles-Cha´vez, C.; Casta˜no, V. M.; Velasco-Santos, C., *Nanoscale Res Lett.*, 2010, 5, 1408
- 15 Lima, A.L.; Gschneidner, K.A.; Pecharsky, V.K.; *J. App. Phy.*, **2004**, 96, 2164,
- 16 Odenbach S. (ed.) *Ferrofluids*, Springer, Berlin, **2002**
- 17 Jun, Y.; Seo, J.; Cheon, J.; *Acc. Chem.. Res.* **2008**, 41, 179

- 
- 18 Edelstein, A. S.; Cammarata, R. C.; *Nanomaterials: Synthesis, Properties and Applications*, Institute of Physics Publishing, Bristol, **2001**
  - 19 Kelsall, R. W.; Hamley, I.W.; Geoghegan, M. *Nanoscale Science and Technology*, John Wiley & Sons Ltd, England, **2005**
  - 20 Givord, D. *Nanomaterials and Nanochemistry*, Chapter 5, Springer-Verlag Berlin Heidelberg, **2007**, 101
  - 21 Diandra, L.; Leslie-Pelecky, Rieke, R. D. *Chem. Mat.* **1996**, 8, 1770.
  - 22 Etienne du Tremolet de Lacheisserie Damien Gignoux, Schlenker, M. *Magnetism – Fundamentals*, Springer Science, New York, **2005**
  - 23 Williams, S. R. *Magnetic Phenomena*, McGraw-Hill Book Company, Inc. New York and London, **1931**
  - 24 O'Handley, R.C. *Modern Magnetic Materials*, Wiley-Interscience Publication, New York, **2000**
  - 25 Mattis, D. C.; *The theory of magnetism made simple: an introduction to physical concepts and to some useful mathematical methods*, World Scientific Publishing Co., New Jersey, **2006**
  - 26 Verschuur. G. L. *Hidden attraction : the mystery and history of magnetism*, Oxford University Press, New York, **1937**
  - 27 Buschow, K. H. J.; De Boer, F. R.; *Physics of Magnetism and Magnetic Materials*, Kluwer Academic /Plenum Publishers, New York, **2003**
  - 28 Aharoni, A. *Introduction to the theory of ferromagnetism*, Oxford university press, Oxford, **2000**
  - 29 Neel, L.; *Annales de physique*, **1932**, 18, 5-105.
  - 30 Cullity, B.D. *Introduction to Magnetic Materials*, Addison-Wesley Publishing Company, Inc. Massachusetts, **1972**
  - 31 Spaldin, N.A.; *Magnetic Materials: Fundamentals and Applications*, Cambridge Univ. Press, USA, **2010**
  - 32 Hubert, A.; Schäfer, R. *Magnetic Domains*, Springer-Verlag Berlin Heidelberg, **1998**
  - 33 Atkinson, R.; Kubrakov, N. F.; O'Neill, M.; Papakonstantinou, P. *J. Mag. Mater.* **1995**, 149, 418
  - 34 Lee, K.; Melikyan, H.; Babajanyan, A.; Sargsyan, T.; Kim, J.; Kim, S.; Friedman, B.; *Ultramicroscopy*, **2009**, 109, 889

- 
- 35 Endo, H.; Hayano, S.; Fujikura, M.; Mogi, H.; Kaido, C.; Saito, Y. *International J. App. Electro. Mech.* **2002**, 15, 409
- 36 Goldman, A. *Modern Ferrite Technology*, Van Nostrand Reinhold, New York, **1990**
- 37 Batlle, X.; Labarta, A.; *J. Phys. D* **2002**, 35, R15.
- 38 Iwaki, T.; Kakihara, Y.; Toda, T.; Abdullah, M.; Okuyama, K.; *J. Appl. Phys.* **2003**, 94, 6807.
- 39 Jiles, D. C. *Introduction to Magnetism and Magnetic Materials*, Chapman, & Hall, New York, **1998**
- 40 Mydosh, J. A. *Spin Glasses: An Experimental Introduction*, Taylor & Francis, London, **1993**
- 41 Kronmüller, H.; Parkin, S. *Handbook of Magnetism and Advanced Magnetic Materials*, John Wiley & Sons, Ltd, USA, **2007**
- 42 Fiorani, D. *Surface Effects in Magnetic Nanoparticles*, Springer, New York, **2005**
- 43 Morales, M. P.; Veintemillas-Verdaguer, S.; Montero, M. I.; Serna, C. *J Chem. Mater.* **1999**, 11, 3058
- 44 Cheon, J.; Kang, N.-J.; Lee, S.-M.; Yoon, J.-H.; Oh, S. J. *J. Am. Chem. Soc.* **2004**, 126, 1950.
- 45 Park, J.-I.; Kang, N.-J.; Jun, Y.; Oh, S. J.; Ri, H. C.; Cheon, J. *Chem. Phys. Chem*, **2002**, 3, 543
- 46 Liu, C.; Zou, B.; Rondinone, A. J.; Zhang, Z.J. *J. Am. Chem. Soc.* **2000**, 122, 6263
- 47 Ghosh, M.; Sampathkumaran, E. V.; Rao, C. N. R. *Chem. Mater.* **2005**, 17, 2348
- 48 Rao, C.N.R.; Muller, A.; Cheetham, A.K. *Nanomaterials Chemistry Recent Developments and New Directions*, Wiley-Vch Verlag GmbH & Co, Weinheim, **2007**
- 49 Rao, C.N.R.; Muller, A.; Cheetham, *The Chemistry of Nanomaterials Synthesis, Properties and Applications in 2 Volumes*, Wiley-Vch Verlag GmbH & Co., Weinheim, **2004**
- 50 Weinberger, P. *Magnetic Anisotropies in Nanostructured Matter*, Taylor & Francis Group, LLC, **2009**

- 
- 51 Respaud, M.; Broto, J. M.; Rakoto, H.; Fert, A. R.; Thomas, L.; Barbara, B.; Verelst, M.; Snoeck, E.; Lecante, P.; Mosset, A.; Osuna, J.; Ould Ely, T.; Amiens, C.; Chaudret, B.; *Phys. Rev. B*, **1998**, 57, 2925
- 52 Bødker, F.; Mørup, S.; Linderoth, S.; *Phys. Rev. Lett.* **1994**, 72, 282.
- 53 Nogués, J.; Sort, J.; Langlais, V.; Skumryev, V.; Suriñach, S.; Muñoz, J. S.; Baró, M. D.; *Phys. Rep.* **2005**, 422, 65.
- 54 Hormes, J.; Modrow, H.; Bönnemann, H.; Kumar, C. S. S. R. *J. Appl. Phys.* **2005**, 97, 10R102.
- 55 Gupta, A. K.; Gupta, M. *Biomaterials*, **2005**, 26, 3995
- 56 Mikhaylova, M.; Kim, D.K.; Bobrysheva, N.; Osmolowsky, M.; Semenov, V.; Tsakalakos, T.; *Langmuir*, **2004**, 20, 2472.
- 57 Bautista, M.C.; Bomati-Miguel, O.; Morales, M.P.; Serna, C.J.; Veintemillas-Verdaguer, S.; *J. Magn. Magn. Mater.* **2005**, 293, 20.
- 58 Jun, Y.; Choi, J.; Cheon, J., *Chem. Commun.*, **2007**, 1203.
- 59 Lu, A. H.; Salabas, E. L.; Schüth, F., *Angew. Chem., Internat. Ed*, **2007**, 46, 1222
- 60 Rice, S. A., *Advances in Chemical Physics volume 128*, John Wiley & Sons, Inc, New Jersey, **2004**
- 61 Dormann, J. L.; Fiorani, D., (Eds.) *Magnetic Properties of Fine Particles*, North-Holland, Amsterdam, **1992**
- 62 Sasaki, M.; Jonsson, P. E.; Takayama, H.; Nordblad, P., *Phys. Rev. Lett.* **2004**, 93, 139701
- 63 Suzuki, M.; Fullem, S. I.; Suzuki, I. S.; Wang, L.; Zhong, C.; *Phys. Rev B* **2009**, 79, 024418
- 64 Sasaki, M.; Jonsson, P. E.; Takayama, H.; Mamiya, H. *Phys. Rev. B*, **2005**, 71, 104405.
- 65 Mamiya, H.; Nakatani, I.; Furubayashi, T. *Phys. Rev. Lett.* **1999**, 82, 4332.
- 66 Mamiya, H.; Nakatani, I.; Furubayashi, T. *Phys. Rev. Lett.* **1998**, 80, 177.
- 67 Jonsson, T.; Mattsson, J.; Djurberg, C.; Khan, F. A.; Nordblad, P.; Svedlindh, P., *Phys. Rev. Lett.* **1995**, 75, 4138
- 68 Luo, W.; Nagel, S. R.; Rosenbaum, T. F.; Rosensweig, R. E., *Phys. Rev. Lett.* **1991**, 67, 2721.

- 
- 69 Djurberg, C.; Svedlindh, P.; Nordblad, P.; Hansen, M. F.; Bødker, F.; Mørup, S.; *Phys. Rev. Lett.* **1997**, 79, 5154
- 70 Sellmy, D.; Skomski, R., *Advanced magnetic nanostructures*, Springer Science, **2006**
- 71 Stohr, J.; Siegmann, H. C.; *Magnetism From Fundamentals to Nanoscale Dynamics*, Springer-Verlag Berlin Heidelberg, **2006**
- 72 Henkel, M.; Pleimling, M.; Sanctuary, R.; *Ageing and the Glass Transition, Lect. Notes Phys. 716*, Springer, Berlin Heidelberg, **2007**
- 73 Mydosh, J. A., *Spin Glasses: An Experimental Introduction*, Taylor & Francis, London, **1993**
- 74 Jonsson, P.; Hansen, M. F.; Nordblad, P.; *Phys. Rev. B*, **2000**, 61, 1261.
- 75 Fisher, D. S.; Huse, D. A., *Phys. Rev. B*, 1988, 38, 373
- 76 Fisher, D. S.; Huse, D. A., *Phys. Rev. B*, 1988, 38, 386
- 77 Rice, S. A.; *Advances in Chemical Physics, vol 98*, John Wiley & Sons Inc, New Jersey, **1997**
- 78 de Almeida, J. R. L.; Thouless, D. J., *J. Phys. A: Math. Gen.* **1978**, 11, 983
- 79 Sun, Y.; Salamon, M. B.; Garnier, K.; Averback, R. S.; *Phys. Rev. Lett.* **2003** 91, 167206
- 80 Östh, M.; Hérisson, D.; Nordblad, P.; De Toro, J. A.; Riveiro, J. M.; *J. Magn. Magn. Mater.* **2007**, 313, 373
- 81 O'Neill, H. St. C.; Navrotsky, A. *Am. Mineral.* **1983**, 68, 181
- 82 Schmocker, U.; Waldner, F., *J. Phys. C: Solid State Phys.* **1976**, 9, L235
- 83 Sickafus, K. E.; Willis, J. M.; Grimes, N. W. *J. Am. Ceram. Soc.* **1999**, 82, 3279
- 84 Wood, B. J.; Kirkpatrick, R. J.; Montez, B. *Am. Mineral.* **1986**, 71, 999
- 85 Maekawa, H.; Kato, S.; Kawamura, K.; Yokokawa, T. *Am. Mineral.* **1997**, 82, 1125
- 86 Millard, R. L.; Peterson, R. C.; Hunter, B. K. *Am. Mineral.* **1992**, 77, 44
- 87 Andreozzi, G. B.; Princivalle, F.; Skogby, H.; Giusta, A. D. *Am. Mineral.* **2000**, 85, 1164
- 88 Peterson, R. C.; Lager, G. A.; Hitterman, R. L. *Am. Mineral.* **1991**, 76, 1455
- 89 Schmocker, U.; Boesch, H. R.; Waldner, F. *Phys. Lett. A*, **1972**, 40, 237
- 90 Weeks, R. A.; Sonder, E. *J. Am. Ceram. Soc.* **1980**, 63, 92

- 
- 91 Montouillout, V.; Massiot, D.; Douy, A.; Coutures, J. P. *J. Am. Ceram. Soc.* **1999**, 82, 3299
- 92 van der Laag, N. J. .; Snel, M. D.; Magusin, P. C. M. M.; de With, G.; *J. Eur. Ceram. Soc.* **2004**, 24, 2417.
- 93 Schwertmann, U.; Cornell, R. M.; *The Iron oxides in the laboratory*, Wiley-Vch Verlag GmbH, Germany, **2000**
- 94 Schwertmann, U.; Cornell, R. M.; *The Iron oxides, Structure properties reactions occurrences and uses*, Wiley-Vch Verlag GmbH, Germany, **2003**
- 95 Smit, J.; Wijn, H. P. J., *Ferrites*, Philips Technical Library, Eindhoven, **1959**
- 96 Lax, B.; Button, K. J., *Microwave Ferrites and Ferrimagnetics*, McGraw Hill Book Company, New York, **1962**
- 97 Valenzuela, R., *Magnetic Ceramics, Chemistry of Solid State Materials*, Series Ed. Cambridge, **1994**
- 98 Reiss, B. D.; Mao, C. B.; Solis, D. J.; Ryan, K. S.; Thomson, T.; Belcher, A. M. *Nano Lett.* **2004**, 4, 1127.
- 99 Laurent, S.; Forge, D.; Port, M.; Roch, A.; Robic, C.; Elst, L. V.; Muller, R. N., *Chem. Rev.*, **2008**, 108, 2064.
- 100 Mbindyo, J. K. N.; Mallouk, T. E.; Mattzela, J. B.; Kratochvilova, J. B.; Razavi, B.; Jackson, T. N.; Mayer, T. S. *J. Am. Chem. Soc.* **2002**, 124, 4020.
- 101 Pan, H.; Chen, W. Z.; Feng, Y. P.; Ji, W.; Lin, J. Y. *Appl. Phys. Lett.* **2006**, 88, 223106
- 102 Jun, Y. W.; Lee J.-H.; Cheon, J. *Angew. Chem., Internat. Ed.*, **2008**, 47, 5122
- 103 Liu, Z.L., Yao, K.L., Du, G.H., Lu, Q.H., Ding, Z.H. Tao, J. *J. Mater. Sci.*, **2004**, 39, 2633.
- 104 Fried, T.; Shemer, G.; Markovich, G.; *Adv. Mater.* **2001**, 13, 1158
- 105 Ge, S.; Shi, X.; Sun, K.; Li, S.; Uher, C.; Baker, J. R.; Holl, B. M. B.; Orr, B.G., *J. Phys. Chem. C*, **2009**, 113, 13593
- 106 Giraldi, T. R.; Arruda, C. C.; da Costa, G. M.; Ribeiro, E. L. C., *J Sol-Gel Sci Technol*, **2009**, 52, 299
- 107 Franger, S.; Berthet, P.; Berthon, J.; *J. Solid State Electr.*, **2004**, 8, 218
- 108 Martinez-Mera, I.; Espinosa, M. E.; Perez-Hernandez, R.; Arenas- Alatorre, J. *Mater. Lett.* **2007**, 61, 4447.
- 109 Massart, R. *IEEE Trans. Magn.* **1981**, 17, 1247.

- 
- 110 Zhao, L.; Zhang, H.; Xing, Y.; Song, S.; Yu, S.; Shi, W.; Guo, W.; Yang, J.; Lei, Y.; Cao, F.; *Chem. Mater.* **2008**, 20, 198
- 111 Yuet, K. P.; Hwang, D. K.; Haghgooie, R.; Doyle, P. S., *Langmuir*, **2010**, 26, 4281.
- 112 Huang, X.; Bronstein, L. M.; Retrum, J.; Dufort, C.; Tsvetkova, I.; Aniagyeyi, S.; Stein, B.; Stucky, G.; McKenna, B.; Remmes, N.; Baxter, D.; Kao, C.; Dragnea, B., *Nano Lett.*, **2007**, 7, 2407
- 113 Verwey, E. J. W.; Overbeek, J. T. G. *Theory of the Stability of Lyophobic Colloids*; Elsevier: Amsterdam, The Netherlands, **1948**
- 114 Vincent, B.; Edwards, J.; Emmett, S.; Jones, A. *Colloids Surf.* **1986**, 18, 261.
- 115 Fritz, G.; Schadler, V.; Willenbacher, N.; Wagner, N. J. *Langmuir*, **2002**, 18, 6381.
- 116 Kobayashi, M.; Skarba, M.; Galletto, P.; Cakara, D.; Borbovec, M. *J. Colloid Interface Sci.* **2005**, 292, 139.
- 117 Lattuada, M.; Sandkuhler, P.; Wu, H.; Sefcik, J.; Morbidelli, M. *Adv. Colloid Interface Sci.* **2003**, 103, 33
- 118 Bloomfield, V. A. *Biopolymers*, **2000**, 54, 168
- 119 Lefebure, S.; Dubois, E.; Cabuil, V.; Neveu, S.; Massart, R. *J. Mater. Res.* **1998**, 13, 2975.
- 120 Lee, C. M.; Jeong, H. J.; Kim, E. M.; Kim, D. W.; Lim, S. T.; Kim, H. T.; Park, I.; Jeong, Y. Y.; Kim, J. W.; Sohn, M. H.; *Magn. Reson. Med.*, **2009**, 62, 1440
- 121 Bourlinos, A. B.; Bakandritsos, A.; Georgakilas, V.; Petridis, D., *Chem. Mater.*, **2002**, 14, 3226
- 122 Sonvico, F.; Mornet, S.; Vasseur, S.; Dubernet, C.; Jaillard, D.; Degrouard, J.; Hoebeke, J.; Duguet, E.; Colombo, P.; Couvreur, P., *Bioconjugate Chem.*, **2005**, 16, 1181
- 123 Larsen, E. K. U.; Nielsen, T.; Wittenborn, T.; Birkedal, H.; Vorup-Jensen, T.; Jakobsen, M. H.; Østergaard, L.; Horsman, M. R.; Besenbacher, F.; Howard, K. A.; Kjems, J.; *ACS Nano*, **2009**, 3, 1947 .
- 124 Huang, G.; Zhang, C.; Li, S.; Khemtong, C.; Yang, S.; Tian, R.; Minna, J. D.; Brownac, K. C.; Gao, J., *J. Mater. Chem.*, **2009**, 19, 6367

- 
- 125 Torchilin, V., *Multifunctional Pharmaceutical Nanocarriers*, Springer, New York, **2008**
- 126 Na, H. B.; Song, I. C.; Hyeon, T., *Adv. Mater.* **2009**, 21, 213
- 127 Kuperman, V., *Magnetic Resonance Imaging Physical Principles and Applications*, Academic Press, New York, **2000**
- 128 McRobbie, D. W.; Moore, E. A.; Graves, M. J.; Graves, M. R., *MRI From Picture to Proton*, Cambridge University Press, UK, **2006**
- 129 Weishaupt, D.; Kochli, V. D.; Marincek, B., *An Introduction to the Physics and Function of Magnetic Resonance Imaging*, Springer Verlag Berlin Heidelberg New York, **2006**
- 130 Jun, Y.; Huh, Y.; Choi, J.; Lee, J.; Song, H.; Kim, S.; Yoon, S.; Kim, K.; Shin, J.; Suh, J.; Cheon, J., *J. Am. Chem. Soc.* **2005**, 127, 5732
- 131 Lee, H.; Huh, Y. M.; Jun, Y.W.; Seo, J.W.; Jang, J.T.; Song, H.T.; Kim, S.; Cho, E.J.; Yoon, H. G.; Suh, J.-S.; Cheon, J., *Nat. Med.* **2007**, 13, 95 .
- 132 Gilchrist R. K., *Annals of Surgery*, **1957**, 146, 596.
- 133 Pankhurst, Q.; Connolly, A.; Jones, J.; Jones, S.K.; Dobson, J., *J. Phys. D: Appl. Phys.*, **2003**, 36, R167
- 134 Berry, C. C.; Curtis, A. S. G. *J. Phys. D: Appl. Phys.* **2003**, 36, R198
- 135 Sonvico, A.; Mornet, S.; Vasseur, S.; Dubernet, C.; Jaillard, D.; Degrouard, J.; Hoebeke, J.; Duguet, E.; Colombo, P.; Couvreur. P.; *Bioconjugate Chem.*, **2005**, 16, 1181
- 136 Kenji, H.; Ono, K.; Suzuki, H.; Sawada, M., Moriya, M.; Sakamoto, W.; Yogo, T., *ACS Appl. Mater. Interfaces*, **2010**, 2, 1903
- 137 Fortin, J. P.; Wilhelm, C.; Servais, J.; Ménager, C.; Bacri, J. C.; Gazeau, F., *J. Am. Chem. Soc.*, **2007**, 129, 2628
- 138 Hayashi, K.; Moriya, M.; Sakamoto, W.; Yogo, T., *Chem. Mater.*, **2009**, 21, 1318
- 139 Pareta, R. A.; Taylor, E.; Webster, T. J., *Nanotechnology*, **2008**, 19, 265101
- 140 Wang, D.; Miller, S.; Sima, M.; Kopecková, P.; Kopeck, J., *Bioconjugate Chem.*, **2003**, 14, 853
- 141 Tran, N.; Pareta, R. A.; Taylor, E.; Webster, T. J., *Adv. Mater. Res.*, **2010**, 89, 411
- 142 Moghimi, M.M.; Hunter, A.C.; Murray, J.C., *Pharmacol. Rev.* **2001**, 53, 283.

- 
- 143 Lassalle, V.; Ferreira, M. L.; *Macro. Biosci.*, **2007**, 7, 767
- 144 Kogan, A.; Garti, N., *Adv. Col. Inter. Sci.* **2006**, 123-126, 369
- 145 Gregoriadis, G.; Florence, A. T.; Patel, H. M.; *Liposomes in drug delivery*, Harwood academic publishers, The Netherlands, **1993**
- 146 Uchegbu, I. F., *Synthetic surfactant vesicles: niosomes and other non-phospholipid vesicular*, Harwood academic publishers, The Netherlands, **2000**
- 147 Jin, Y.; Tong, L.; Ai, P.; Li, M.; Hou, X.; *Inter. J. Pharm.*, **2006**, 309, 199
- 148 Park, J.; Maltzahn, G. V.; Ruoslahti, E.; Bhatia, S. N.; Sailor, M.J., *Angew. Chem. Inter. Edit.* **2008**, 47, 7284
- 149 Harris, T. J.; Maltzahn, G. V.; Derfus, A. M.; Ruoslahti, E.; Bhatia, S. N., *Angew. Chem.* **2006**, 118, 19, 3233
- 150 Black, C. T.; Murray, C. B.; Sandstrom, R. L.; Sun, S., *Science*, **2000**, 290, 1131
- 151 Bennett, L. H.; Watson, R. E., *Magnetic multilayers*, World scientific publishing co, Singapore, **1994**
- 152 Goya, G. F.; Berquo, T. S.; Fonseca, F. C. *J. Appl. Phys.* **2003**, 94, 3520
- 153 Johnson, M., *Magnetolectronics*, Elsevier, The Netherlands, **2004**
- 154 Bachmann, J.; Jing, J.; Knez, M.; Barth, S.; Shen, H.; Mathur, S.; Gosele, U.; Nielsch, K.; *J. Am. Chem. Soc.* **2007**, 129, 9554
- 155 Wu, W.; He, Q.; Jiang, C., *Nanoscale Res. Lett.* **2008**, 3, 397
- 156 Shin, S.; Yoon, H.; Jang, J., *Catal. Commun.* **2008**, 10, 178
- 157 Zeng, T.; Chen, W. W.; Cirtiu, C. M.; Moores, A.; Song, G.; Li, C. J.; *Green Chem.*, **2010**, 12, 570
- 158 Zhou, S.; Johnson, M.; Veinot, J. G. C., *Chem. Commun.*, **2010**, 46, 2411

## CHAPTER 2

### SYNTHESIS METHODS AND CHARACTERISATION

#### 2.1 Introduction

This chapter discusses the methods used in this work for the synthesis nanocrystalline spinel oxides and various experimental techniques used for the characterization of materials. Such techniques involve the methods of synthesis of the spinel type oxides under study and characterization of the structure, morphology, magnetic properties, etc. The components which govern the properties of the nanomaterials under study are characterized as accurately and as broadly as possible, in order to better understand their particular characteristics.

#### 2.2 Synthesis

There are several methods available for the synthesis of spinel type oxide materials in the nanostructured forms such thermal decomposition, sol-gel, citrate precursor method, combustion, co-precipitation, etc [1]. In the present work, the different oxide materials are synthesized in nanocrystalline forms by using the conventional coprecipitation method and the glycine-nitrate autocombustion method.

##### 2.2.1 Coprecipitation method

Coprecipitation of various salts (nitrates, sulphates, chlorides, perchlorates etc.) under a fine control of pH by using NaOH or NH<sub>4</sub>OH solutions yields corresponding spinel oxide nanoparticles [2]. Coprecipitation reactions [3] tend to exhibit the following characteristics: (i) The products of precipitation reactions are generally sparingly soluble species formed under conditions of high supersaturation. (ii) Such conditions dictate that nucleation will be a key step of the precipitation process and that a large number of small particles will be formed. (iii) Secondary processes, such as Ostwald ripening and aggregation, will dramatically affect the size, morphology, and properties of the products. (iv) The supersaturation conditions necessary to induce precipitation are usually the result of a chemical reaction. As such, any reaction conditions influencing the mixing process, such as rate of reactant addition and stirring rate, must be considered relevant to product size, morphology,

and particle size distribution. Particle size of the coprecipitated material is strongly dependent on pH of the precipitation medium and concentration of the starting precursors. Consequently, adjusting the different parameters, particle size control can be easily achieved.

Coprecipitation method offers some advantages. They are:

- Simple and rapid preparation.
- Various possibilities to modify the particle surface state and overall homogeneity.
- Large scale production

Coprecipitation method are classified into two types. They are direct or normal coprecipitation method and the reverse coprecipitation method. In the normal coprecipitation reaction, alkali solution is added to the metal salt solution where as in reverse coprecipitation method metal solution is added to the alkali solution. During a normal coprecipitation method, the pH value gradually increases, because alkali solution is dropped into the mixed metal solution. In the case of the reverse coprecipitation method, the mixed metal solution is directly dropped into an alkaline solution. In this case, there is not much variation in the pH of the alkaline solution and hence a constant pH can be maintained during the precipitation reaction. Consequently, it is expected that the nanoparticles, once formed, does not grow much in size in this reverse method as compared to the normal coprecipitation method. The reverse coprecipitation method is very effective for synthesizing fine nanoparticles of poly-metallic oxides [4].

### **2.2.2 Glycine-Nitrate autocombustion method**

The autocombustion method of synthesis [5] of metal oxides using redox mixtures involves a mixture of oxidizing reagent such as nitrates of metals and a fuel such as glycine, urea, citric acid, hydrazine, glycerol, etc, which acts as a reducing reagent. The method is actually self-sustainable after the reaction is initiated and owing to the exothermic nature of the reaction, high internal temperature ensures the crystallization and formation of the oxides. The advantages of the autocombustion

process are that, one will get batches of yield (>96%) in a short time period. Some of the salient features of the process are:

- It is an easy and fast process that uses relatively simple equipments.
- Composition, structure, homogeneity, and stoichiometry of the products can be controlled.
- Formation of high-purity products are ensured by this method.
- High exothermicity of the metal nitrate–fuel reaction permits incorporation of desired quantity of impurity ions or dopants in the oxide hosts to prepare industrially useful materials like magnetic oxides, pigments and phosphors as well as high- $T_c$  cuprates, and M/oxide catalysts and tough materials.
- Stabilization of metastable phases ( $\gamma$ -Fe<sub>2</sub>O<sub>3</sub>, t-ZrO<sub>2</sub>, anatase TiO<sub>2</sub>, etc.) is possible by this method.
- Formation of products of virtually any size (micron to nano) and shape (spherical to hexagonal) can be achieved by this process.
- This method involves lower costs of preparation compared to conventional ceramic methods.
- It is economically attractive and easy to scale up.
- Uniform distribution of the dopants takes place throughout the host material due to the atomic mixing of the reactants in the initial solution.

In the present work, the synthesis method used is the glycine-nitrate process (GNP) where glycine is used as the fuel [6]. In the case of GNP, the low molecular weight amino acid, glycine (H<sub>2</sub>NCH<sub>2</sub>COOH), which act as a 'zwitterion' or bi-dentate ligand, prevents elective precipitation of the metal ions from the solution. Glycine has a more negative heat of combustion (3.24 kcal/g) as compared to some other combustion fuels such as urea (2.98 kcal/g) or citric acid (2.76 kcal/g). It serves as a fuel for the combustion reaction and oxidized by the nitrate ions easily. In GNP, the glycine-to-nitrate ion (G/N) ratio can be adjusted to get product particles of different sizes, good particle morphology and homogeneity, because G/N ratio affects the flame temperature and combustion velocity or reaction time [6,7].

### 2.2.3 Surface coating of nanoparticles

There are several factors of interest when considering a given synthetic approach: (1) thermal stability, (2) dispersability in diverse media, and (3) chemical compatibility and ease of chemical manipulation [8]. Here we focused on two different modes of capping of iron oxide nanoparticles

a) Direct Method: In this mode of synthesis, surfactants are mixed with ammonia solution and then precipitate the iron oxide nanoparticles by using iron solution. The nanoparticles so produced are called capped nanoparticles or protected nanoparticles. A surfactant layer has a characteristic chemical affinity to the nanoparticles core, due to its specific atoms or groups. For example, in the case of an oxide nanoparticle, the metal at the surface can link with the surfactant either by physisorption or chemisorption. The chemical bond so formed gives thermal stability to the nanoparticle system. This method is considered as the easiest way to synthesise monodispersed functionalised iron oxide nanoparticles.

b) Indirect Method: In this method, iron oxide nanoparticles was synthesised by coprecipitation method and washed thoroughly in order to remove ammonia and dried. This dried sample was used for further functionalisation studies using a suitable capping agent.

## 2.3 Characterization and Measurement Techniques

### 2.3.1 Powder X-Ray Diffraction (XRD)

The materials studied in the present work have been phase identified by the powder X-ray diffraction (XRD) method. X-ray diffraction is the most important and useful technique in the field of solid state chemistry. Powder XRD is used to determine the structure of the crystalline materials without the need for large single crystals. The XRD pattern is the finger print of a crystalline material [9] as this technique gives information on the structure, phase and purity of a material. The Bragg's law is used widely to treat diffraction from crystals. The Bragg's law is given as

$$n\lambda = 2d\sin\theta \quad (2.1)$$

where  $d$  is the spacing between two adjacent lattice planes,  $\lambda$  is the wave length of the X-radiation,  $n$  is an integer (=1) and  $\theta$  is known as the diffraction angle or Bragg's angle [10]. It is known that the width of a diffraction peak increases when the crystallite size is reduced below a certain limit ( $< 100$  nm). Therefore, XRD patterns can be used to estimate the average size of very small crystallites, from the measured width of the peaks in the diffraction patterns. The commonly accepted formula for the determination of crystallite size from XRD line broadening is the Scherrer formula [10],

$$t = \frac{0.9\lambda}{\beta\cos\theta} \quad (2.2)$$

where  $t$  is the thickness of the crystallites (in Å),  $\lambda$  is the X-ray wavelength,  $\theta$  is the diffraction angle and  $\beta$  is the width of the diffraction peak (in radians). Generally, there will be a contribution to line broadening from the instrument due to various factors and this natural line width is corrected as

$$\beta^2 = \beta_M^2 - \beta_S^2 \quad (2.3)$$

where  $\beta_M$  is the measured peak width at half peak height and  $\beta_S$  is the contribution from the instrumental line broadening, in radians.  $\beta_S$  is obtained from the width of the XRD pattern of a standard bulk material. The thickness of the crystallite or the average crystallite size  $t$  is generalized as the average particle size in the following chapters.

In the present study, the phase analysis of the samples was carried out using a Philips PW 1830 and Panalytical X'pert Pro diffractometers, and using Ni filtered Cu K $\alpha$  radiation. The wavelength of Cu K $\alpha$  radiation is 1.5418 Å. The diffractometer was calibrated with reference to standard Si wafer. For the general phase analysis the scan rate used was 4°/minute. The lattice parameters and  $d$ -spacings were calculated using the computer program, PowderCell for Windows (PCW) [11]. The same program was used for the simulation of the XRD patterns from the known single crystal data of the different compounds.

### 2.3.2 Transmission Electron Microscopy (TEM)

Transmission electron microscopy (TEM) is an imaging technique whereby a beam of electrons is focused onto a specimen causing an enlarged version to appear on a fluorescent screen or a layer of photographic film, or to be detected by a CCD camera. TEM operates on the same basic principles as the light microscope but uses electrons instead of light. Virtually, TEM is useful for determining size, shape and arrangement of the particles which make up the specimen. Moreover, it is highly useful for determination of the lattice planes and the detection of atomic-scale defects in areas of few nanometers in diameter with the help of selected area electron diffraction (SAED) technique [12,13]. The  $d$ -spacing between lattice planes of crystalline materials can be calculated from a SAED pattern using the relationship,

$$dr = \lambda L \quad (2.4)$$

where  $L$  is the distance between the specimen and the photographic plate,  $\lambda L$  is known as the camera constant and  $r$  is the radius of diffracted rings. It is easy to measure  $r$  directly from the photographic plate, and  $\lambda L$  can be established from the instrument by calibrating it with a standard material (usually Ag), and hence one can easily get  $d$  values. Since each  $d$  value corresponds to a specific lattice plane for a specific crystal structure, a minimum description of the crystal structure of a crystalline specimen can be obtained from a SAED pattern. In some cases, SAED pattern is more helpful as compared to XRD, due to the limited detection limit of XRD instruments.

In the present work, the TEM measurements were performed on a Jeol model 1200 EX instrument and on model FEI Technai 30 system. Joel model operating at 120 kV, camera length of 80 cm and field limited aperture of 100  $\mu\text{m}$  whereas FEI Technai model operated at 300 kV. Prior to TEM measurements, the samples were dispersed in a suitable organic solvent (isoamyl acetate, acetone, toluene, etc.) and a drop of the solution was poured on carbon-coated TEM grids. The film formed on the TEM grids was allowed to dry for 2 minutes following which the extra solvent was removed using a blotting paper and the TEM measurements were performed.

### 2.3.3 Photon correlation spectroscopy

Photon correlation spectroscopy (PCS) [14], also called dynamic light scattering (DLS), is a common technique to obtain nanoparticle size. The determination of the diffusion coefficient of the nanoparticles in solution gives access to the hydrodynamic radius of a corresponding sphere and the polydispersity of the colloidal solution.

When light hits small particles, the light scatters in all directions (Rayleigh scattering) so long as the particles are small compared to the wavelength (below 250 nm). If the light source is a laser, and thus is monochromatic and coherent, then one observes a time-dependent fluctuation in the scattering intensity. These fluctuations are due to the fact that the small molecules in solutions are undergoing Brownian motion and so the distance between the scatterers in the solution is constantly changing with time. This scattered light then undergoes either constructive or destructive interference by the surrounding particles and within this intensity fluctuation, information is contained about the time scale of movement of the scatterers.

There are several ways to derive dynamic information about particles' movement in solution by Brownian motion. One such method is dynamic light scattering, also known as quasi-elastic laser light scattering. The dynamic information of the particles is derived from an autocorrelation of the intensity trace recorded during the experiment. The second order autocorrelation curve is generated from the intensity trace as follows

$$g^2(q; \tau) = \frac{\langle I(t)I(t+\tau) \rangle}{\langle I(t) \rangle^2} \quad (2.5)$$

where  $g^2(q; \tau)$  is the autocorrelation function at a particular wave vector,  $q$ , and delay time,  $\tau$ , and  $I$  is the intensity. At short time delays, the correlation is high because the particles do not have a chance to move to a great extent from the initial state that they were in. The two signals are thus essentially unchanged when compared after only a very short time interval. As the time delays become longer, the correlation starts to exponentially decay to zero, meaning that after a long time period has elapsed, there is

no correlation between the scattered intensity of the initial and final states. This exponential decay is related to the motion of the particles, specifically to the diffusion coefficient. To fit the decay (i.e., the autocorrelation function), numerical methods are used, based on calculations of assumed distributions. If the sample is monodisperse then the decay is simply a single exponential. The most important use of the autocorrelation function is its use for size determination.

Researchers noticed that the hydrodynamic size values obtained by laser light scattering are often larger than diameters obtained from transmission electron microscopic (TEM) measurements and, for the same sample, the hydrodynamic size can change with the suspension conditions [15,16]. There are many theories regarding the nature of this discrepancy. One is the “hairy layer” model that attributes the larger apparent size to a hairy layer formed by surface molecular chains [17]. Another is the hydration model that uses surface hydration and the electric double layer to explain the observed difference [18,19]. Probably both phenomena give rise to this discrepancy because the water and coating electronic density are not surveyed by TEM and X-ray diffractions techniques. The discrepancy between the hydrodynamic size and the solid dimension of the particles poses a challenge regarding the reliability of applying only one technique as dynamic light scattering which is commonly used for stability studies. This effect is particularly relevant for superparamagnetic iron oxide nanoparticles because there is a great difference between their crystal and their hydrodynamic size.

In the present work, the DLS measurements were carried out on the coated iron oxide samples using a Brookaven Particle Size Analyser by making aqueous solutions.

#### **2.3.4 Infrared (IR) spectroscopy**

IR spectroscopy [20] is a useful tool for the understanding of the functional group of any organic molecule. FT-IR [21] has been widely used to confirm the attachment of different functional groups in each step of functionalization. The atoms in a molecule do not remain in a fixed relative position and vibrate about some mean position. Due to this vibrational motion if there is a periodic alternation in the dipole moment then such mode of vibration is infrared (IR) active. The IR region of the

electromagnetic spectrum is 100 to 1  $\mu\text{m}$  wavelength. The vibrating molecule absorbs energy only from radiation with which it can coherently interact, *i.e.* the radiation of its own oscillation frequency. The appearance or non-appearance of certain bands in an IR spectrum at certain vibrational frequencies gives valuable information about the structure of a particular molecule. The frequency of vibration is given by the relation

$$\vartheta = \frac{1}{2\pi} \sqrt{\frac{k}{\mu}} \quad (2.6)$$

where  $k$  is force constant and  $\mu$  is reduced mass.

In the present work, the IR studies were carried out on the iron oxide samples using a Perkin Elmer Spectrum-One FTIR Spectrometer in the frequency range 400 to 4000  $\text{cm}^{-1}$  by properly mixing the sample with spectroscopic grade KBr.

### 2.3.5 Thermogravimetric Analysis (TGA)

TGA [22] has been performed to get quantitative information on the amount of molecules coated on the surface of the nanoparticles and to confirm the coating formation (especially surfactants or polymers) to estimate the binding efficiency on the surface of magnetic nanoparticles

In the present study, dynamic thermogravimetry (TG) technique is used, in which the sample is heated in an environment whose temperature is changing in a predetermined manner, at a linear rate. There are many events considered in TG, such as desorption, absorption, sublimation, vaporization, oxidation, reduction and decomposition. Moreover, TG is used to characterize the decomposition and thermal stability of materials under a variety conditions [23]. TG curves are usually recorded using a thermobalance.

A Seiko 32 thermal analyzer was used to perform the thermogravimetric analysis (TGA) of various precursors and samples. Thermal analysis was carried out up to 1000  $^{\circ}\text{C}$  in flowing air, at a heating rate 10  $^{\circ}\text{C}/\text{min}$ .

### 2.3.6 UV-Visible Spectroscopy

UV-Visible spectroscopy is the measurement of the intensity of absorption of near ultraviolet and visible light by a sample. Ultraviolet and visible light are energetic enough to promote outer electrons in an atom to higher energy levels. UV-Vis spectroscopy is usually applied to molecules and inorganic ions or complexes in solution or solid samples [24]. The UV-Vis spectra have broad features that are of limited use for sample identification but it is a very useful technique for quantitative measurements. Moreover, UV-Vis spectroscopy is used to determine the optical band gap transitions of semiconductors.

In the present study, UV-Vis spectroscopy measurements of the solid samples at room temperature were carried out on a Jasco UV-Vis spectrophotometer (V570 UV-VIS-NIR) operated at a resolution of 1 nm.

### 2.3.7 Magnetic measurements

The magnetic characteristics of the different materials were measured on a Vibrating Sample Magnetometer (VSM), as a function of the applied field at different temperatures and as a function of temperature at different applied field strengths [25]. A VSM is a device in which a sample is vibrated in a uniform magnetic field, and the induced voltage in a properly positioned set of coils, which is proportional to the magnetization of the material, is detected. The instrument allows precise magnetization measurements to be made as a function of magnetic field strength, temperature, and crystallographic orientation [26].

An EG&G PAR 4500 vibrating sample magnetometer was used in the present work. The magnetometer was calibrated using a standard Ni sample. Field dependence of magnetization was measured up to a maximum field of 15 kOe. For the temperature variation of magnetization, a constant magnetic field is applied and the magnetization is measured by varying the temperature at a constant heating rate of 2 °C/min. A closed cycle helium cryostat was used for low temperature measurements (12-300K). The sample holder used for room temperature and low temperature measurements is made of a non-magnetic polymer material, Kel-F (poly(chlorotrifluoro)ethelene). For the zero field cooled (ZFC) measurements, the

sample was first cooled to the lowest possible temperature (12 K) in zero magnetic field and magnetization was recorded while warming the sample. In the field cooled (FC) magnetization measurements, the sample was cooled under an applied field and the magnetization was measured while heating in the same field.

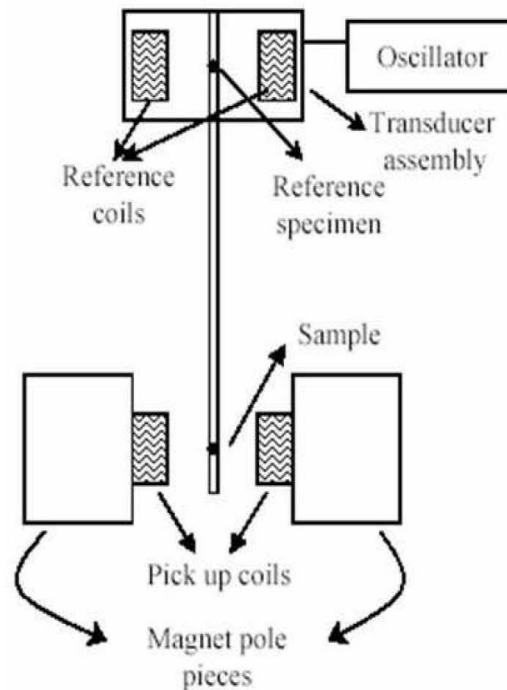


Figure 2.1. Schematic diagram of the VSM components [26].

Aging, rejuvenation and memory experiments were used for various samples which showed spin-glass type behavior and for magnetic nanoparticles. Here, two methods were employed, FC and ZFC protocols with temperature steps and cycling. The spin glass systems are known to show aging and memory effects. Recent interest in various magnetic nanoparticle systems also makes them important to study such closely resembling properties. For this, commonly multiple memory experiments are used. In the present work, single or double memory experiments are mainly employed. A typical memory experiment (by *dc* method) employed in the present work is as illustrated in Figures 2.2, (a) and (b) for FC and ZFC methods, respectively. The sample was initially cooled to a lower temperature below the existence of spin glass-like phase by FC or ZFC methods. Sufficient waiting time is

given at one or more temperatures during cooling. The magnetization was then recorded on heating. It is important that the heating/cooling should be in a controlled fashion and a heating/cooling rate of 2 K/min has been used in the present work.

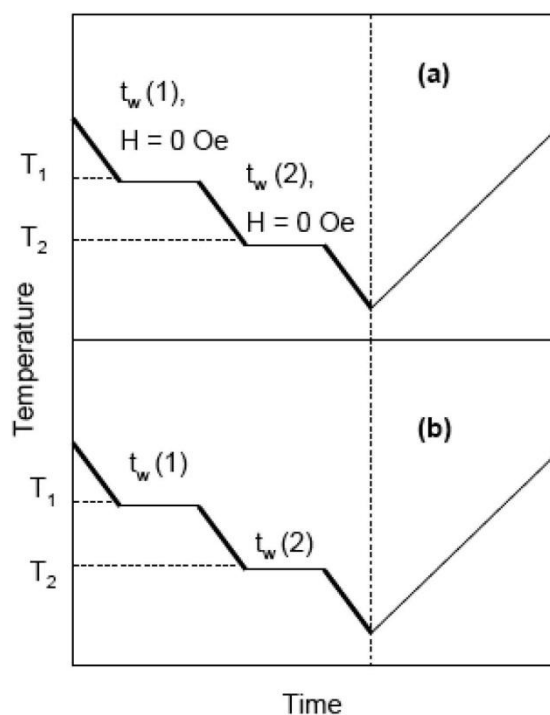


Figure 2.2. Typical memory experiments following (a) FC protocol and (b) ZFC protocol.  $T_1$  and  $T_2$  are two temperatures in the spin glass-like regime where the sample is aged or allowed for waiting times of  $t_w(1)$  and  $t_w(2)$ , respectively. Field,  $H=0$  at the halts, but a finite value of  $H$  (say, 50 Oe) is maintained during cooling in the FC method. The measurement was carried out during heating by applying a low field (say, 50 Oe).

### 2.3.8 Nuclear Magnetic Resonance (NMR) Spectroscopy

NMR [27] is an extremely valuable analytical technique and the desire to develop it as a probe for solids and surfaces has been intense among researchers. Today NMR spectroscopists have at their disposal a huge battery of solid-state NMR experiments that allow the features of molecular structure and molecular dynamics to be determined. We can get information regarding molecular structure, inter molecular packing, inter nuclear distance, nature of interaction, molecular dynamics, molecular

degrees of freedom etc of a lot of polymers, catalysts and proteins, which are solid in nature. The excellent feature of this technique is that it can be used effectively even in inhomogeneous or amorphous systems.

NMR [28] depends on the nature of nucleus of an atom. Most nuclei have the property of spin similar to electrons. Electrons have the spin quantum number of  $\frac{1}{2}$  and pair up with the antiparallel spins in atomic orbital. Protons and neutrons (nucleons) are also spin  $\frac{1}{2}$  particles and arrange themselves in energy states somewhat similar to atomic orbital. If nucleus has both an even number of protons (Z) and even number of neutrons (N), then all the nucleon spin will be paired and there is no net spin. All other nuclei possess spin (such as  $^1\text{H}$  and  $^{13}\text{C}$ ). The spin of the nucleus is usually given by the symbol I, called the spin quantum number. Since nucleon spin is quantized at  $\frac{1}{2}$ , the net nuclear spin I is also quantized.

The solid state NMR [29,30] experiments can be set up such that the anisotropic nuclear spin interaction, which vanishes in solution state NMR experiments, remains in force. Thus, the anisotropy of nuclear spin interactions such as chemical shift anisotropy, dipole-dipole interactions, and quadrupole interactions can all be used by the chemist to get quantitative information on molecular structure, conformation and dynamics. The spectral resolution used to be a problem in solid state NMR. There are several factors contributing to the breadth of the resonance lines in solid state NMR spectra such as dipole-dipole interaction, quadrupolar coupling etc.

A deeper understanding to the origin of the limitations faced by sample spinning towards the removal of spectral broadening was achieved about decades ago, and lead to the development of Magic Angle Spinning.

#### **2.3.8.1 Magic angle spinning (MAS)**

MAS is an invaluable line narrowing technique in solid state NMR. The spinning of sample about an angle  $\theta_R$  with respect to the applied field in effect scales the anisotropy of any interaction by a factor  $(3\cos^2 \theta_R - 1)$ . This factor is zero at the magic angle  $54.74^\circ$  but non-zero if the angle is mis-set. To set the magic angle, a sample is required which gives a good signal in a single scan, and which gives lots of

spinning side bands at moderately spinning rate i.e., observed nucleus should be affected by an inhomogeneous interaction with an anisotropy of an order of 100 kHz. The most commonly used standard for setting the magic angle is  $^{79}\text{Br}$  ( $I = 3/2$ ) resonance in solid KBr.

### 2.3.8.2 Multiple Quantum Magic-Angle Spinning (MQMAS)

The MQMAS experiment was first proposed in 1995 for achieving high resolution for half integer quadrupolar nuclei while spinning the sample at just one angle, the magic angle, throughout the experiment. It is a two-dimensional experiment and achieves the resolution via refocusing of evolution during  $t_1$  period in a second period of precession  $kt_1$ . In order to do this a change in transition frequency is needed between the two periods, which is done by changing the order of evolving coherences. In particular multiple quantum coherence corresponding to a symmetric  $+m \rightarrow -m$  transition evolves during  $t_1$ . This is then converted to single quantum coherence, which evolves during  $kt_1$ .

Disregarding the anisotropic dipolar and chemical shift contributions and allowing only for isotropic chemical shielding  $\nu^{\text{cs}}_{\text{iso}}$  the transition frequencies that will result for any symmetric  $-m \leftrightarrow +m$  transition upon subjecting  $H_Q^2$  to fast spinning can be written as:

$$\begin{aligned} \nu(m, \chi) = & \nu^{\text{cs}}_{\text{iso}} 2m + \nu^{\text{Q}}_0 C_0^{\text{I}}(m) P_0 \cos \chi + \nu^{\text{Q}}_2 (\varphi, \theta) C_2^{\text{I}}(m) P_2 \cos \chi \\ & + \nu^{\text{Q}}_4 (\varphi, \theta) C_4^{\text{I}}(m) P_4 \cos \chi \end{aligned} \quad (2.7)$$

The spinning angle  $\chi$  and quantum number  $m$  dependencies originated from  $\{A_{2n}\}$  and  $I_z$  operators.  $(\varphi, \theta)$  are powder angles orienting a given crystallite with respect to the rotor frame. The shielding and dipolar anisotropies can solely scaled by  $P_2 \cos \chi$  and susceptible to averaging by MAS, the second order nature introduces a new  $P_4 \cos \chi$  term. This again is consequence of quadratic dependence of  $H_Q^2$  on the  $\{A_{2n}\}$  elements. Although the individual  $P_2$  and  $P_4$  polynomials that scales the spectral broadening can be zeroed at particular choices of spinning axis, no single  $\chi$  value can remove simultaneously  $\nu_2^{\text{Q}}(\varphi, \theta)$ ,  $\nu_4^{\text{Q}}(\varphi, \theta)$  anisotropies.

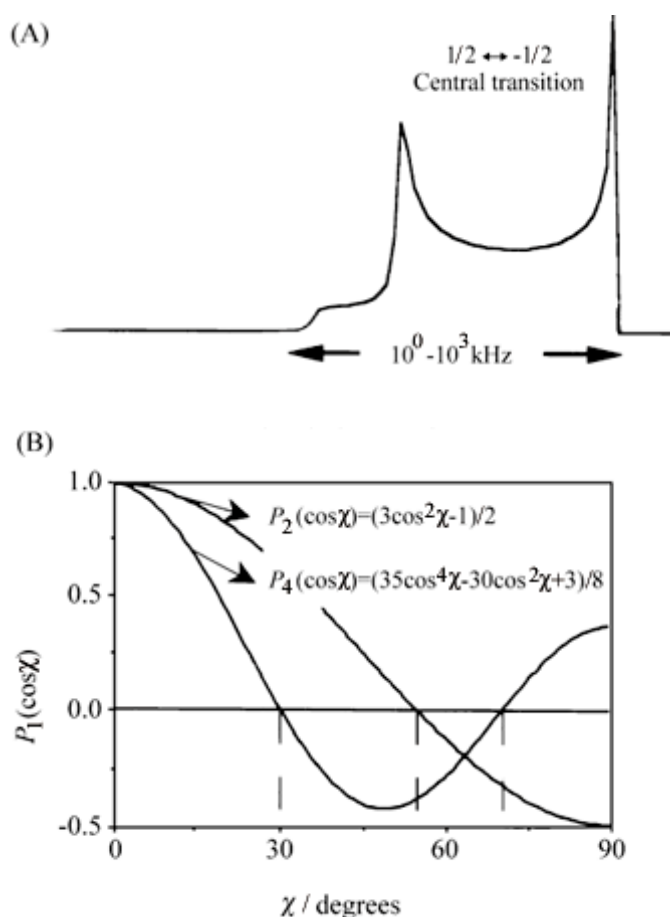


Figure 2.3. (A) Effects of the second-order frequency shifts  $\Delta 2(\varphi, \theta)$  on the central transition spectrum arising from a static powder. Although much smaller than first-order effects, these broadenings are still large enough to prevent the resolution of chemically-inequivalent sites in a sample. (B) Orientation dependence of the two Legendre polynomials  $\{P_l(\cos\chi)\}_{l=2,4}$  that define the line broadening of central transition quadrupolar patterns, showing the positions of their non-coincident roots and the consequent inability of  $\chi = 54.7^\circ$  magic angle) to average all broadenings away [30].

In MQMAS experiment the averaging is done by changing the order of evolving coherences. The multiple quantum coherence of order  $2m$  is first excited and allowed to evolve during  $t_1$ . The experiment is conducted under magic angle spinning which may be assumed to average to zero the second rank terms throughout the experiment. The only anisotropy in the evolution during  $t_1$  arises from  $P_4 \cos \chi$ . At the end of  $t_1$  second rf pulses transfer the remaining multiple quantum coherences to single quantum coherence associated with  $+1/2 \rightarrow -1/2$  transition. The important point

is that the evolution of multiple quantum coherences during  $t_1$  is now 'undone' by the evolutions of single quantum coherence during  $kt_1$  associated with the central transition second order quadrupole broadening. The value of  $k$  is given by the ratio of co-efficient of second order quadrupole coupling term in frequency of multiple quantum coherence and the central transition  $R_4(I, m)$ . At the end of  $kt_1$ , a normal FID is collected. A two-dimensional data set is collected. In MQMAS data, an echo analogous to the DAS is seen to shift in time with increasing  $t_1$  values. Fourier transformation results in a two-dimensional frequency spectrum in which the  $f_1$  dimension exhibits an isotropic spectrum and the  $f_2$  dimension, the anisotropic powder patterns associated with central transition of different sites. The amplitude of multiple quantum coherence generated depends upon the strength of quadrupole coupling.

All measurements were carried out on a Bruker AV 300 and A V 500 MHz NMR spectrometer. AV 300 MHz NMR spectrometer equipped with a 7.05 Tesla wide bore superconducting magnet. After inserting sample into the probe, it was spun at 12.5 kHz for reducing all the interactions, which causes broadening of the spectra. The probe was tuned to the required frequency using the wobbler mode.  $^{27}\text{Al}$  is 100% abundant nucleus and the spin of  $^{27}\text{Al}$  is  $5/2$ .  $^{27}\text{Al}$  gives a resonance frequency of 78.172 MHz. The samples were packed in 4 mm zirconia rotors. The spinning rates of 12.5 k Hz are used. The free induction decay spectra were taken with a single excitation pulse. For  $^{27}\text{Al}$ , a short pulse of  $0.6\mu\text{s}$  was used. Size of free induction decay was 32kilobites and number of scans used was 4000. The  $^{27}\text{Al}$  spectra were referenced to 0.1M aqueous solutions of  $\text{Al}_2(\text{SO}_4)_3$ . On the AV500 spectrometer, the samples were packed into 2.5-mm zirconia rotor and spun at the magic angle at a spinning speed of 34.1 kHz.

$^{27}\text{Al}$  MAS NMR resonances are typically broadened by non-negligible second-order anisotropic effects. Recently experimental methods have been developed utilizing a combination of MAS and multiple quantum evolution which serves to provide a high resolution spectra of  $I = 5/2$  spins. For  $^{27}\text{Al}$  MQMAS experiment, a standard two-pulse z-filtered pulse sequence (shown in the Figure 2.4) was used. The spinning rate was 12.5 kHz. The length of the first pulse (MQ creation pulse) was  $3.4\mu\text{s}$  conversion pulse  $1.1\mu\text{s}$ . The z-filter pulse was  $22\mu\text{s}$ . The rf power for the MQ creation pulse and the conversion pulse were 78 kHz and that for the z-filter pulse was

5kHz. The size of Fourier induction decay (FID) was 2048 and 420 number of scans were collected for each  $t_1$  point. Data was acquired and processed using states method and the data was shear transformed in the indirect dimension. The quadrupole coupling parameters which includes the second order quadrupole effects  $SOQE = C_Q (1 + \eta^2/3)$ , where  $C_Q$  is the quadrupole coupling constant and  $\eta$  is the asymmetry parameter and isotropic chemical shifts ( $\delta_{iso}$ ) have been estimated for the analysis of the resonance position in the unshared spectra.

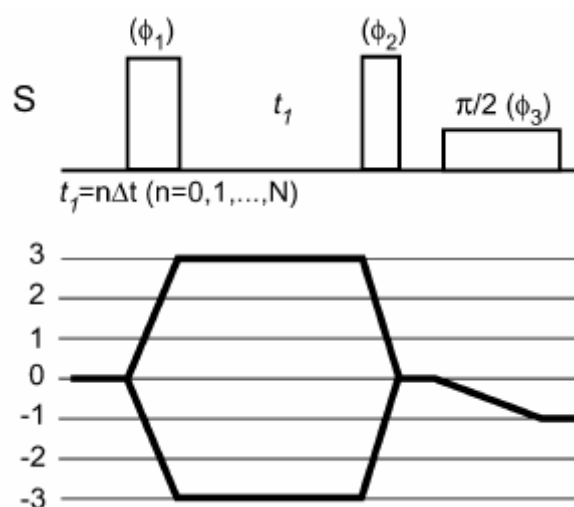


Figure 2.4. Pulse sequence and coherence diagram used

3QMAS NMR method has been widely used in MQMAS NMR technique, because triple quantum coherence is most readily excited and converted to single quantum coherences. The used pulse sequence and coherence diagram are given above. This pulse sequence is designed to select the 3Q coherences after the first pulse. After the  $t_1$  evolution, the second pulse converts the 3Q coherence to the zero quantum coherence. After a short delay (20  $\mu$ s), the z-filter pulse converts the zero-quantum coherence to the observable single quantum coherence. The results of the MAS as well as MQMAS experiments are discussed in chapter 5.

---

**References**

- 1 Edelstein, A. S.; Cammarata, R. C., *Nanomaterials: Synthesis, Properties and Applications*, Institute of Physics Publishing, Bristol and Philadelphia, **2001**
- 2 Paike, V. V.; Niphadkar, P. S.; Bokade, V.V.; Joshi, P.N., *J. Am. Ceram. Soc.*, **2007** 90, 3009
- 3 Laurent, S.; Forge, D.; Port, M.; Roch, A.; Robic, C.; Elst, L.V.; Muller, R.N. *Chem. Rev.*, **2008**, 108, 6, 2064.
- 4 Aono, H.; Hirazawa, H.; Naohara, T.; Maehara, T.; Kikkawa, H.; Watanabe, H., *Mater. Resear. Bull.* **2005**, 40, 1126.
- 5 Patil, K.C.; Hegde, M.S.; Rattan, T.; Aruna, S. T., *Chemistry of Nanocrystalline Oxide Materials: Combustion Synthesis, Properties and Applications*, World Scientific Publishing Co., Singapore, **2008**
- 6 Chick, L. A.; Pederson, L. R.; Maupin, G. D.; Bates, J. L.; Thomas, L. E.; Exarhos, G.J. *Mater. Lett.* **1990**, 10, 6.
- 7 Kikukawa, N.; Takemori, M.; Nagano, Y.; Sugasawa, M.; Kobayashi, S., *J. Magn. Mater.* **2004**, 284, 206.
- 8 Lu, A. H.; Salabas, E. L. Schuth, F., *Angew. Chem. Int. Ed.* **2007**, 46, 1222
- 9 West, A. R. *Solid State Chemistry and its Applications*, John Wiley & Sons, Singapore, **2003**
- 10 Cullity, B. D. *Elements of X-Ray Diffraction 2nd ed.* Addison-Wesley, Reading, Massachusetts, **1978**
- 11 Kraus, W.; Nolze, G., *PowderCell for Windows (PCW), version 2.4* (The software is freely available from <http://www.ccp14.ac.uk>.)
- 12 Thomas, G., *Transmission Electron Microscopy of Metals*, John Wiley & Sons, Inc, New York, **1962**
- 13 Williams, D. B.; Carter, C. B., *Transmission Electron Microscopy: A Textbook for Materials Science Vol. I-IV*, Plenum Press, New York, **1996**
- 14 Pecora, R, *Dynamic light scattering: applications of photon correlation spectroscopy*, Springer, Berlin, **1985**
- 15 Prescott, J. H.; Shiau, S. J.; Rowell, R. L., *Langmuir*, **1993**, 9, 2071
- 16 Prescott, J. H.; Shiau, S. J.; Rowell, R. L., *Langmuir*, **1997**, 13, 1978
- 17 Seebergh, J.E.; Berg, J. C., *Colloids Surf A*, **1995**, 100, 139

- 
- 18 Johnson, P. *Langmuir*, **1993**, 9, 2318
  - 19 Fischer, C.H.; Kenndler, E. J., *J Chromatogr A*, **1997**, 773, 179
  - 20 Nyquist, R., *Interpreting Infrared, Raman, and Nuclear Magnetic Resonance Spectra*, Academic Press, New York, **2001**
  - 21 Rittner D.; Bailey, R. A. *Encyclopedia of Chemistry*, Facts On File, Inc. New York
  - 22 Wendlant, W. W. M., *Thermal Methods of Analysis*, 2nd ed. John Wiley & Sons, New York, **1974**
  - 23 Hatakeyama, T.; Quinn, F. X., *Thermal Analysis: Fundamentals and Applications to Polymer Science*, John Wiley & Sons, New York, **1995**
  - 24 Lever, A. B. P., *Inorganic Electronic Spectroscopy: Studies in Physical and Theoretical Chemistry*, V. 33, 2nd ed. Elsevier Science Publishers, Amsterdam, **1984**
  - 25 Cullity, B. D., *Introduction to Magnetic Materials*, Addison-Wesley Publishing Company, Massachusetts, **1972**
  - 26 S. Foner, *Rev. Sci. Inst.* **1959**, 30, 548.
  - 27 Macomber, R. S., *A complete introduction to modern spectroscopy*, John Wiley & Sons Inc., New York, **1997**
  - 28 Derome, A. E., *Modern NMR techniques for Chemistry Research*, Volume 6, Pergamon, Oxford, **1987**
  - 29 Duer, M. J., *Introduction to Solid-state NMR spectroscopy*, Blackwell publishing Ltd, Oxford, **2004**
  - 30 Levitt, M. H., *Spin dynamics Basics of Nuclear Magnetic Resonance*, John Wiley & Sons Ltd., UK, **2001**

## CHAPTER 3

### SYNTHESIS AND MAGNETIC PROPERTIES OF IRON OXIDE NANOPARTICLES

#### 3.1 Introduction

Superparamagnetic iron oxide nanoparticles (SPIONs) of  $\gamma$ -Fe<sub>2</sub>O<sub>3</sub> (maghemite) or Fe<sub>3</sub>O<sub>4</sub> (magnetite) are suitable candidates for many biomedical applications such as magnetic carriers for targeted drug delivery, magnetically mediated hyperthermia, separation of biochemical products, contrast enhancement agent for magnetic resonance imaging, etc. [1,2]. Apart from the biomedical applications [3,4], the iron oxide nanoparticles are of technological importance due to their applications in many fields including high density magnetic storage devices [5], ferrofluids [6,7], magnetic refrigeration systems, and catalysis [8,9]. Therefore, in the recent years, studies on nanometer-sized iron oxide magnetic particles have been the focus of intense fundamental and applied research, with special emphasis on the size-dependent magnetic properties. In this respect, the synthesis of chemically stable  $\gamma$ -Fe<sub>2</sub>O<sub>3</sub> and Fe<sub>3</sub>O<sub>4</sub> has become very important in modern research. For several decades, iron oxides have been used in various magnetic applications, such as in magnetic recording tapes and other devices. Therefore, study of this material has a long history, and the recent focus is on these nanosized particles, in view of the various technological and bio medical applications.

Various methods are known for the synthesis of iron oxide nanoparticles such as co-precipitation [10,11], vaporization–condensation [12], microemulsion [13], thermal decomposition [14], thermolysis [15], sonochemical [16], hydrothermal [17], etc. Very recently, Bharde et al. reported microorganisms based synthesis of magnetite at ambient conditions, using bacteria and fungi [18,19]. Recently, several research groups [20, 21] have attempted to understand the factors that tailor particle size and influence of particle size on magnetic properties. Despite many modes of control, most studies [22,23] have achieved sizes in the 3–20 nm range and very few studies have shown particles with average diameters below 4 nm [24]. The most recent foci for attaining size control have been methods aimed at the separation of nucleation from growth processes. Recently, Sun et al. [25] have described the

synthesis of magnetite nanoparticles by organic solution base decomposition of iron precursors which can lead to monodispersed nanoparticles. However, the processes associated with decomposition reaction and subsequent particle formation is extremely complex and ill-understood. One of the main drawbacks of such strategies is the low amount of sample produced in a single batch, which is probably the main limitation for further applications. Moreover, the materials used for this method of synthesis are quite expensive and carcinogenic as compared to the conventional coprecipitation method. Current or future synthetic routes based on controlled nucleation and growth phenomena will be probably more appropriate from the viewpoint of their yield and cost.

The co-precipitation [26,27] technique is generally employed by various researchers for the synthesis of  $\gamma$ - $\text{Fe}_2\text{O}_3$  nanoparticles and this route involves the initial formation of  $\text{Fe}_3\text{O}_4$  from a mixed solution containing  $\text{Fe}^{2+}$  and  $\text{Fe}^{3+}$  and the magnetite formed is oxidized to  $\text{Fe}_2\text{O}_3$ . Many papers report on the synthesis of fine  $\text{Fe}_3\text{O}_4$  nanoparticles with 2–10 nm in diameter by the coprecipitation reaction. Some of these reports describe synthesis conditions for controlling the particle size in the range of 2–20 nm in diameter. None of these reports mention about the formation of uniform sized iron oxide nanoparticles obtained by coprecipitation method. Hence, it is a challenge to synthesise monodisperse iron oxide nanoparticles by coprecipitation method. The Massart process [28] describes the coprecipitation of  $\text{Fe}_3\text{O}_4$  without molecules for stabilization. In the original synthesis, magnetite ( $\text{Fe}_3\text{O}_4$ ) particles were roughly spherical, and their crystallite size measured by XRD was 12 nm. Many researchers have studied the influence of different parameters, including the iron media and the iron concentration, pH, temperature etc [29,30].

Various reports show that magnetite nanoparticles play interesting magnetic behaviour [31] which are not observed in bulk materials and the properties can be tuned by adjusting the particle size [32,33]. Wu et al [34] have studied the magnetic behaviour of iron oxide nanoparticles with average particle sizes ranging from 2 to 4 nm. It was found that there is a contradiction between the magnetic properties reported for iron oxide nanoparticles in number of research articles [35,36]. A good example for this difference is obvious in the work reported by Wu et al [34] and Iida et al [37]. The superparamagnetic blocking temperature reported for 4 nm iron oxide

nanoparticles are different but the shape of the ZFC and FC magnetization curves remain same in both cases. Similarly, there is a difference in the saturation magnetisation for 9 nm iron oxide nanoparticles reported by Iida et al [37]. Hitherto there is no correct explanation for the arguments on size dependent magnetic properties of iron oxide nanoparticles. In almost all applications using magnetite nanoparticles, the preparation method plays a major role in determining the particle size, shape, the size distribution, the surface chemistry of the particles and consequently their magnetic properties which in turn depends on the cation distribution present in the sample. It is therefore instructive to look into size dependent magnetic properties of iron oxide nanoparticles.

One of the main intentions of this work is to develop a simple and reproducible route for the synthesis of iron oxide nanoparticles by modifying the existing coprecipitation method to achieve monodisperse iron oxide nanoparticles and tune the magnetic properties with respect to particle size. This is likely to be possible by adjusting the cooking parameters involved during the synthesis. In this chapter we describe studies on the synthesis of iron oxide nanoparticles by the simple reverse coprecipitation method.

Table 3.1. Comparison of the properties of iron oxide nanoparticles reported in the literature. LT – low temperature, RT – room temperature

No.	Synthesis method	Type of magnetic measurement	Particle size (nm)	M <sub>s</sub> (emu/g)	T <sub>b</sub> (K)	T <sub>irr</sub> (K)	Measuring Field (Oe)	Reference
1.	Thermal Decomposition	LT	4 13 16		25 185 290		100	[13]
2.	Thermal Decomposition	LT	4 6 8 9 11 12 13 15		8 30 70 100 190 200 185 280	8 30 70 100 190 200	100	[21]
3.	Hydrolysis	RT	8 37	46.7 86.6			10000	[22]
4.	Coprecipitation	RT	2.5 3.6 4.5 5.3	19.2 16.8 20.2 24.1			40000	[34]
		LT	2.5 3.6 4.5 5.3		60 70 150 170	60 70 220 300	100	
5.	Reduction	RT	4 11.5 47.7 150	31.8 60.1 65.4 75.6				[36]

		LT	4 11.5 47.7 150		45 107 300	50 115 400	500G	
6.	Thermal Decomposition	RT	4	36.2			2000	[38]
		LT	4		20	20	1000	
7.	Thermal Decomposition	RT	8	58.7			30000	[39]
8.	Microemulsion	LT	1.9		45	45	5	[40]
			2.4		60	60		
			3.6		75	75		
			5.6		140	140		
			7.3		210	210		
9.	Solvothermal	RT	12.7	84			50000	[41]
		LT	12.7		95	230	500	
10.	Coprecipitation	RT	8.9 10.3 13.5	54.8 62.3 69.6			10000	[42]
11	Coprecipitation	RT	10.9	47.1			10000	[43]
			4.9	59.4				
			15.2	56.5				
			11.5	56.3				
			15.0	51.8				
			6.6	62.2				
			16.8	63.4				
			24.6	67.9				

### 3.2 Synthesis of Magnetite Nanoparticles

Coprecipitation is a facile and convenient way to synthesize iron oxides (either  $\text{Fe}_3\text{O}_4$  or  $\gamma\text{-Fe}_2\text{O}_3$ ) from aqueous  $\text{Fe}^{2+}/\text{Fe}^{3+}$  salt solutions by the addition of a base under inert atmosphere at room temperature or at elevated temperature. The size, shape, and composition of the magnetic nanoparticles very much depend on the type of salts used (e.g. chlorides, sulfates, nitrates), the  $\text{Fe}^{2+}/\text{Fe}^{3+}$  ratio, the reaction temperature, the pH value and ionic strength of the media. With this method of synthesis, once the synthetic conditions are fixed, the quality of the magnetite nanoparticles is fully reproducible. The experimental challenge in the synthesis of  $\text{Fe}_3\text{O}_4$  by coprecipitation lies in the control of the particle size and thus achieving a narrow particle size distribution.

The main advantage of the coprecipitation process is that a large amount of nanoparticles can be synthesized in a single batch. However, the control of particle size distribution is limited, because only kinetic factors are controlling the growth of the crystal. In the coprecipitation process, two stages are involved: a short burst of nucleation occurs when the concentration of the species reaches critical super saturation, and then, there is a slow growth of the nuclei by diffusion of the solutes to the surface of the crystal. Particles prepared by coprecipitation, unfortunately, are polydisperse in nature. It is well known that a short burst of nucleation and subsequent slow controlled growth is crucial to produce monodisperse particles. Controlling these processes is therefore the key in the production of monodisperse iron oxide nanoparticles.

We have explored the synthesis of magnetite nanoparticles over a range of particle size based on an underlying reaction scheme that relies on the reverse coprecipitation of iron solution by using ammonia. This type of approach is not established in nanoscale syntheses. By optimizing the reaction conditions, one can get reproducible formation of magnetite nanoparticles of desired particle size. Recently Alvarez et al. [44] synthesised iron oxide nanoparticles by flow injection method in a capillary reactor. They obtained magnetite nanoparticles had a narrow size distribution in the range 2–7 nm. This synthesis strategy lead to well defined iron oxide nanoparticles, however, the yield of the product, reproducibility of the synthesis

method, cost due to capillary reactor, etc are not known. Thus, there is an open avenue to the researchers for the synthesis of iron oxide nanoparticles.

Although the coprecipitation method is the simplest and the most efficient chemical pathway to obtain magnetite particles, it has disadvantages such as large particle size distribution, aggregation and poor crystallinity, resulting in low saturation magnetization values. These disadvantages have led to the development of advanced methods of magnetite synthesis. Here we highlight the influence of the mode of addition of iron solution in the reverse coprecipitation reaction for the synthesis of iron oxide nanoparticles.

As described in the LaMer diagram [45], for homogeneous precipitation, as concentration increases to past saturation, a point is reached where nucleation occurs. Particle growth most likely transpires by a combination of diffusion of atoms onto nuclei and irreversible aggregation of nuclei. In order to produce monodisperse particles, nucleation should be avoided during the period of crystal growth. To control the particle size, three different schemes of addition of iron solution to the base were used such as addition of Fe solution using a burette (slow and controlled addition), addition of iron solution by separating funnel (fast and controlled addition), by direct pouring (very fast, uncontrolled addition) of Fe solution to ammonia. The sample codes are shown in table 3.2. The mode of addition is found to be influence on the particle size and particle size distribution and this was confirmed by PXRD, TEM and VSM studies.

The coprecipitation reaction was carried out by taking 0.1 moles of  $\text{FeCl}_2$  and 0.2 moles of  $\text{FeCl}_3$  in the 1:1 ratio. 20 ml of the mixture of  $\text{Fe}^{2+}$  and  $\text{Fe}^{3+}$  was precipitated by using 100 ml of 10N  $\text{NH}_4\text{OH}$ . Then the mixture was stirred for 15 min at room temperature. Iron oxide nanoparticles were prepared by three different mode of addition of iron stock solution to ammonia solution in order to control the particle size. All the syntheses were carried out under argon gas passing through the solution media to avoid possible oxygen contamination during the operations. The precipitate was washed thoroughly, several cycles with distilled water, and then dried in an oven at 35 °C.

Table 3.2. Sample codes and mode of addition

Sample Code	Mode of addition
Fe1	Burette addition
Fe2	Separating funnel addition
Fe3	Direct addition

### 3.2.1 Addition of Fe stock solution by a burette

In the burette addition method for synthesising magnetite nanoparticles, the Fe solution is added through the small orifice of the burette that leads to the formation of small droplets and controls the addition process. For confirming the reproducibility of the synthesis method, the iron oxide nanoparticles were synthesized in two different batches and are designated as Fe1a and Fe1b. Both samples are characterised by XRD and VSM. In order to get large amount samples for further surface functionalization studies, magnetite nanoparticles were synthesised by taking double the amount of the mixture of  $\text{Fe}^{2+}$  and  $\text{Fe}^{3+}$  was added to the double the volume of base by using a burette. This sample is named as Fe1c.

#### 3.2.1.1 PXRD Analysis

The XRD patterns of the samples are compared with the simulated pattern of  $\text{Fe}_3\text{O}_4$  in Figure 3.1. The XRD results indicate that observed patterns correspond to the  $\text{Fe}_3\text{O}_4$  spinel structure with face-centered cubic lattice according to the standard JCPDS file No. 19-629. No impurities are detected in any of the samples. The broadness of the XRD peaks can be due to the small size of the particles. The average crystallite size is calculated from the XRD line broadening, using the Scherrer formula [46]. The XRD patterns are indexed to a cubic structure with space group  $\text{Fd}3\text{m}$ , and the calculated lattice parameter for the different samples are shown in Table 3.3 and the values are consistent with that reported in the literature [47].

Table 3.3. Sample codes and crystallite size of synthesized samples

Sample Code	Crystallite size ( $\pm 1$ nm)	Lattice parameter ( $\text{Å}$ )
Fe1a	10	8.39
Fe1b	10	8.36
Fe1c	10	8.38

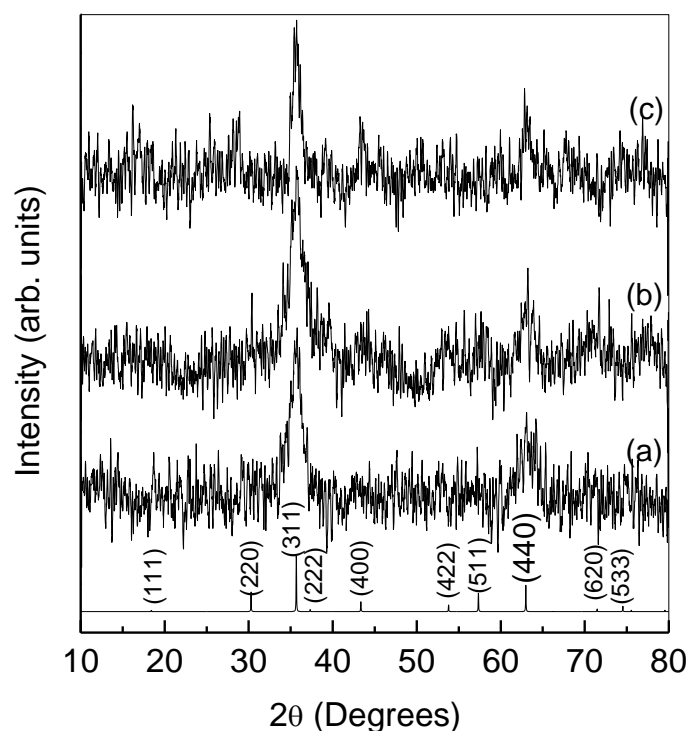


Figure 3.1. Powder XRD patterns of a) Fe1a, b) Fe1b, and c) Fe1c. The simulated pattern of  $\text{Fe}_3\text{O}_4$  is shown at the bottom and indexed.

### 3.2.1.2 TEM Analysis

Transmission electron micrographs have been recorded by drop casting the dispersed magnetite nanoparticles in toluene, on a copper grid. Analysis of TEM images for all the samples showed that the samples consist of non-uniform sized particles with spherical shape and the particles are agglomerated because of the high surface energy of these particles. The TEM image of Fe1c is shown in Figure 3.2. The selected area electron diffraction pattern of Fe1c, shown in the inset of the Figure 3.2,

show diffuse rings, indicating nanocrystalline nature of the particles. The ED patterns correspond to that of magnetite phase, agreeing with the results obtained from XRD.

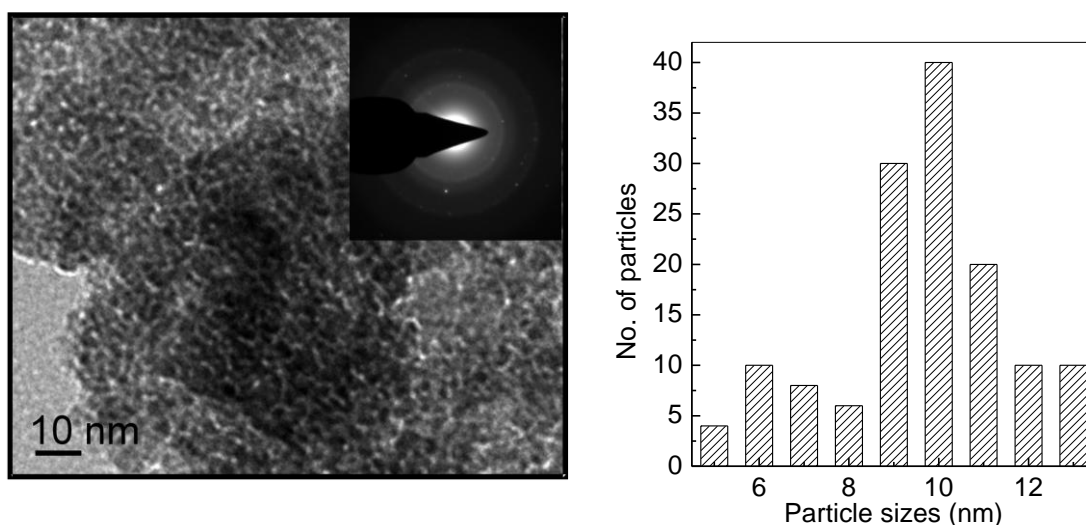


Figure 3.2 TEM micrograph of Fe1c sample (left) and TEM histogram of the particle size distribution

### 3.2.1.3 Magnetic Measurement

Figure 3.3 shows the field dependence of magnetization of Fe1a and Fe1c, measured at room temperature. Both curves are almost identical with similar shape and almost identical magnetization. Magnetic hysteresis is not observed for both samples and this indicates the superparamagnetic nature of the particles.

The temperature dependence of magnetization is recorded in an applied magnetic field of 50 Oe for all the synthesised samples. Figure 3.4 shows the temperature-dependent magnetization measured at 50 Oe from 300 to 12 K. The zero-field cooled (ZFC) magnetization curves of Fe1a and Fe1b show a maximum at 99 K and drops below this temperature. For superparamagnetic particles, the maximum in the ZFC magnetization curve is observed at the blocking temperature ( $T_B$ ). Both samples show same blocking temperature of 99 K. Above the blocking temperature, the nanoparticles showed superparamagnetic behavior due to its single magnetic domain nature as evident from the ZFC measurements. The features of the ZFC magnetization curve such as the broadness of the curve, shape, blocking temperature, etc. are determined the size of the magnetic particles, particle size distribution, etc.

Since both Fe1a and Fe1b show almost identical features in the ZFC magnetization curve, the results indicate that the particle size and distribution are almost comparable and highly reproducible.

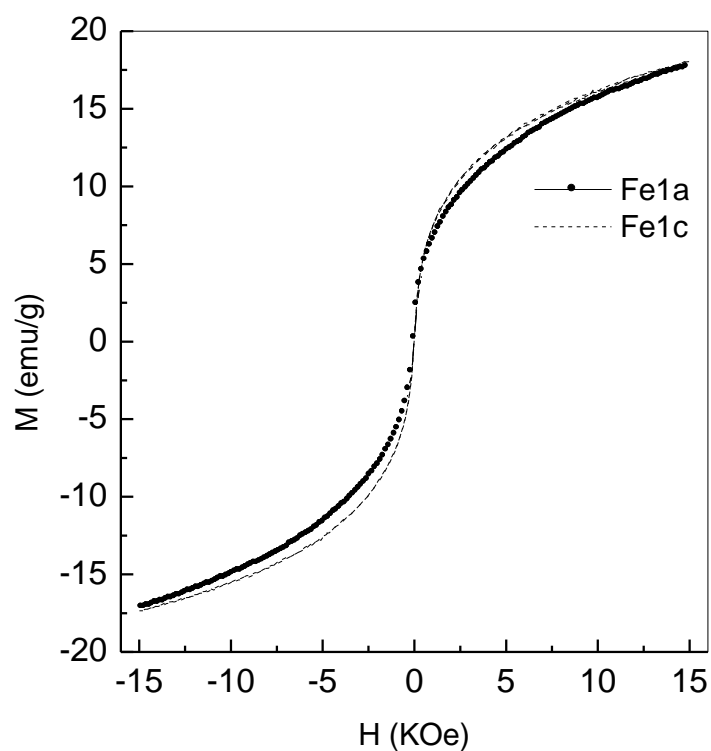


Figure 3.3 Field dependence of magnetisation of Fe1a and Fe1c samples, at room temperature.

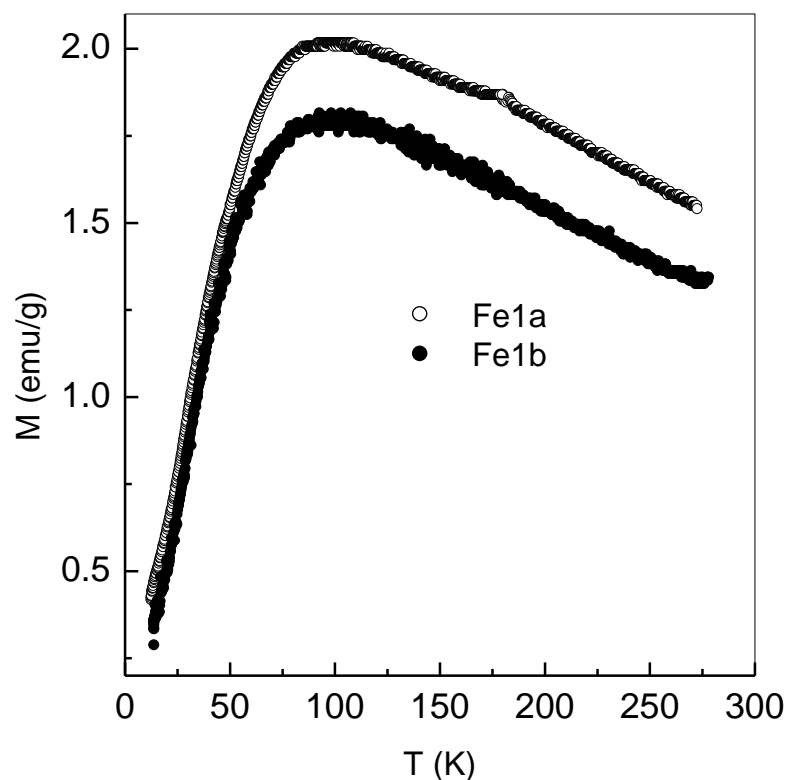


Figure 3.4. ZFC curve of Fe1a and Fe1b samples.

Figure 3.5 compares the ZFC and FC magnetization curves of Fe1a and Fe1c. The two samples are prepared by taking different volumes of the starting chemicals. A striking feature is that both samples show almost identical magnetic characteristics. The FC magnetization remains almost constant below the blocking temperature indicating strong interaction between the particles [48]. The deviation between the FC and ZFC magnetization curves, for both samples, starts below  $\sim 230$  K. However, the blocking temperature of Fe1c is obtained as 109 K, slightly larger than that of Fe1a. As the superparamagnetic blocking temperature is proportional to the particle size, the larger  $T_B$  of Fe1c is indicative of probably the presence of slightly larger amounts of larger particles in Fe1c, with almost comparable distribution. The relatively larger size of the particles in Fe1c is also evident from the relatively larger magnetization at the peak temperature. The fact that the properties are reproducible for Fe1a and Fe1b indicates that the particle size and distribution can be reproduced using a particular concentration and volume of the starting chemicals.

Since it was found possible to synthesize magnetite nanoparticles with a particular average size and size distribution, Fe1c sample was used for further functionalisation studies by using dextran and ascorbic acid, as described in chapter 4. The temperature at which the ZFC peak is maximum, called blocking temperature which depends on particle volume, anisotropy and orientation with respect to the applied field. The magnetic anisotropic constant is calculated from the value of blocking temperature using the relation  $KV \approx 25k_B T_B$ . For Fe1a, K is calculated as  $6.5 \times 10^5 \text{ erg/cm}^3$  from  $T_B = 99 \text{ K}$  and for Fe1c K is obtained as  $7.1 \times 10^5 \text{ erg/cm}^3$ . The differences in the values of  $T_B$  and K for Fe1a and Fe1c are due to the difference in the particle size distribution present in the two samples.

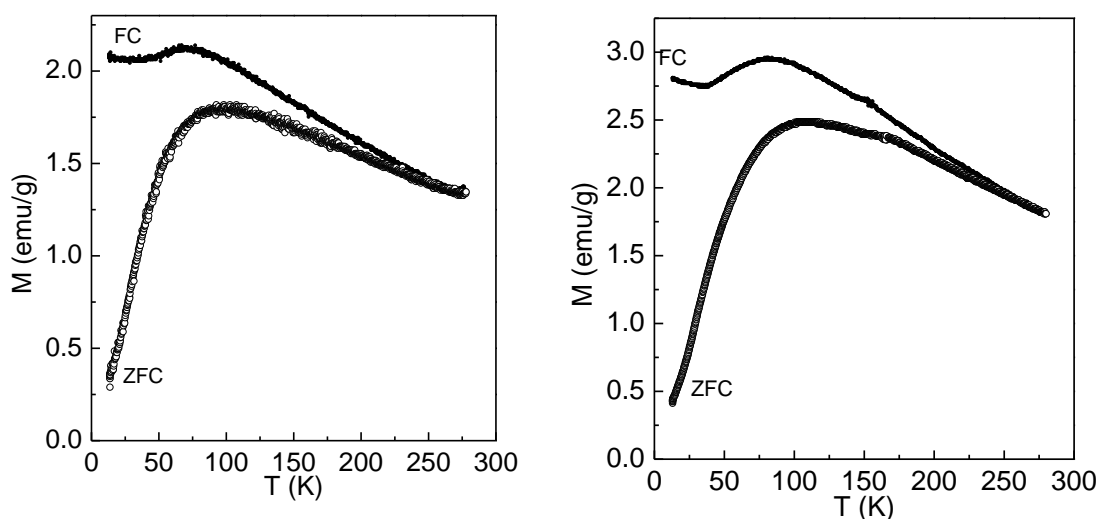


Figure 3.5 Temperature dependent magnetisation curve of Fe1a and Fe1c samples,

### 3.2.2 Addition of Fe stock solution by a separating funnel

In this method, Fe solution was added to the base by using a separating funnel. This method is a relatively fast addition and is not a properly controlled addition of Fe solution due to the higher diameter of the nozzle of the separating funnel as compared to the burette nozzle. The synthesis was repeated to compare the reproducibility of the results.

### 3.2.2.1 PXRD Analysis

The crystallographic analysis of the samples was performed by powder X-ray diffraction (XRD). Figure 3.6 shows the XRD patterns of the magnetite samples synthesised in two separate batches. The diffraction peaks are very broad and the positions of the Bragg reflections match very well with the simulated pattern of magnetite. However, the broadness of the peaks is different for the two different samples, indicating that the synthesis does not yield reproducible results. Calculated crystallite sizes and lattice parameters are shown in table 3.4. This result was further supported by magnetic measurements.

Table 3.4. Sample codes and crystallite size of synthesized samples

Sample Code	Crystallite size ( $\pm 1$ nm)	Lattice parameter ( $\text{\AA}$ )
Fe2a	7	8.38
Fe2b	5	8.36

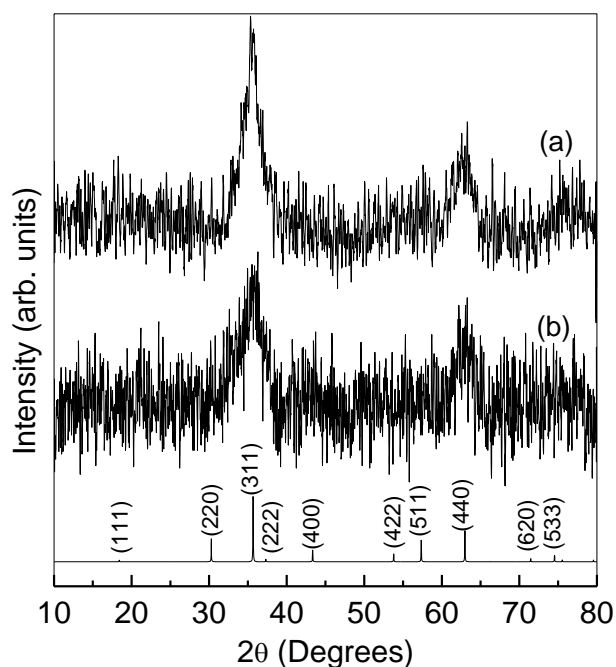


Figure 3.6 XRD pattern of a) Fe2a, b) Fe2b. The simulated pattern of Fe<sub>3</sub>O<sub>4</sub> is shown at the bottom and indexed.

### 3.2.2.2 TEM Analysis

TEM image of Fe2a shows agglomerated nature of the sample because of the high surface energy of these particles. The results indicate that the Fe2a sample are spherical in morphology and narrow particle size distribution. The particle size obtained from TEM is in good agreement with XRD results. The selected area electron diffraction pattern, shown in the inset of the Figure 3.7 for the sample Fe2a is diffused, indicating nanocrystalline nature of the particles. The ED pattern correspond to that of magnetite phase, agreeing with the results obtained from XRD.

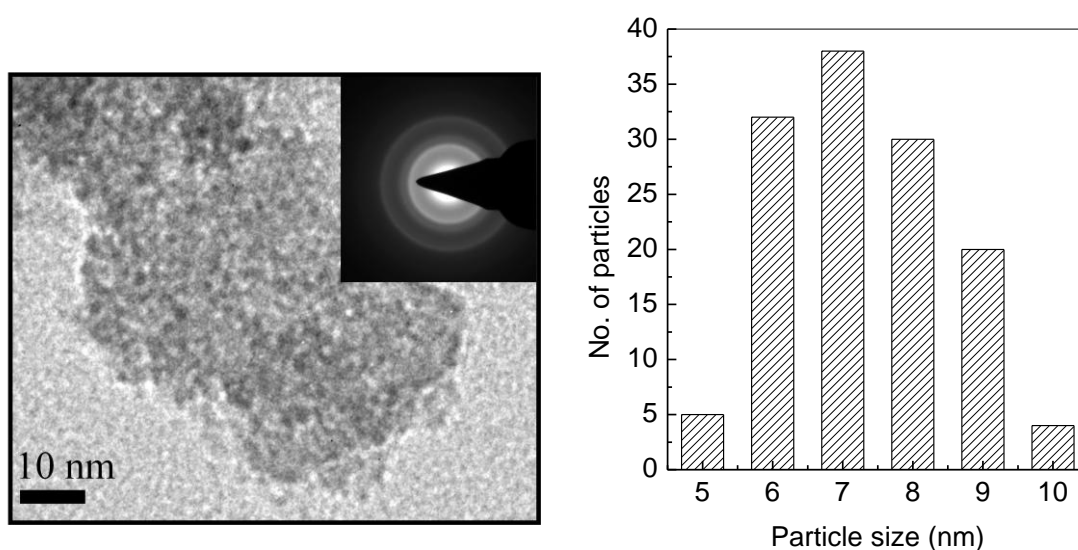


Figure 3.7 TEM micrograph of Fe2a sample (left) and TEM histogram of the particle size distribution.

### 3.2.2.3 Magnetic measurements

Figure 3.8 shows the  $M(H)$  measurement that were measured at room temperature in the range of approximately  $-15$  to  $+15$  kOe. The magnetization for sample synthesized demonstrates a typical superparamagnetic behavior with zero coercivity and zero remanence. Figure 3.9 shows low temperature FC and ZFC magnetisation curves of samples Fe2a and Fe2b, synthesised by the same method in two batches. The observed superparamagnetic blocking temperature,  $T_B$ , for the samples are 72 K and 92 K. The magnetizations of the samples is low when compared to the magnetization measured at the same field for the Fe1 series of samples (burette

addition), indicating that the particle size is smaller compared to the previous batch. The result also corroborates with that from the XRD and TEM analysis. The temperature below which the bifurcation of FC and ZFC magnetizations is observed,  $T_{irr}$ , is different for the two different samples and this difference is due to the difference in the particle size distribution present in the samples.

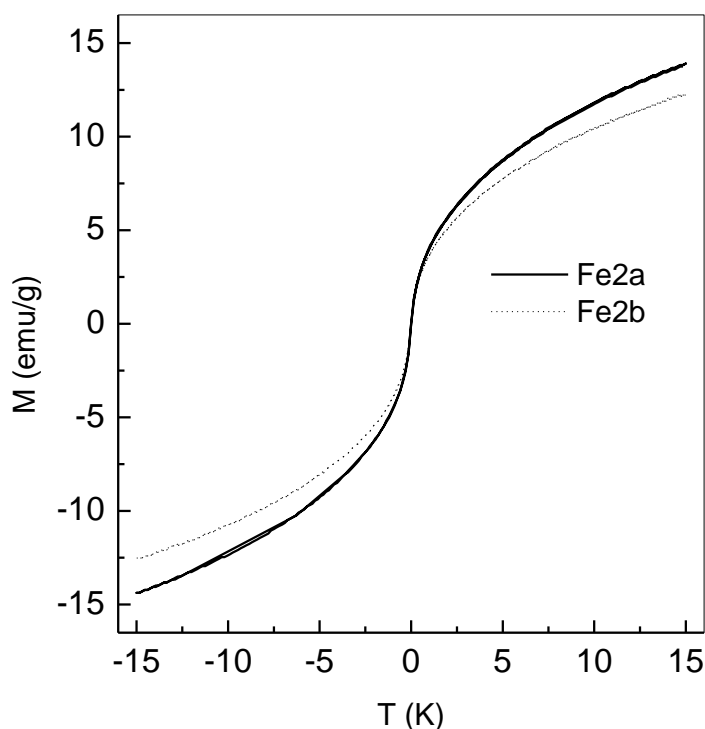


Figure 3.8 Field dependence of magnetisation of Fe2a and Fe2b samples

From the results, it may be concluded that the relatively faster addition of the Fe solution from a separating funnel gives rise to relatively smaller particles with wider particle size distribution with less reproducibility.

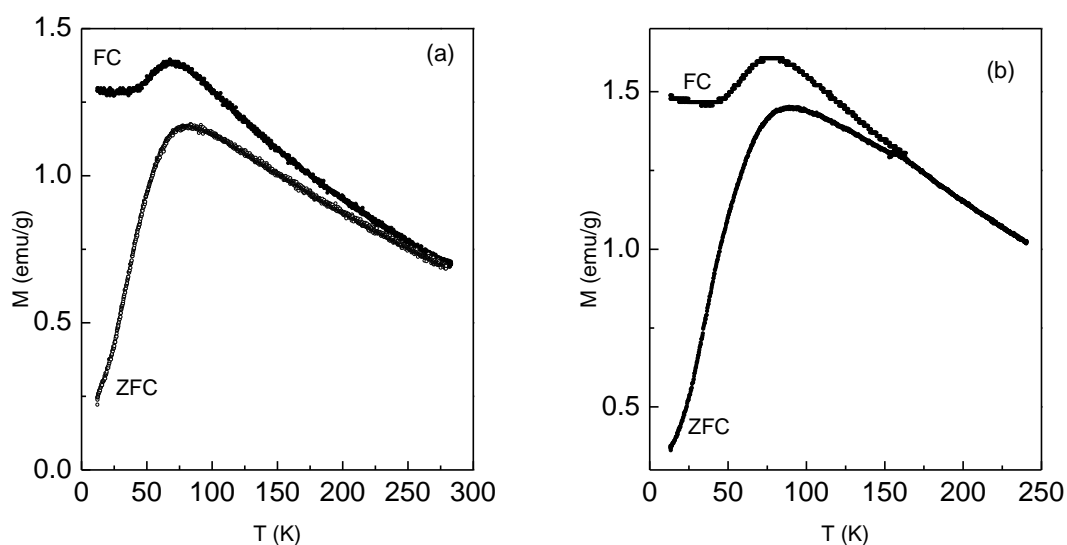


Figure 3.9 Temperature dependent magnetisation curves of a) Fe2a and b) Fe2b samples

### 3.2.3 Direct addition of Fe stock solution

Previously reported coprecipitation method used drop wise addition with the aim of achieving a slow, continuous nucleation and growth process [17]. It is hard to achieve this for  $\text{Fe}_3\text{O}_4$  because of the difficulty of controlling nucleation and growth. Initially, the iron precursors are hydrolyzed under alkaline conditions and then condensed into iron oxide nuclei. With increased nuclei concentration, Ostwald ripening process takes place and grows into large sized nuclei. The continuous drop wise addition of precursors yields different-sized iron oxide nanoparticles and hence gives rise to a broad size distribution. But in this scheme of synthesis, Fe solution was added by directly pouring the solution to the ammonia solution which results in the the formation of nearly monodispersed iron oxide nanoparticles, as there is not much time available for the growth of the particles. However, the method is unlikely to be reproducible due to the difficulty in controlling the time required to add the Fe solution in every batch of synthesis. To study the effect of reaction temperature on the particle size and distribution, the synthesis was repeated at a high temperature (80 °C), room temperature, and at a low temperature (10 °C). The sample was designated as Fe3a, Fe3c and Fe3d. For checking the reproducibility of the synthesis method, the synthesis was repeated at room temperature and the sample is designated as Fe3b. At

low temperatures the reaction rate and the diffusion of active species are expected to decrease, which narrows the particle size distribution. The reverse is expected at the high temperature. The effect of the reaction conditions was monitored by comparing the XRD and magnetic measurements.

Table 3.5. Sample codes crystallite size, particle size and lattice parameter of synthesized samples

Sample Code	Reaction temperature (°C)	Crystallite size ( $\pm 1$ nm)	Lattice parameter ( $\text{Å}$ )
Fe3a	80	12	8.36
Fe3b	35	5	8.35
Fe3c	35	5	8.38
Fe3d	10	3	8.35

### 3.2.3.1 PXRD Analysis

The powder XRD patterns of the different samples are compared with the simulated pattern  $\text{Fe}_3\text{O}_4$  in Figure 3.10. All the peaks in the diffraction patterns of the different samples correspond to the peaks in the simulated pattern, indicating the formation of  $\text{Fe}_3\text{O}_4$ . No impurity peaks are observed for any of the samples. The broadness of the XRD peaks can be expected due to the small size of the particles. The widths of the peaks decrease with increasing reaction temperature, indicating increase in the particle size. This is evident from the average crystallite size calculated using the Scherrer formula (Table 3.5). The crystallite size decreases with decreasing reaction temperature from 80 °C to 10 °C. The variation of the crystallite size with temperature is shown in Figure 3.11a.

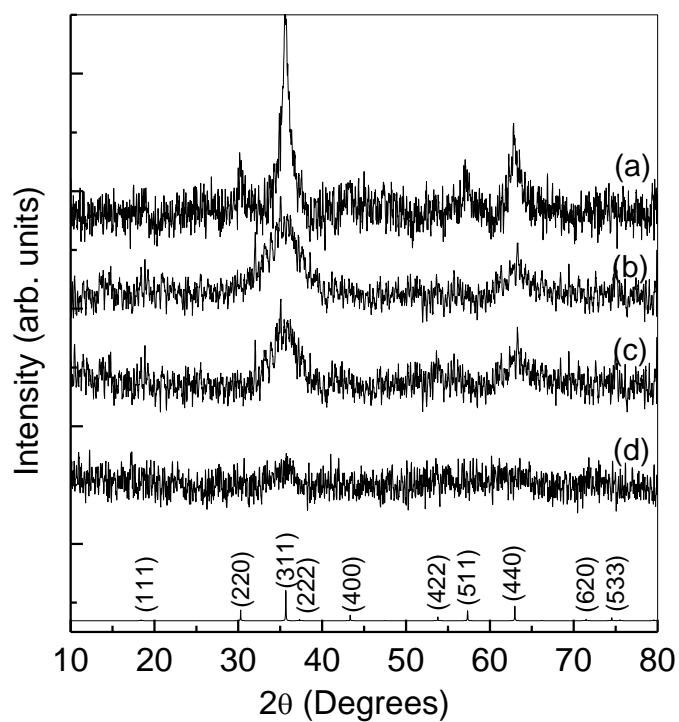


Figure 3.10 XRD pattern of a) Fe<sub>3</sub>a, b) Fe<sub>3</sub>b, c) Fe<sub>3</sub>c and d) Fe<sub>3</sub>d. The simulated pattern of Fe<sub>3</sub>O<sub>4</sub> is shown at the bottom and indexed.

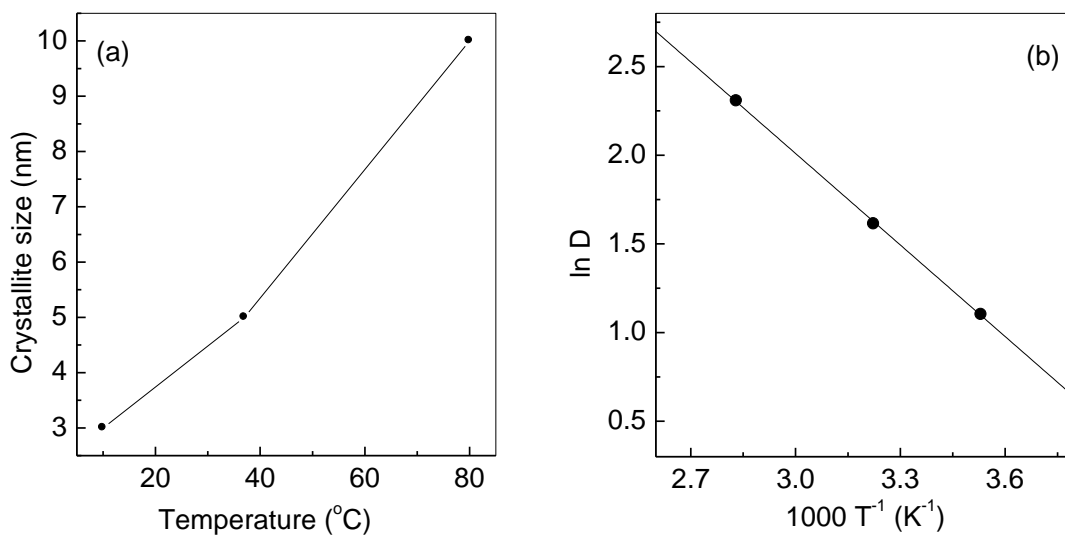


Figure 3.11. a) Change in the crystallite size with synthesis temperature b) Arrhenius plot of  $\ln(D)$  against  $1/T$  for the samples synthesised at different temperatures.

Activation energy for the growth of magnetite nanoparticles by the reverse coprecipitation method at different temperatures can be calculated using the Arrhenius equation [49, 50]

$$D = C \exp\left(\frac{-E}{RT}\right)$$

where, D is the crystallite size of magnetite nanoparticles, R the universal gas constant (1.98588 cal/mol), T is the reaction temperature in Kelvin, E is the activation energy and C is a constant which may depend on the initial value of crystal size. The change in the crystallite size, ln(D) is plotted against the reaction temperature 1/T for the samples prepared at temperatures in the range 10-80 °C and is presented in Figure 3.10. Activation energy is calculated from the slope of the graph and is obtained as 3.41 cal/mol. We believe that the high activation energy is due to non uniformity of morphology and wide particle size distribution. This activation energy is responsible for initiating the complex process of nucleation and Ostwald ripening process [51].

### 3.2.3.2 TEM Analysis

Figure 3.12 shows transmission electron microscopy images of iron oxide nanoparticles obtained directly by single-shot addition at room temperature (Fe3c) and at low temperature (Fe3d). The average particle size obtained is 4.5 nm for Fe3c and 3 nm for Fe3d which are comparable with the results obtained from XRD patterns. For both samples, the particle size distribution is slightly wide. The selected area electron diffraction patterns, shown in the insets of the Figure 3.12 for all the samples are diffused, indicating nanocrystalline nature of the particles.

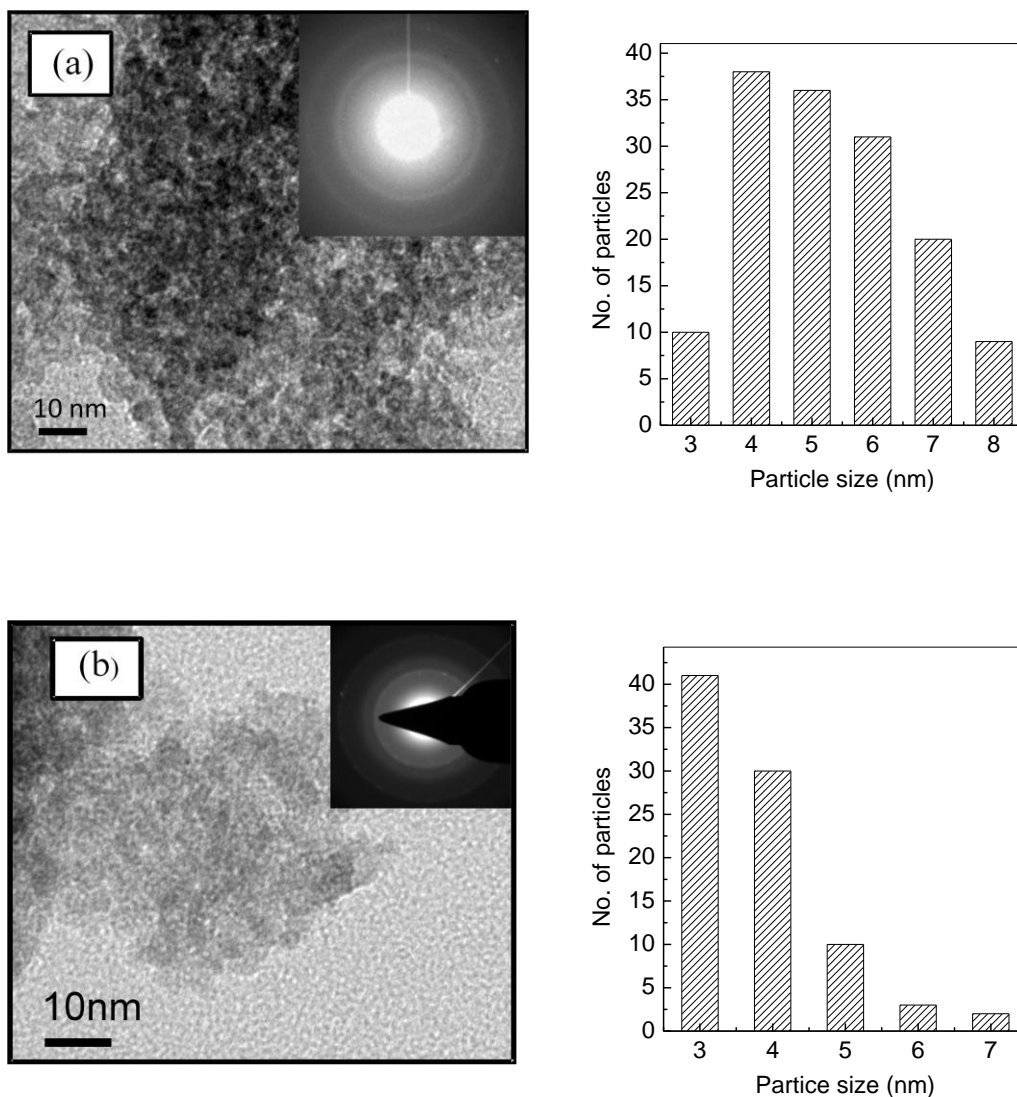


Figure 3.12 TEM micrographs of a)Fe<sub>3</sub>c and b) Fe<sub>3</sub>d (left) and TEM histogram of the particle size distribution.

### 3.2.3.3 Magnetic measurements

Magnetic properties of the samples were measured at room temperature with a VSM. The plot is shown in the Figure 3.13. All the samples show superparamagnetic behavior. The saturation magnetization of synthesized samples seems to increase linearly with the increasing reaction temperature. This behavior may be attributed to the surface effects that are aroused by the distortion of the magnetic moments at the surface of the nanoparticles.

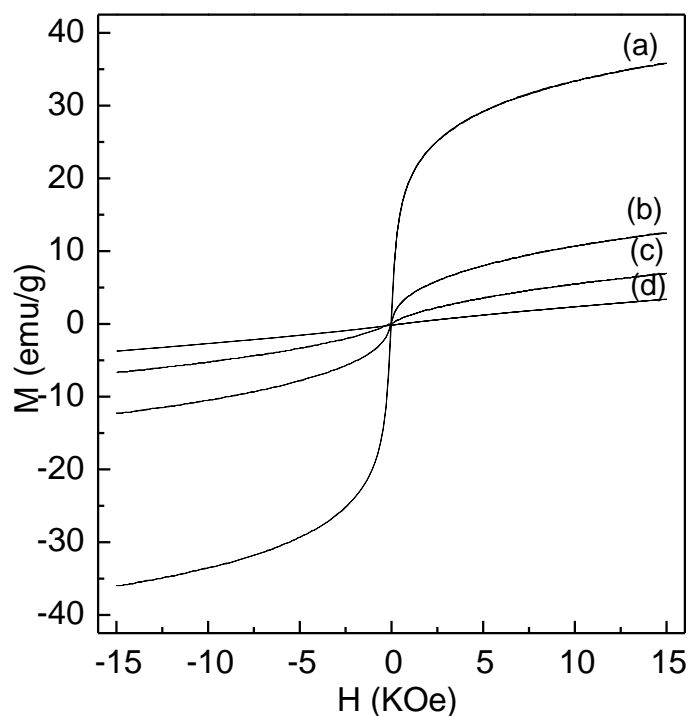


Figure 3.13 Field dependent magnetisation curves of a) Fe3a, b) Fe3b, c) Fe3c and d) Fe3d.

Figure 3.14 presents the temperature dependence of the magnetization measured with zero-field cooling (ZFC) and field cooling (FC) procedures in an applied magnetic field of 50 Oe from 12 to 300 K. The temperature at which the maximum is observed in the ZFC magnetization curve is defined as the blocking temperature ( $T_B$ ). The correlation between  $T_B$  and the volume of the nanoparticles was explained in chapter 1 of the thesis. For 4.5 nm and 3 nm  $\text{Fe}_3\text{O}_4$  nanoparticles, ZFC and FC curves clearly show divergence below the blocking temperature of 72 K and 61 K, respectively. This indicates narrow particle size distribution, because if larger particles are present, the divergence happens above the blocking temperature. Above the blocking temperature, the magnetization decreases sharply and presents superparamagnetic behavior. This sharp change not only reflects the size-dependent magnetic property, but also indicates the particle size distribution. Kim and co-workers [17] reported the synthesis of 2-4 nm magnetite nanoparticles by co-precipitation route. In this particular research paper, the blocking temperature

obtained for 3 nm is 60 K which is exactly matching with the result obtained in our synthesis

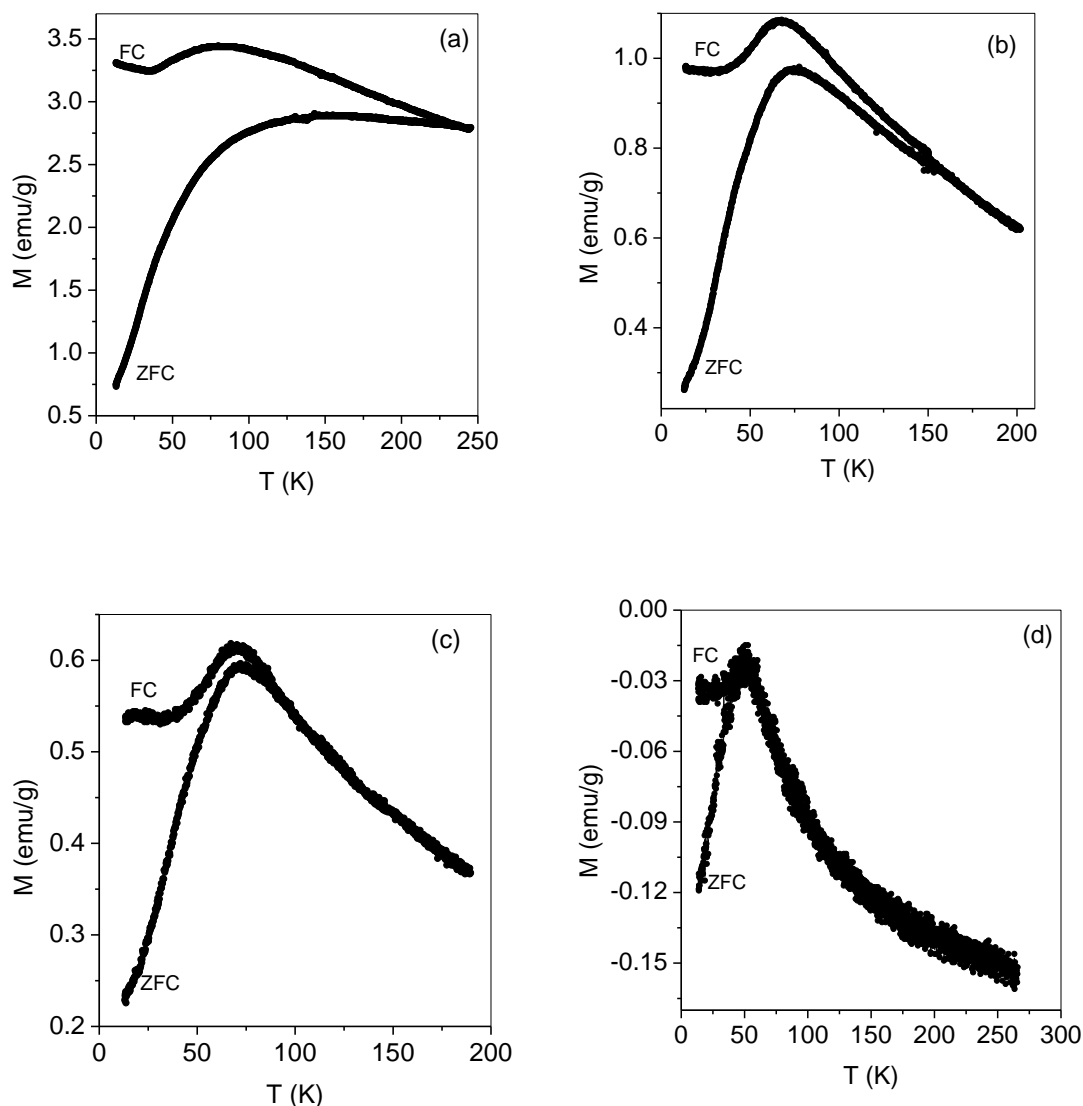


Figure 3.14 Temperature dependent magnetisation curve of a) Fe3a, b) Fe3b, c) Fe3c and d) Fe3d.

For samples Fe3a and Fe3b, the ZFC magnetization curves are very broad and the deviation between the ZFC and FC magnetization curves occur at a higher temperature than the corresponding blocking temperatures (180 K and 92 K). From these data, it can be inferred that Fe3a has a much wider particle size distribution than the Fe3b sample. Fe<sub>3</sub>O<sub>4</sub> nanoparticles (Fe3b) with a mean size of 5 nm display a

higher blocking temperature of 92 K and a less pronounced decrease of the magnetization with increasing temperature owing to the larger particle size and the broader size distribution. The blocking temperature (92 K) of the sample with the broader size distribution is much higher than that of the 4.5 nm particles of  $\text{Fe}_3\text{O}_4$ . This result indicates that the particle size distribution has an important effect on the measured blocking temperature, which is sensitive to the presence of even a small percentage of larger particles.

### **3.3. Comparison of magnetic properties of magnetite nanoparticles with different particle size**

#### **3.3.1 Field and temperature dependence**

The field dependence of magnetization recorded at room temperature for some of the samples synthesized by the three different mode of addition and the temperature dependence of magnetization for the same samples recorded in an applied magnetic field of 50 Oe are compared in Figure 3.15 and Figure 3.16. None of the samples are saturated up to 15 kOe. This behavior, typical of magnetite particles with diameters smaller than 15 nm, has been consistently reported in the literature [52,53] and arises from the difficulty for aligning the magnetic moments of the surface atoms [54,55] That is, the magnetically dead layer on the surface of the particles, which constitute the surface order/disorder interaction [56] of the magnetic spin moment and the disturbance in the spinel structure [57, 58]. This surface spin disorder arises from the broken bonds and reduced coordination on the particle surface.

There is no coercivity for the synthesised magnetite nanoparticles as compared to the bulk value of 115–150 Oe. This is due to the superparamagnetic behavior of nanosized magnetite particles. This behavior was expected because of the very small sizes of the particles. Superparamagnetism implies that the magnetic nanoparticles have essentially single domains, i.e., all magnetic moments in the particle are aligned in one direction [59], and as is well known, magnetic nanoparticles below 10 nm show single domain structure [60].

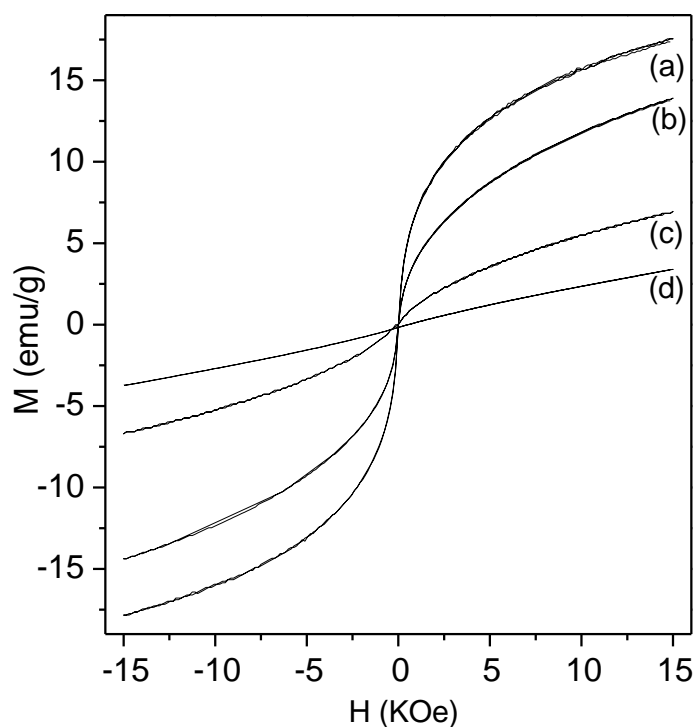


Figure 3.15 (a) Room temperature magnetisation of (a) Fe1c, (b) Fe2a, (c) Fe3c (d) Fe3d.

The blocking temperature,  $T_B$ , is observed as the maximum in the ZFC curve in the case of Fe1c and Fe2a samples but in the case of Fe3c and Fe3d samples the blocking temperature is observed at the point of divergence between ZFC and FC curves. This is because of particle size distribution present in the samples and is agglomerated in nature which was explained by TEM results. It should be noted that FC curves remains almost constant below the blocking temperature for all of the samples, suggesting the presence of strong inter-particle interactions. The decrease in blocking temperature with decreasing particle size is observed, as compared in Table 3.6, and is supported by the fact that the blocking temperature is directly proportional to the anisotropy energy barrier ( $E=KV$ ).

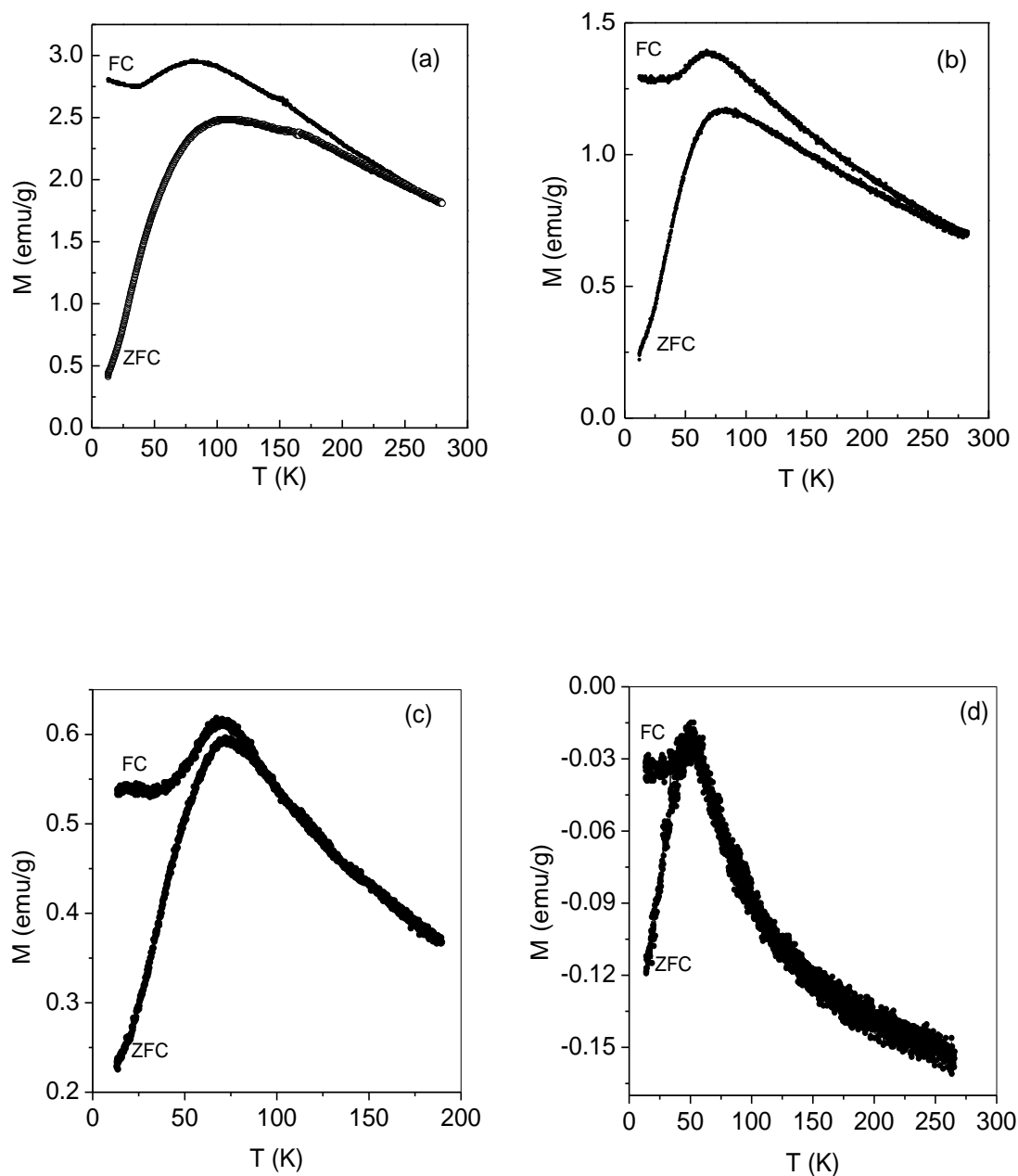


Figure 3.16 (a) Temperature dependent magnetisation of (a) Fe1c, (b) Fe2a, (c) Fe3c (d) Fe3d.

Table 3.6 Magnetic data of samples with different particle sizes

Sample Code	Particle size (nm)	$T_B$ (K)	$K$ (erg/cm <sup>3</sup> )	$M_s$ (emu/g)
Fe1c	10	109	$7.1 * 10^5$	21
Fe2a	7	77	$1.4 * 10^6$	18
Fe3c	5	73	$3.8 * 10^6$	10
Fe3d	3	61	$1.5 * 10^7$	6

Considering that all the particles are spherical, anisotropy constant can be calculated by using the equation  $KV \approx 25k_B T_B$ . For spherical nanoparticles, the dominant anisotropy is the magnetocrystalline anisotropy [61] and there is no contribution from shape anisotropy. The anisotropy constant,  $K$ , of the superparamagnetic particles for various samples are calculated and listed in Table 3.3. The variation of blocking temperature and crystalline anisotropy is displayed in Figure 3.17.  $K$  is decreased as the particle size increased and  $K$  for all samples is larger than that of bulk  $Fe_3O_4$  ( $1.35 \times 10^5$  ergs/cm<sup>3</sup>). For smaller particles, because of the increased magnetocrystalline anisotropy [62], larger magnetic fields will be required to attain saturation. The larger anisotropy in the small particles is due to the surface anisotropy which becomes relatively more important in the smaller particles.

The particle sizes are larger for the samples synthesized by burette addition when compared to the material obtained by direct addition at low temperature. The reason of this reduction in particle size is suggested to be due to the reduced growth kinetics of the particles. The particle size obtained for direct addition at low temperature is small as compared to the other schemes of synthesis. The addition rate can be varied to maintain required productivity of the system without affecting properties of the product. Among these synthesis procedures the sample synthesised by the addition of Fe solution to ammonia by using burette is found to be reproducible for several batches of synthesis.

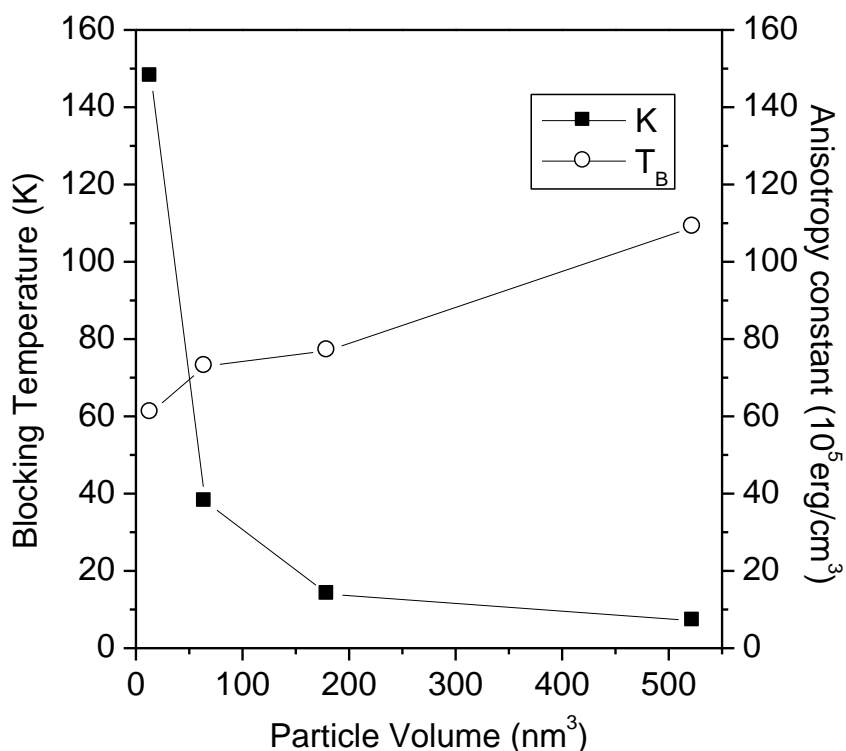


Fig 3.17. Variation of blocking temperature and crystalline anisotropy with particle volume of magnetite nanoparticles.

### 3.4 Conclusions

Iron oxide nanoparticles are successfully synthesised by the reverse co-precipitation method, by varying the mode of addition of the mixed Fe solution to the base. The products in each case are characterised by structural, microstructural and magnetic measurements. It is found that the crystallite and average particle size of the Fe<sub>3</sub>O<sub>4</sub> nanoparticles depend on the mode of addition of Fe stock solution to ammonia solution. Slower addition leads to larger particles with narrow size distribution and the characteristics can be reproduced. On the other hand, faster addition leads to smaller particle size but with wider distribution of the size of the particles and it is found that the method is not reproducible. The difference in the magnetic properties for particles of comparable sizes, reported in the literature, can be explained based on the difference in the synthesis parameters. The iron oxide nanoparticles of size less than

---

10 nm do not show magnetic hysteresis at room temperature, which is usually considered as superparamagnetic characteristics. However, further detailed magnetic studies shows that there is strong interaction between the particles, leading to superspin glass nature of the single domain nanoparticles.

---

**References**

- 1 Neuberger, T.; Schopf, B.; Hofmann, H.; Hofmann, M.; von Rechenberg, B., *J. Magn. Magn. Mater.* **2005**, 293, 483.
- 2 Pankhurst, Q.A.; Connolly, J.; Jones, S.K.; Dobson, J., *J. Phys. D: Appl. Phys.* **2003**, 36, R167
- 3 Hultman, K.L.; Raffo, A.J.; Grzenda, A.L.; Harris, P.E.; Brown, T.R.; O'Brien, S., *ACS Nano*, **2008**, 2, 477
- 4 Senpan, A.; Caruthers, S.D.; Rhee, I.; Mauro, N. A.; Pan, D.; Hu, G.; Scott, M. J.; Fuhrhop, R. W.; Gaffney, P. J.; Wickline S. A.; Lanza G.M., *ACS Nano*, **2009**, 3, 3917
- 5 Frey, N. A.; Peng, S.; Cheng, K.; Sun, S.; *Chem. Soc. Rev.* **2009**, 38, 2532
- 6 Gonzales-Weimuller, M.; Zeisberger, M.; Krishnan, K. M., *J. Magn. Magn. Mater.* **2009**, 321, 1947
- 7 Tzitzios, V.; Basina, G.; Bakandritsos, A.; Hadjipanayis, C.G.; Mao, H.; Niarchos, D.; Hadjipanayis, G.C.; Tucek, J.; Zboril J., *J Mater Chem.* **2010**, 20, 5418
- 8 Hermanek, M.; Zboril, R.; Medrik, I.; Pechousek, J.; Gregor, C., *J. Am. Chem. Soc.*, **2007**, 129, 10929
- 9 Park, J.; Lee, Y.; Khanna, P.K.; Jun, K.; Bae, J.W.; Kim, Y.H., *J. Mol. Catal. A: Chemical*, **2010**, 323, 84
- 10 Tronc, E.; Ezzir, A.; Cherkaoui, R.; ChaneH, C.; Nogue, M.; Kachkachi, H.; Fiorani, D.; Testa, A.M.; Greneche, J. M.; Jolivet, J.P.; *J. Magn. Magn. Mater.* **2000**, 221, 63.
- 11 Chatterjee, J.; Haik, Y.; Chen, C.-J.; *J. Magn. Magn. Mater.* **2003**, 257, 113.
- 12 Rouanet, A.; Solmon, H.; Pichelin, G.; Roucau, C.; Sibieude, F.; Monty, C.; *Nanostruct. Mater.* **1995**, 6, 283.
- 13 Nakanishi, T.; Iida, H.; Osaka, T.; *Chem. Lett.* **2003**, 32, 1166.
- 14 Narasimhan, B.R.V.; Prabhakar, S.; Manohar, P.; Gnanam, F.D., *Mater. Lett.* **2002**, 52, 295.
- 15 Hyeon, T.; Lee, S.S.; Park, J.; Chung, Y.; Na, H.B., *J. Am. Chem. Soc.* **2001**, 123, 12798.

- 
- 16 Shafi, K.V.P.M.; Ulman, A.; Yan, X.; Yang, N.-L.; Estournes, C.; White, H.; Rafailovich, M.; *Langmuir*, **2001**, 17, 5093.
  - 17 Chen, D.; Xu, R.; *J. Solid State Chem.* **1998**, 137, 185.
  - 18 Bharde, A.; Wani, A.; Shouche, Y.; Joy, P. A.; Prasad, B.L.V.; Sastry, M.; *J. Am. Chem. Soc.* **2005**, 127, 9326.
  - 19 Bharde, A.; Rautaray, D.; Bansal, V.; Ahmad, A.; Sarkar, I.; Yusuf, S.M.; Sanyal, M.; Sastry, M.; *Small*, **2006**, 2, 135.
  - 20 Tan, Y.; Zhuang, Z.; Peng, Q.; Li, Y.; *Chem. Mater.*, **2008**, 20, 5029–5034.
  - 21 Hyeon, H.; Lee, S. S.; Park, J.; Chung, Y.; Na, H. B.; *J. Am. Chem. Soc.*, **2001**, 123, 12798
  - 22 Ai, Z.; Deng, K.; Wan, Q.; Zhang, L.; Lee, S.; *J. Phys. Chem. C*, **2010**, 114 , 6237
  - 23 Psaro, P.; Fusi, Ugo, R.; Basset, J. M.; Smith, S.K.; Hugues, F.; *J. Mol. Catal.*, **1980**, 7, 511
  - 24 Jeong, U.; Teng, X. W.; Wang, Y.; Yang, H.; Xia, Y. N.; *Adv.Mater.*, **2007**, 19, 33
  - 25 Sun, S.; Zeng, H.; *J. Am. Chem. Soc.*, **2002**, 124, 8204
  - 26 Yu, S.;Chow, G.M.; *J. Mater. Chem.* 2004, 14, 2781.
  - 27 Kang, Y,S.; Risbud, S.; Rabolt, J. F.; Stroeve, P.; *Chem. Mater.*, **1996**, 8, 2209
  - 28 Massart.; *IEEE Trans Magn* **1981**, 17, 1247
  - 29 Jolivet, J. P.; Belleville, P.; Tronc, E.; *Clays and Clay Minerals* **1992**, 40, 531
  - 30 Vayssières, L.; Chanéac, C.; Tronc, E.; *J Colloid and Interface Sci.* **1998**, 205, 205
  - 31 Chatterjee, J.; Haik, Y.; Chen, C.; *J. Magn. Magn. Mater.* **2003**, 257, 113
  - 32 Zhao, F.; Sun, H.; Su, G.; Gao, S.; *small* **2006**, 2, 244
  - 33 Woo, K.; Hong, J.; Choi, S.; Lee, H.; Ahn, J.; Kim, C.S.; Lee, S. W.; *Chem. Mater.*, **2004**, 16, 2814
  - 34 Wu, J. H.; Ko, S. P.; Liu, H.; Kim, S.; Ju, J.; Kim, Y. K.; *Mater. Lett.* **2007**, 61, 3124-3129
  - 35 Roca, A. G.; Marco, J. F.; Morales, M.P.; Serna, C. J.; *J. Phys. Chem. C*, **2007**, 111, 18577
  - 36 Goya, G. F.; Berquó, T. S.; Fonseca, F. C.; Morales, M. P.; *J. Appl. Phys.* **2003**, 94, 3520

- 
- 37 Iida, H.; Takayanagi, K.; Nakanishi, T.; Osaka, T.; *J Colloid and Interface Sci.* **2007**, 314, 274
- 38 Parvin, K.; Ma, J.; LyX. J.; Sun, C.; Nikles, K, D. E.; Sun.; Wang. L. M.; *J. Appl. Phys.* **2004**, 95, 8979
- 39 Yang, T.; Shen, C.; Li, Z.; Zhang, H.; Xiao, C.; Chen, S.; Xu, Z.; Shi, D.; Li, J.; Gao, H., *J. Phys. Chem. B*, 2005, 109, 23233
- 40 López Pérez, J. A.; López Quintela M. A.; Mira, J.; Rivas, J.; Charles, S. W.; *J. Phys. Chem. B*, **1997**, 101, 8045
- 41 Si, S.; Li, C.; Wang, X.; Yu, D.; Peng, Q.; Li, Y., *Crystal Growth & Design*, **2005**, 5, 391
- 42 Morales, M.P.; Veintemillas-Verdaguer, S.; Montero, M. I.; Serna, C. J.; *Chem. Mater.*, **1999**, 11, 3058
- 43 Iwasakia, T.; Mizutania, N.; Watanoa, S.; Yanagidab, T.; Kawaiib, T.; *J. Expt. Nano.* **2010**, 5, 251
- 44 Salazar-Alvarez, G.; Muhammed, M.; Zagorodni. A. A.; *Chem. Eng. Sci.* **2006**, 61, 4625
- 45 LaMer, V.; Dinegar, R.; *J. Am. Chem. Soc.*, **1950**, 72, 4847
- 46 B.D. Cullity, S.R. Stock, *Elements of X-Ray Diffraction (3rd ed.)*, Prentice-Hall, New Jersey, **2001**, 170.
- 47 Wan, J.; Tang, G.; Qian, Y.; *Appl. Phys. A*, **2007**, 86, 261
- 48 Vargas, J. M.; Nunes, W. C.; Socolovsky, L. M.; Knobel, M.; Zanchet, D.; *Phy. Rev. B.*, **2005**, 72, 184428
- 49 Tang, J.; Myers, M.; Bosnick, K. A.; Brus, L. E.; *J. Phys. Chem. B*, **2003**, 107, 7501
- 50 Kotera, Y.; Saito, .; Terada, M.; *Bull Chem Soc Jpn.*, **1963**, 36, 195
- 51 Park, K. Y.; Jeong, H. J.; *Korean J. Chem. Eng.*, **1999**, 16, 64
- 52 Tartaj, P.; Morales, M. P.; Veintemillas-Verdaguer, S.; Gonz´alez-Carre ño, T.; Serna, C. J.; *J. Phys. D: Appl. Phys.* **2003**, 36, R182
- 53 Liz, L.; Lopez-Quintela, M. A.; Mira, J.; Rivas, J.; *J Mater Sci.*, **1994**, 29, 3797
- 54 Santra, S.; Tapeç, R.; Theodoropoulou, N.; Dobson, J.; Hebard, A.; Tan, W.; *Langmuir*, **2001**, 17, 1900

- 
- 55 Liu, Z.L.; Wang, X.; Yao, K.L.; Du, G. H.; Lu, Q.H.; Ding, Z.H.; Tao. J.; Ning, Q.; Luo, X.P.; Tian, D. Y.; Xi, D.; *J Mater Sci.* **2004**, 39, 2633
- 56 Lee, Y.; Lee, J.; Bae, C. J.; Park, J. G.; Noh, H. J.; Park, J. H.; Hyeon, T.; *Adv Funct Mater*, **2005**, 15, 503
- 57 Lopez-Perez, J.A.; Lopez-Quintela, M. A.; Mira, J.; Rivas, J.; *IEEE Trans Magn.*, **1997**, 33, 4359.
- 58 Cornell R. M, Schwertmann, U (1996) *The iron oxides. structure, properties, reactions, occurrence and uses*. VCH, Weinheim, Germany.
- 59 B.D. Cullity, *Introduction to Magnetic Materials*, Addison-Wesley, Reading, MA , **1972**, 410418.
- 60 Kodama, R.H.; *J Magn Magn Mater*, **1999**, 200, 359
- 61 Goldman, A.; *Modern Ferrite Technology*, Van Nostrand Reinhold, New York, **1990**
- 62 Dorman, J. L.; Fiorani, D.; *Magnetic Properties of Fine Particles* (North-Holland, Amsterdam, **1992**

## CHAPTER 4

### SURFACE MODIFICATION OF MAGNETITE NANOPARTICLES AND THEIR CHARACTERIZATION

#### 4.1 Introduction

In recent years, studies on nanomagnetism emerged as a major area of research due to the potential applications of the nanosized magnetic materials. Magnetic nanoparticles are suitable for biomedical applications such as drug targeting, contrast enhancement in MRI, magnetic hyperthermia, and separation of biomolecules [1,2]. Among various magnetic materials, nanoparticles of magnetic iron oxides such as  $\gamma$ -Fe<sub>2</sub>O<sub>3</sub> and Fe<sub>3</sub>O<sub>4</sub> are the most studied for biomedical applications [3]. Superparamagnetic iron oxide nanoparticles, known as SPIONs, can be synthesized relatively easily without much precaution. The iron oxides can be easily coated with biocompatible molecules and can be further functionalized with drug or other molecules for appropriate applications. Therefore, much importance is given to the synthesis and studies of surface functionalized magnetic iron oxide nanoparticles. Applications in biology, medical diagnosis and therapy require the magnetic particles to be stable in water at neutral pH and physiological salinity. Recently, great efforts have been made in the direction of developing aqueous ferrofluids for their biomedical applications. For *in-vivo* applications, the magnetic particles must be coated with a biological polymer so as to prevent the formation of large aggregates. The polymer will also allow bonding of drugs by covalent attachment, adsorption or entrapment on the particles.

Understanding the properties of magnetic nanoparticles is a subject of intensive research from the viewpoint of probing their magnetic behaviour related to size and surface effects as well as applications [4]. Apart from the magnetocrystalline and magnetostatic anisotropies present in the bulk materials which are also operative in nanoparticles, other kinds of anisotropy contributions also come into picture in magnetic nanoparticles [5]. These are the surface anisotropy due to the changes in the coordination, broken bonds and magnetic exchanges at the surface of a particle. Since the surface area to volume ratio of a fine particle is larger than that of the bulk, the surface anisotropy contributions to the total anisotropy is considerable.

Again, due to the smaller size of the particles, there will be considerable strain on the surface and this also contributes in the form of strain anisotropy. Finally, if the magnetic nanoparticles are closer together, there will be magnetic dipolar interactions between the particles and different types of magnetic exchange interactions at the interface between the particles. These two interactions also contribute to magnetic anisotropy. Hence, for magnetic nanoparticles, the additional magnetic anisotropy contributions determine the overall magnetic properties. Understanding the magnetic characteristics of the nanoparticles, especially after coating with suitable biocompatible molecules, is very important for various applications.

This chapter describes the studies on surface modification of superparamagnetic iron oxide nanoparticles, prepared by co-precipitation method, by the biocompatible molecules dextran and ascorbic acid. The burette addition method, as described in the previous chapter is found to be effective in synthesizing magnetite nanoparticles with sufficient narrow distribution, with high reproducibility. Hence, this method is used to prepare the uncoated and coated magnetite nanoparticle. The materials are characterized by x-ray diffraction, thermal analysis, TEM, infrared spectroscopy, and magnetic measurements. There are not much studies reported in the literature on the comparison of the magnetic properties of uncoated and coated magnetite nanoparticles and the extent of inter-particle magnetic interactions. In this chapter, we report a direct comparison of the magnetic interaction behaviour of uncoated and surfactant coated magnetite nanoparticles.

## **4.2 Synthesis and Magnetic Properties of Dextran Coated Magnetite Nanoparticles**

We have explored the synthesis of dextran functionalised magnetite nanoparticles, over a range of particle sizes, based on different reaction schemes that rely on the coprecipitation of iron oxide nanoparticles in the absence/presence of dextran as surfactants. The surfactants affect the chemistry of the synthesis and control nanocrystal nucleation and growth in their capacity as ligands that reduce the surface energy of the crystal. This type of approach is well established in nanoscale syntheses. By optimizing the reaction conditions, one can get very stable water dispersible ferrofluids.

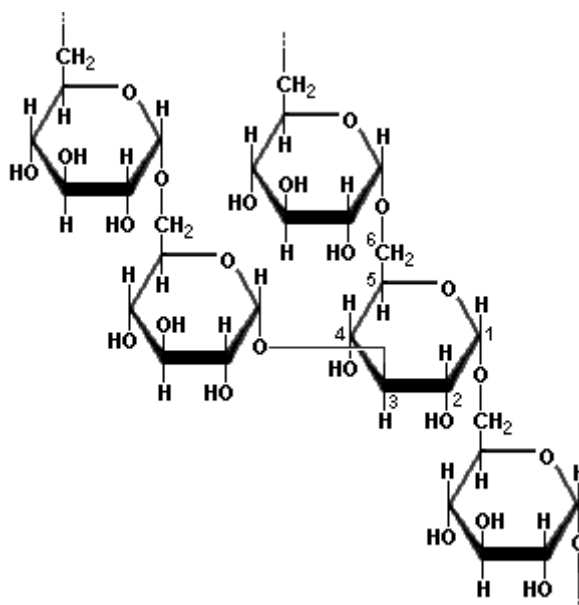


Figure 4.1. Structure of dextran molecule

Dextran and their derivatives are excellent candidates for coating on iron oxide nanoparticles [6] and for biomedical applications. Dextran is a long chain hydrophilic polymer of polysaccharides composed of glucose having alpha 1,6, glycosidic linkages. More than twenty years ago, Molday and Mackenzie [7] prepared iron oxide nanoparticles modified with dextran. Similar preparations were then repeated and studied by various researchers [8]. In aqueous solutions, dextran interacts with metals and covers their surface, yielding aggregates with hydrodynamic diameters between 20 and 150 nm as reported by Shen et. Al [9]. M. Carmen Bautista [8] and his group recently synthesised dextran coated iron oxide nanoparticles by laser pyrolysis method and has been shown to form aggregates of functionalised nanoparticles of hydrodynamic diameter 50 nm. The high biological activity of these modified particles has been demonstrated and justified their extensive use as contrast agents for magnetic-resonance imaging (MRI) [10,11]. But none of reports are so far explained about the systematic study of dextran functionalised nanoparticles and their influence of cooking parameters with respect to particle size. Moreover, there are no studies reported in the literature on the comparison of the magnetic properties of uncoated and dextran coated magnetite nanoparticles and the extent of inter-particle magnetic interactions. Here, we describe a detailed account of the systematic study of

surface modification and magnetic properties of dextran coated magnetite nanoparticles.

### 4.2.1 Synthesis

The chemicals  $\text{FeCl}_2 \cdot 4\text{H}_2\text{O}$ ,  $\text{FeCl}_3 \cdot 6\text{H}_2\text{O}$  (Fluka USA) and dextran (Fluka, USA) were used as-received. Aqueous dispersions of uncoated and dextran coated magnetic nanoparticles were obtained by the reverse coprecipitation route. Three different synthesis procedures are employed for functionalizing the magnetite nanoparticles with dextran. The primary synthetic goal is to synthesize coated magnetic nanoparticles with diameters of 3-5 nm. To avoid agglomeration and to improve chemical stability, the magnetic nanoparticles are usually coated with a suitable surfactant containing polymeric or functional groups. After coating, the magnetic nanoparticles acquire stability and improve their dispersion characteristics. Coating will also improve the biocompatibility of the particles and are used for biomedical applications such as targeted drug delivery, contrast agent for MRI, etc.

#### 4.2.1.1 Method 1

The reaction was carried out by taking 0.1 moles of  $\text{FeCl}_2$  and 0.2 moles of  $\text{FeCl}_3$ . 20 ml of the mixture of  $\text{Fe}^{2+}$  and  $\text{Fe}^{3+}$  was precipitated by using 100 ml of 10N  $\text{NH}_4\text{OH}$ .  $\text{Fe}_3\text{O}_4$  nanoparticles were obtained by adding the mixed Fe solution from a burette as described in the previous chapter. This dried precipitate is labeled as Fe1. This sample was then used for further functionalisation using dextran. The ratio of magnetite and dextran used for the synthesis is 3:5. 0.3 g of magnetite was dispersed in 100 ml of distilled water was mixed with 0.5 g of dextran dissolved in 100 ml of distilled water. dil.  $\text{HNO}_3$  (5N) was added drop-wise to the suspension to attain pH = 3.5. The mixture was then stirred for 1 hr at 80 °C. The colloidal solution was cooled to room temperature and dialysed for 4 days against distilled water and was dried at 60 °C in an oven. The sample is designated as Fedx1

#### 4.2.1.2 Method 2

$\text{Fe}_3\text{O}_4$  was precipitated from 20 ml of the solution containing stoichiometric amounts of  $\text{Fe}^{2+}$  and  $\text{Fe}^{3+}$  by using 100 ml of 10 N ammonia solution under argon

atmosphere. The suspension was continuously stirred for 15 minutes after precipitation and then 0.5 g dextran was added to the suspension and dil. HNO<sub>3</sub> (5N) was added drop-wise to the suspension to attain pH = 3.5. The resultant suspension was kept at 80 °C for 30 min under magnetic stirring. The suspension was finally dialyzed for 4 days against distilled water and was dried at 60 °C in an oven. The sample is designated as Fedx2

#### 4.2.1.3 Method 3

Fe<sub>3</sub>O<sub>4</sub> was precipitated from 20 ml of the Fe stock solution by using 100 ml of 10 N ammonia solution containing 0.5 g of dextran under argon atmosphere. After precipitation, dil. HNO<sub>3</sub> (5N) was added drop-wise to the suspension to attain pH = 3.5. The resultant suspension was kept at 80 °C for 30 min under magnetic stirring. The suspension was finally dialyzed for 4 days against distilled water and was dried at 60 °C in an oven and the sample is designated as Fedx3

### 4.2.2 Powder XRD Analysis

The synthesised dextran coated magnetite nanoparticles are characterized by powder XRD studies and the results are shown in Figure 4.2. A comparison of the XRD patterns of the different samples with the simulated XRD pattern of Fe<sub>3</sub>O<sub>4</sub> indicates that the peaks observed in the experimental patterns corroborate well with the simulated pattern and no extra peaks corresponding to any impurities are observed. All the reflections in the experimental patterns are very broad indicating nanocrystalline nature of the samples. There is an overall decrease in the intensities of the corresponding peaks of the dextran coated sample, indicating effective coating of the particles with dextran. The Scherrer equation [12] was used to calculate the crystallite size from the major peaks in the corresponding powder diffraction patterns and the calculated crystallite sizes are shown in Table 4.1. The broadening of the peaks and decreased intensity of the XRD pattern of Fedx1 are predominantly due to the decrease in the crystallite size on coating with surfactants. It is known that when the particle size decreases, the peaks are broadened and the intensities decrease. The extremely broad XRD peaks are due to the very fine nature of the nanoparticles.

Table 4.1 Particle size obtained from TEM, XRD and DLS

Sample Code	Crystallite size ( $\pm 1$ nm)	TEM Particle size ( $\pm 0.2$ nm)	Hydrodynamic size (nm)	Lattice parameter ( $\text{\AA}$ )
Fe1	10	9		8.38
Fedx1	6	6	68	8.36
Fedx2	6	6	28	8.37
Fedx3	4	5	10	8.36

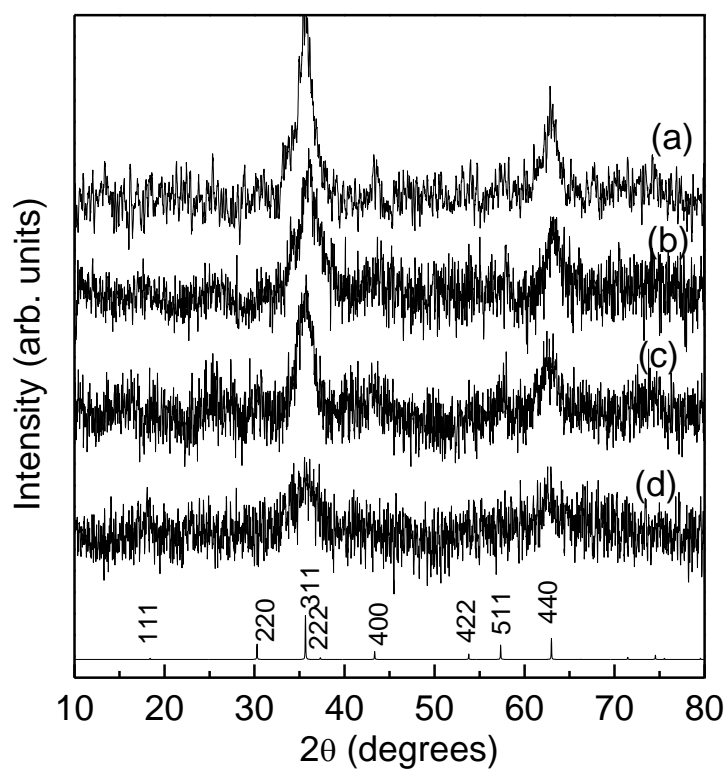
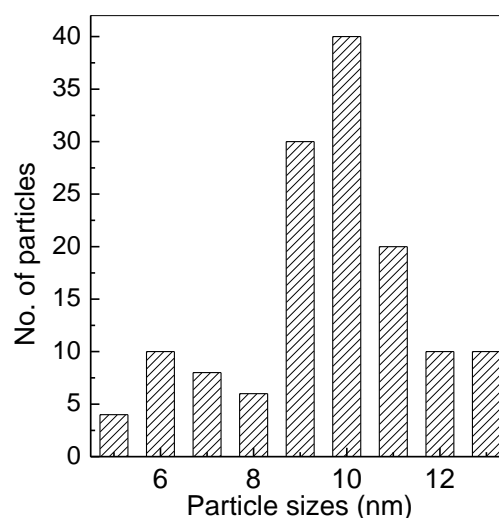
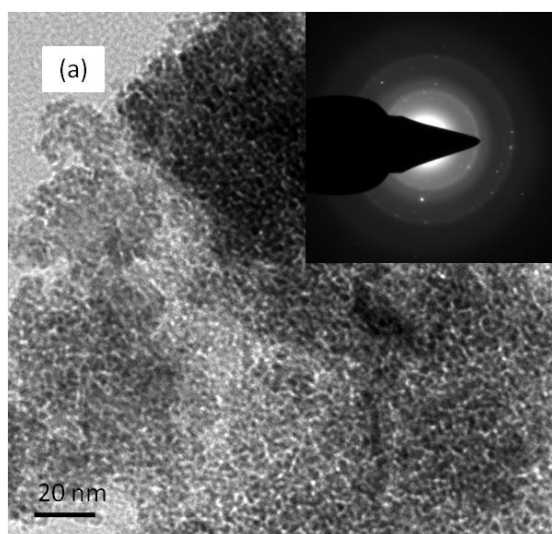


Figure 4.2. XRD patterns of (a) Fe1, (b) Fedx1, (c) Fedx2, and (d) Fedx3. The simulated pattern of Fe<sub>3</sub>O<sub>4</sub> is shown and indexed at the bottom.

### 4.2.3 TEM Analysis

Figure 4.3 shows the TEM images of the different samples. The TEM image of the uncoated  $\text{Fe}_3\text{O}_4$  shows that the sample consists of agglomerated particles whereas particles are well separated after coating with dextran. The average crystallite size calculated from X-ray line broadening and the particle size obtained from TEM are comparable for the dextran coated samples, indicating that the particles are well dispersed. The agglomerated nature of the uncoated particles (Fe1) is due to the strong magnetic interactions between the particles. TEM images point out that in the case of Fedx1 samples, a number of magnetite nanoparticles together, or clusters, are covered by dextran molecules. This will strongly influence the magnetic properties of the sample as described in section 4.2.7. In the case of Fedx2 and Fedx3, individual monodispersed particles are clearly seen, The particle sizes of synthesized samples are less than that reported in the literature [13].



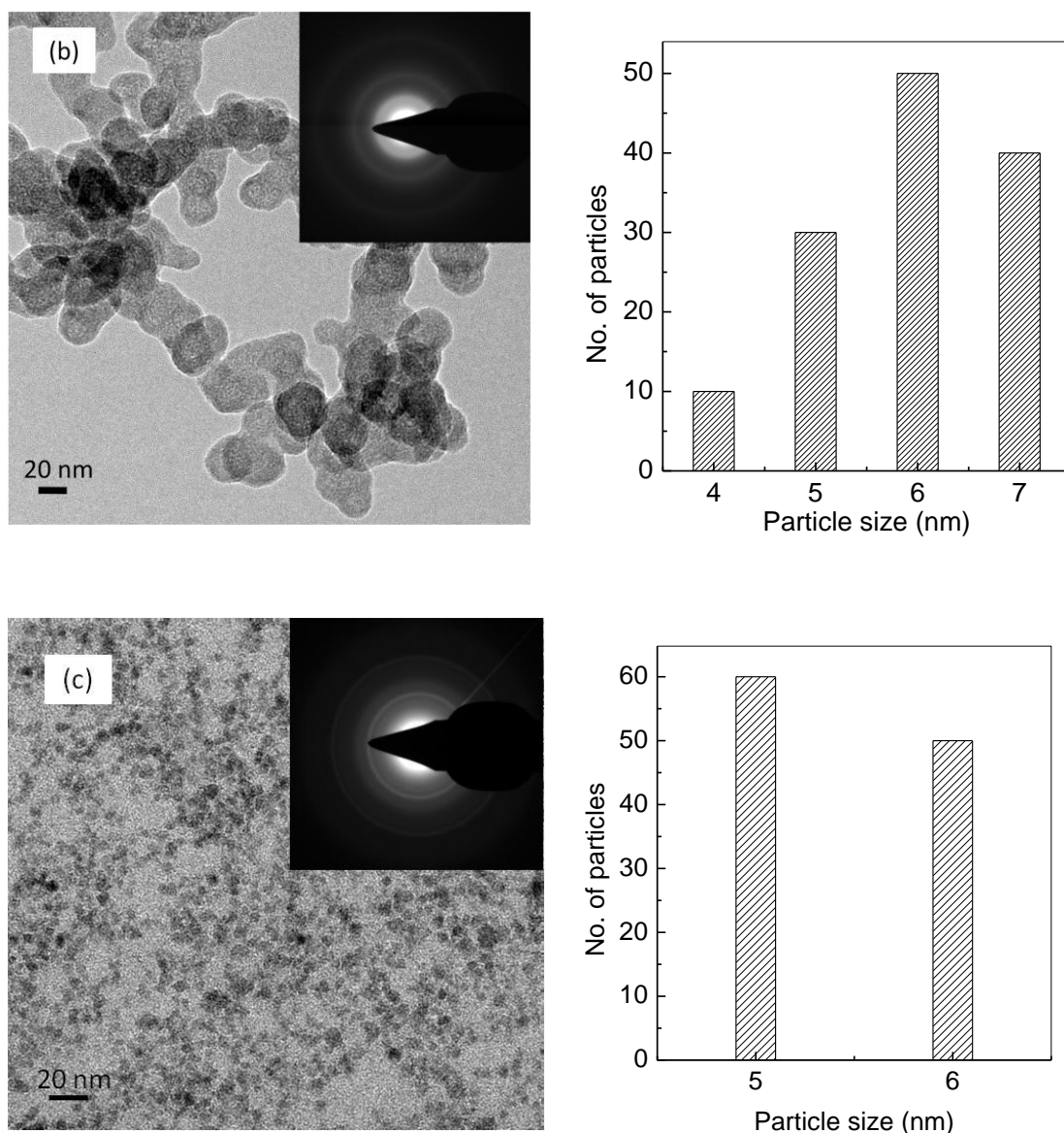


Figure 4.3. Transmission electron micrographs (left) and the corresponding particle size distribution (right) of a) Fe1 b) Fedx1 c) Fedx2

#### 4.2.4 Dynamic light scattering Analysis

Large difference is observed between hydrodynamic diameter and particle size obtained from TEM as well as XRD studies of the nanoparticles. The average hydrodynamic diameter of the dextran coated particles in the first case (coating of dextran after the magnetite particles are dried and further dispersed) is 68 nm and the value is larger than that obtained by insitu coating of the particles (method 3) due to formation of aggregates of functionalised particles. The Fedx2 and Fedx3 samples are

nearly monodispersed in nature and the hydrodynamic diameter is found to be 29 and 10 nm, respectively. The increased hydrodynamic diameter of dextran functionalised iron oxide nanoparticles is resulting from the size of the inorganic core and the dextran moiety that swells in a solvent increasing the nanoparticles diameter. By contrast, the magnetic nanoparticles are surrounded by a thin layer of the collapsed polymer and therefore their diameters obtained from TEM are smaller than the particle diameter obtained by DLS.

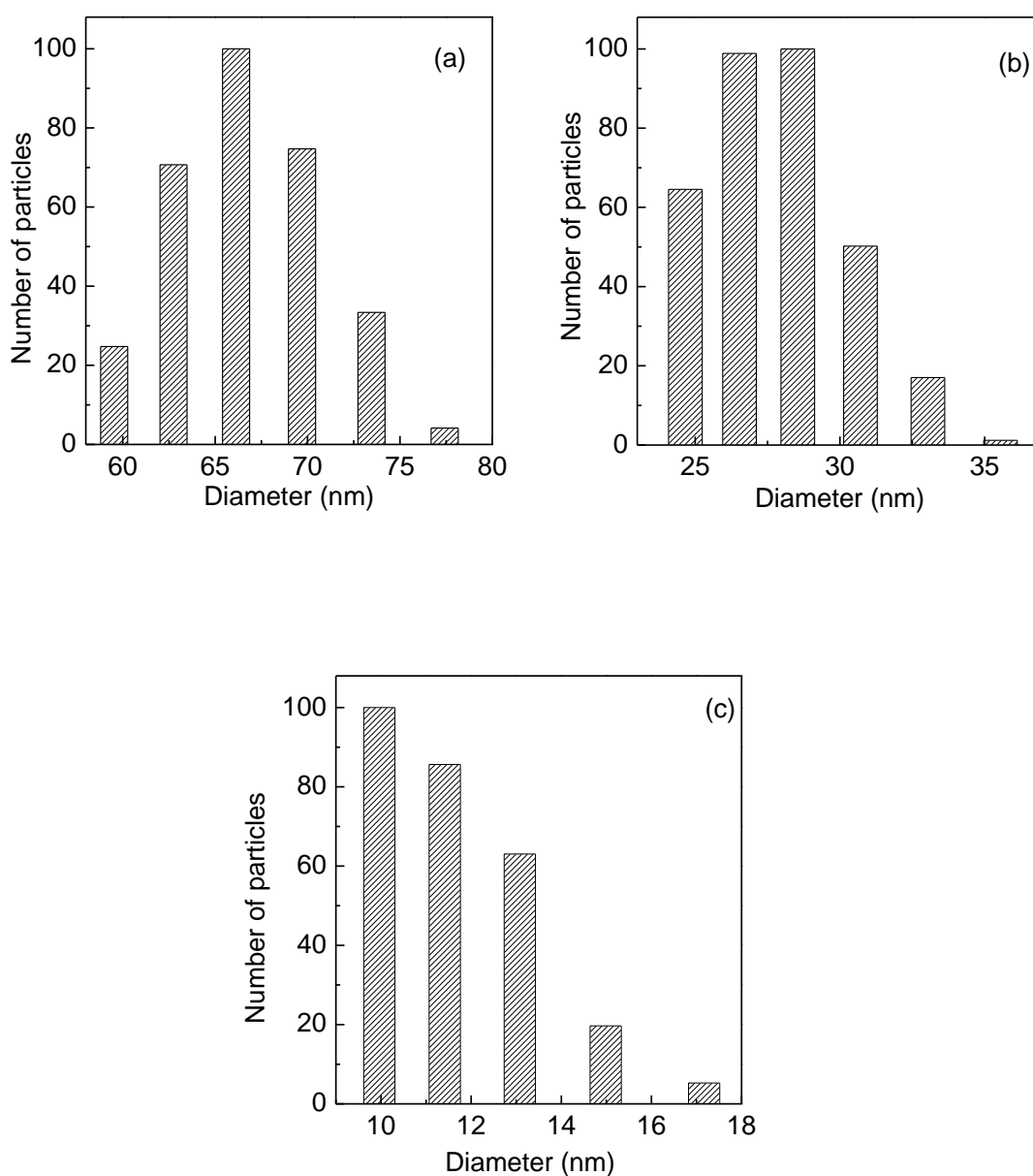


Figure 4.4. DLS particle size distribution of a) Fedx1 b) Fedx2 c) Fedx3

#### 4.2.5 FTIR Studies

The effectiveness of the coating of the magnetite nanoparticles by dextran is studied by FTIR spectroscopy. Figure 4.5 compares the IR spectra of uncoated and dextran coated magnetite nanoparticles along with that of dextran. The spectrum of dextran shows the characteristic absorption bands of polysaccharide at  $3316\text{ cm}^{-1}$  due to the O–H stretching and at  $1652\text{ cm}^{-1}$  due to bending vibration of the water molecule [11]. These bands are absent in the dextran coated magnetite nanoparticles. This observation indicates that the OH groups present in the glycosidic moieties play a vital role in the binding of dextran with magnetite nanoparticles [14]. The high binding affinity of OH groups present in dextran towards iron oxide surfaces results in a high particle stability. The surface-grafted magnetite nanoparticles could be easily dispersed in water to form a uniform suspension and be stably preserved for several months, suggesting that the tendency for the aggregation of particles is considerably weakened, whereas the suspension made from the bare magnetic nanoparticles is completely precipitated from the solvent in only a few minutes without stirring. The IR bands of dextran at  $2916$ ,  $1430$  and  $1360\text{ cm}^{-1}$  are due to the C–H vibrational modes, bands at  $1151$  and  $1036\text{ cm}^{-1}$  are due to C–O vibrations and the bands at  $916$ ,  $850$  and  $766\text{ cm}^{-1}$  correspond to the  $\alpha$ -glucopyranose ring of dextran. These bands are present in the spectrum of the dextran coated sample, indicating that dextran is coated on the surface of the nanoparticles. Thus the IR spectroscopic studies confirm that dextran is effectively coated on the surface of the magnetite nanoparticles.

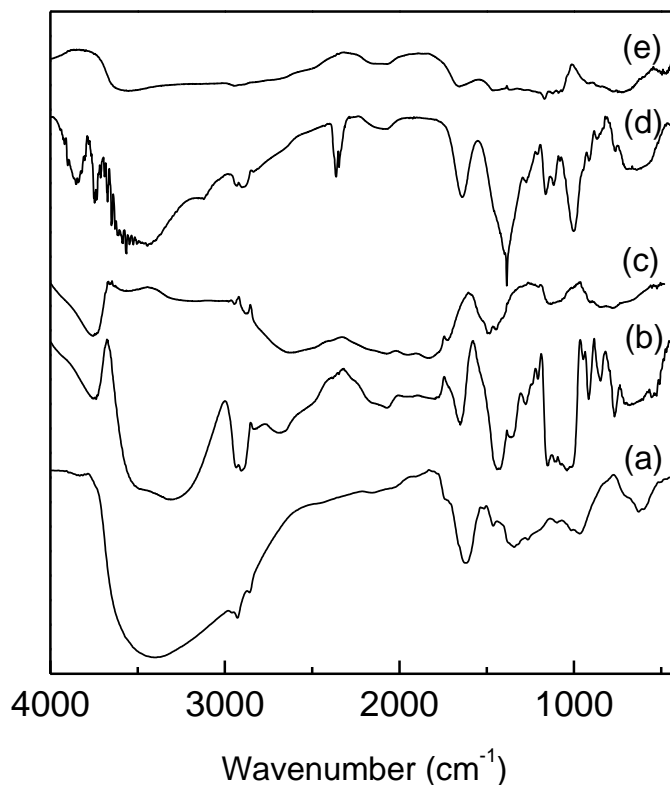


Figure 4.5. Infrared spectra of (a) Fe1, (b) Pure Dextran, (c) Fedx3, (d) Fedx2, and (e) Fedx1

#### 4.2.6 Thermal Analysis

The dextran content in the coated magnetite nanoparticles were measured using thermogravimetric analysis in air atmosphere at the heating rate of 10 °C/min. The thermal decomposition curves of the dextran coated magnetite particles are shown in Figure 4.6 depicting the variations of residual masses of the samples with temperature [15]. The first weight loss stage (below 140 °C) can be ascribed to the loss of adsorbed water molecules from the samples, while the major weight loss above 200 °C is due to the decomposition of dextran. The decomposition of pure dextran in air commences with the breaking of polymer bonds due to the thermal effect. The organic materials in the samples are completely burned to generate gaseous products and the magnetite is converted into Fe<sub>2</sub>O<sub>3</sub> at elevated temperatures, respectively. The percentage weight loss is shown in Table 4.2. The percentage weight loss due to dextran in Fedx2 and Fedx3 is almost the same but more than that of Fedx1 which is

due to the less amount of dextran capped on the agglomerated particles. Thermogravimetric studies for Fedx1 indicated that approximately 60% of the weight of the coated sample is due to dextran. The magnetization of the Fedx1 sample at 15 kOe is ~41% of that of the uncoated sample, in agreement with the results obtained from TG studies.

Table 4.2 Sample codes and weight loss of dextran coated magnetite obtained from TGA

Sample Code	Weight loss (%)
Fedx1	60
Fedx2	76
Fedx3	73

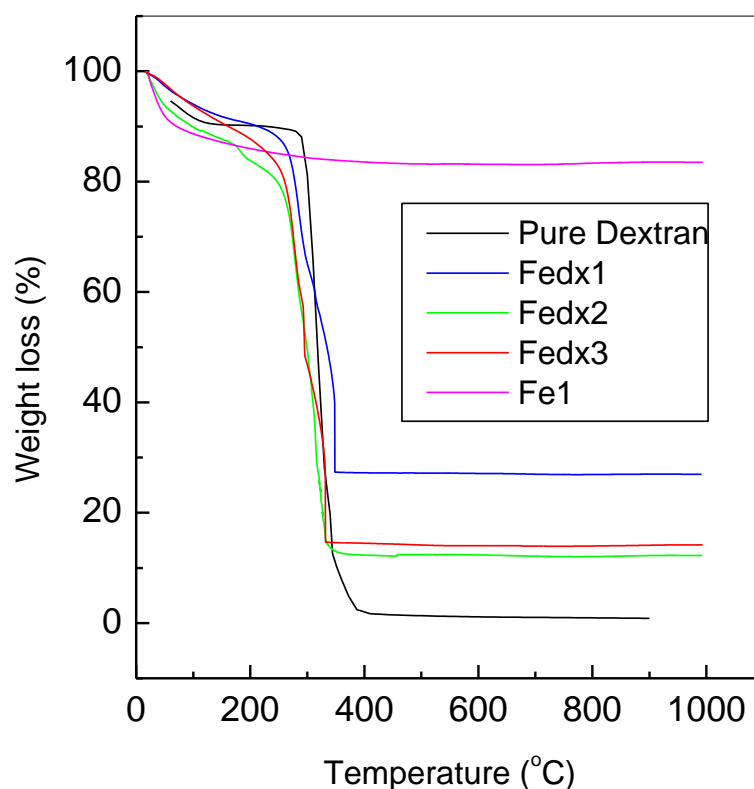


Figure 4.6. Thermograms of Fe1, Fedx1, Fedx2, and Fedx3.

### 4.2.7 Magnetic Measurements

Figure 4.7 shows the magnetization of the uncoated and coated samples as a function of magnetic field, measured at room temperature. As expected, all samples show superparamagnetic behaviour with no magnetic hysteresis. [16]. Thus, the magnetic characteristics show that the uncoated and coated magnetite nanoparticles are superparamagnetic at room temperature. The lower magnetization of the coated sample at higher fields is due to the non-magnetic nature of the coated dextran, as the magnetization is calculated per gram of the whole sample.

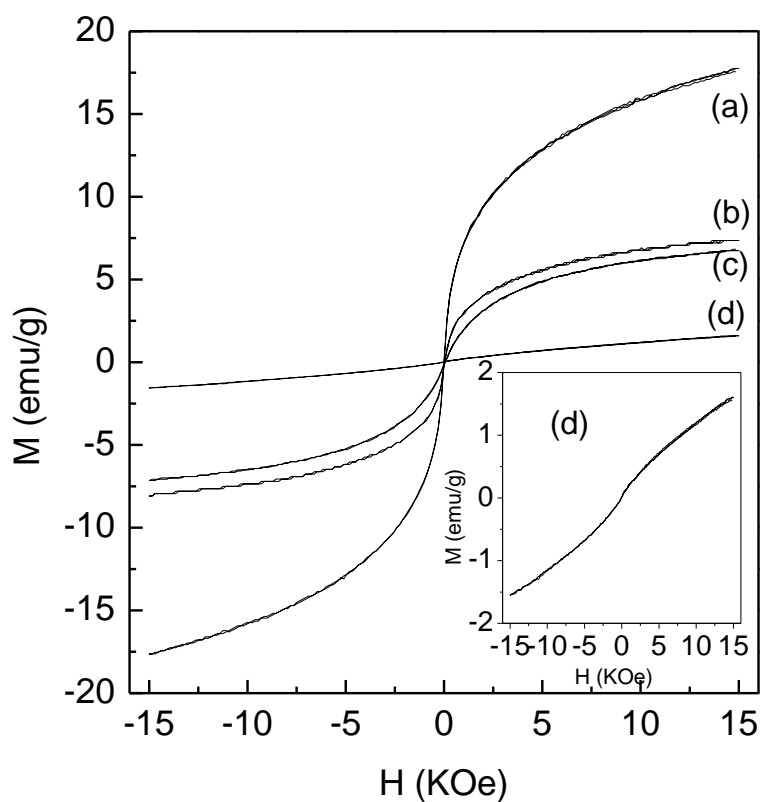


Figure 4.7. Room temperature magnetic measurements of (a) Fe1, (b) Fedx1, (c) Fedx2, (d) Fedx3.

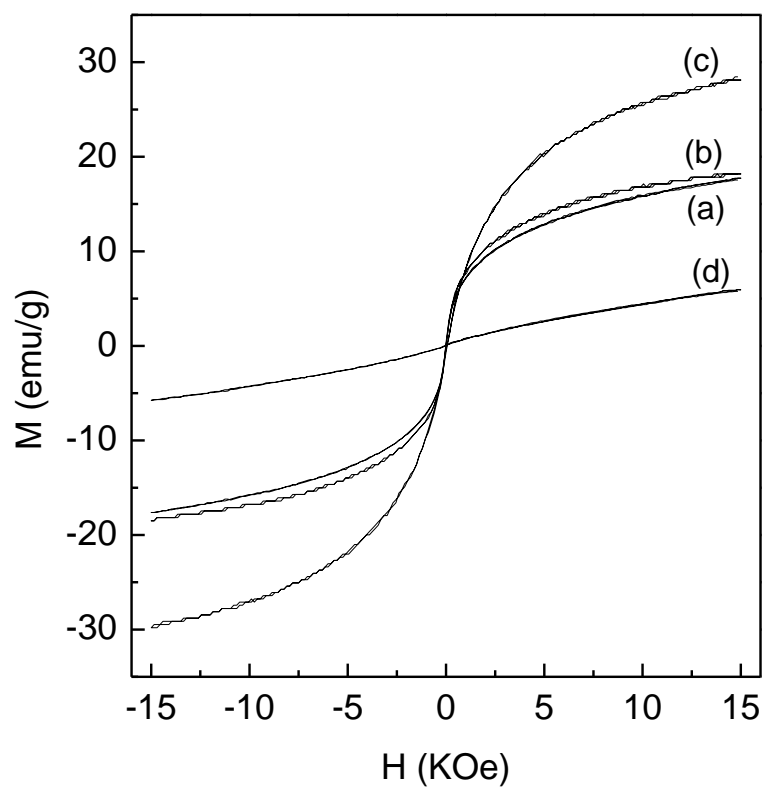


Figure 4.8. M-H Curves of (a) Fe1, (b) Fedx1, (c) Fedx2, and (d) Fedx3 based on weight loss of dextran (per gram of  $\text{Fe}_3\text{O}_4$ )

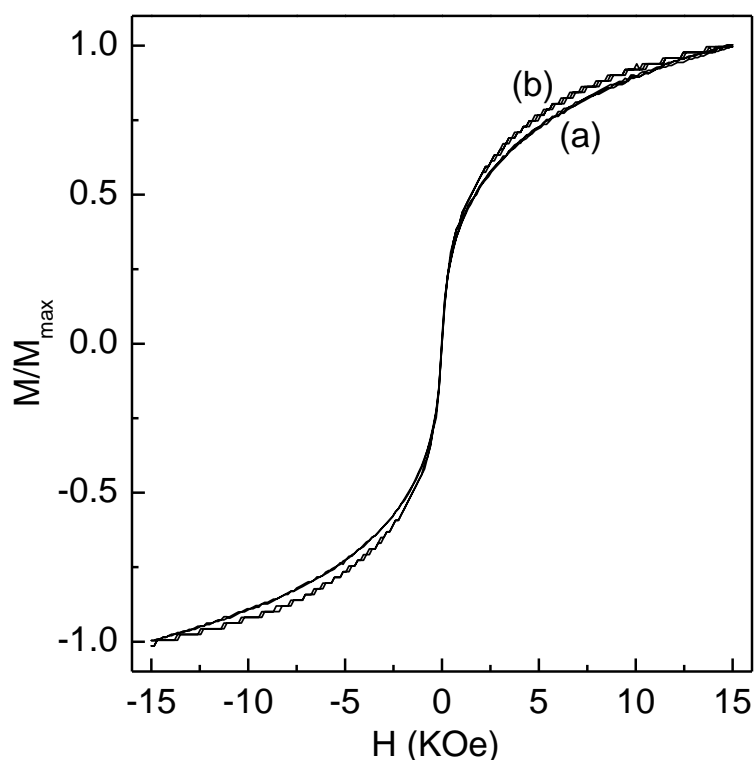


Figure 4.9. Normalised Curve of uncoated (Fe1) and dextran coated sample (Fedx1)

The saturation magnetization is calculated by extrapolating  $M$  vs  $1/H$  curve to  $1/H=0$ . All the samples have lower saturation magnetization values than the bulk  $\text{Fe}_3\text{O}_4$  ( $\sim 92$  emu/g) and is shown in Figure 4.7. This agrees with the known fact that magnetization of nanoparticles depends on particle size and their crystallinity. This is attributed to the increased surface effects with decreasing particle size which affects the magnetic properties of the particles due to the magnetically dead layer on the surface of the particles. The particle size variation of saturation magnetisation is depicted in Figure 4.10

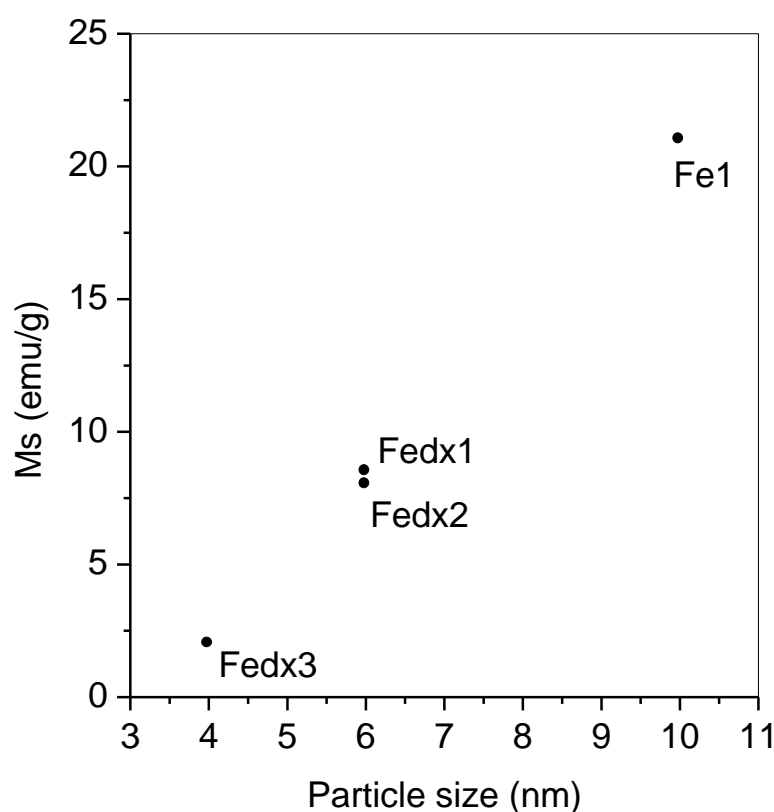
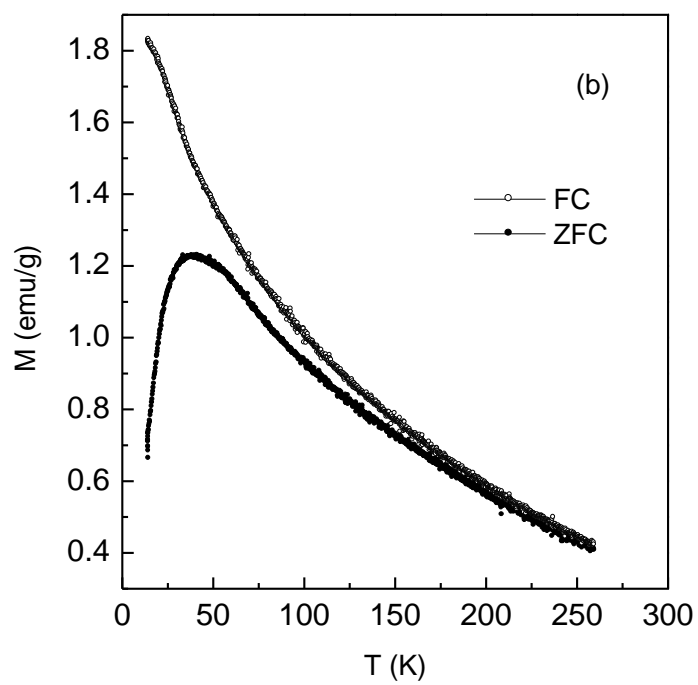
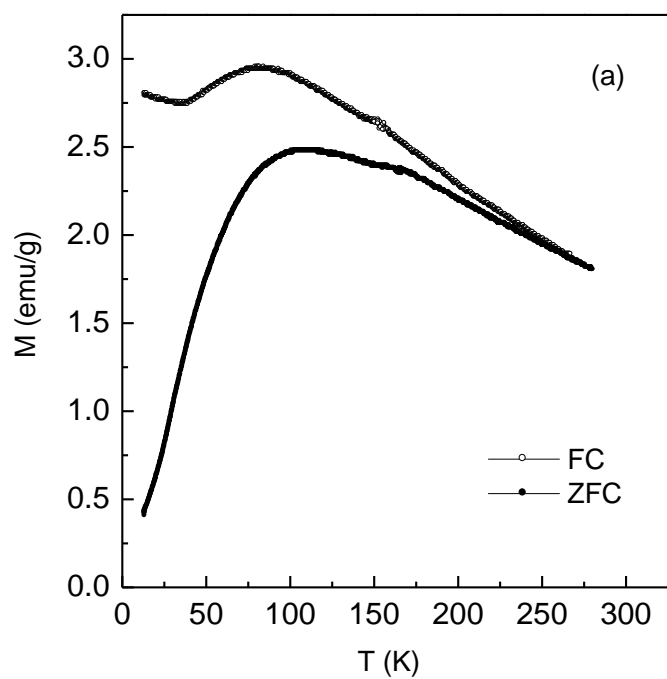


Figure 4.10 Variation of saturation magnetisation with particle size

Figure 4.11 shows the field cooled (FC) and zero field cooled (ZFC) magnetization curves of the uncoated and the different dextran coated samples from 12 K to 300 K at 50 Oe. For the field cooled measurement, the sample is cooled from room temperature to 12 K in a magnetic field of 50 Oe and the magnetization is measured as a function of temperature in the same field while warming at a constant rate. For zero field cooled measurement, the sample is cooled to 12 K in zero magnetic field and then the magnetization is measured in a field of 50 Oe while warming. For Fedx1 the ZFC and FC curves are separated below 200 K. The ZFC curve shows a broad peak at 42 K indicative of the characteristic blocking temperature for superparamagnetic particle whereas the uncoated magnetite particles (Fe1) shows the blocking temperature as 109 K. The broad peak in the ZFC curve generally implies wide distribution in particle size and larger magnetic anisotropy of the nanoparticles. The broad nature of the ZFC peaks of Fe1 and Fedx1 could be ascribed to wide size distribution caused by the agglomeration of particles in order to reduce the surface energy of the particles.

As shown in the Figure. 4.2, the TEM study revealed that the size of agglomerated magnetic nanoparticles is ranged from 6-12 nm for uncoated and 4-7 for coated samples. FC behaviour of Fe1 sample shows interacting nature of the sample (as described in the previous chapter). On the other hand, the FC magnetization curve of Fedx1 increases continuously below the blocking temperature, and this indicates non-interacting nature of the particles. Fe1, after coating with dextran shows decreased blocking temperature indicating decreased contribution of magnetic anisotropy. Similarly, for Fedx2, synthesized by a modified method, the blocking temperature is much lower than that of Fedx1 (24 K). The ZFC magnetization curve of Fedx2 is relatively narrow, the bifurcation between FC and ZFC curves is just above the blocking temperature and the FC magnetization increases sharply below the blocking temperature. These characteristics are indicative of narrower particle size distribution and reduced inter-particle interactions due to the effective capping of the particles with dextran. In-situ coating of the nanoparticles, as soon as the particles are formed (method 3) helps in reducing the particle size, as evidenced by the low blocking temperature (16 K) for Fedx3. The sharp peak in the ZFC magnetization curve of this sample and the bifurcation between FC and ZFC magnetizations below the blocking temperature are directly supporting this observation.



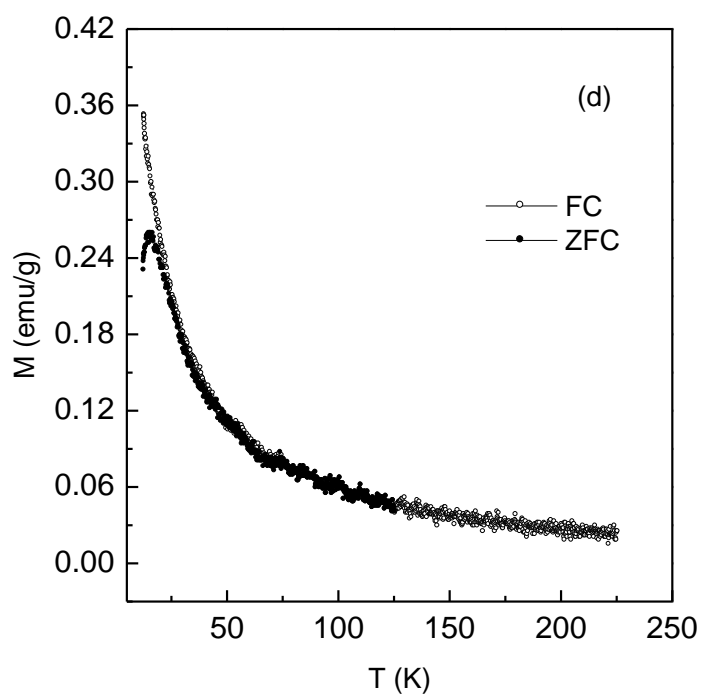
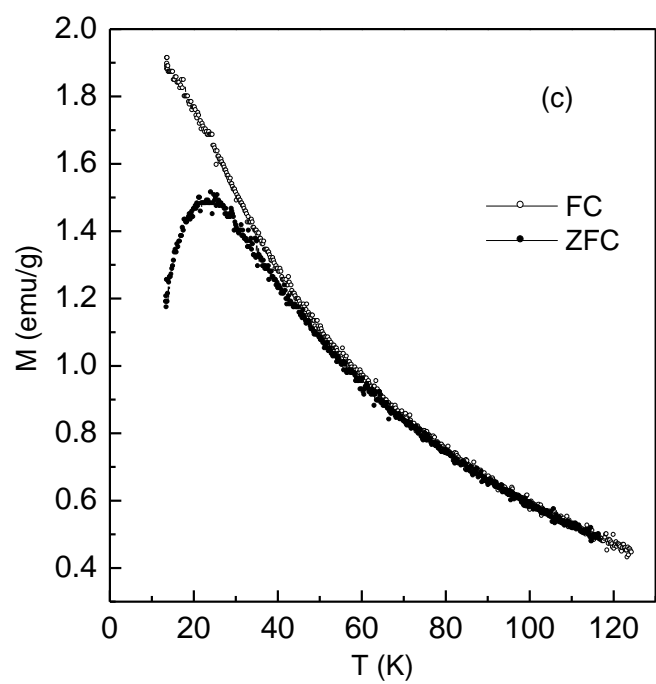


Figure 4.11 ZFC and FC magnetization curves of a) Fe1, b) Fedx1, c) Fedx2, and d) Fedx3

The blocking temperature for the different samples is compared in Table 4.3. The blocking temperatures of the uncoated and dextran coated particles are comparable to that reported for uncoated [17] and commercial dextran coated ferrofluids [18] having similar particle sizes. The decrease in the blocking temperature after coating with dextran is due to the decreased magnetic anisotropy contributions from inter-particle magnetic interactions [19]. The superparamagnetic blocking temperature of magnetic nanoparticles is given by  $KV \approx 25 k_B T_B$ , [20] where  $K$  is the magnetic anisotropy constant,  $V$  is the volume of a particle, and  $k_B$  is Boltzmann's constant. Assuming that the particles are spherical, the anisotropy constant  $K$  was calculated.

Table 4.3. Magnetic data of synthesised samples

Sample name	Crystallite size (nm)	$M_s$ (emu/g)	$T_B$ (K)	$K$ (erg/cm <sup>3</sup> )
Fe1	10	21	109	$7 \cdot 10^5$
Fedx1	6	8	42	$2.2 \cdot 10^6$
Fedx2	6	8	24	$1.2 \cdot 10^6$
Fedx3	4	2	16	$6.9 \cdot 10^5$

On the other hand, the FC magnetization curves increases continuously below the blocking temperature for the coated samples. It is known that the characteristics of the FC magnetization curve depend on the nature of the interaction between the particles [21,22].

The magnetic characteristics of uncoated and dextran coated nanoparticles of magnetite ( $Fe_3O_4$ ) studied to understand the effect of inter-particle magnetic interactions on the magnetic properties of the uncoated and coated samples. IR spectroscopic studies gave evidence for the effective coating of the magnetite nanoparticles by dextran. Comparison of the field dependent magnetization as well as the zero field cooled and field cooled magnetization measurements gave evidence for the suppressed inter-particle magnetic interactions in the dextran coated sample.

### **4.3 Synthesis and Magnetic Properties of L-Ascorbic Acid Coated Magnetite Nanoparticles.**

In this section, we report the studies on functionalising magnetite nanoparticles by vitamin C, a weak sugar acid and a good green reducing agent [23]. Vitamin C [24, 25] is naturally occurring L-enantiomer of ascorbate and is present in blood plasma include the brain, spleen, adrenal glands etc. For the functionalisation of vitamin C on magnetite nanoparticles, one must reckon the stereochemistry, binding functional groups, stability, most importantly prevention of particle agglomeration. It has been proved that hydroxyl group has strong affinity for the functionalisation of metal oxide nanoparticles in the case dextran, starch [26], etc. This is the first study which strongly illuminated the functionalisation of magnetite nanoparticles by L-ascorbic acid.

#### **4.3.1 Synthesis**

The ascorbic acid functionalised magnetite nanoparticles are synthesised by two different pathways

##### **4.3.1.2 Method 1**

In this synthesis method, magnetite nanoparticles was synthesised, washed and dried. This material is used for the functionalisation by using ascorbic acid. The sample Fe1 was used for the functionalisation by l-ascorbic acid. The neat magnetite nanoparticles and ascorbic acid were taken in 3:5 ratio. The 0.3 g of dried Fe1 sample was again dispersed in 100 ml of deionised water by ultrasonication. The pH of the solution is maintained by adding 10N ammonium hydroxide until the pH reaches 12.87. The dispersed iron oxide nanoparticles are mixed with 0.5 g of vitamin C and the dispersion was heated at 80°C for 1 hr under magnetic stirring. The product formed was dialysed for 4 days and dried. The sample was designated as FeAc1

##### **4.3.1.1 Method 2**

Aqueous dispersion of ascorbic acid coated magnetic nanoparticles was obtained by insitu co-precipitation method. The reaction was carried out by taking 0.1 moles of FeCl<sub>2</sub> and 0.2 moles of FeCl<sub>3</sub> and 0.5 gm of ascorbic acid. 20 ml of the mixture of

$\text{Fe}^{2+}$  and  $\text{Fe}^{3+}$  was added to 100 ml of 10 N  $\text{NH}_4\text{OH}$  and the mixture was stirred for 15 min. The resultant suspension was kept at  $80^\circ\text{C}$  for 30 min under magnetic stirring. The suspension was finally dialyzed for 4 days against distilled water and was dried at  $60^\circ\text{C}$  in the oven. The dried sample was designated as FeAc2 and are used for magnetic charecterisation, IR, TEM , XRD etc.

### 4.3.2 PXRD Analysis

The uncoated and ascorbic acid coated magnetite nanoparticles are characterized by powder XRD studies. Figure 4.12 shows the XRD patterns of the uncoated and coated samples. A comparison of the two patterns with the simulated XRD pattern of  $\text{Fe}_3\text{O}_4$  indicates that the peaks observed in the experimental patterns corroborate well with the simulated pattern and no extra peaks corresponding to any impurities are observed. The cubic lattice parameter is calculated as  $8.38 \text{ \AA}$  for uncoated samples and  $8.36 \text{ \AA}$  for the coated samples, which is comparable to the value reported for  $\text{Fe}_3\text{O}_4$ . All the reflections in the experimental patterns are very broad indicating nanocrystalline nature of the samples. There is an overall decrease in the intensities of the corresponding peaks of the ascorbic acid coated samples, indicating effective coating of the particles with ascorbic acid. The average crystallite sizes of the uncoated and coated samples are calculated from XRD line broadening using the Scherrer formula. The average crystallite sizes are calculated as 10 nm for the uncoated, 6 nm for ascorbic acid coated sample by method1 (FeAc1) and 3 nm for insitu functionalized sample (FeAc2). The broadening and decreased intensity of XRD patterns of FeAc1 and FeAc2 are due to the decrease in crystallite size on coating with surfactants. Therefore, the broad peaks indicate the formation of nanosized  $\text{Fe}_3\text{O}_4$  particles coated with ascorbic acid.

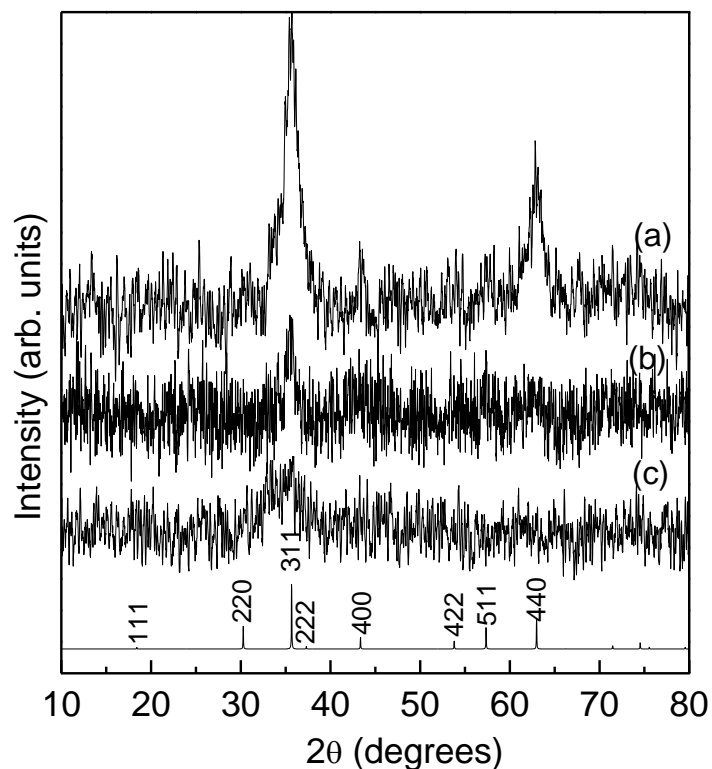
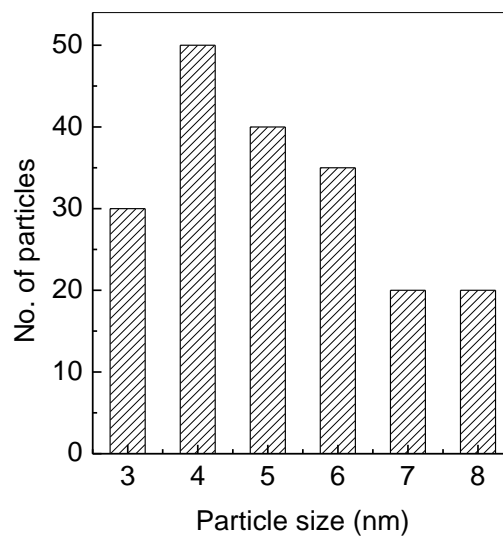
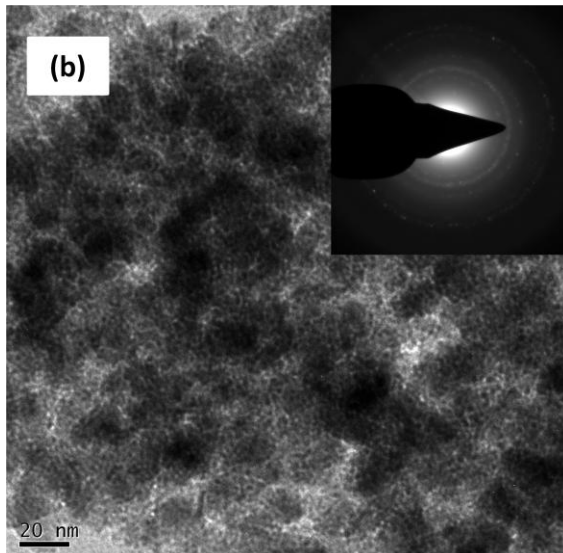
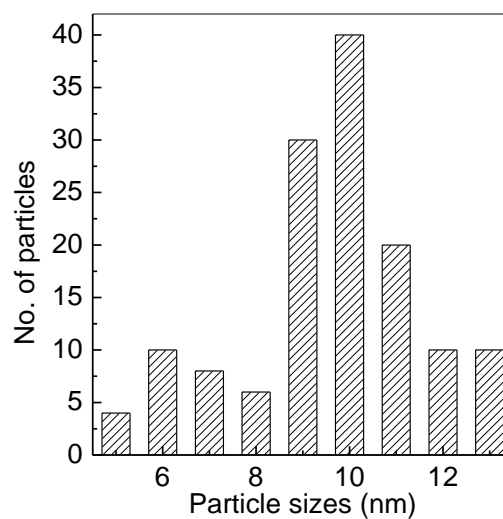
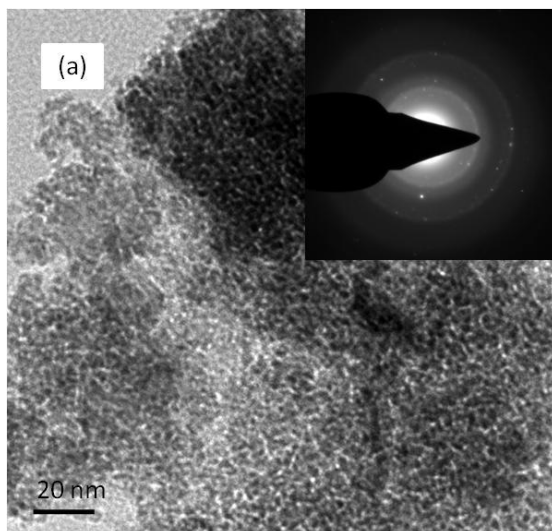


Figure 4.12. XRD pattern (a) Fe1 (b) FeAc1 (c) FeAc2. The simulated pattern of Fe<sub>3</sub>O<sub>4</sub> is shown and indexed at the bottom.

### 4.3.3 TEM Analysis

Figure 4.13 show a comparison of the the TEM images of the uncoated and the two ascorbic acid coated samples. The TEM image of the uncoated Fe<sub>3</sub>O<sub>4</sub> shows that the sample consists of agglomerated particles whereas group of particles are functionalized together in case of FeAc1 sample. Average particle size of 5 nm is obtained after coating with ascorbic acid for FeAc1. On the other hand, the particles in FeAc2 are well isolated, indicating that individual particles are coated by ascorbic acid. The average particle size is around 3 nm. Thus, the average crystallite size calculated from X-ray line broadening and the particle size obtained from TEM are comparable for the ascorbic acid coated sample. The agglomerated nature of the uncoated particles is due to the strong magnetic interactions between the particles. The particle size distribution from the TEM analysis results the nanoparticles are agglomerated for FeAc1 samples as compared to the FeAc2 sample synthesized by

method 2. The diffused ring patterns, shown in the inset of Figure 4.13, indicate the nanocrystalline nature of both samples, which can be indexed to iron oxide nanoparticles. The result obtained from TEM is consistent with that of the XRD results.



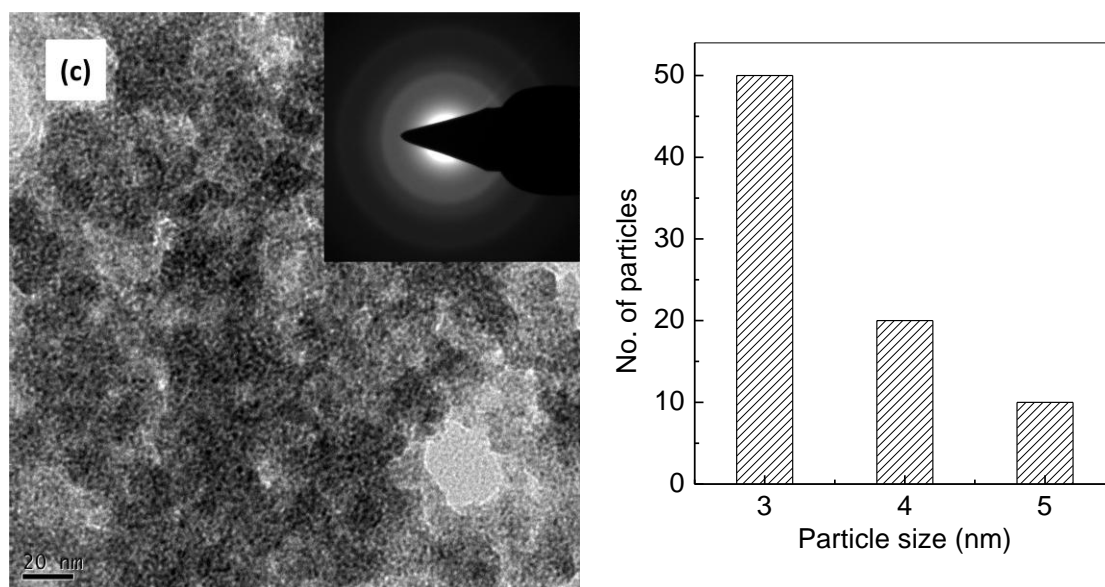


Figure 4.13 Transmission electron micrographs (left) and the corresponding particle size distribution (right) of a) Fe1 b) FeAc1 c) FeAc2

#### 4.3.4 DLS Measurement

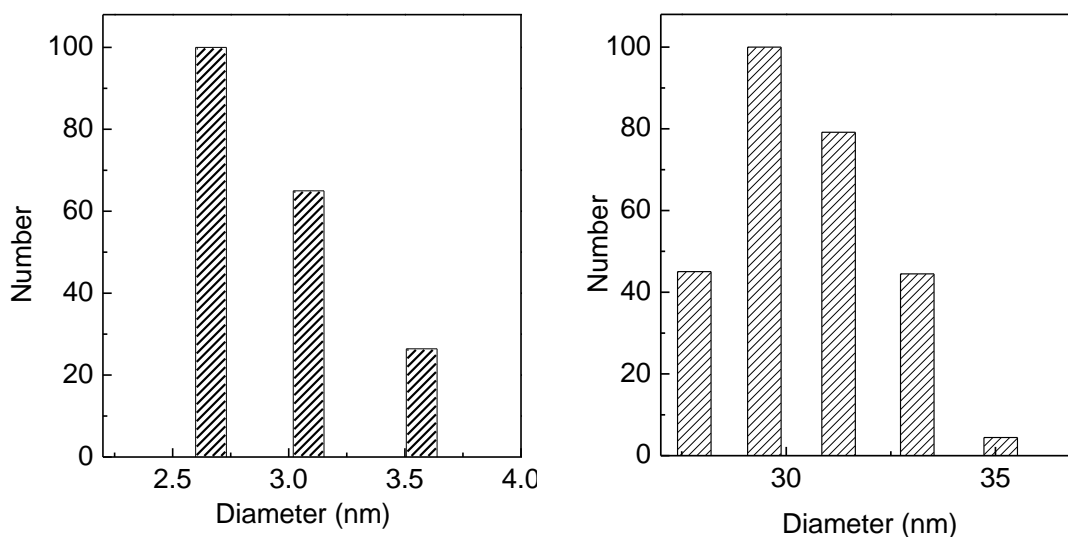


Figure 4.14 DLS particle size distribution of FeAc2 (left) and FeAc1 (right) samples

The dissemblance between hydrodynamic diameter and particle size obtained from TEM and XRD was observed in synthesised nanoparticles. The average

hydrodynamic diameter of FeAc1 particles are 29 nm and are larger than FeAc2 particles due to formation of aggregates of functionalised particles. The FeAc2 nanoparticles are nearly monodispersed in nature and the hydrodynamic diameter is found to be 3nm which corroborates the results obtained from TEM and XRD.

#### 4.3.5 FTIR Studies

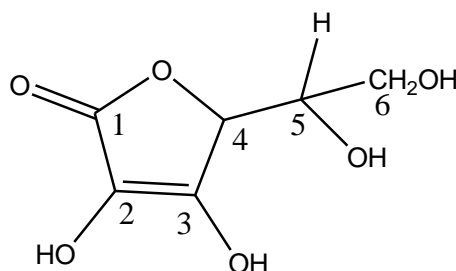


Figure 4.15 Structure of ascorbic acid molecule

The hydroxyl groups present on the surface of magnetite nanoparticles play vital role for the functionalisation strategies as reported in the literature [27]. When considering the coating of magnetite nanoparticles by L-ascorbic acid, the surface hydroxyl groups meld with the carboxyl groups present in ascorbic acid. This has been confirmed by IR investigation. Based on the IR investigation [28], the four O-H bands observed in ascorbic acid can be assigned as follows: C(6)-OH ( $3540\text{ cm}^{-1}$ ), C(3)-OH ( $3425\text{ cm}^{-1}$ ), C(5)-OH ( $3330\text{ cm}^{-1}$ ), C(2)-OH ( $3232\text{ cm}^{-1}$ ) which was observed in the case of functionalized samples. The bands at  $1760\text{ cm}^{-1}$  disappears in functionalised sample which attributes that the coordination with magnetite nanoparticles occurs through C=O group. Moreover, the reduced intensity of the Fe-O band due to  $\text{Fe}_3\text{O}_4$ , at  $\sim 600\text{ cm}^{-1}$ , suggests the effective capping of the magnetite nanoparticles.

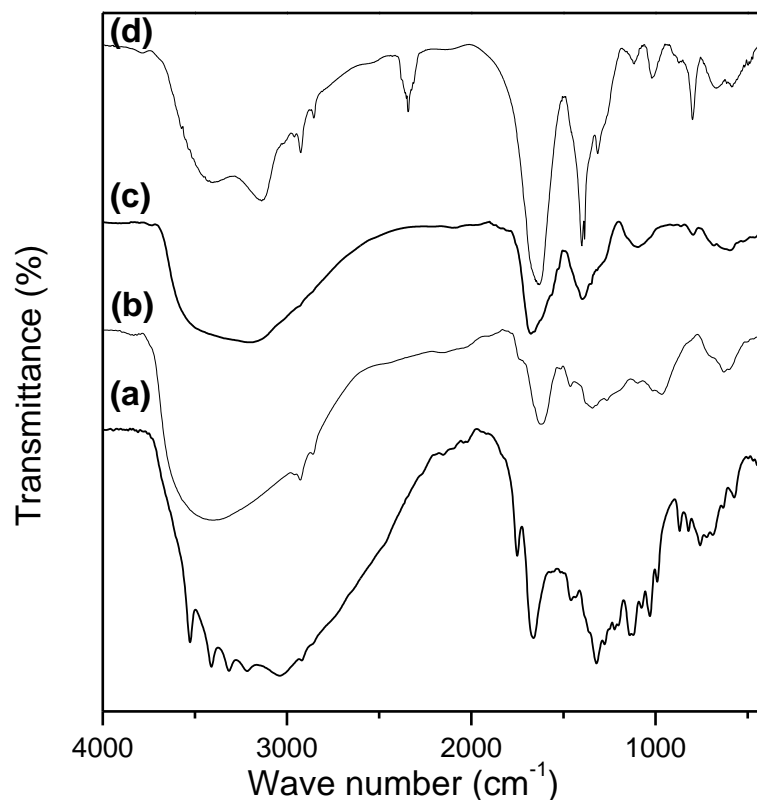


Figure 4.16 FTIR spectra (a) pure ascorbic acid, (b) Fe1, (c) FeAc2, (d) FeAc1

#### 4.3.6 Thermal analysis

The ascorbic acid content in the coated particles were measured by TGA carried out in air at the heating rate of 10°C/min. The thermal decomposition curves of the ascorbic acid coated samples are shown in Figure 4.27 depicting the variations of residual masses of the samples with temperature. The organic materials and magnetite of the samples were completely burned to generate gas products and converted into Fe<sub>2</sub>O<sub>3</sub> at elevated temperatures. The decomposition of pure ascorbic acid in air commences with the decomposition of organic moiety. The first weight loss stage (below 140°C) can be ascribed to the loss of adsorbed water molecules in the samples, while the other stage beginning at about 200°C was due to the decomposition of ascorbic acid. The percentage weight loss in each case is shown in table 3.4. The

percentage decomposition of dextran in FeAc1 is more than that of FeAc2 which is due to the ascorbic acid present in the aggregates of nanoparticles

Table 4.4. Sample code and weight loss of ascorbic acid obtained from TGA

Sample Code	Weight loss (%)
FeAc1	27
FeAc2	64

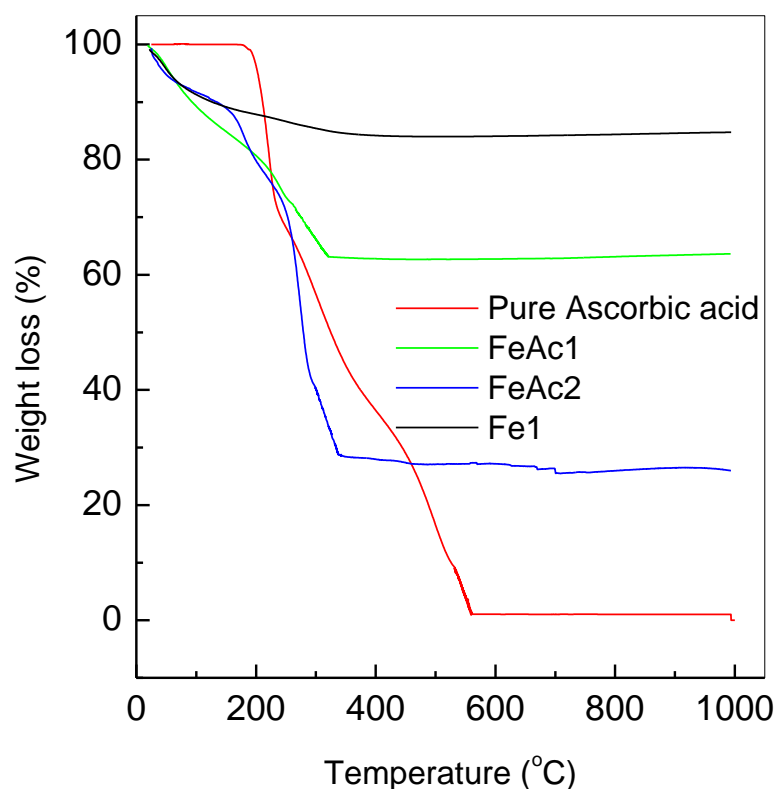
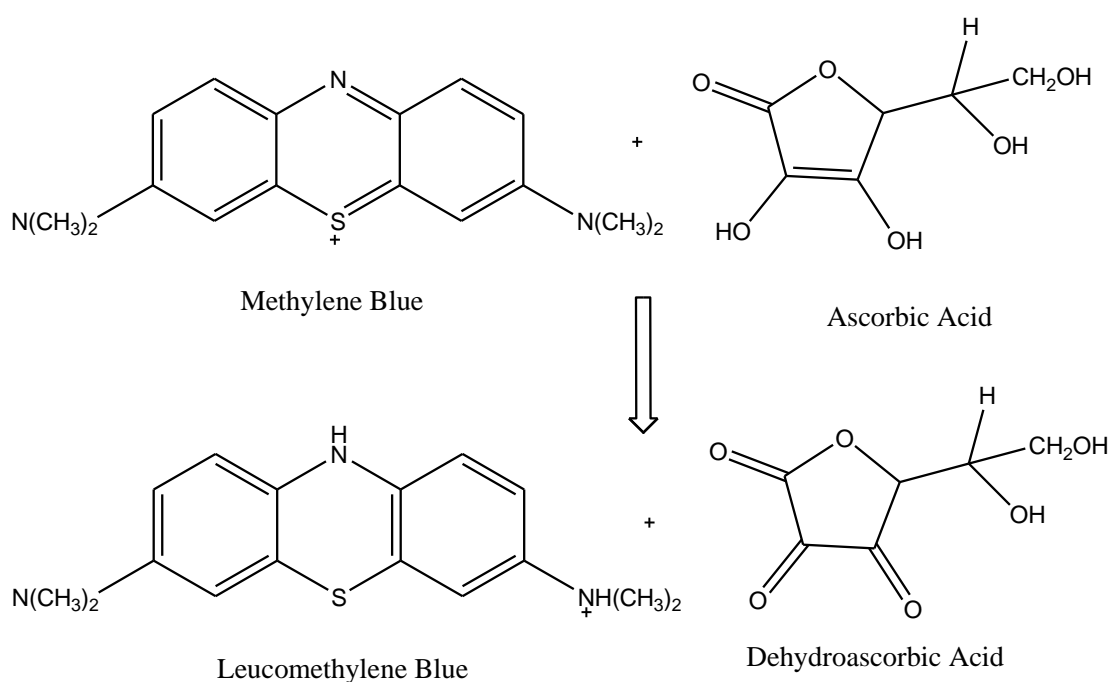


Figure 4.17 Thermograms of pure ascorbic acid, Fe1, FeAc1 and FeAc2.

#### 4.3.7 Reduction studies using ascorbic acid coated magnetite nanoparticles

Ascorbic acid is a single electron reducing agent even though not a vigorous reducing agent and is capable of reducing many carbonyl compounds [29], heme proteins [30] etc. To study whether the ascorbic acid coated on the magnetite nanoparticles is active

for chemical reactions, the reduction behaviour of ascorbic acid functionalised on the magnetic nanoparticles is studied by using the well known magic blue bottle reaction [31, 32]. The famous blue bottle reaction is a redox reaction where the methylene blue dye act as an oxidising agent and the sugar act as a reducing agent. This reaction is a stupendous tool for launching the key concept of reduction and oxidation reactions. In this particular reaction ascorbic acid reduces methylene blue to leuco form of the dye as show below.



The reduction reaction was carried out by using 1 g of ascorbic acid coated magnetite nanoparticles (FeAc1) and 10 ml of  $10^{-3}$  M methylene blue solution. The mixed solution was shaken vigorously for 10 min until the solution became colorless. During shaking magnetite nanoparticles are well dispersed and after the reaction, the magnetite particles were separated using an external magnetic field. The resultant solution was used for UV spectroscopic studies. UV-visible spectra of ascorbic acid, methylene blue and the solution after reduction are shown in Figure 4.18. All UV-visible spectra were recorded at room temperature by using water as reference sample. A strong absorption peak of the ascorbic acid at approximately 237 nm indicates the  $\pi$ - $\pi^*$  excitation of C=C double bond which is absent in the case of the leuco form of methylene blue[33]. This strongly reveals that ascorbic acid is not leached away from the surface of magnetite nanoparticles when dispersed in water and is as effective as

free ascorbic acid. This observed characteristic was supported by using FTIR studies. Figure 4.19 shows the FTIR spectra of ascorbic acid coated magnetite nanoparticles before and after reduction using methylene blue.

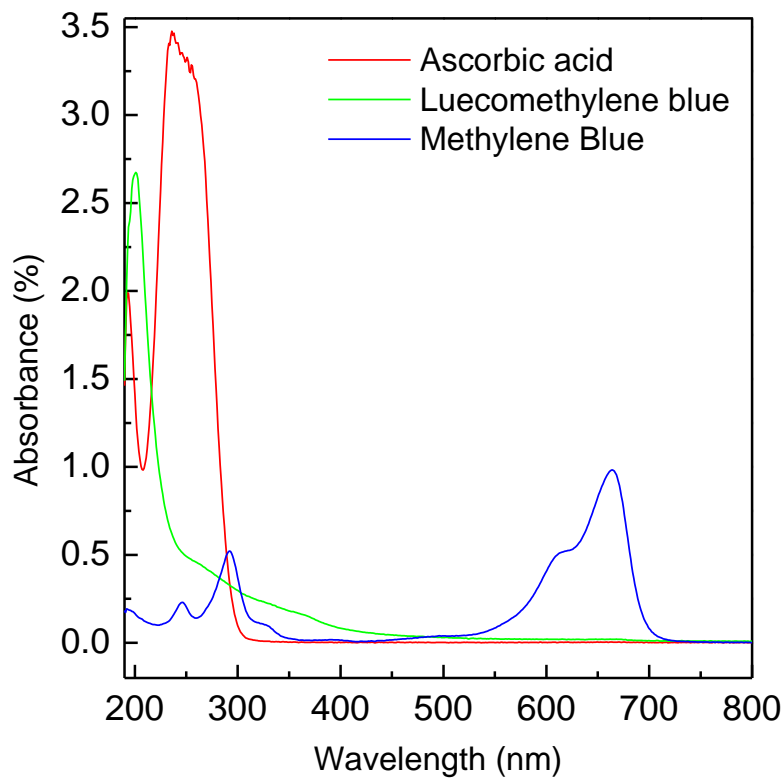


Figure 4.18 UV-Vis spectra of ascorbic acid and methylene blue before and after reduction with ascorbic acid coated magnetite nanoparticles.

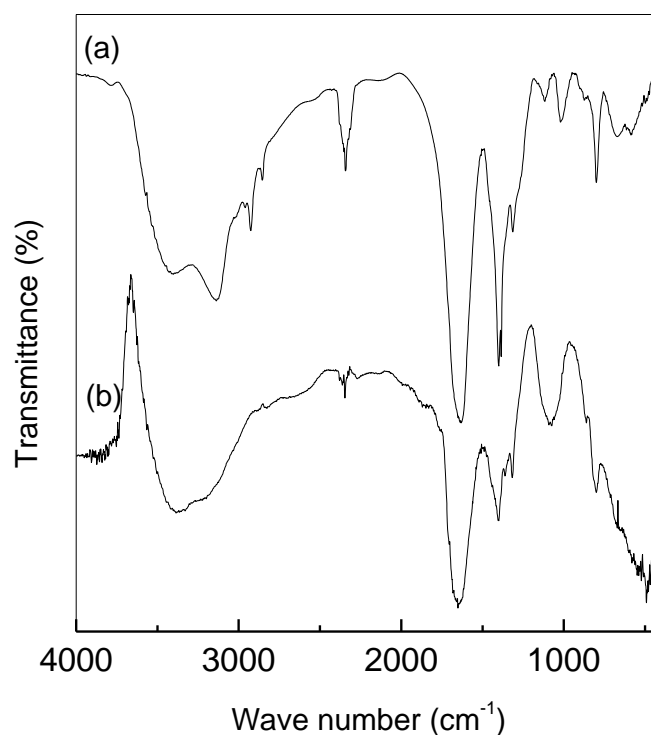


Figure 4.19. FTIR spectra of FeAc1 a)after reduction, b) before reduction

We may expect that this type of utile material can be used in synthesis of organic compounds especially in the reductive amination reaction. Recently Ying Yu et al [34] reported a facile method for the reductive amination of aryl boronic acid with nitroso aromatic group in presence of ascorbic acid as a reducing agent. Instead of ascorbic acid we can use the ascorbic acid coated magnetite nanoparticle and the dehydroascorbic acid [35] formed during the reduction reaction can be easily removed in the presence of external magnetic field.

#### 4.3.8. Magnetic measurement

Figure 4.20 shows the magnetization of the uncoated and coated samples as a function of magnetic field, measured at room temperature. Magnetic hysteresis is not observed for both the samples. Superparamagnetic nanoparticles are characterized by the absence of magnetic hysteresis. Thus, the magnetic characteristics show that the uncoated and coated magnetite nanoparticles are superparamagnetic at room temperature. The lower magnetization of the coated sample at higher fields is due to

the non-magnetic nature of the coated ascorbic acid, as the magnetization is calculated per gram of the sample. Apart from this, it is observed that the magnetization continuously increases for the uncoated sample at higher fields where as magnetization is almost saturated for the coated sample. The normalized magnetization curves, shown Figure 4.22, indicate that the magnetization is higher at low magnetic fields for the coated sample. These observations can be explained in terms of the reduced magnetic anisotropy after coating, where the contribution of the anisotropy due to inter-particle magnetic interactions is suppressed. Thus, smaller magnetic fields are sufficient to orient the magnetic moments in the direction of the applied field, whereas larger fields are required for the uncoated sample to attain the same value of magnetization due to the magnetic anisotropy. FeAc<sub>2</sub> shows almost paramagnetic behavior at room temperature. This is due to the very small particle size of this sample.

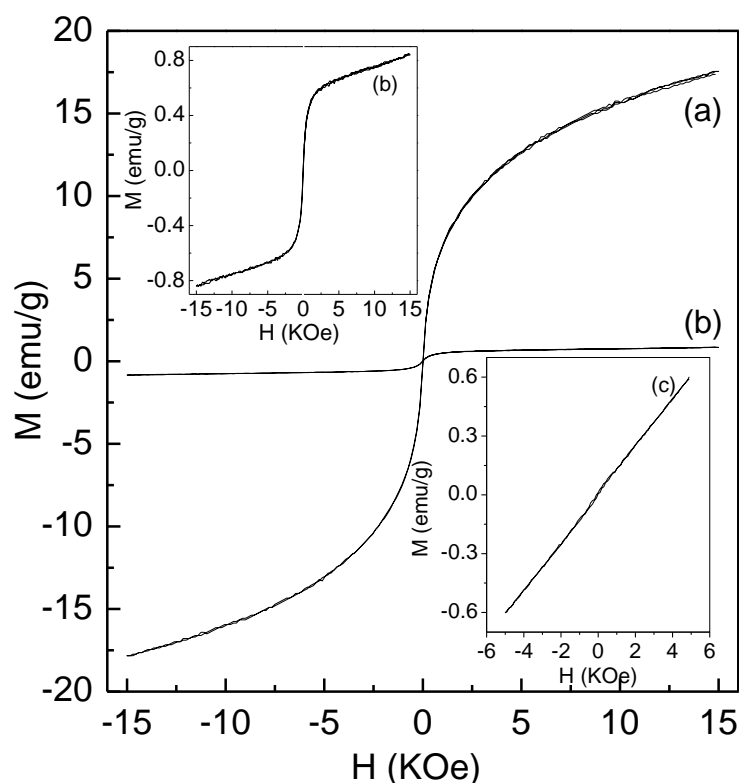


Figure 4.20 Room temperature magnetisation curves of a) Fe1, b) FeAc1, c) FeAc2 samples.

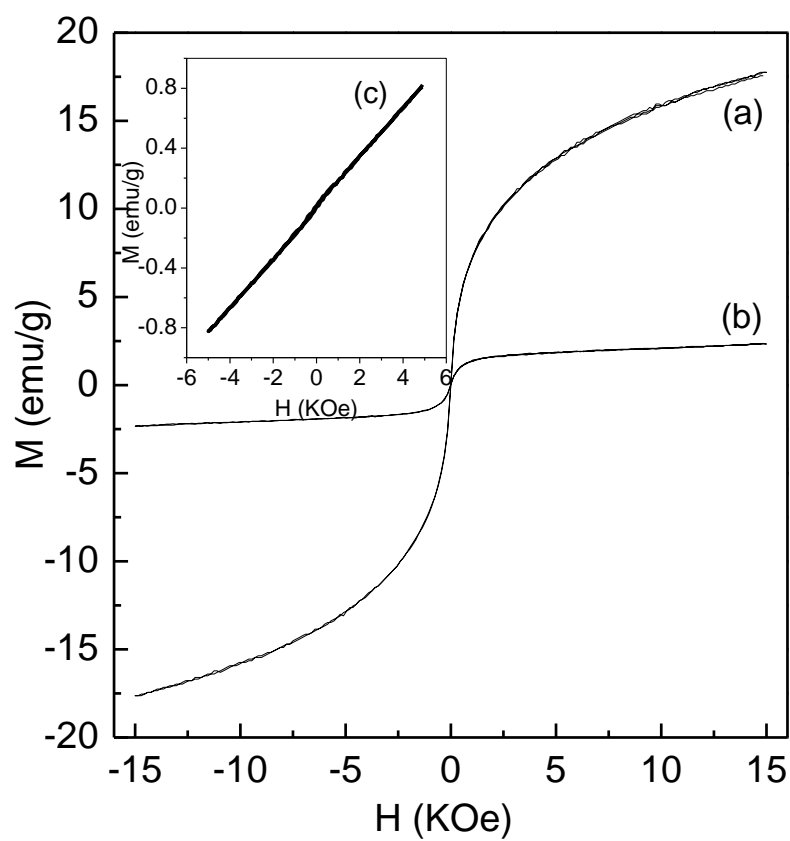


Figure 4.21 M-H Curve of (a) Fe1, (b) FeAc1, (c) FeAc2 based on weight loss of dextran (calculated per gram of  $\text{Fe}_3\text{O}_4$ )

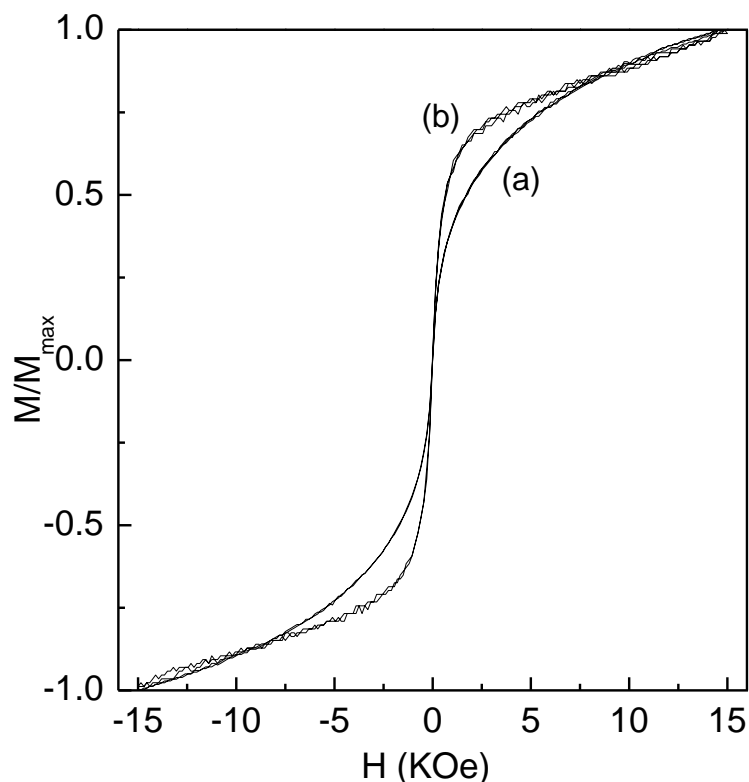


Figure 4.22 Normalised Curve of uncoated and ascorbic acid coated (Fe Ac1) samples

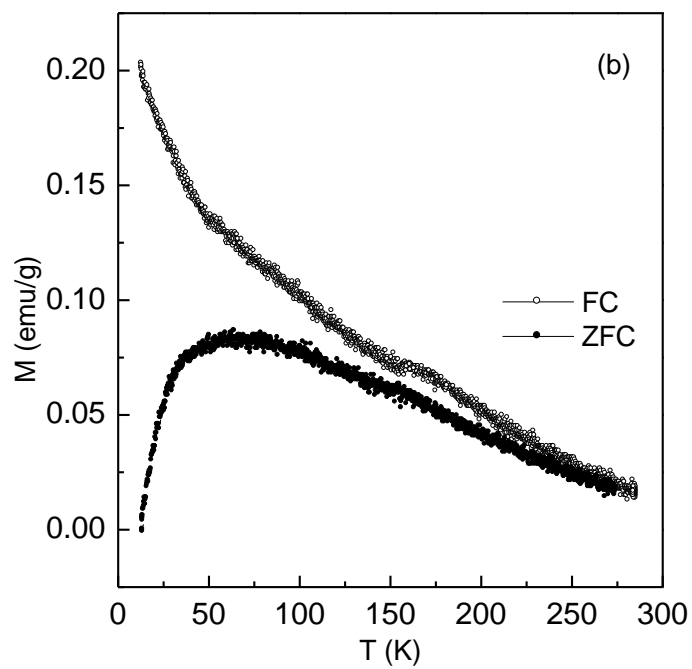
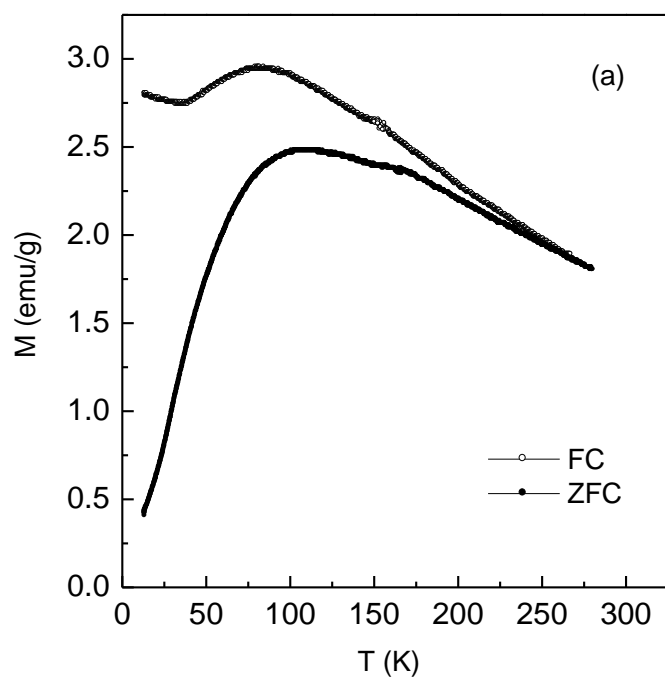
Figure 4.23 shows the field cooled (FC) and zero field cooled (ZFC) magnetization curves of the uncoated and coated samples. For the uncoated particles, the blocking temperature is obtained as 109 K where as this temperature is decreased to 70 K for FeAc1 after coating with ascorbic acid. On the other hand, the blocking temperature was found to be 16 K for FeAc2 where the particle size is very small. This sample showed almost paramagnetic behaviour at room temperature. The decrease in the blocking temperature after coating with ascorbic acid is due to the decreased magnetic anisotropy contributions from inter-particle magnetic interactions [14]. The superparamagnetic blocking temperature of magnetic nanoparticles is given by  $KV \approx 25 k_B T_B$ , where  $K$  is the magnetic anisotropy constant,  $V$  is the volume of a particle, and  $k_B$  is Boltzmann's constant. Assuming that the particles are spherical, the magnetic anisotropy was calculated and is depicted in the table 4.4. The FC magnetization also shows a broad maximum at the blocking temperature and the magnetization decreases slightly below this temperature and then remains constant as

the temperature is decreased. On the other hand, the FC magnetization increases continuously below the blocking temperature for the coated samples. It is known that the characteristics of the FC magnetization curve depend on the nature of the interaction between the particles. The dynamics of the nanoparticle systems are governed by the distribution of the relaxation times of the individual particles, arising from the particle size distribution. If the particles are well separated in a non-magnetic matrix or by proper surface coatings, the different types of interactions between the particles such as dipolar interactions or exchange interactions are suppressed. In this case, the FC magnetization continuously increases below  $T_B$  as the temperature is decreased whereas the FC magnetization remains constant or decrease slightly below  $T_B$  depending on the strength of the interactions between the particles. Thus, the nature of the FC magnetization curve indicates that the magnetic interactions are completely suppressed after coating the magnetite particles with ascorbic acid. This information gives additional evidence for the effective coating of the particles.

Table 4.5 Magnetic data of synthesised samples

Sample name	Particle size (nm)	$T_B$ (K)	K (erg/cm <sup>3</sup> )
Fe1	10	109	$7 \cdot 10^5$
FeAc1	5	70	$3.7 \cdot 10^6$
FeAc2	3	24	$2.4 \cdot 10^6$

The uncoated sample shows divergence between FC and ZFC magnetization curves below 250 K, much above the blocking temperature, with a broad maximum in the ZFC magnetization curve. Similar behavior is observed for the coated sample FeAc1 also. This is due to the wide particle size distribution. On the other hand, the divergence is observed below the blocking temperature for FeAc2 and the maximum in the ZFC magnetization is not very broad. This is indicative of narrower particle size distribution and effective coating of the individual particles, as compared to the coating of aggregates of particles in the case of FeAc1.



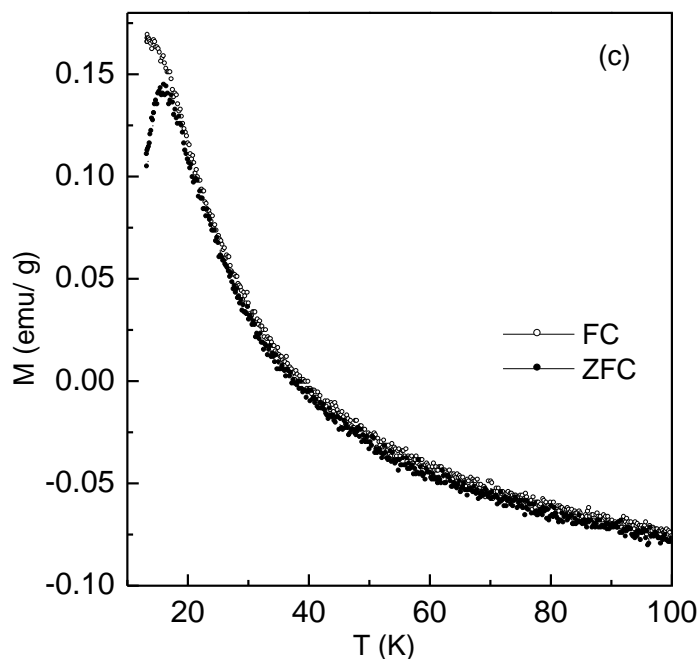


Figure 4.23 Temperature variation of magnetisation of a) Fe1, b) FeAc1 and c) FeAc2 samples

#### 4.3.9 $T_1$ and $T_2$ measurements

Since superparamagnetic  $\text{Fe}_3\text{O}_4$  nanoparticles are good  $T_2$ -type (negative) contrast agents in MRI [36], and vitamin C is a biocompatible molecule, the effect of vitamin C functionalised magnetic nanoparticles was investigated in terms of MR signal-enhancing property. An attempt to study the  $T_1$  and  $T_2$  relaxation of various concentrations of vitamin C functionalised  $\text{Fe}_3\text{O}_4$  nanoparticles in water was shown in Figure 4.24.  $^1\text{H}$  relaxation time measurements were also done on a 400-MHz spectrometer. Spin lattice relaxation times of the dispersed iron oxide solutions were measured using the conventional inversion recovery sequence [37]. For this measurement, 8 scans were collected with a relaxation delay of 20s with  $\tau$  delays varying from 0.5 ms to 20 s in a pseudo 2D mode. The data was analyzed with the help of Bruker  $T_1/T_2$  analytical routine.

It can be seen that the NMR signal intensity for the samples of different concentrations is not identical. With increasing nanoparticles concentration in water,

the NMR signal is enhanced significantly. The  $T_2$  relaxation process occurs because of the exchange of energy between protons in water molecules. In the presence of an externally applied magnetic field, superparamagnetic iron oxide nanoparticles [38] create inhomogeneity in the magnetic field affecting the environment that results in dephasing of the magnetic moments of protons. The inhomogeneities that the particles present lead to further decreased  $T_2$  relaxation times of the healthy tissue. The larger difference between the two  $T_2$  relaxation times leads to greater contrast between the healthy tissue and diseased tissue.

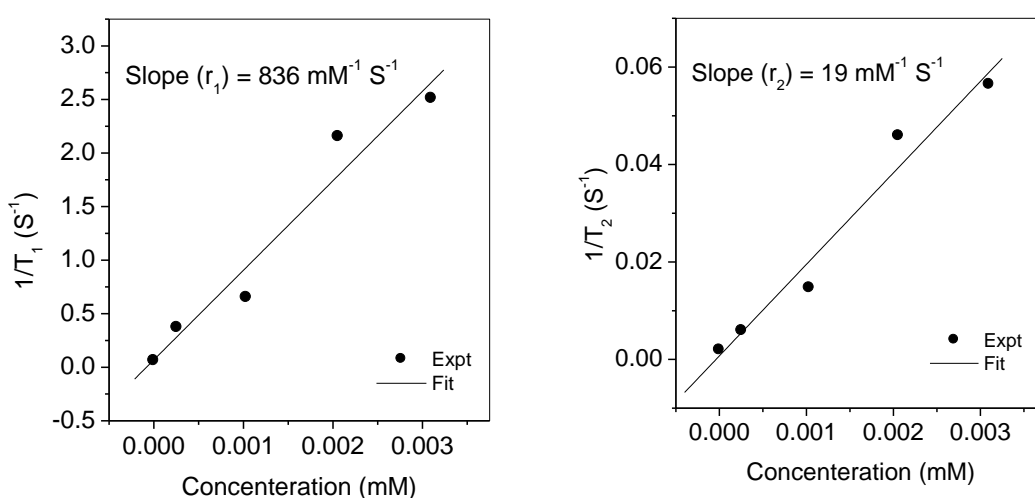


Figure 4.24. Plots of inverse relaxation times (a)  $1/T_1$  and (b)  $1/T_2$  as a function of iron concentration.

FeAc1 sample was used for relaxation measurement. The longitudinal  $T_1$  and the transverse  $T_2$  relaxation times were first measured at four iron concentrations at room temperature. Inverse relaxation times ( $1/T_1$  and  $1/T_2$ ) were then calculated and plotted as a function of iron oxide concentration was plotted in the Figure. The straight line plot obtained for both cases are not comparable for that reported in literature [39,]. Several factors are influencing the contrast effect which depends on the size of the magnetite core, magnetisation, molecular weight of the biocompatible molecule, etc. As described in the literature, dextran-based iron oxide nanoparticles [37] have been applied to conventional clinical imaging and molecular imaging for the last 20 years. Dextran coated iron oxide nanoparticles [37, 40] show the  $r_1$  value of 10.1 mM<sup>-1</sup>S<sup>-1</sup> and  $r_2$  value of 120 mM<sup>-1</sup>S<sup>-1</sup> which was not comparable for the obtained results. However further studies is required for ascorbic acid coated magnetite nanoparticles

to understand the discrepancies of the obtained results as well as the biocompatibility and their use in clinical applications.

To summarize, we prepared highly water-dispersible vitamin c coated superparamagnetic iron oxide nanoparticles by a simple surfactant mediated coprecipitation route. The vitamin c was successfully functionalised on the surface of iron oxide nanoparticles and was confirmed by XRD, TEM and Magnetic measurement.

#### **4.4 Conclusions**

Fe<sub>3</sub>O<sub>4</sub> nanoparticles are coated with the biocompatible molecules dextran and ascorbic acid. The coated nanoparticles are characterized using different techniques to verify the effectiveness of coating. Thermogravimetric studies give information on the amount of coated molecules. IR spectroscopic studies gave evidence for the effective coating of the magnetite nanoparticles by dextran. The magnetic characteristics of uncoated and dextran as well as ascorbic acid coated nanoparticles of magnetite (Fe<sub>3</sub>O<sub>4</sub>) studied to understand the effectiveness of coating as evidenced from the reduced inter-particle magnetic interactions on the magnetic properties of the uncoated and coated samples. Comparison of the field dependent magnetization as well as the zero field cooled and field cooled magnetization measurements gave evidence for the suppressed inter-particle magnetic interactions in the coated samples.

---

**References**

- 1 Pankhurst, Q. A.; Connolly, J.; Jones, S.K.; Dobson, J.; *J. Phys. D: Appl. Phys.*, **2003**, 36, R167
- 2 Neuberger, T.; Schopf, B.; Hofmann, H.; Hofmann, M.; von Rechenberg, B.; *J. Magn. Magn. Mater.*, **2005**, 293, 483
- 3 Laurent, S.; Forge, D.; Port, M.; Roch, A.; Robic, C.; Elst, L.V.; Muller, R.N.; *Chem. Rev.*, **2008**, 108, 2064
- 4 Bobo, J.F.; Gabillet, L.; Bibes, M.; *J. Phys.: Condens. Matter*, **2004**, 16, .S471
- 5 Dormann, J.L.; Fiorani, D.; Tronc, E.; *Adv. Chem. Phys.*, **1997**, 98, 283.
- 6 Thorek, D. L. J.; Chen, A. K.; Czupryna, J.; Tsourkas, A., *Annals of Biomedical Engineering*, **2006**, 34,23
- 7 Molday, R.S.; Mackenzie., *J Immunol Methods*. **1982**, 52, 353
- 8 Bautista, M.C.; Bomati-Miguel, O.; Morales, M.P.; Serna, C.J.; Veintemillas-Verdaguer, S.; *J. Magn. Magn. Mater.* **2005**, 293, 20
- 9 Shen, T.T.; Weissleder, R.; Papisov, M.; Bogdanov, A., Jr, Brady, T.J., *Magn. Reson. Med.* **1993**, 29, 599
- 10 Xu, X.Q.; Shen, H.; Xu, J.R.; Xu, J.; Li, X.J.; Xiong, X.M., *App. Surf. Sci.*, **2005**, 252, .494
- 11 Zhang, L-Y.; Gu, H-C.; Wang, X-M., *J. Magn. Magn. Mater.*, **2007**, 311, 228
- 12 Cullity, B. D., *Elements of X-ray Diffraction*, 2nd ed.; Addison-Wesley: Reading, PA, **1978**, p 99.
- 13 Dutza, S.; Andra, W.; Hergta, R.; Mullera, R.; Oestreich, C.; Schmidtd, C.; Topferd, J.; Zeisbergera, M.; Bellemann, M. E., *J. Magn. Magn. Mater*, **2007**, 311, 51
- 14 Jung, C. W., *Magn. Res. Imag.*, **1995**, 13, 675
- 15 Carp, O.; Patron, L.; Culita, D. C.; Budrugaec, P.; Feder, M.; Diamandescu, L., *J. Therm. Anal. Calorim.* **2010**, 101, 181
- 16 Knobel, M.; Nunes, W.C.; Socolovsky, L.M.; De Biasi, E.; Vargas, J.M.; Denardin, J. C., *J. Nanosci. Nanotech.*, **2008**, 8, 2836
- 17 Hyeon, H.; Lee, S. S.; Park, J.; Chung, Y.; Na, H. B.; *J. Am. Chem. Soc.*, **2001**, 123, 12798–12801

- 
- 18 Arelaro, A. D.; Brandl, A. L.; Lima, E.; Gamarra, L. F.; Brito, G. E.S.; Pontuschka, W. M.; Goya, G. F.; *J. Appl. Phys.* 2005, **97**, 10J316
- 19 Vargas, J.M.; Nunes, W.C.; Socolovsky, L.M.; Knobel, M.; Zanchet, D., *Phys. Rev. B*, **2005**, 72, 184428.1
- 20 Cullity, B.D. *Introduction to Magnetic Materials*, Addison-Wesley Publishing Company, Inc. Massachusetts, **1972**
- 21 Sasaki, M.; Jonsson, P.E.; Takayama, H.; Mamiya, H., *Phys. Rev. B*, **2005**, 71, 104405.1
- 22 Sankar, C.R.; Vijayanand, S.; Verma, S.; and Joy, P.A., *Solid State Commun.*, **2007**, 141, 307.
- 23 Songping, W.; Shuyuan, M., *Mater. Chem. Phys.* **2005**, 89, 423
- 24 Davis, M. B.; Austin, J.; Patridge, D. A., *Vitamin C - Its Chemistry and Biochemistry*, The Royal Society of Chemistry, **1991**
- 25 Chen, B.; Lee, Y.; Lin, W.; lin, F.; lin, K., *Biomed Eng Appl Basis Comm*, **2006**, 18, 30
- 26 Dung, T. T.; Danh, T. M.; Hoa, L. T. M.; Chien, D. M.; Duc, N. H., *J. Expt. Nano.*, 2009, 4, 259
- 27 Mahmoudi, M.; Simchi, A.; Imani, M.; Milani, A.S.; Stroeve, P., *J. Phys. Chem. B*, **2008**, 112, 14470
- 28 Lohmann, W.; Pagel, D.; Penka, V., *Eur. J. Biochem.* **1984**, 138, 479
- 29 Isaacs, N.S.; Eldik, R. V., *J. Chem. Soc., Perkin Trans.* **1997**, 2, 1465
- 30 Al-ayash, A. I.; Wilson, M. T.; *Biochem. J.* **1979**, 177, 641
- 31 Mowry, S.; Ogren, P. J., *J. Chem. Educ.*, **1999**, 76, 970
- 32 Hallock, A. J.; Berman, E. S. F.; Zare, R. N., *J. Am. Chem. Soc.*, **2003**, 125, 1158
- 33 Shukla, M.K.; Mishra, P.C., *J. Mol. Stru.* **1996**, 377, 247
- 34 Yu, Y.; Srogl, J.; Liebeskind, L. S., *Org. Lett.*, 2004, 6, 2631
- 35 Deutsch, J. C., *J. Chromatography A*, 2000, 881, 299
- 36 Weishaupt, D.; Kochli, V. D.; Marincek, B., *An Introduction to the Physics and Function of Magnetic Resonance Imaging*, Springer Verlag Berlin Heidelberg New York, **2006**
- 37 Kuperman, V., *Magnetic Resonance Imaging Physical Principles and Applications*, Academic Press, New York, **2000**

- 
- 38 Wang, Y. J.; Hussain, S. M.; Krestin, G. P., *Eur. Radiol.* **2001**, 11, 2319
- 39 Corot, C.; Robert, P.; Idée, J. M.; Port, M., *Adv. Drug Deliv. Rev.*, **2006**, 58, 1471
- 40 Tong, S.; Hou, S.; Zheng, Z.; Zhou, J.; Bao, G.; *Nano Lett.*, **2010**, 10, 4607

## CHAPTER 5

### COMPARISON OF THE MAGNETIC PROPERTIES OF BARE AND SURFACE COATED MAGNETITE NANOPARTICLES

#### 5.1 Introduction

As described in the first chapter, superparamagnetic particles are characterized by a maximum in the temperature variation of ac susceptibility and zero-field-cooled susceptibility measured in a small dc magnetic field. In the zero field cooled (ZFC) magnetic measurements, the sample is cooled to the lowest possible temperature in the absence of a magnetic field and measurements are made while heating the sample in the presence of a small dc magnetic field. The temperature at which a maximum is observed is at the superparamagnetic blocking temperature  $T_B$ . The shape of the zero-field-cooled magnetization curve is determined by the particle size, shape and size distribution. Thus, it is possible to have the same  $T_B$  for a fine particle system with wider or narrower size distributions but the shape of the curves will be different in the two cases; broader in one case and narrower in the other. Another measurement is called a field cooled (FC) magnetization measurement. In an FC measurement, a sample is cooled to the lowest possible temperature in the presence of a small magnetic field and measurements are made while cooling or heating in the same field after cooling. When the same sample is cooled under a magnetic field, the magnetization remains almost constant below the blocking temperature. Thus FC and ZFC magnetizations deviate below  $T_B$  and overlap when the temperature rises above  $T_B$ . Such temperature dependence of the ZFC magnetization and the divergence of ZFC and FC magnetizations below  $T_B$  are the characteristic features of superparamagnetism. Opening up of the magnetic hysteresis loop is also expected below the blocking temperature.

The characteristics of the field cooled (FC) magnetization curve depend on the nature of the interactions between the particles [1]. If the particles are well separated in a non-magnetic matrix or by proper surface coatings, the different types of interactions between the particles such as dipolar interactions or exchange interactions are suppressed. In this case, the FC magnetization continuously increases below  $T_B$  as the temperature is

decreased whereas the FC magnetization remains constant or decrease slightly below  $T_B$  depending on the strength of the interactions between the particles [2]. The dynamics of the nanoparticle systems are governed by the distribution of the relaxation times of the individual particles, arising from the particle size distribution.

The magnetic characteristics of the un-coated  $\text{Fe}_3\text{O}_4$  particles (see chapter 3) and that of the dextran coated and ascorbic acid coated particles (see chapter 4) are compared in detail to understand the changes that taking place when the  $\text{Fe}_3\text{O}_4$  nanoparticles are coated with dextran and ascorbic acid and to study the effect of inter-particle magnetic interactions in deciding the magnetic properties of the un-coated and coated magnetite nanoparticles. Details of these studies are described in the following sections.

## **5.2 Comparison of the magnetic properties before and after coating with dextran**

The ZFC and FC magnetization curves of the uncoated and dextran coated particles are shown in Figure 5.1. For the field cooled measurement, the sample is cooled from room temperature to 12 K in a magnetic field of 50 Oe and the magnetization is measured as a function of temperature in the same field while warming at a constant rate. For zero field cooled measurement, the sample is cooled to 12 K in zero magnetic field and then the magnetization is measured in a field of 50 Oe while warming. A maximum in the temperature variation of the ZFC magnetization is observed at 109 K for the uncoated particles and this temperature is shifted to 42 K after coating with dextran. The temperature at which a maximum in the ZFC magnetization is observed is at the superparamagnetic blocking temperature,  $T_B$ . Similarly, there are changes in the FC magnetization also after coating. For the uncoated particles, the FC magnetization decreases after going through a maximum as the temperature is decreased. In the case of the dextran coated particles, the FC magnetization is continuously increased as the temperature is decreased. This is evidence for coating of the nanoparticles and the changes are due to the decreased inter-particle magnetic interactions. The additional magnetic anisotropy arising from the inter-particle magnetic interactions and due to this,

the blocking temperature is decrease, as the anisotropy is directly proportional to the volume of the particles.

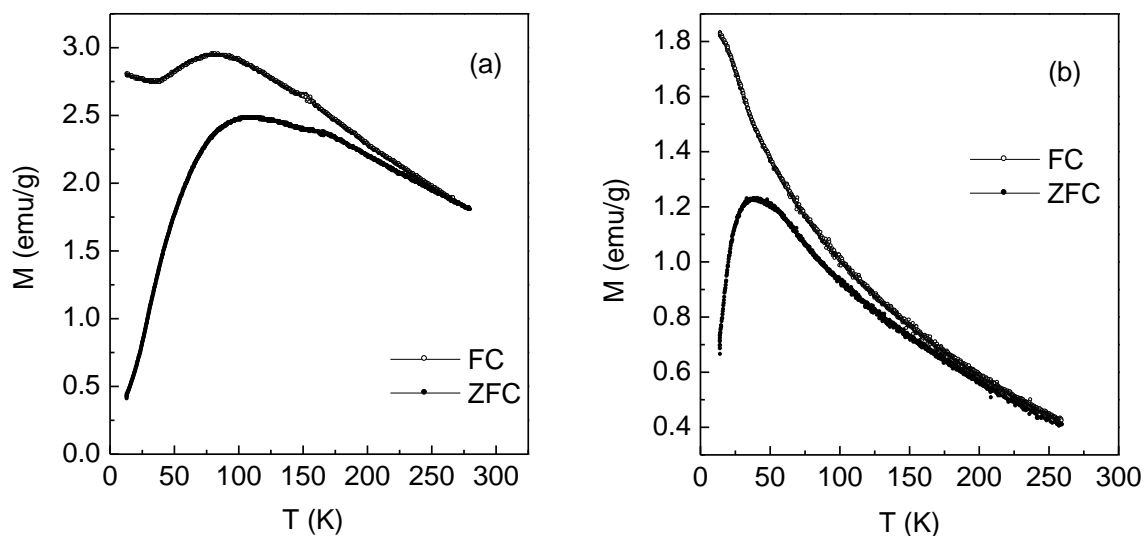


Figure 5.1 ZFC and FC magnetization curves of a) Fe1c and b) Fedx1

The magnetic field dependence of the magnetization at different temperatures for uncoated and dextran coated nanoparticles are shown in Figure 5.2 and Figure 5.3. The magnetization is almost saturated for the dextran coated sample, as compared to the uncoated sample. This is clearly evident from Figure 5.4 which compares the normalized magnetization curves of the two samples at 12 K. The coated particles show higher magnetization at lower fields, due to the lower anisotropy. The coercivity is also substantially decreased after coating. The coercivity is decreased by more than half after coating. The coercivities of the uncoated and coated samples, as a function of temperature are shown in Figure 5.5. There is considerable decrease in the coercivity of the dextran coated sample Fedx1 compared to that of the uncoated sample. This is again due to the decrease in the magnetic anisotropy contribution from inter-particle interactions.

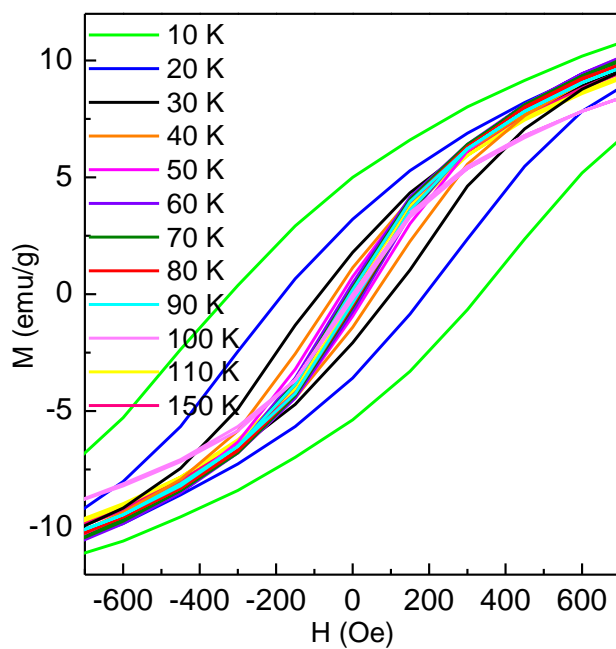
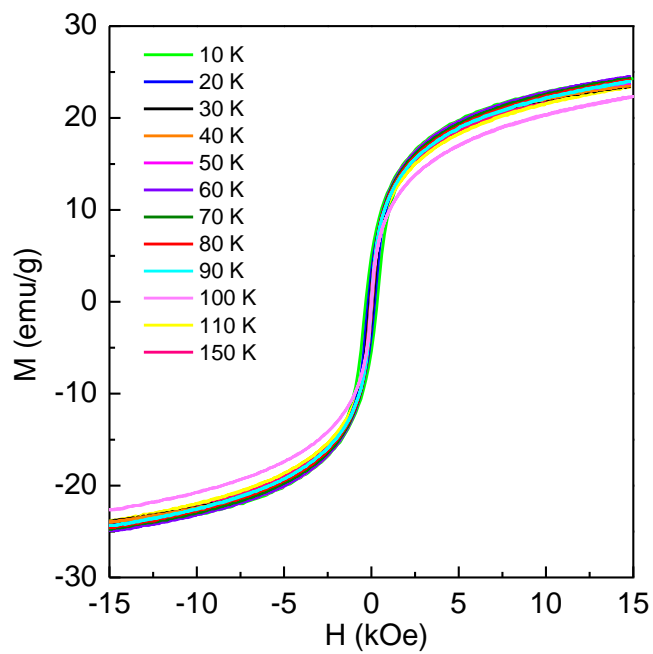


Figure 5.2 Magnetisation curves of Fe1 at different temperatures

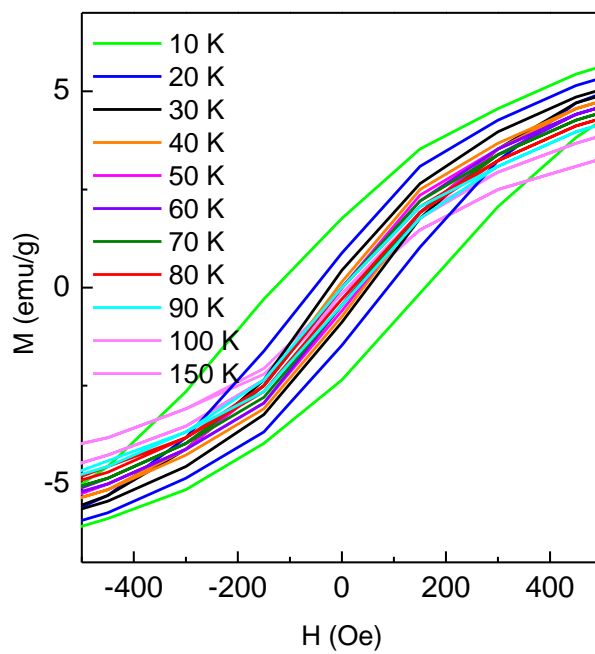
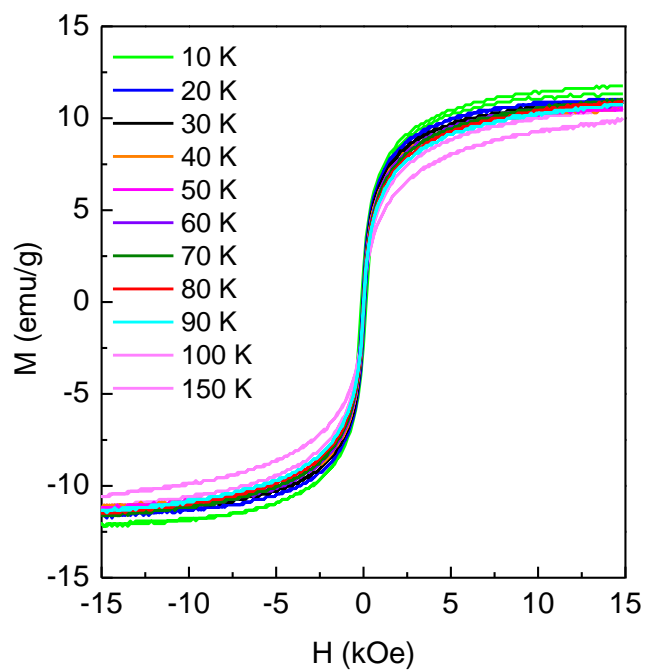


Figure 5.3 Magnetisation curves of Fedx1 at different temperatures.

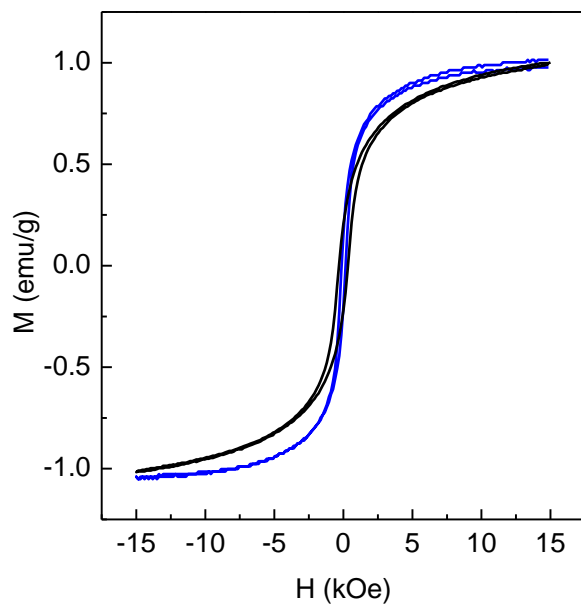


Figure 5.4. Normalized magnetization curves of Fe1 and Fedx1 at 12 K.

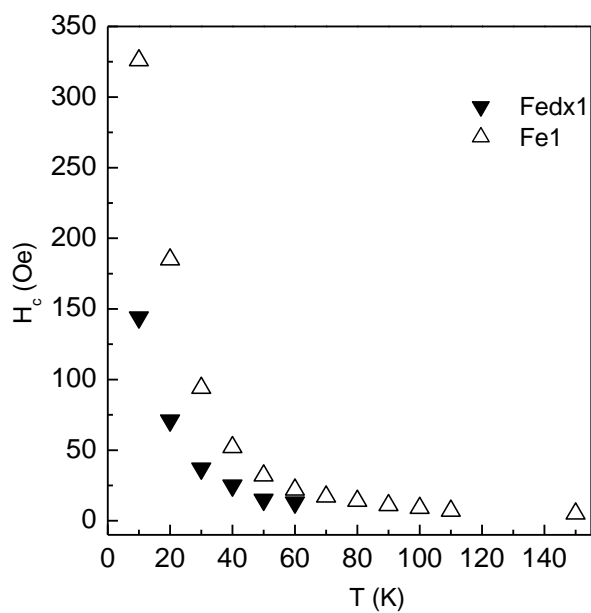


Figure 5.5. Temperature variation of coercivity of coated and uncoated magnetite nanoparticles.

There will be very strong inter-particle magnetic interactions between the particles when fine magnetic nanoparticles are densely packed. The strength of these inter-particle magnetic interactions depends on factors such as size and type of the particles, distance between the particles, surface characteristics, etc. [1]. These interactions are mainly due to dipolar and magnetic exchange interactions between the magnetic particles. Such magnetic interactions between the magnetic nanoparticles give rise to a collective behavior rather than the typical superparamagnetic behavior [3-7]. The random antiferromagnetic and/or ferromagnetic superexchange interactions between the adjacent particles give rise to magnetic frustration similar to that present in a spin glass. Therefore, the magnetic properties of such interacting magnetic nanoparticles give rise to superspin glass behavior because of the interaction between the individual single domain particles which are called superspins [2]. Because of these strong inter-particle interactions between the magnetic nanoparticles, such systems show a spin-glass-like magnetic state, which is commonly known as a superspin glass. The strong magnetic dipolar interactions are largely responsible for such superspin glass behavior. The collective dynamics in a superspin glass system give rise to magnetic relaxation and magnetic aging effects [2, 8-10]. It has been shown that aging and memory effects in a superspin glass are reflections of the interacting behavior of such nanoparticles. Field cooled (FC) and zero field cooled (ZFC) magnetization measurements have been widely used in aging experiments to evaluate the interacting nature of these nanoparticles [10–16].

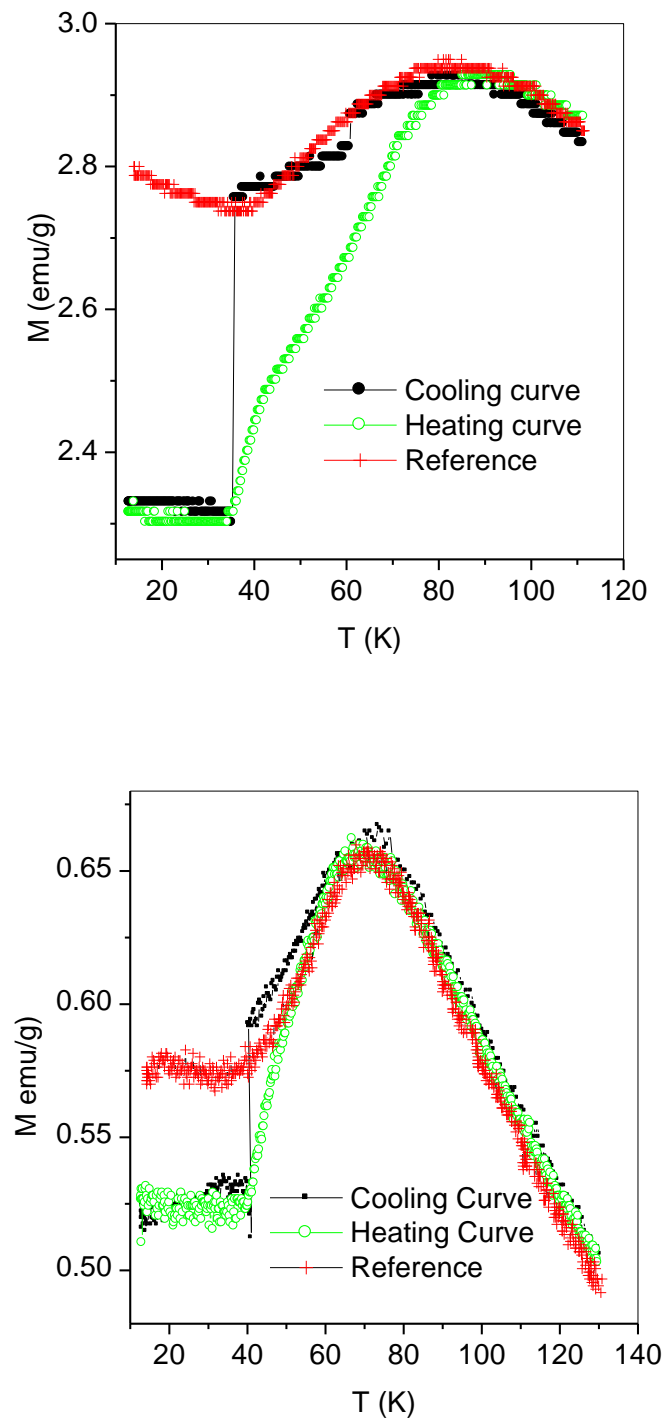


Figure 5.6. FC memory experiments of the un-coated  $\text{Fe}_3\text{O}_4$  nanoparticles Fe1c (left) and Fe3c (right) samples (see chapter 3). Original FC curve (red); Cooling curve with magnetic field switched off at a constant temperature (black); Heating curve in the same magnetic field while the field is on (green)

An important feature is reported for the field cooled magnetization (FCM) curve below  $T_B$ , for the interacting and non-interacting magnetic nanoparticles system. FCM either remains constant below  $T_B$  or slightly decreases after going through a maximum if the interaction between the magnetic nanoparticles is very strong. On the other hand, FCM slightly increases below  $T_B$  if interactions are very weak [12, 17] and a large increase in FCM is observed for non-interacting particles. In the present case, for all samples, the FCM goes through a maximum and then decreases, suggesting that the inter-particle magnetic interactions are very strong. The strength of these interactions also depend on the particle size. When the magnetic particle size is decreased, there will be more and more neighbouring particles in the vicinity of a given particle and therefore the overall strength of the inter-particle interactions will be enhanced. Therefore, a larger drop in the FCM below  $T_B$  can be expected for smaller particles. This is directly obvious in the case of Fe3c, shown in Figure 5.6, where the size of the particles is less than that of the sample Fe1c.

There are some features common to conventional spin glasses and interacting magnetic nanoparticles. These are the aging, rejuvenation and memory effects they exhibit [12,18-23]. To observe these characteristics, the magnetization is measured under field cooled conditions. The sample is initially cooled in the presence of a small external field, as in the case of FC magnetization measurements and the magnetic field is reduced to zero at some fixed temperatures below  $T_B$  [19, 24]. The field is again switched on and the sample is further cooled to the lowest temperature. The magnetization is recorded continuously during the cooling cycle. The sample is then warmed in the same external field while recording the magnetization. If experiments are conducted under such conditions, sharp memory effects are expected during the final heating in the case of typical spin glasses or interacting magnetic nanoparticles at temperatures where the system was allowed a waiting time in the absence of field.

Results of the memory experiment studies are shown in Figure 5.6 for Fe1c and Fe3c. The temperature dependence of the FC magnetization is measured during cooling under a  $H = 50$  Oe. In the case of Fe1c, the field is switched off ( $H = 0$  Oe) at 60 K while cooling

for a waiting time of 5000 s. This is the aging process. The magnetic field is then switched on to 50 Oe and the sample is cooled again, to a lower temperature of 36 K, where a minimum is observed in the original FC curve. The aging process is repeated at 36 K for the same waiting time. After this, the sample is cooled again to the lowest possible temperature after switching on the field. The magnetization is further recorded while heating back to room temperature after cooling to the lowest temperature. Similar experiments are conducted in the case of Fe<sub>3</sub>C also. The field is switched off at 40 K while cooling and sharp memory effect is observed at this temperature while warming up in a field of 50 Oe.

The cooling curves shown in Figure 5.6 show aging effects and very weak rejuvenation. Rejuvenation is the small increase or upturn in the magnetization while cooling when the field is again switched on after aging at 60 K and 36 K in the case of Fe<sub>1</sub>C and at 40 K for Fe<sub>3</sub>C. Also, sharp jumps in the magnetization, or memory effects, are observed at 36 K and 60 K for Fe<sub>1</sub>C and at 40 K for Fe<sub>3</sub>C, while warming up, as shown in Figure 3.16. These observations indicate the presence of strong interactions between the individual nanosized particles, leading to superspin glass characteristics [12]. Thus the magnetic properties of iron oxide nanoparticles are similar to that of a spin glass system due to magnetic interactions between the particles, instead of ideal superparamagnetism expected for non-interacting particles.

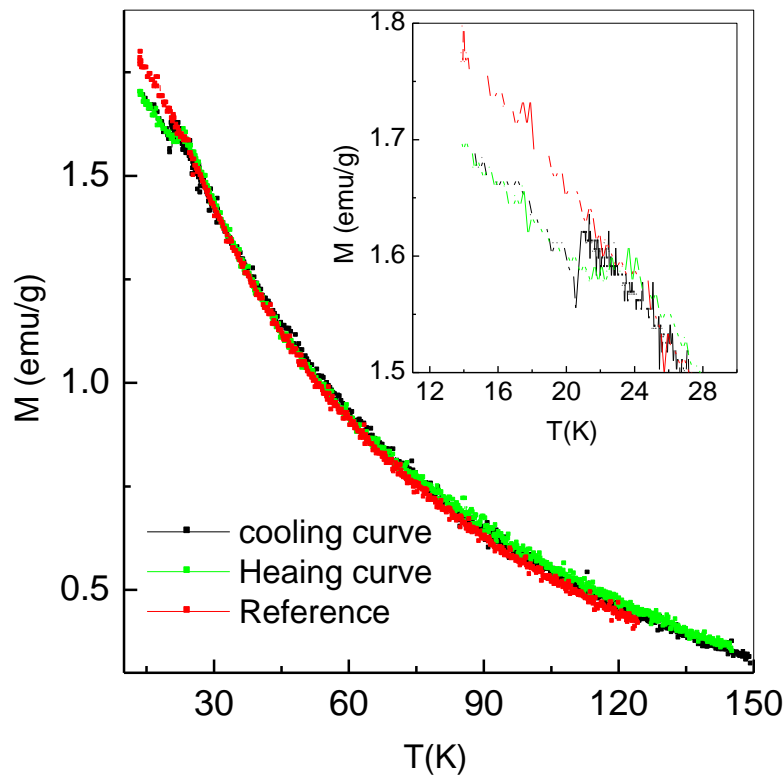


Figure 5.7 Memory effect studies on the dextran coated magnetite sample Fedx1.

The memory experiments on the dextran coated magnetite sample, Fedx1, are shown in Figure 5.7. The Fedx1 sample is derived from the uncoated sample Fe1c, whose memory characteristics are shown in Figure 5.6. The dynamics of the nanoparticle systems are governed by the distribution of the relaxation times of the individual particles, arising from the particle size distribution. If the particles are well separated by proper surface coatings, the different types of interactions between the particles such as dipolar interactions or exchange interactions are suppressed. In this case, the FC magnetization continuously increases below  $T_B$ . Very weak memory effect is observed when the FC magnetization is measured after the sample is cooled to the lowest temperature after the magnetic field is switched off at 20 K and a waiting time of 2 hrs at this temperature. Larger increase in the magnetization is observed after the waiting period, while cooling, when the field is switched on again. This larger rejuvenation is

another evidence for the decreased inter-particle interactions. Thus comparative studies on uncoated and dextran coated samples show that the uncoated sample behaves like a superspin glass system whereas the coated samples, due to the absence of inter-particle magnetic interactions, show ideal superparamagnetic properties, as reported in the literature [25,26].

### **5.3 Comparison of the Magnetic Behavior dextran coated powder and fluid samples**

Ferrofluid of dextran coated magnetite nanoparticles is prepared by dispersing 2 weight percent of the sample Fedx2 in water. This fluid was used for the magnetic studies. Usually, in a ferrofluid, there are two mechanisms for magnetization rotation. According to the Brownian mechanism [27,28] the magnetic moment is rotated together with the nanoparticle in the carrier liquid under the influence of an external magnetic field. On the other hand, in the Neel mechanism [27,28] the magnetic moment can rotate inside a nanoparticle. These two mechanisms of rotation are operative depending on the particle size and sometimes both mechanisms can take place simultaneously and the measured magnetic moment will be the effective one. The variation of magnetization, with an applied field, for both the powder and fluid samples shows no magnetic hysteresis; that is, both the remnance and coercivity are zero (Figure 5.8). This indicates superparamagnetic behaviour as expected for nanoscale dimension of the particles. The magnitude of magnetization, calculated for per gram of the coated sample present in the fluid and the powder sample are comparable, suggesting that there is not much decrease in the anisotropy when the coated nanoparticles are dispersed in water. That is, for the powder sample itself, the coating is very effective to suppress the inter-particle interactions and there is no effect on the dilution of the sample by dispersion in water.

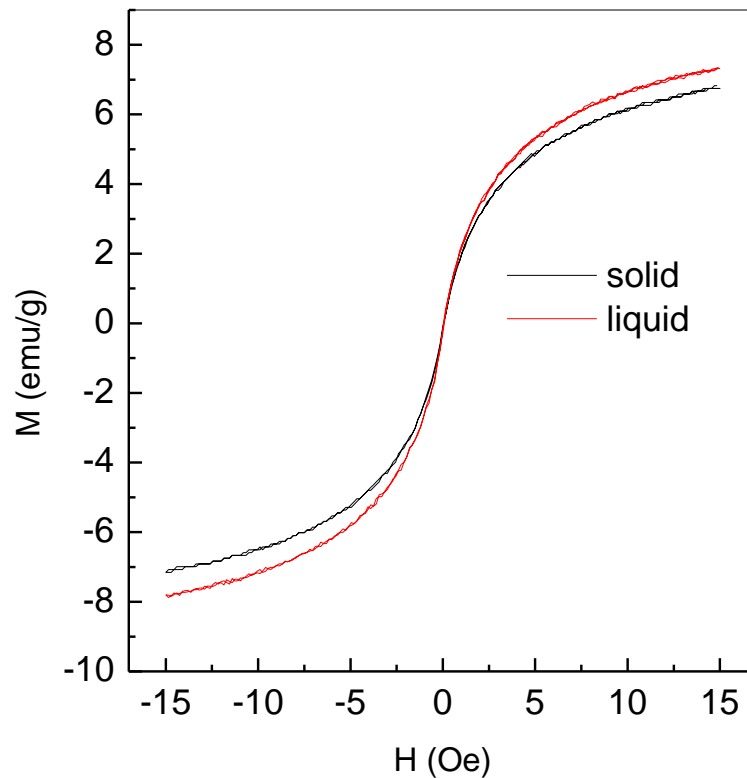


Figure 5.8 Field dependence of magnetisation of dextran coated magnetite samples (Fedx2) in the form of powder and fluid.

Results of the ZFC and FC magnetization measurements of the dried powder and fluid samples are shown in figure 5.9. The characteristic blocking temperature for both samples are at 24 K indicating that dextran is perfectly coated on the surface of iron oxide nanoparticles. Similarly, the fluid sample show almost identical memory and relaxation behavior compared to that of the dextran coated powder sample, as shown in Figure 5.10. Comparison of the magnetization of the powder and fluid samples is shown in Figure 5.11. Both samples show almost identical behavior, with not much change in the coercivity, except for the diamagnetic contribution in the fluid sample, at higher fields.

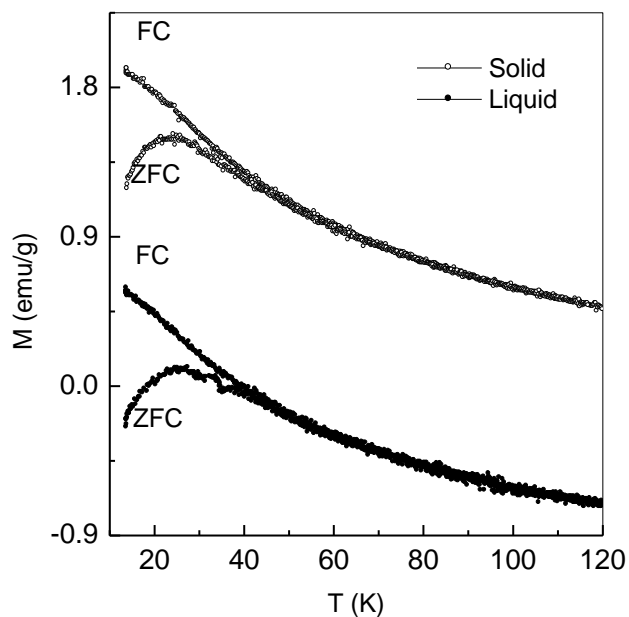


Figure 5.9 ZFC and FC magnetization curves of dextran coated magnetite samples (Fedx2) in the form of powder and fluid in water.

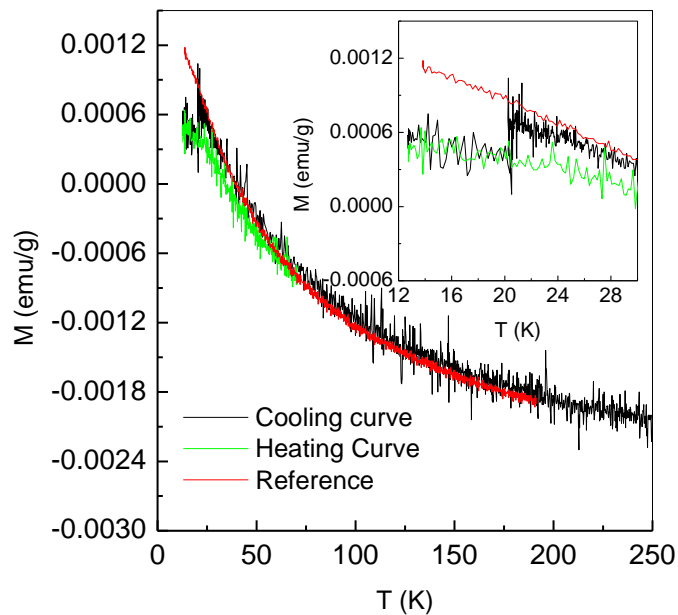


Figure 5.10 Memory effect studies on the dextran coated magnetite sample in the fluid form Fedx2.

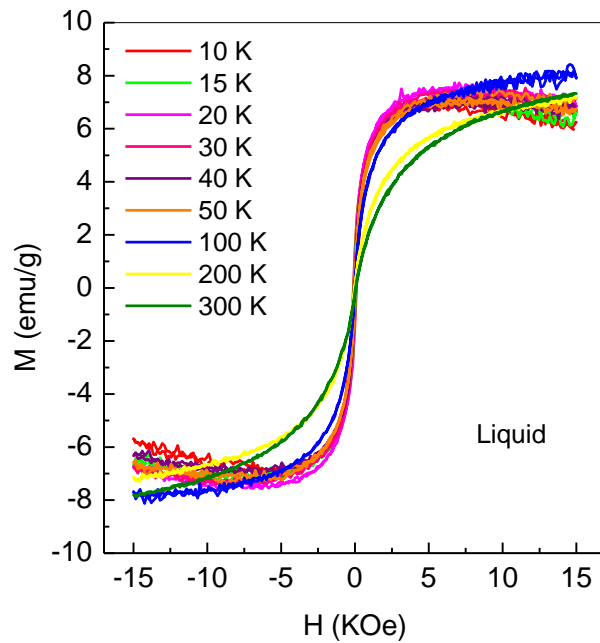
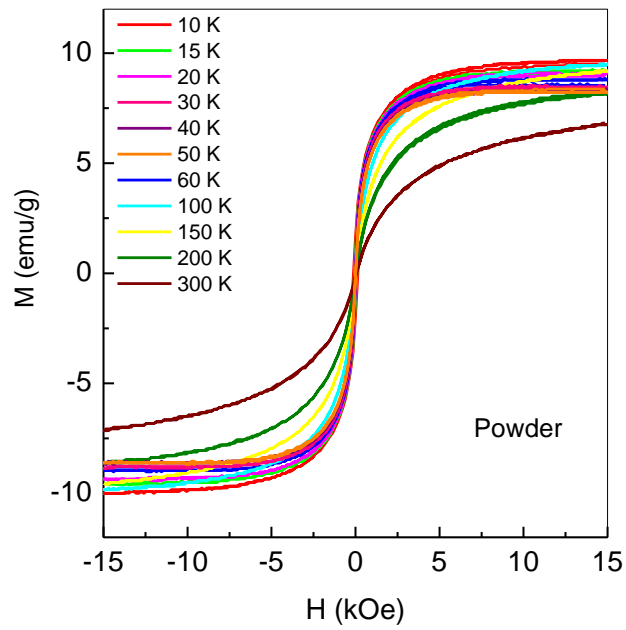


Figure 5.11 Magnetization as a function of magnetic field for the dextran coated magnetite nanoparticles (Fedx2), measured at different low temperatures, a) in the powder form and b) as fluid.

#### 5.4 Comparison of the magnetic properties before and after coating with ascorbic acid

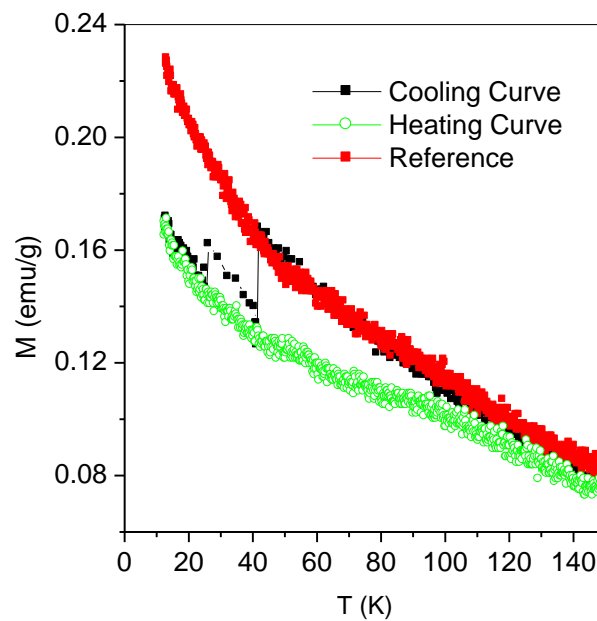
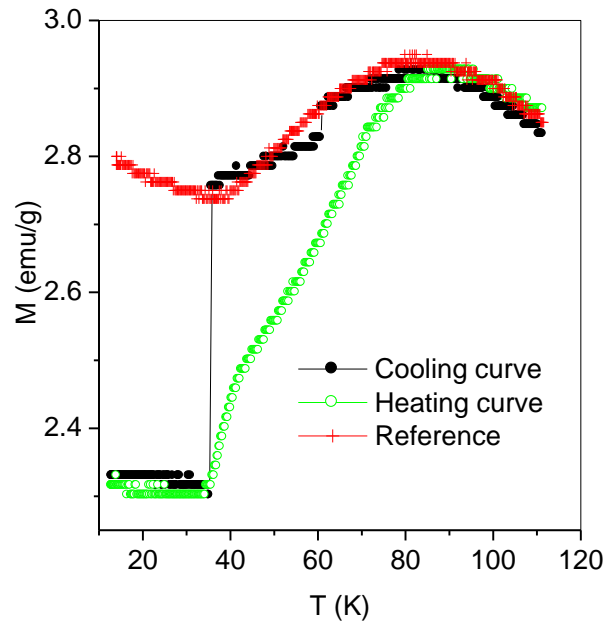


Figure 5.12 FC memory experiments of Fe<sub>1c</sub> (top) and FeAc<sub>2</sub> (bottom) samples. Original FC curve (red); Cooling curve with magnetic field switched off at a constant temperature (black); Heating curve in the same magnetic field while the field is on (green)

Figure 5.12 shows the comparison of the memory experiments on the uncoated and ascorbic acid coated samples. The characteristics of the uncoated sample are described in the previous section. Double memory experiment has been carried in both cases. The ascorbic acid coated sample shows rejuvenation effect after field is switched on from  $H=0$  while cooling. Also, no memory is observed while warming the sample back, at the temperatures where the field was switched off while cooling. Strong memory effect is observed for the uncoated sample. This again shows the ideal superparamagnetic characteristic of the coated sample, compared to the superspin glass behavior of the bare sample due to inter-particle magnetic interactions.

## 5.5 Conclusions

The magnetic properties of uncoated and that of dextran coated as well as ascorbic acid coated  $\text{Fe}_3\text{O}_4$  nanoparticles have been compared by performing field dependent and temperature dependent magnetization measurements. Higher magnetization at lower fields, continuously increasing magnetization below the blocking temperature, shift of the blocking temperature to lower temperatures after coating, etc., are found to be evidences for effective coating of the nanoparticles by dextran as well as ascorbic acid. These changes also suggest decreased inter-particle magnetic interactions due to the effective coating. For the coated powder and fluid samples, similar magnetic characteristics are observed. Relaxation and aging studies have been performed to understand the effect of coating. The uncoated nanoparticles show superspin glass behavior whereas superparamagnetic nature is observed for the coated nanoparticles.

---

**References**

- 1 Parker, D.; Ladieu, F.; Vincent, E.; Meriguet, G.; Dubois, E.; Dupuis, V.; Perzynski, R., *J. Appl. Phys.* **2005**, 97, 10A502.
- 2 Dormann, J.L.; Fiorani, D.; Tronc, E.; *Adv. Chem. Phys.* **1997**, 98, 283
- 3 Luo, W.; Nagel, S.R.; Rosenbaum, T.F.; Rosenweig, R.E., *Phys. Rev. Lett.* **1991**, 67, 2721
- 4 Djurberg, C.; Svedlindh, P.; Nordblad, P.; Hansen, M. F.; Bodker, F.; Morup, S., *Phys. Rev. Lett.* **1997**, 79, 5154
- 5 Fiorani, D.; Dormann, J.; Cherkaoui, R.; Tronc, E.; Lucari, F.; D’Orazio, F.; Spinu, L.; Nogues, M.; Garcia, A.; Testa, A.M.; *J. Magn. Magn. Mater.* **1999**, 196
- 6 Hellman, F.; Queen, D. R.; R.M. Potok and B.L. Zink, *Phys. Rev. Lett.* **2000**, 84, 5411.
- 7 Poddar, P.; Telem-Shafir, T.; Fried, T.; Markovich, G., *Phys. Rev. B*, **2002**, 66, 060403.
- 8 Jonsson, T.; Mattson, J.; Djurberg, C.; Khan, F.A.; Nordblad, P.; Svedlindh, P.; *Phys. Rev. Lett.* **1995**, 75, 4138.
- 9 S. Sahoo, O. Petravic, W. Kleemann, P. Nordblad, S. Cardoso and P.P. Freitas, *Phys. Rev. B*, **2001**, 67, 214422.
- 10 Jonsson, P.E., *Adv. Chem. Phys.* **2004**, 128, 191
- 11 Sun, Y.; Salamon, M.B.; Garnier, K.; Averbach, R.S., *Phys. Rev. Lett.* **2003**, 91, 67206.
- 12 Sasaki, M.; Jonsson, P.E.; Takayama, H.; Mamiya, H., *Phys. Rev. B*, **2005**, 71, 104405.
- 13 Parker, D.; Ladieu, F.; Vincent, E.; Meriguet, G.; Dubois, E.; Dupuis, V.; Perzynski, V., *J. Appl. Phys.*, **2005**, 97, 10A502.
- 14 Zheng, R.K.; Gu, H.; Xu, B.; Zhang, XX., *Phys. Rev. B*, **2005**, 72, 014416.
- 15 Tsoi, G.M.; Wenger, L.E.; Senaratne, U.; Tackette, R.J.; Bue, E.C.; Naik, R.; Vaishnava, P.P.; Naik, V., *Phys. Rev. B*, **2005**, 72, 014445.
- 16 Dormann, J.L.; Bessais, L.; Fiorani, D.; *J. Phys. C.: Solid State Phys.*, **1988**, 21, 2015.

- 
- 17 Zysler, R.D.; Fiorani, D.; Testa, A.M., *J. Magn. Magn. Mater.*, **2001**, 224, 5
  - 18 Vincent, E.; Bouchaud, J.P.; Hammann, J.; Lefloch, F., *Phil. Mag. B*, **1995**, 71, 489.
  - 19 Jonason, K.; Vincent, E.; Hammann, J.; Bouchaud, J.P.; Nordblad, P., *Phys. Rev. Lett.* **1998**, 81, 3243.
  - 20 Dupuis, V.; Vincent, E.; Bouchaud, J.P.; Hammann, J.; Ito, A.; Katori, H.A., *Phys. Rev. B*, **2001**, 64, 174204.
  - 21 Mathieu, R.; Jonsson, P.E.; Nordblad, P.; Katori, H. A.; Ito, A., *Phys. Rev. B*, **2001**, 65, 012411.
  - 22 Zotev, V.S.; Rodriguez, G.F.; Kenning, G.G.; Orbach, R.; Vincent, E.; Hammann, J., *Phys. Rev. B*, 2003, 67, 184422.
  - 23 Bert, F.; Dupuis, V.; Vincent, E.; Hammann, J.; Bouchaud, J.P.; *Phys. Rev. Lett.* 2004, 92, 167203.
  - 24 Mydosh, J.A., *Spin Glasses: An Experimental Introduction*, Taylor & Francis, Singapore, **1993**
  - 25 Cótica, L. F.; Santos, I. A.; Giroto, E. M.; Ferri, E. V.; Coelho, A. A., *J. Appl. Phys.*, 2010, 108, 064325
  - 26 Kim, M. J.; Choa, Y. H.; Kim, D. H.; Kim, K. H., *IEEE Trans. Magn*, 2009, 45, 2446
  - 27 Dormann, J. L.; Fiorani, D., (Eds.) *Magnetic Properties of Fine Particles*, North-Holland, Amsterdam, **1992**
  - 28 Odenbach S. (ed.) *Ferrofluids*, Springer, Berlin, **2002**

## CHAPTER 6

### SOLID STATE NMR STUDIES ON NANOCRYSTALLINE ALUMINATE SPINELS

#### 6.1 Introduction

Among the spinel-type oxides having the general formula  $AB_2O_4$ , ferrites,  $AFe_2O_4$ , are important oxides having many technological applications [1]. Because of the presence of Fe in different oxidation states such as  $Fe^{2+}$  and  $Fe^{3+}$  with many unpaired electrons, these materials are magnetic and generally they show ferrimagnetic properties at room temperature. Because of their peculiar electrical and magnetic properties and high Curie temperatures, the spinel-type ferrites are used for many high-frequency applications. The important properties of the spinel ferrites, such as magnetic and electrical properties, based on which the materials are used for different applications, are governed by the distribution of the cations A and Fe in the tetrahedral and octahedral sites of the spinel lattice. Apart from the general parameters controlling the distribution of the ions in the two crystallographic sites, the crystal field stabilization energy (CFSE) also determines the site preference of the different transition metal ions [2]. For example, in  $ZnFe_2O_4$ , the  $Zn^{2+}$  ions are always located in the tetrahedral sites, so that this ferrite is a normal spinel and not magnetic at room temperature, whereas in the case of  $NiFe_2O_4$ , the CFSE is less for  $Ni^{2+}$  in the octahedral coordination, and therefore, the ferrite forms an inverse spinel arrangement. Apart from all of these factors, the preparation and processing conditions also decide the cationic distribution [3].

There are numerous studies reported in the recent literature on nanometer-sized particles of different ferrites. The importance of these studies is to understand the effect of finite size on the different properties of the ferrites [4,5], apart from the many potential applications. Ferrite nanoparticles [6,7] are potentially important in many areas, such as biomedical applications as contrast enhancement agents for magnetic resonance imaging [8], magnetically mediated hyperthermia [9], magnetic carriers for targeted drug delivery [10], catalysis [11], and so forth. Decreasing the particle size increases the surface area-to-volume ratio so that the number of ions on the surface will be more than that in the bulk for very small particles. This is likely to

change the coordination behavior at the surface of the particles [12,13]. Also, it is possible that the cationic distribution will be different in the nanoparticles as compared to that in the bulk. Therefore, decreasing the size of the ferrite particles to nanometer range will strongly influence the magnetic properties of this class of materials. This is because, the strength of the magnetic exchange interactions are mainly determined by the A-O-Fe angle and the nature of the A ion. If the coordination and number of A and Fe ions at the surface of the nanoparticles are different from that in the bulk, then considerable changes in the magnetic properties are expected. From many studies, it has been shown that unusual cation distributions in the octahedral and tetrahedral sites can be obtained in ferrite nanoparticles, so that normal ferrites become mixed ferrites, as in the case of  $\text{ZnFe}_2\text{O}_4$  [14,15], or there is an enhancement in the Curie temperature, as observed in the case of  $\text{MnFe}_2\text{O}_4$  [16],  $\text{NiFe}_2\text{O}_4$  [17], and  $\text{Ni}_{0.5}\text{Zn}_{0.5}\text{Fe}_2\text{O}_4$  [18]. The degree of distribution of the Fe ions in the ferrites, in the bulk as well as in the nanoparticle form, can be determined from Mössbauer spectroscopic studies [19]. However, Mössbauer spectroscopic studies do not give accurate estimation of the degree of distribution of the Fe ions in the tetrahedral and octahedral sites of the ferrite nanoparticles, due to the broad nature of the spectral features. Few recent Mössbauer studies indicated the presence of more than two different sites in the ferrite nanoparticles [20,21]. Also, no structural studies can give information on the local surface coordination in the nanoparticles.

Solid state NMR is an important tool to get information on local structural variations [22,23]. However, it is difficult to analyze magnetic materials using NMR because the signal is usually broad and weak at room temperature, and high external magnetic fields are required at low temperatures to resolve the various hyperfine components [24,25]. One of the options is to synthesize nanoparticles of a nonmagnetic model compound having similar structure as that of the ferrites and study its structural characteristics using solid state NMR and then extrapolate the results to magnetic spinels. However, it may be noted that the extrapolation of the NMR results from nonmagnetic to magnetic spinels may not be that straightforward because there are other factors, such as the ionic radii and charge of the cations, crystal field stabilization energy which is cation dependent, etc., which control the local disorder as well as cation distribution in the tetrahedral and octahedral sites in the spinel lattice. Two spinel-type nonmagnetic oxides, magnesium aluminate

( $\text{MgAl}_2\text{O}_4$ ) and zinc aluminate ( $\text{ZnAl}_2\text{O}_4$ ) are selected for such studies as the  $^{27}\text{Al}$  nuclei can be easily probed by NMR studies. The intention is to study the effect of the two different A ions,  $\text{Mg}^{2+}$  and  $\text{Zn}^{2+}$ , whose ionic sizes are different, which influences the site preference in the spinel lattice.

## 6.2 Solid State NMR Studies on $\text{MgAl}_2\text{O}_4$ Nanoparticles

One of the suitable candidates for the NMR study is magnesium aluminate,  $\text{MgAl}_2\text{O}_4$ , which is the original spinel. In this case,  $^{27}\text{Al}$  nuclei can be easily probed by solid-state NMR. Previous studies have shown that  $\text{MgAl}_2\text{O}_4$  has partially inverse spinel structure [26,27]. The disordered behavior of bulk  $\text{MgAl}_2\text{O}_4$  and the deviation of the structural parameters as a function of temperature have been studied by solid-state NMR [28], X-ray diffraction [29], neutron diffraction [30], ESR [31], and electrical conductivity measurements [32]. A recent  $^{27}\text{Al}$  MAS NMR study, on  $\text{MgAl}_2\text{O}_4$  precursor powders of very high specific surface area synthesized at low temperatures, has reported the presence of a five-coordinated Al site apart from the octahedral and tetrahedral Al coordinated sites [33]. Presence of five coordinated Al sites is also observed after irradiation of bulk  $\text{MgAl}_2\text{O}_4$  and  $\text{ZnAl}_2\text{O}_4$  with Kr ions and this has been assigned to amorphization [34]. A change in the inversion parameter is observed after irradiation. The effects of particle size on the degree of distribution of Al and the distorted coordination environments have not been studied so far. In this chapter, we describe a systematic study on the local structural variations in the spinel as a function of the particle size.

### 6.2.1 Synthesis of $\text{MgAl}_2\text{O}_4$ nanoparticles

$\text{MgAl}_2\text{O}_4$  nanoparticles were synthesized by the glycine-nitrate combustion method [44]. The starting materials,  $\text{Al}(\text{NO}_3)_3 \cdot 9\text{H}_2\text{O}$  (Merck Fine, AR),  $\text{Mg}(\text{NO}_3)_2 \cdot 6\text{H}_2\text{O}$  (Aldrich Chemicals), and glycine (Merck Fine, AR), were used as-received without further purification. Normally, a metal-to-glycine ratio of 1:2 is used for the combustion synthesis of oxides using glycine. However, decreasing the amount of glycine reduces the flame temperature during combustion and, hence, the particle size of the resulting oxide [35, 36]. Stoichiometric amounts of magnesium nitrate and aluminum nitrate, in the 1:2 molar ratio and 0.25 moles of glycine per mole of metal ion were used for the synthesis. 4.75 g of magnesium nitrate, 13.93 g of

aluminum nitrate, and 1.04 g of glycine were individually dissolved in minimum amounts of distilled water and the individual solutions were mixed together in a large beaker. The final mixed solution was slowly evaporated on a water bath to form a honey-like viscous gel. The gel was then placed on a hot plate at 200 °C, and this allowed a rapid combustion reaction. During the reaction, ignition took place, resulting in a dry, white, and very fragile foam that easily crumbled into powder. The resulting powder was divided into several portions and annealed at 400, 600, 800, 1000, 1200, and 1400 °C. The powder samples annealed at these temperatures are labeled as MA1, MA2, MA3, MA4, MA5, and MA6, respectively. The sample codes and the corresponding particle sizes are given in Table 6.1.

Table 6.1. Sample codes, annealing Temperatures, and the particle sizes obtained from XRD and TEM

Sample code	Annealing temperature (°C)	Lattice parameter (Å)	Particle size	
			TEM (±0.2 nm)	XRD (±1 nm)
MA1	400	8.1(1)	3	
MA2	600	8.1(1)	5	
MA3	800	8.0815(7)		18
MA4	1000	8.0831(5)		32
MA5	1200	8.0855(4)		60
MA6	1400	8.0871(4)		98

### 6.2.2 Powder XRD Analysis

All of the samples were initially characterized by powder X-ray diffraction to confirm the formation of magnesium aluminate and to compare the particle sizes after annealing at different temperatures. Figure 6.1 shows the powder XRD patterns of  $\text{MgAl}_2\text{O}_4$  annealed at different temperatures. The simulated powder XRD pattern of  $\text{MgAl}_2\text{O}_4$  is shown in Figure 6.1 (a) for comparison. The XRD pattern is simulated using the computer program PowderCell [37] for windows, with the unit cell lattice parameter  $a = 8.086 \text{ \AA}$ . For the samples annealed at 400 °C (MA1) and 600 °C (MA2), only few and broad reflections are observed. This is due to the nanoparticle nature of the samples and overlapping of the group of reflections in the same  $2\theta$  region [38]. It is known that when the crystallite size decreases, the peaks are broadened and the intensities of the peaks decrease. Also, when nanoparticles are heated at higher temperatures, the individual particles grow in size at the expenses of others [39]. The positions of the two most intense reflections (311) and (440) are comparable to that of the bulk material for MA1. For MA2, the (400) reflection is clearly resolved, indicating an increase in the particle size. For the sample annealed at 800 °C, all of the reflections are clearly resolved and all of the observed reflections correspond to that of magnesium aluminate.

However, still all of the reflections are broad when compared to the sample annealed at 1400 °C. For the samples annealed above 600 °C, the intensities and positions of the different peaks observed in the experimental pattern are consistent with the simulated pattern. There are no additional peaks observed in the XRD patterns, indicating the absence of any impurities. This confirms the formation of single-phase  $\text{MgAl}_2\text{O}_4$  by the present method of synthesis. For all of the samples, the XRD peaks are very broad, and the broadness decreases and the intensities of the peaks increase with increasing annealing temperature. The decreasing broadness with increasing intensities of the peaks indicates increasing crystallite size.

The average crystallite size is calculated using the Scherrer formula,  $D = 0.9\lambda/\beta\cos\theta$ , where  $D$  is the crystallite size,  $\lambda$  is the wavelength of X-rays,  $\beta$  is the full width at half-maximum of the individual peaks, and  $\theta$  is the Bragg angle [40]. The crystallite size is calculated after correcting for the contribution from instrumental

broadening,  $\beta = \beta_{\text{obs}} - \beta_{\text{inst}}$ , where  $\beta_{\text{obs}}$  is the observed line width and  $\beta_{\text{inst}}$  is the instrumental contribution to line width. Apart from the contribution due to instrumental line broadening, strain is also another factor contributing toward broadness of the diffraction peaks. The contribution from strain is corrected using the Williamson–Hall analysis,  $\beta \cos\theta = 0.9\lambda/D + 4\varepsilon \sin\theta$ , where  $\varepsilon$  is the strain. The contribution from strain is found to be very low ( $<0.2\%$ ). Due to the extreme broadness and overlapping of the reflections for the samples MA1 and MA2, their crystallite sizes could not be calculated from the XRD data. Crystallite sizes are calculated for the remaining samples and the calculated average crystallite sizes are shown in Table 6.1. Hereafter, the average crystallite size is considered as the particle size while comparing the results of different samples annealed above 600 °C.

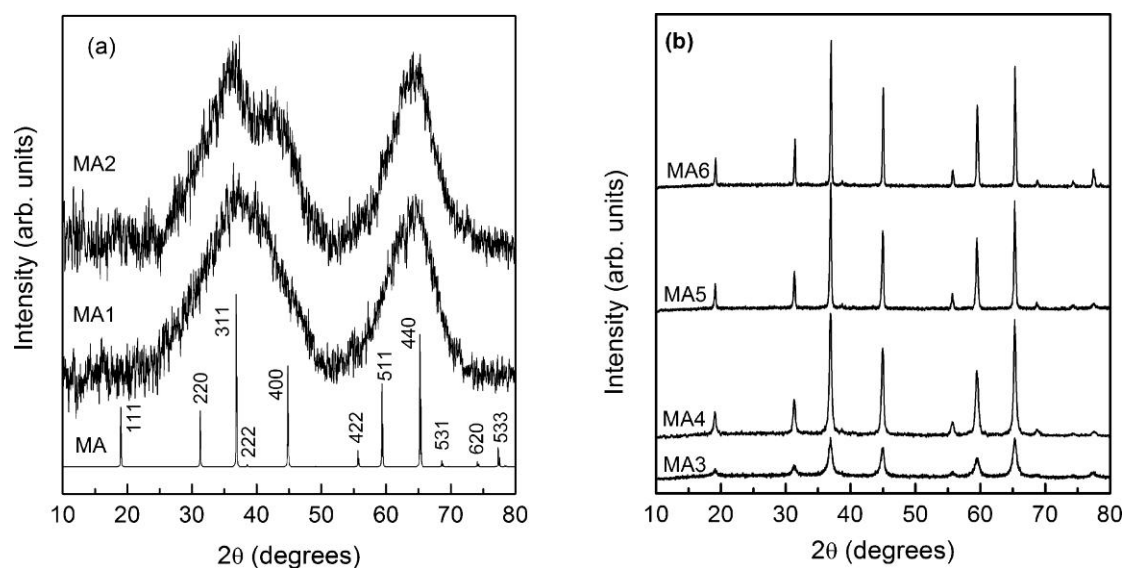


Figure 6.1. Power XRD patterns of  $\text{MgAl}_2\text{O}_4$  nanoparticles annealed at different temperatures, MA1 – 400 °C, MA2 – 600 °C, MA3 – 800 °C, MA4 – 1000 °C, MA5 – 1200 °C, MA6 – 1400 °C. The simulated pattern of  $\text{MgAl}_2\text{O}_4$  (MA) is shown and indexed for comparison.

$\text{MgAl}_2\text{O}_4$  crystallizes in the face centered cubic crystal system with space group  $Fd\bar{3}m$ . The cubic cell parameter is obtained by least-squares refinement of the diffraction pattern using the computer program PowderCell [41] for windows. The lattice parameter could not be calculated for the samples MA1 and MA2 due to the broad nature and overlapping of the peaks. However, from the  $d$  values of the (311) and (440) reflections, the lattice parameter is obtained as 8.1 Å, which is very close to

the value for the bulk material (8.086 Å). The calculated values are given in Table 6.1. For the sample annealed at 1400 °C, the cubic cell parameter is comparable to that reported in the literature for MgAl<sub>2</sub>O<sub>4</sub> (JCPDS PDF # 21-1152). The lattice parameter is slightly lower for the sample annealed at 800 °C (MA3) and increases with increasing crystallite size toward the bulk value.

### 6.2.3 TEM Analysis

The average particle sizes of MA1 and MA2 are obtained from TEM studies. TEM micrographs of the samples annealed at 400 °C (MA1) and 600 °C (MA2) are shown in Figure 6.2. Very small particles of average size of 3 nm are clearly seen in the TEM micrograph. The inset in Figure 6.2 shows the electron diffraction pattern from the particles. The pattern is highly diffused and showing rings indicating the polycrystalline nature of the fine particles. For the sample annealed at 600 °C, the average particle size is obtained as 5 nm from the TEM measurements.

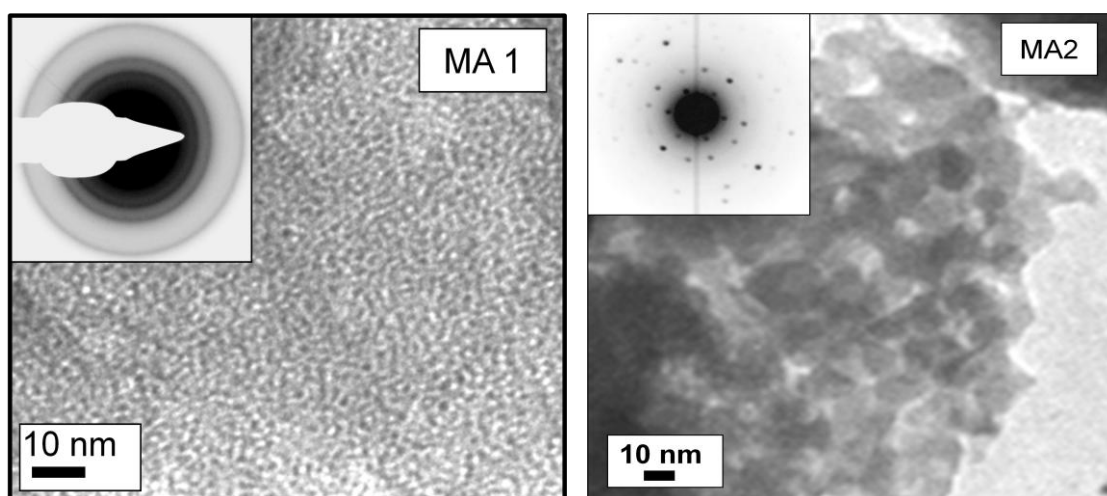


Figure 6.2. Transmission electron micrograph of the sample annealed at 400 °C (MA1) and 600 °C (MA2). The inset shows the corresponding electron diffraction pattern.

### 6.2.4 Solid state NMR studies

The objective of the <sup>27</sup>Al MAS NMR experiment was to resolve and calculate relative populations of the different Al co-ordination environments. The <sup>27</sup>Al MAS spectra of all the samples are shown in Figure 6.3 and Figure 6.4. Figure 6.3 shows the spectra recorded at a field of 7.04 T (AV 300 spectrometer) with a spinning speed of 12.5 kHz and Figure 6.4 shows the spectra recorded at a field of 11.7 T (AV 500

spectrometer) with a spinning speed of 34.1 kHz. The spectra contain a central region composed of three to four main resonances and a set of spinning sidebands of the central transition ( $-1/2, 1/2$ ) and the satellite transitions ( $\pm 3/2, \pm 1/2$ ). The outer satellite transition ( $\pm 5/2, \pm 3/2$ ) is not observed. In the case of the spectra at 7.04 T, the sidebands overlap the central transition since the spread of the central transition region is more than the sample spinning frequency of 12.5 kHz. Therefore, it was necessary to record the spectra at a higher spinning speed. A 2.5 mm probe capable of spinning with higher frequency was available only on a spectrometer with a higher field of 11.7 T (AV 500) and the spectra were recorded on this spectrometer at a spinning speed of 34.1 kHz. In Figure 6.4, the spinning sidebands are well separated from the central transition, and it is possible to extract quantitative information from these spectra. The dipolar interaction and the chemical shift anisotropy, which are of the order of a few kHz, are averaged out by the fast magic-angle spinning. Therefore, the line width of the central transition is due to the second-order quadrupolar interaction and the distribution in the isotropic chemical shift.

For the samples MA1 and MA2 with particle size  $<10$  nm, there are two main resonances observed in the range of 70–80 and 10–20 ppm and an additional broad resonance in the range of 40–50 ppm. For bulk  $\text{MgAl}_2\text{O}_4$  (MA6), only two major resonances are observed in the 70–80 and 10–20 ppm regions. These two resonances are characteristic of Al in 4-fold ( $\text{Al}_{\text{IV}}$ ) and 6-fold ( $\text{Al}_{\text{VI}}$ ) coordinations in  $\text{MgAl}_2\text{O}_4$  [42]. MA3 clearly shows the contributions from the  $\text{Al}_{\text{IV}}$  and the  $\text{Al}_{\text{VI}}$  sites and also a broad shoulder in the 40–50 ppm region. However, a shoulder at  $\sim 0$  ppm appears on the right-hand side of the  $\text{Al}_{\text{VI}}$  resonance peak of MA3, in Figure 6.3. The intensity of the second  $\text{Al}_{\text{VI}}$  peak increases with increasing particle size. Also, a broadening is observed at the right-hand side of  $\text{Al}_{\text{VI}}$  resonance peak in MA1 and MA2. Although the second peak is not observed in Figure 6.4, this feature is observed as an additional broadening on the right side of the  $\text{Al}_{\text{VI}}$  resonance peak. All of the resonances have broad asymmetric line-shape with a steep low-field edge and a trailing high-field edge. These shapes arise due to a distribution of the electric field gradient (EFG) at the aluminum site which leads to a distribution in the quadrupolar coupling constants.

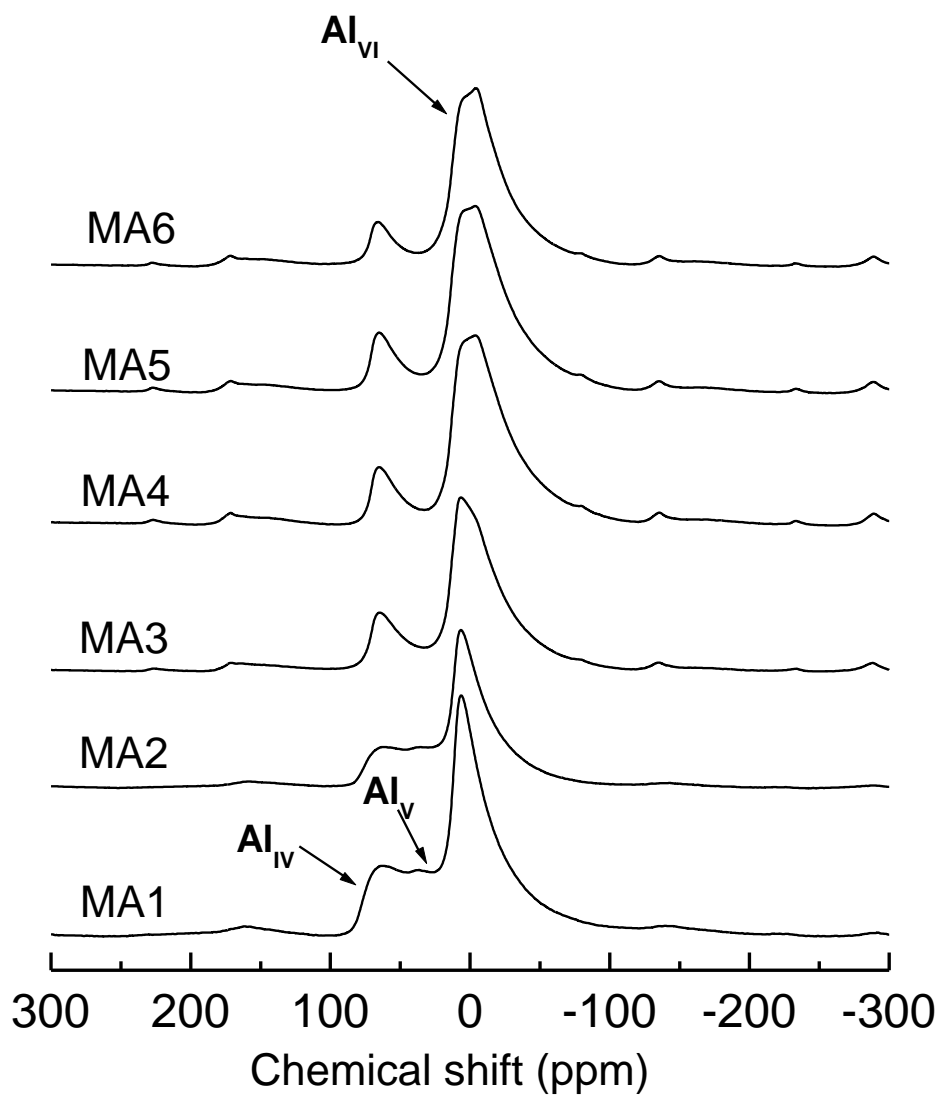


Figure 6.3.  $^{27}\text{Al}$  MAS NMR spectra of  $\text{MgAl}_2\text{O}_4$  of different particle sizes, recorded on AV300 spectrometer at a sample spinning speed of 12.5 kHz. The sample codes are defined in Table 6.1.

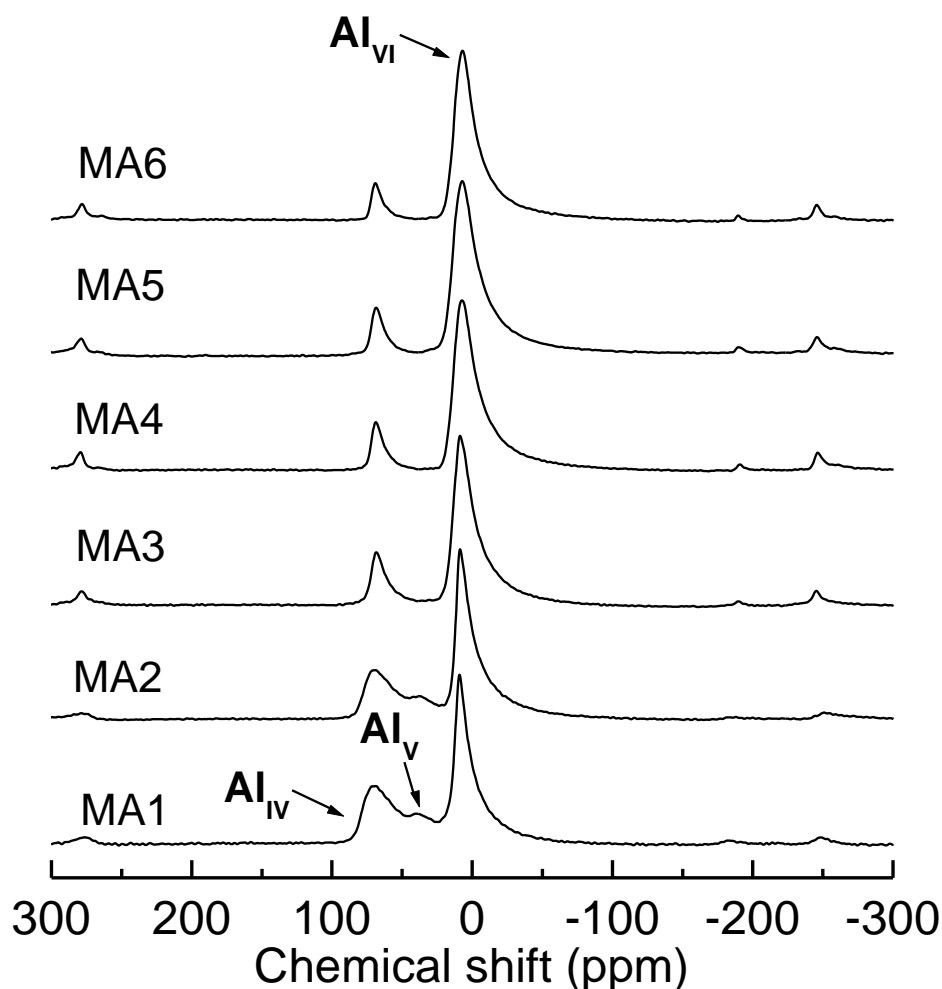


Figure 6.4.  $^{27}\text{Al}$  MAS NMR spectra of  $\text{MgAl}_2\text{O}_4$  of different particle sizes, recorded on AV500 spectrometer at a sample spinning speed of 34.1 kHz. The sample codes are defined in Table 6.1.

The observed NMR spectral features showing dependence on particle size clearly indicate that the coordination environment of Al in the spinel changes with particle size when the particles are of nanometer size. A resonance peak in the range of  $\sim 40$  ppm is reported for barium aluminum glycolate as well as andalusite [43] and rapidly quenched aluminosilicate glasses [44] and has been assigned to Al in 5-fold coordination. It has been reported that five-coordinated Al can be identified by a resonance peak at  $\sim 35$  ppm [45], midway between the resonance peaks for four coordinated and six coordinated Al, from NMR spectroscopy. In the case of ball-

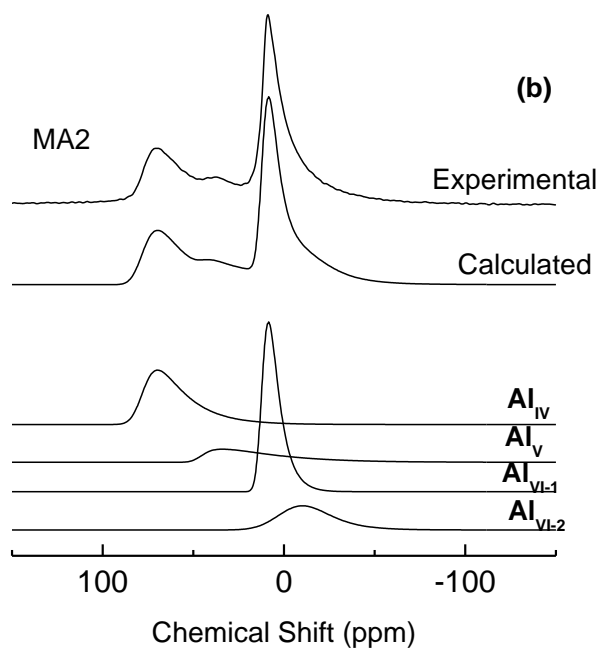
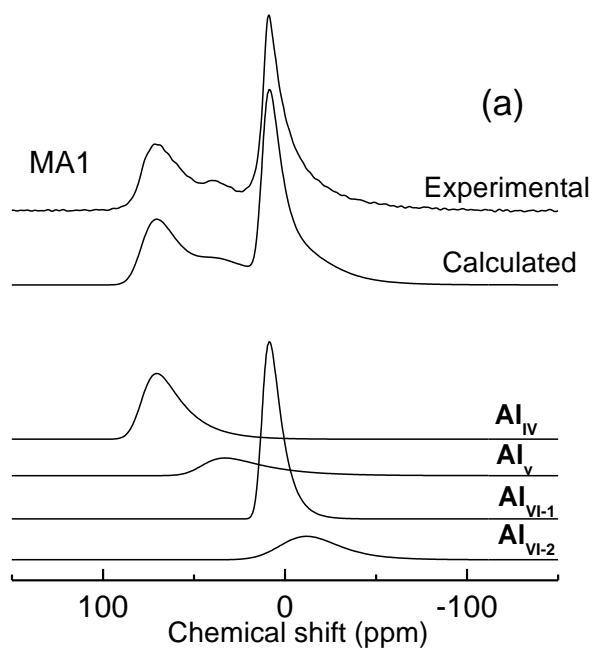
milled mullite [46], where the particle size is decreased on ball milling, it has been shown that Al in 5-fold coordination appears for smaller particles and the peak intensity for Al in 5-fold coordination increases with decreasing particle size. This is also associated with a decrease in the intensities of peaks due to tetrahedral and octahedral coordinated Al. The broad resonance peak at ~40 ppm is previously observed for low-temperature synthesized magnesium aluminate powders with very high specific surface area and this peak is assigned to aluminum in 5-fold coordination. Therefore, the new resonance peak observed at ~40 ppm for the smaller particles can be assigned to aluminum in the 5-fold coordination ( $Al_V$ ) which is not observed for bulk  $MgAl_2O_4$ . For the sample MA3, the peak due to  $Al_V$  is not clearly visible. However, this sample shows a broad feature in the 40–50 ppm region, and therefore, it can be assumed that  $Al_V$  coordination is also present in this sample in lesser amounts. A second octahedral Al peak in the region of –10–0 ppm is reported in the previous  $^{27}Al$  MAS NMR studies on quenched bulk, as well as ball milled  $MgAl_2O_4$  [42] due to the changes in the inversion parameter. The second peak observed at ~0 ppm can be assigned to the contribution from an additional octahedral site.

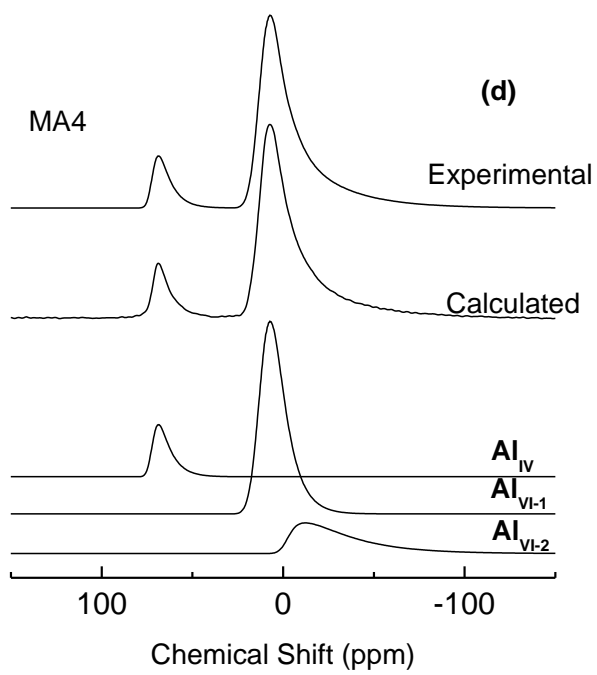
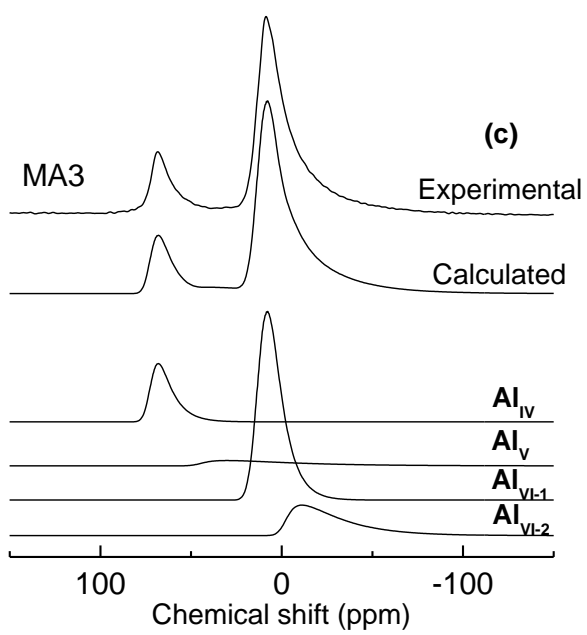
To estimate whether there is any change in the degree of distribution of the cations present in the spinel, with increasing particle size, apart from the changes in the contributions from the 5-fold and second 6-fold coordination environments, the line shapes of the experimental spectra (from AV 500 spectrometer) have been simulated. The integrated intensities of each line and the relative intensities of the different co-ordination environments are calculated from the simulated spectra. Figure 6.5 shows the simulated spectra of MA1, MA2, MA3, MA4, MA5 and MA6. Simulating the exact spectra is difficult since there is distribution of the isotropic chemical shift as well as a distribution in the quadrupolar coupling constants which arise from electric field gradient (EFG) at the site of the observed nucleus. Neuville et al. [47] have shown that, for glassy systems containing aluminum, which has a distribution of quadrupolar coupling constants, the Gaussian isotropic model (GIM) of the Czjck distribution is the simplest and physically consistent. In this model, the EFG is assumed to follow a statistical disorder and the probability of a given  $C_Q$ ,  $\eta_Q$  pair [called the quadrupolar product  $C_Q^* = C_Q(1 - \eta_Q^2)^{1/2}$ , where  $C_Q$  is the quadrupolar coupling constant, and  $\eta_Q$  is the asymmetry parameter] can be computed.

The  $C_Q^*$  characterizes the EFG or the quadrupolar tensor which depends on a single parameter that is related to the quadratic mean of the quadrupolar product.

The GIM distribution function has been incorporated into the DMFIT computer program developed by Massiot et al. [48], and this program is used for the line shape simulations. The line shape fitting procedure is as follows: The fitting is started from approximate line shape with guess parameters for isotropic shift (iso), the distribution of isotropic chemical shift ( $\delta_{\text{iso}}$ ) and the quadrupole product  $C_Q^*$  and then followed by iteration of the  $C_Q^*$  and iso,  $\delta_{\text{iso}}$  and the amplitude to get a good match between the experimental and the simulated spectra. Comparison of the experimental and the simulated spectra for the samples MA1, MA2, MA3, MA4, MA5 and MA6 is shown in Figure 6.5.

It can be seen that there is a very good match between the experimental and the simulated spectra. This procedure is repeated many times and was carried out on the spectra of all the samples and the results are summarized in Table 6.2. The distribution of Al in the different co-ordination environments is shown in Figure 6.6. Important observations from the fitted data shown in Table 6.2 and Figure 6.6 are that (i) the intensity of the peak from  $\text{Al}_V$  decreases with increasing particle size and this peak is not observed for larger particles (>18 nm); (ii) there is a corresponding increase in the intensity of  $\text{Al}_{VI(2)}$  peak and the intensity of this peak becomes almost constant for larger particles; and (iii) the intensity of the resonance peak due to  $\text{Al}_V$  decreases with increasing particle size, and there is a corresponding increase in the intensity of the peak due to  $\text{Al}_{VI(1)}$ .





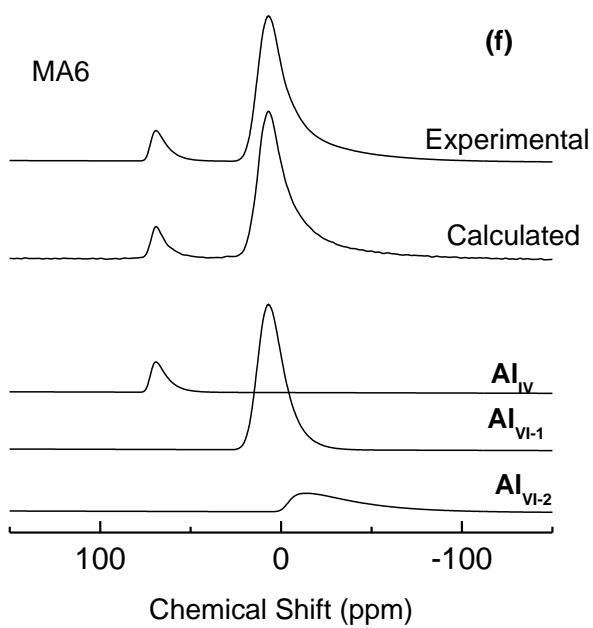
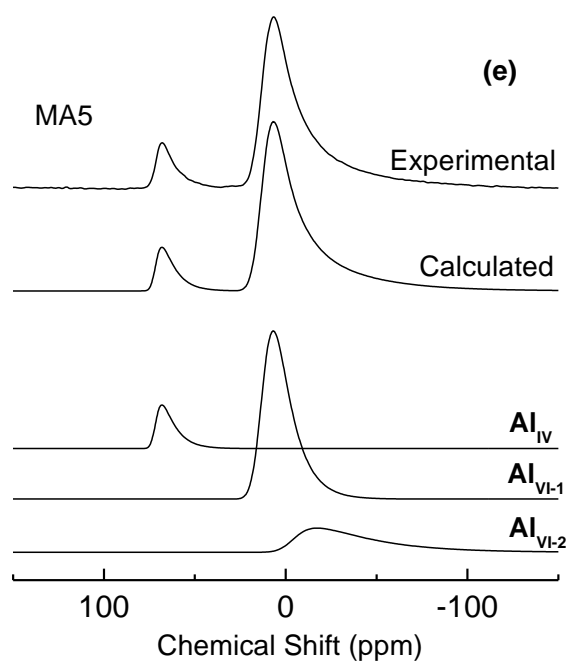


Figure 6.5. Experimental and calculated  $^{27}Al$  MAS NMR spectra for the samples (a) MA1 (b) MA2, (c) MA3, d) MA4, (e) MA5 and (f) MA6. The bottom traces show the separate components for the different aluminum coordinations.

Although the  $Al_V$  peak is not clearly visible in the spectra of the sample MA3, a comparison of the simulated spectra clearly indicated this feature for this sample. The presence of  $Al_V$  can be attributed to the fact that the size of the particles in the samples MA1, MA2, and MA3 are very small (<18 nm). As the surface-to-volume ratio increases with decreasing particle size, the  $Al_V$  contributions are likely to come from the surface. This is possible because decreased coordination environment is expected at the surface of the particles. The five-coordinated Al is likely to be formed on the surface due to the distortion of the octahedral coordinated sites from oxygen vacancies. This assumption is further supported by the decreased contribution from this five-coordinated surface Al species with increasing particle size. Presence of five-coordinated Al sites has been recently reported in swift heavy ions irradiated bulk  $MgAl_2O_4$  [34]. It has been concluded that these five-coordinated Al sites are associated with amorphous structures and they are considered as structural defects. In the present case also, it is possible that such amorphous structures are present on the surface of the  $MgAl_2O_4$  particles synthesized by the combustion method, giving rise to reduced coordination.

If the  $Al_V$  species is formed at the surface due to the distortion of the octahedral coordination, then there are equal chances for a distorted tetrahedral coordination at the surface, leading to 3-fold coordinated  $Al_{III}$  species. There are few reports in the literature on the observation of three-coordinated Al in the  $^{27}Al$  NMR spectra [49] of some aluminosilicates and this is directly confirmed [50] from Al K-edge XANES measurements. The NMR resonance peak due to the  $Al_{III}$  species is observed at a slightly higher chemical shift value when compared to that of the  $Al_{IV}$  species or as a broadening of the  $Al_{IV}$  peak [51].  $^{27}Al$  NMR signal is very sensitive to the coordination environment around the Al atom and this is usually reflected in the line width. The normalized NMR spectra of MA1, MA2, and MA3 (the intensities are normalized with respect to the  $Al_{VI}$  as well as the  $Al_{IV}$  peaks) are compared in Figure 6.7. It can be seen that there are no shifts in the peak positions of  $Al_{VI}$  and  $Al_{IV}$ . However, the  $Al_{IV}$  peak is broader on the left side for MA1 and MA2 and this contribution is disappeared in the spectra of MA3. This is concomitant with the changes in the spectral intensity of the  $Al_V$  peak indicating that the broader  $Al_{IV}$  resonance peaks of MA1 and MA2 might include contribution from  $Al_{III}$  species also.

Table 6.2. NMR Parameters Obtained from the  $^{27}\text{Al}$  MAS Experiments, Using the DMFIT Program

Sample code	Al site	<sup>a</sup> $\delta_{\text{iso}}$ (ppm)	<sup>b</sup> $d_{\text{CSA}}$ (ppm)	<sup>c</sup> $C^*_Q$ (MHz)	Distribution (%)	<sup>d</sup> Inversion Parameter
MA 1	Al <sub>IV</sub>	79.6	10.6	6.6	34.1	0.68
	Al <sub>V</sub>	46.7	9.6	9.2	19.1	
	Al <sub>VI-1</sub>	13.1	6.5	3.8	34.9	
	Al <sub>VI-2</sub>	0.9	8.2	6.0	11.8	
MA 2	Al <sub>IV</sub>	78.7	9.2	6.5	29.1	0.58
	Al <sub>V</sub>	46.8	9.2	8.9	11.2	
	Al <sub>VI-1</sub>	12.1	6.5	3.9	41.6	
	Al <sub>VI-2</sub>	-0.8	9.2	7.0	17.9	
MA 3	Al <sub>IV</sub>	72.8	8.1	4.2	16.3	0.33
	Al <sub>V</sub>	46.2	9.3	8.8	4.7	
	Al <sub>VI-1</sub>	13.3	9.4	4.2	58.2	
	Al <sub>VI-2</sub>	-1.1	9.4	7.8	20.7	
MA 4	Al <sub>IV</sub>	72.5	7.5	3.6	11.8	0.24
	Al <sub>VI-1</sub>	12.9	10.5	4.3	64.1	
	Al <sub>VI-2</sub>	-1.1	7.5	7.9	23.9	
MA 5	Al <sub>IV</sub>	72.0	6.5	3.8	11.3	0.23
	Al <sub>VI-1</sub>	13.4	10.5	4.6	65.7	
	Al <sub>VI-2</sub>	-2.4	8.5	8.3	22.9	
MA 6	Al <sub>IV</sub>	72.6	5.8	3.8	10.1	0.20
	Al <sub>VI-1</sub>	12.6	10.5	4.3	67.8	
	Al <sub>VI-2</sub>	-2.5	6.0	8.3	22.0	

<sup>a</sup> Isotropic chemical shift, <sup>b</sup> Width of Gaussian distribution, <sup>c</sup> Quadrupolar product.

<sup>d</sup> Inversion parameter is calculated assuming that Al<sub>V</sub> is derived from Al<sub>VI</sub> due to decreased coordination on the surface of the particles. The errors in the various parameters are estimated from the reproducibility of the simulation process as described in ref 34.

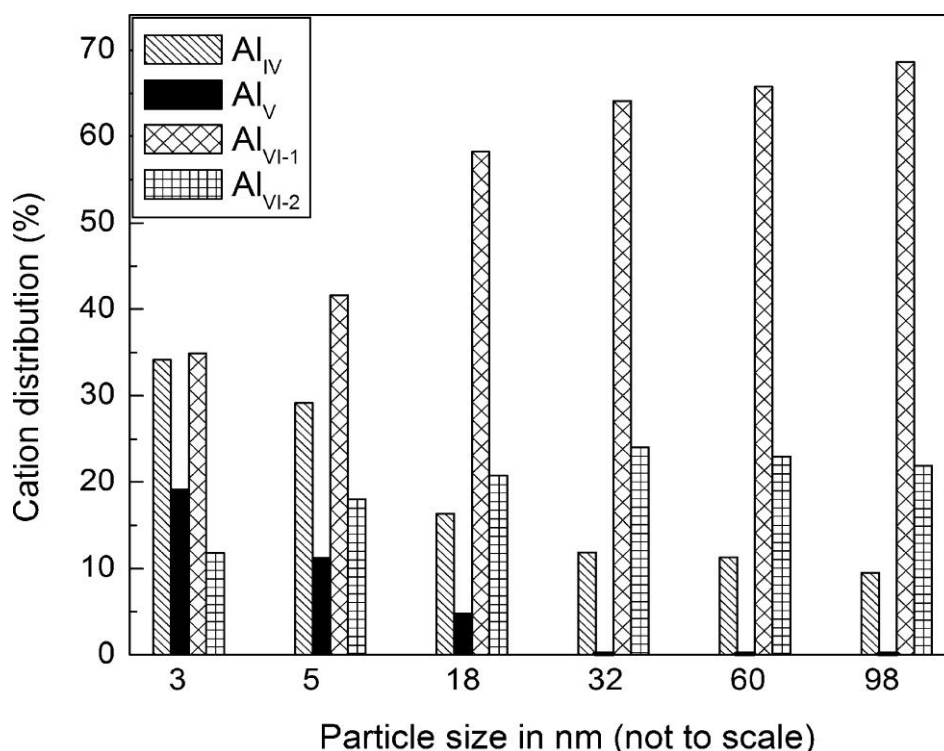


Figure 6.6. Cation distribution in  $\text{MgAl}_2\text{O}_4$  nanoparticles obtained from fitting the  $^{27}\text{Al}$  MAS NMR spectra, plotted as a function of particle size. Note that the  $x$ -axis is not to scale.

Observation of a second  $\text{Al}_{\text{VI}}$  peak for larger particles is of further interest. From Table 6.2 and Figure 6.6, it can be seen that the contribution of the  $\text{Al}_{\text{VI}}$  species initially increases and becomes almost constant as the particle size is increased (for MA4 to MA6). A similar but exactly reverse trend in the distribution of Al in the tetrahedral sites is observed. These results can be explained on the basis of a scenario of local structural distortion. It is possible that the second  $\text{Al}_{\text{VI}}$  peak is likely to be due to local structural distortions in the octahedral sites. The  $\text{AlO}_6$  octahedra adjacent to the larger  $\text{Mg}^{2+}$  cations will be more distorted than the ones away from the  $\text{Mg}^{2+}$  ions. When the inversion parameter is decreased (less number of  $\text{Mg}^{2+}$  ions in the octahedral site), the relative number of such distorted octahedral sites will be more in the lattice as compared to the case of higher amount of inversion. Similar feature due to the isotropic chemical shift of the second octahedral Al peak in the region of  $-10$ – $0$  ppm is reported in the previous  $^{27}\text{Al}$  MAS NMR studies on bulk  $\text{MgAl}_2\text{O}_4$  [27]. It has been reported that the intensity of the second  $\text{Al}_{\text{VI}}$  peak increases when bulk  $\text{MgAl}_2\text{O}_4$  is heated at increasing temperatures and quenched to room temperature [27]. It has been concluded that cation disorder affects the local coordination

environments of both the 4- and 6-coordinated Al atoms. Further, it was shown that every cation exchange to the tetrahedral site causes 5- to 6-fold increase in the intensity of  $\text{Al}_{\text{IV}}$  peak. This is explained based on the fact that six adjacent edge-sharing octahedra are affected by the cation exchange between Al and Mg ions. Although the observation of a splitting of the  $\text{Al}_{\text{VI}}$  peak is not commented, a decrease in the intensity of a second peak with decreasing inversion parameter is observed for  $\text{MgAl}_2\text{O}_4$  after ball milling.

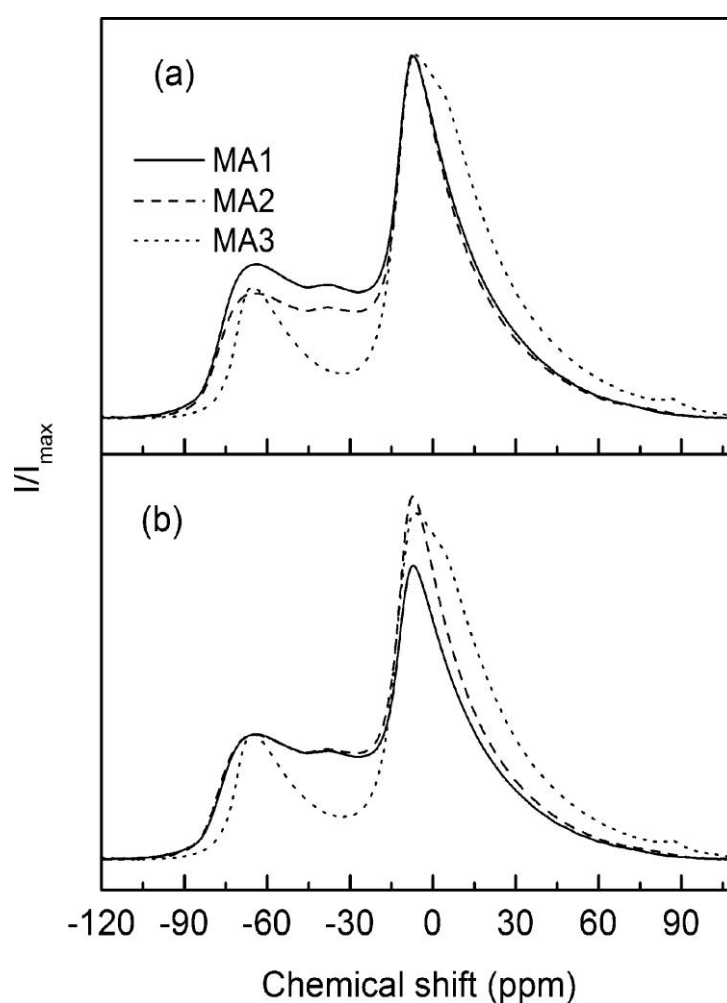


Figure 6.7. Normalized AV300  $^{27}\text{Al}$  MAS NMR spectra of the  $\text{MgAl}_2\text{O}_4$  samples MA1, MA2, and MA3. The intensities are normalized with respect to the (a)  $\text{Al}_{\text{VI}}$  as well as the (b)  $\text{Al}_{\text{IV}}$  peaks.

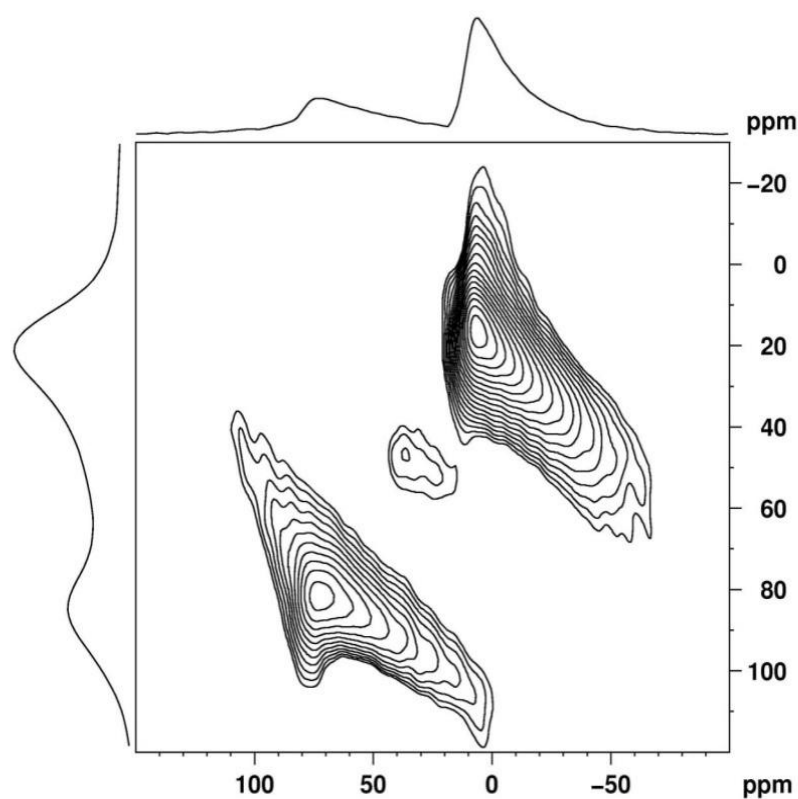


Figure 6.8. MQMAS NMR of MA2 (600 °C heated sample)

The spectrum of the MA-2 sample, which is heated at 600 °C contains all the three sites corresponding to the  $Al_{IV}$ ,  $Al_V$  and  $Al_{VI}$  as confirmed by MAS experiment. This is also confirmed by the MQMAS spectrum (figure 6.8) which clearly shows the presence of all the three sites. The presence of the  $Al_V$  can be attributed to the fact that the particle size of this sample is very small (<10 nm) thus increasing the surface to volume ratio and the  $Al_V$  contributions are coming from the surface. This is possible because decreased coordination environment is expected at the surface of the particles.

### 6.3 Solid State NMR Study on ZnAl<sub>2</sub>O<sub>4</sub> Nanoparticles

ZnAl<sub>2</sub>O<sub>4</sub> is a normal spinel with Zn<sup>2+</sup> in the tetrahedral site and Al<sup>3+</sup> ions occupied in the octahedral site. However, it has been reported that bulk ZnAl<sub>2</sub>O<sub>4</sub> has very small amount of inversion [52]. It is well known catalyst for various reactions like transesterification of vegetable oils [53], combustion of trichloroethylene [54], dehydrogenation of alkenes [55], etc. Similarly, optical properties of ZnAl<sub>2</sub>O<sub>4</sub> are widely studied [56]. NMR studies on ZnAl<sub>2</sub>O<sub>4</sub> reported that the preparation method has profound influence on the inversion parameter of zinc aluminate nanoparticles. [57, 58]. In the present work, the main focus is to explore the particle size dependence of the Al coordination environment in zinc aluminate nanoparticles. We have synthesized zinc aluminate nanoparticles by the glycine-nitrate combustion method and the samples are annealed at various temperatures for getting particles of different sizes.

#### 6.3.1 Synthesis

ZnAl<sub>2</sub>O<sub>4</sub> nanoparticles were synthesized by the glycine-nitrate combustion method. The starting materials, Al(NO<sub>3</sub>)<sub>3</sub>·9H<sub>2</sub>O (Merck Fine, AR), Zn(NO<sub>3</sub>)<sub>2</sub>·6H<sub>2</sub>O (Aldrich Chemicals), and glycine (Merck Fine, AR), were used as-received without further purification. Stoichiometric amounts of zinc nitrate and aluminum nitrate, in the 1:2 molar ratio and 0.25 moles of glycine per mole of metal ion were used for the synthesis. 5.49 g of zinc nitrate, 13.93 g of aluminum nitrate, and 1.04 g of glycine were individually dissolved in minimum amounts of distilled water and the individual solutions were mixed together in a large beaker. The final mixed solution was slowly evaporated on a water bath to form a honey-like viscous gel. The gel was then placed on a hot plate at 200 °C, and this allowed a rapid combustion reaction. During the reaction, ignition took place, resulting in a dry, white, and very fragile foam that easily crumbled into powder. The resulting powder was divided into several portions and annealed at 400, 450, 500, 600, 800, and 1000 °C. The powder samples annealed at these temperatures are labeled as ZA1, ZA2, ZA3, ZA4, ZA5, and ZA6, respectively. The sample codes and the corresponding particle sizes are given in Table 6.3

Table 6.3. Sample codes, annealing temperatures, and the particle sizes obtained from XRD and TEM

ZnAl <sub>2</sub> O <sub>4</sub>				
Sample Code	Annealing temperature (°C)	Lattice parameter (Å)	Particle size	
			TEM (±0.2 nm)	XRD (±1 nm)
ZA1	400	8.106	10	9
ZA2	450	8.089		21
ZA3	500	8.113	20	24
ZA4	600	8.089		44
ZA5	800	8.094		89
ZA6	1000	8.085		100

### 6.3.2 PXRD analysis

The powder XRD patterns ZnAl<sub>2</sub>O<sub>4</sub> samples annealed at different temperatures are shown in Figure 6.9. For the heated samples the intensities and positions of the different peaks observed in the experimental pattern are consistent with the simulated pattern. This confirms the formation of single-phase ZnAl<sub>2</sub>O<sub>4</sub> by the present method of synthesis. For all of the samples, the XRD peaks are very broad, and the broadness decreases and the intensities of the peaks increase with increasing annealing temperature. The decreasing broadness with increasing intensities of the peaks indicates increasing crystallite size. The crystallite size of zinc aluminate particles formed at 400 °C is 9 nm which is larger than the size of the particles of magnesium aluminate formed at 400 °C. The same trend is observed in the case of samples annealed at 800 and 1000 °C. This is due to the difference in the rate of diffusion of zinc and magnesium ions during the heating process which in turn depends on the size of the ions. The cubic lattice parameters of all samples were calculated by the least squares refinement method. The calculated lattice parameter is comparable to that reported for the bulk material (JCPDS No – 82-1043).

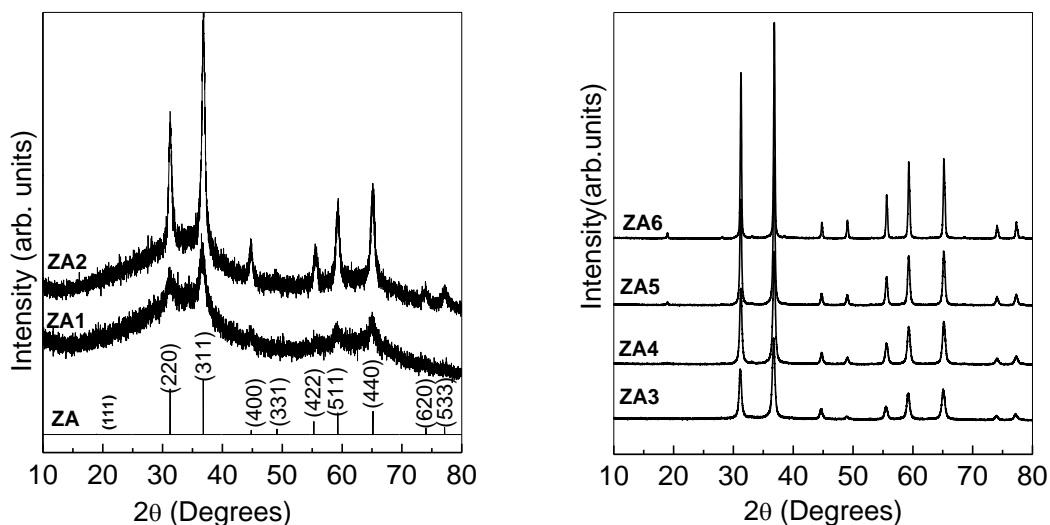


Figure 6.9. Power XRD patterns of  $\text{ZnAl}_2\text{O}_4$  nanoparticles annealed at different temperatures, ZA1 – 400 °C, ZA2 – 450 °C, ZA3 – 500 °C, ZA4 – 600 °C, ZA5 – 800 °C, ZA6 – 1000 °C. The simulated pattern of  $\text{ZnAl}_2\text{O}_4$  (ZA) is shown and indexed for comparison.

### 6.3.3 TEM Analysis

Figure 6.10 shows the TEM images of ZA1 and ZA3. The TEM images reveal the agglomerated nature of the particles of ZA1 where as the agglomeration is reduced in the case of ZA3. The average particle size obtained from TEM studies is compared with the average crystallite size calculated from XRD patterns in table 6.3. The particle sizes are comparable to the average crystallite sizes calculated from the XRD patterns. Hence the crystallite size is considered as the average particle size for all samples.

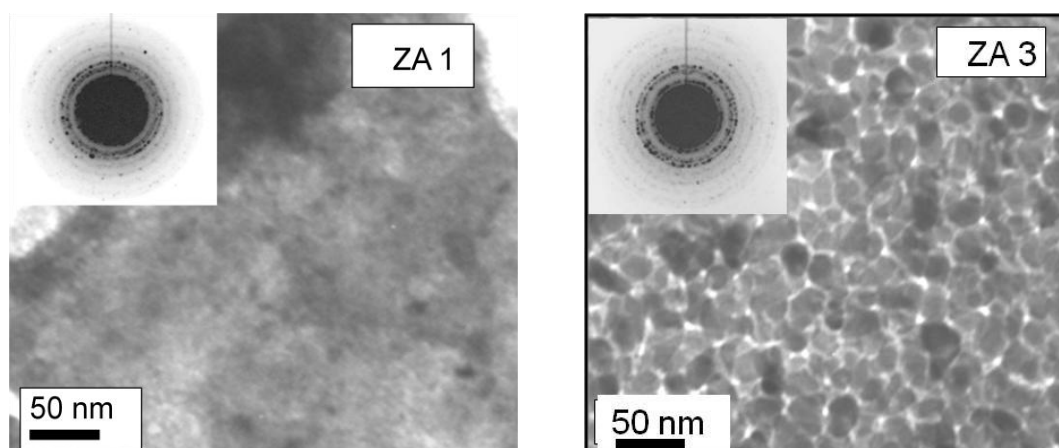


Figure 6.10. Transmission electron micrographs of the samples annealed at 400 °C (ZA1) and 500°C (ZA3). The inset shows the corresponding electron diffraction pattern.

### 6.3.4 Solid state NMR studies

Figure 6.11 and Figure 6.12 show the  $^{27}\text{Al}$  NMR spectra of different  $\text{ZnAl}_2\text{O}_4$  samples having different particle sizes. Figure 6.11 shows the  $^{27}\text{Al}$  MAS NMR spectra of  $\text{ZnAl}_2\text{O}_4$  samples recorded at a field of 7.04 T (AV300 spectrometer) with the spinning speed of 12KHz. Figure 6.12 shows  $^{27}\text{Al}$  MAS NMR spectra of samples recorded at a field of 11.7 T (AV500 spectrometer) with a spinning speed of 34.1 KHz.

Even though  $\text{ZnAl}_2\text{O}_4$  is considered as a normal spinel, some of the previous studies reported its inverted character [33] and the inversion depends upon the preparation method, particle size, etc. Figure 6.11 and Figure 6.12 clearly show that there is considerable amount of inversion for samples of low particle sizes. The different chemical shift regions in the spectra correspond to different Al coordination sites. The chemical shift regions at  $\sim 70$  ppm,  $\sim 45$  ppm,  $\sim 12$  ppm and at  $\sim 1$  ppm indicate the presence of tetrahedral ( $\text{Al}_{\text{IV}}$ ), five-coordinated ( $\text{Al}_{\text{V}}$ ), octahedral ( $\text{Al}_{\text{VI-1}}$ ) and second octahedral ( $\text{Al}_{\text{VI-2}}$ ) aluminium coordinated sites, respectively. Second octahedral site is different from the normal octahedral sites due to its distorted symmetry and presence of this site in magnesium aluminate has been studied in the previous section. For the samples ZA1 (9 nm), ZA2 (21 nm) and ZA3 (24 nm), the four resonance peaks corresponding to  $\text{Al}_{\text{IV}}$ ,  $\text{Al}_{\text{V}}$ ,  $\text{Al}_{\text{VI-1}}$  and  $\text{Al}_{\text{VI-2}}$  coordinated sites are observed. The intensity of  $\text{Al}_{\text{V}}$  coordinated site decreases from ZA1 to ZA3 and it is

totally disappeared for ZA4 (44nm). The octahedral site  $\text{Al}_{\text{VI-2}}$  is clearly observed as a second resonance peak at the octahedral region in the spectra recorded at low spinning speed and the intensity of this peak increases with increasing particle size. In the spectra which are recorded at high field, this second peak at octahedral region is not clearly visible. But the broadening at the right side of first octahedral site shows the presence of  $\text{Al}_{\text{VI-2}}$  coordination. The contribution from  $\text{Al}_{\text{IV}}$  coordinated site decreases from ZA1 to ZA5 (59 nm) and is totally absent in ZA6 (100nm). It clearly shows that  $\text{ZnAl}_2\text{O}_4$  tend to be a normal spinel at larger particle sizes.

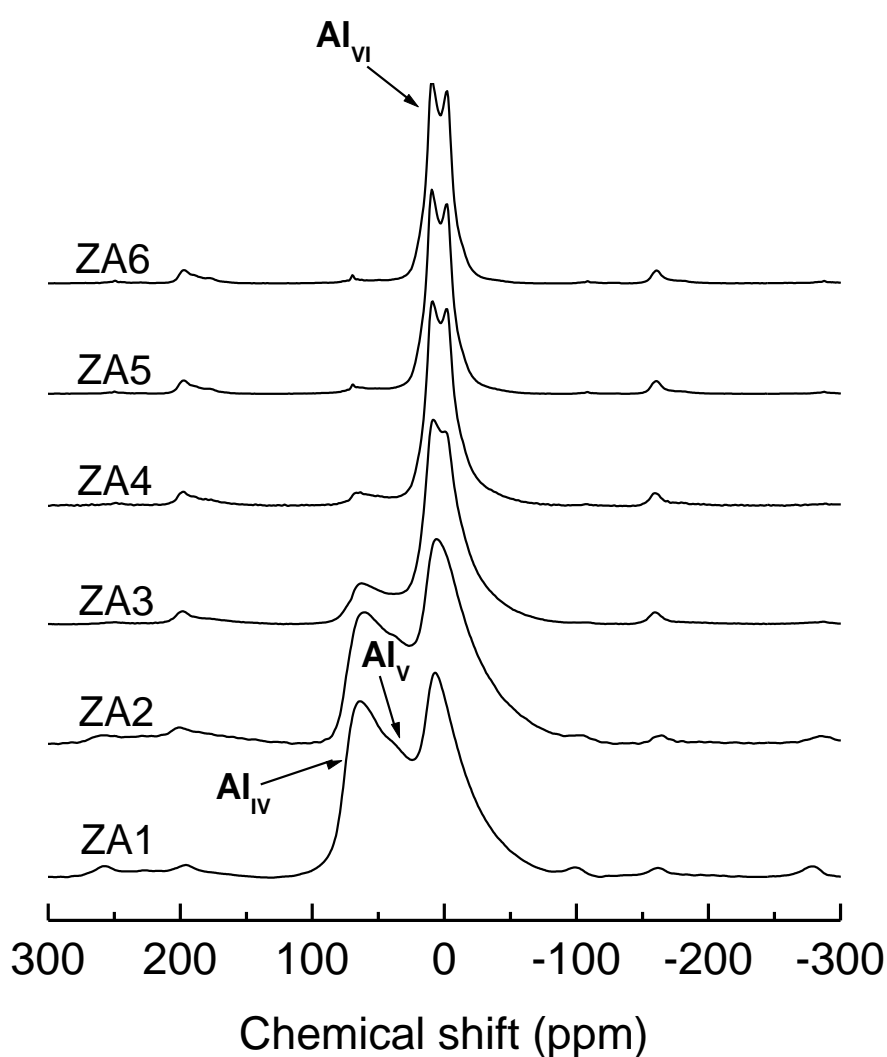


Figure 6.11.  $^{27}\text{Al}$  MAS NMR spectra of  $\text{ZnAl}_2\text{O}_4$  of different particle sizes, recorded on AV300 spectrometer at a sample spinning speed of 12.5 kHz

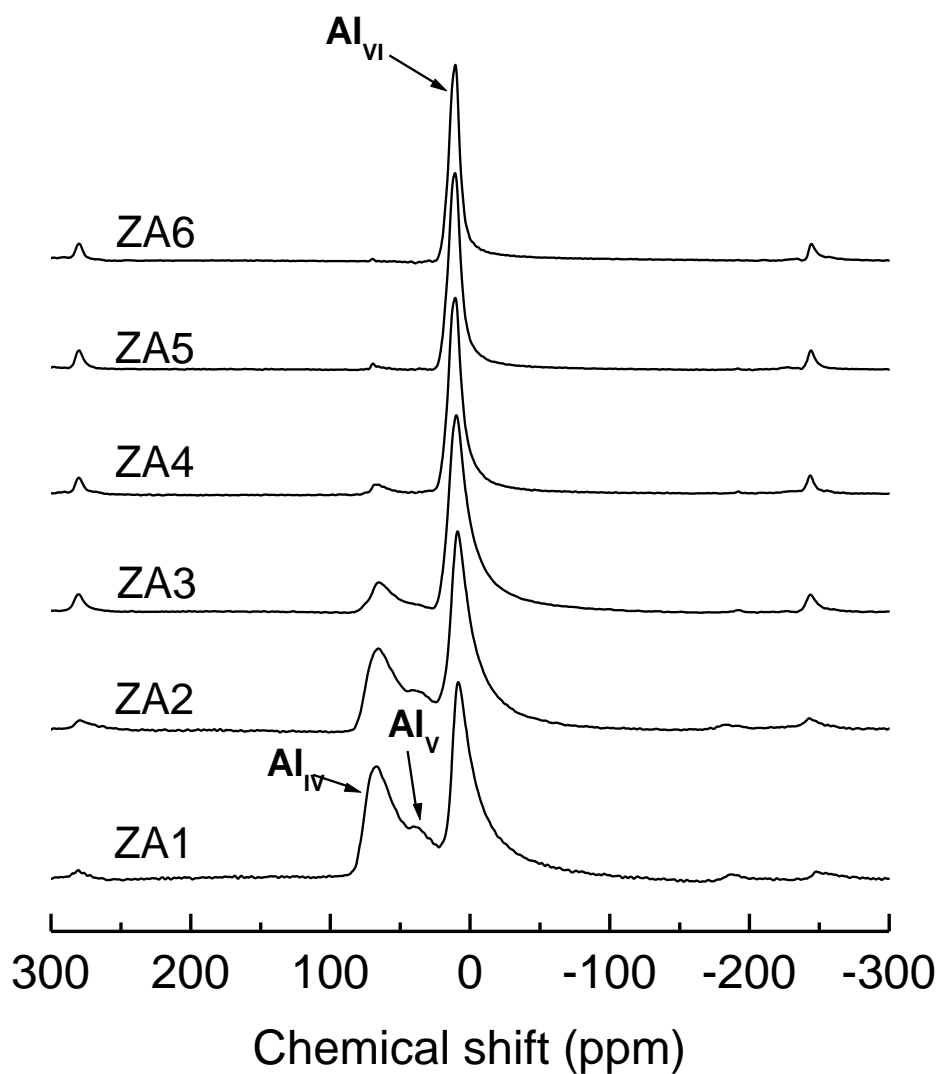


Figure 6.12.  $^{27}\text{Al}$  MAS NMR spectra of  $\text{ZnAl}_2\text{O}_4$  of different particle sizes, recorded on AV500 spectrometer at a sample spinning speed of 34.1 kHz. The sample codes are defined in Table 6.3.

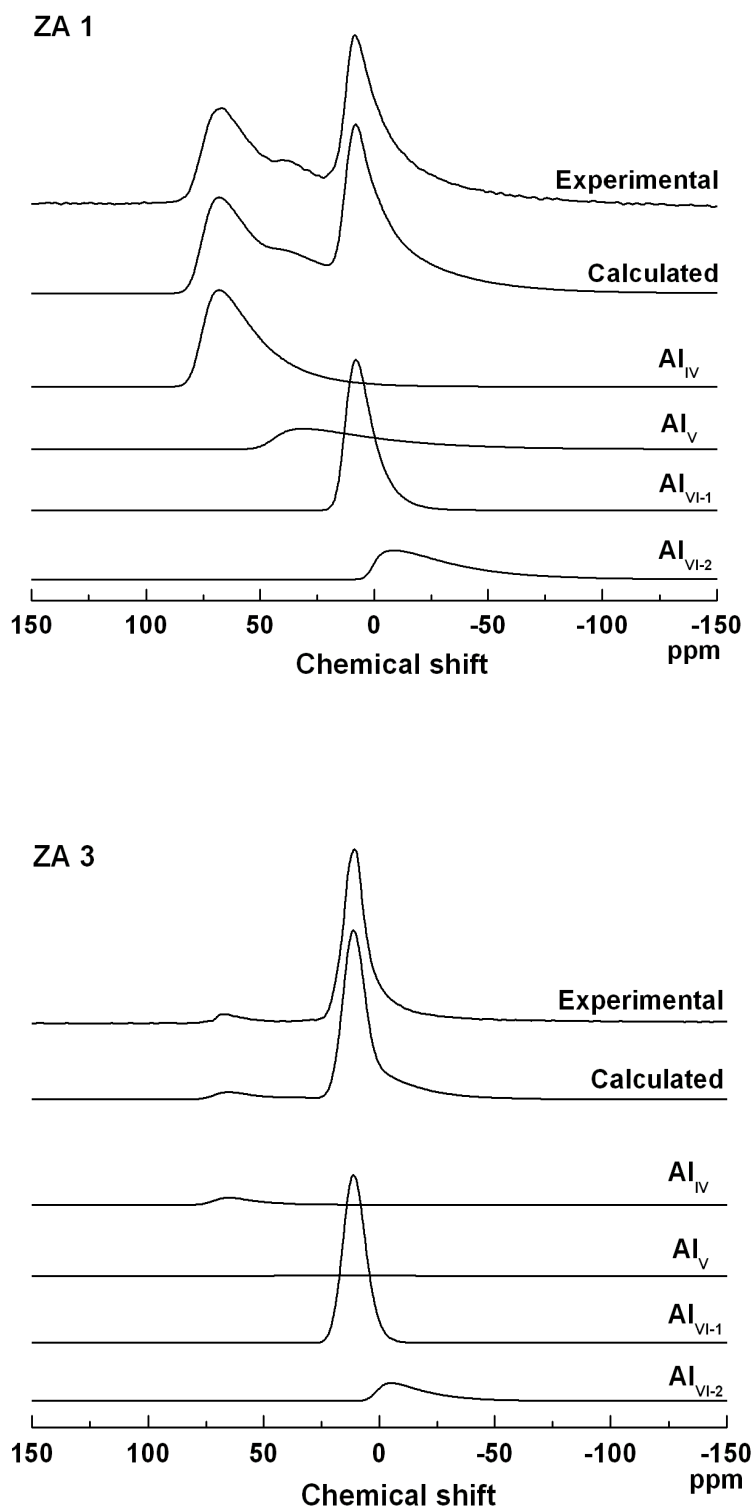


Figure 6.13. Experimental and calculated  $^{27}\text{Al}$  MAS NMR spectra for the samples ZA1 and ZA3. The bottom traces in both cases show the separate components for the different aluminum coordinations.

For getting the exact contribution of each Al coordinated site, the different spectra have been simulated. By this process, it is possible to calculate the relative intensities of each Al coordinated sites and its different parameters which determines the coordination behaviour. Different spectra are simulated as described in the case of  $\text{MgAl}_2\text{O}_4$  and the results are tabulated in the Table 6.4. The simulated spectra and individual components in the spectra of two samples ZA1 and ZA3 are shown in the Figure 6.13.

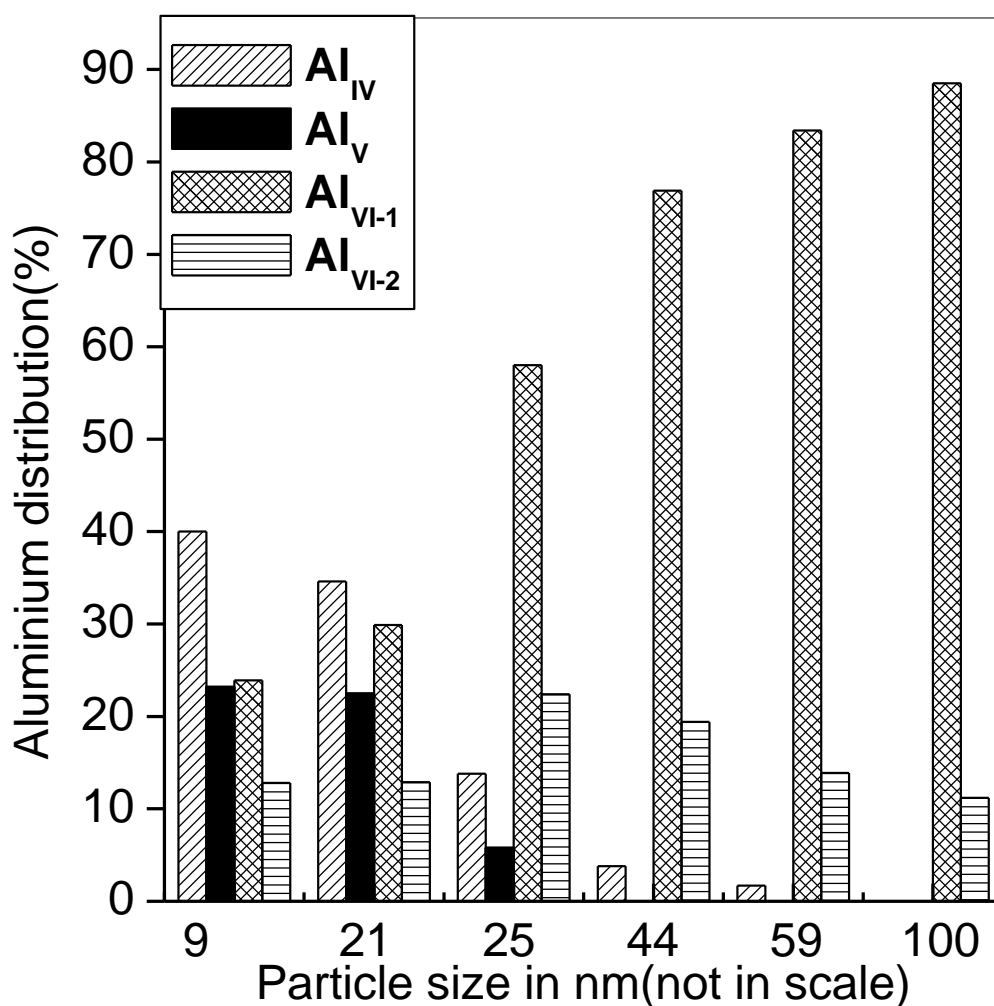


Figure 6.14. Cation distribution in  $\text{ZnAl}_2\text{O}_4$  nanoparticles obtained from fitting the  $^{27}\text{Al}$  MAS NMR spectra, plotted as a function of particle size. Note that the  $x$ -axis is not to scale.

Table 6.4. NMR Parameters Obtained from the  $^{27}\text{Al}$  MAS Experiments, Using the DMFIT Program

Sample code	Al site	$^a\delta_{\text{iso}}$ (ppm)	$^b d_{\text{CSA}}$ (ppm)	$^c C^*_Q$ (MHz)	Distribution (%)	$^d$ Inversion parameter
ZA1	Al <sub>IV</sub>	76.6	10.1	6.7	40.0	0.80
	Al <sub>V</sub>	45.3	7.5	11.1	23.2	
	Al <sub>VI-1</sub>	12.2	8.1	3.5	23.9	
	Al <sub>VI-2</sub>	3.3	5.2	6.4	12.8	
ZA2	Al <sub>IV</sub>	75.8	11.9	6.3	34.6	0.69
	Al <sub>V</sub>	45.2	11.1	10.4	22.5	
	Al <sub>VI-1</sub>	12.1	10.2	2.9	29.9	
	Al <sub>VI-2</sub>	2.9	5.2	5.7	12.9	
ZA3	Al <sub>IV</sub>	72.1	12.0	5.3	13.8	0.28
	Al <sub>V</sub>	45	6.0	10.0	5.8	
	Al <sub>VI-1</sub>	14.6	10.3	2.9	58.0	
	Al <sub>VI-2</sub>	2.5	3.7	5.7	22.4	
ZA4	Al <sub>IV</sub>	70.2	6.1	3.8	3.8	0.08
	Al <sub>VI-1</sub>	14.4	8.6	3.1	76.9	
	Al <sub>VI-2</sub>	2.1	5.2	6.3	19.4	
ZA5	Al <sub>IV</sub>	71.7	1.4	3.5	1.7	0.03
	Al <sub>VI-1</sub>	12.6	10.2	1.8	83.4	
	Al <sub>VI-2</sub>	2.4	5.0	5.1	13.9	
ZA6	Al <sub>VI-1</sub>	12.2	9.5	1.2	88.5	~0
	Al <sub>VI-2</sub>	3.2	4.5	4.8	11.2	

<sup>a</sup> Isotropic chemical shift, <sup>b</sup> Width of Gaussian distribution, <sup>c</sup> Quadrupolar product.

<sup>d</sup> Inversion parameter is calculated assuming that Al<sub>V</sub> is derived from Al<sub>VI</sub> due to decreased coordination on the surface of the particles. The errors in the various parameters are estimated from the reproducibility of the simulation process as described in ref 34

The distribution of Al in the different co-ordination environments is shown in Figure 6.14. Important observations from the fitted data shown in Table 6.4 and Figure 6.14 are that (i) the intensity of the peak from  $Al_V$  decreases with increasing particle size and this peak is not observed for larger particles; (ii) there is a corresponding increase in the intensity of  $Al_{VI(2)}$  peak and the intensity of this peak initially increases as the particle size is increased and then decreases for larger particles; and (iii) the intensity of the resonance peak due to  $Al_{IV}$  decreases with increasing particle size, and there is a corresponding increase in the intensity of the peak due to  $Al_{VI(1)}$ .

#### 6.4 Conclusions

$^{27}Al$  MAS NMR studies on the nanoparticles of the spinel oxides  $MgAl_2O_4$  and  $ZnAl_2O_4$  having different particle sizes have been carried out to identify the contributions from the surface of the nanoparticles as well as the changes in the degree of distribution of the  $Al^{3+}$  ions in the tetrahedral and octahedral sites of the spinel lattice. Apart from these two coordination environments, direct evidence is obtained for Al ions in 5-fold coordination and indirect evidence for Al in 3-fold coordination in nanoparticles. The five- and three- coordinated Al ions are likely to be located on the surface of the particles and observed in the NMR spectra due to the large surface contribution when the particles are extremely small. It is observed that the degree of distribution (the percentage of Al ions in the tetrahedral sites) decreases with increasing particle size. Apart from the normal 6-fold coordination, evidence for an additional octahedral environment is observed in the NMR spectra, for larger particles. This additional octahedral site can be explained in terms of local structural distortion. Thus, the present NMR studies give direct evidence for the changes in the coordination environments when the particle size of the spinel is reduced to nanometer scales.

The present results have direct relevance and can be extended to spinel-type ferrites having the same structure as that of magnesium and zinc aluminates. In fact, there are some direct correlations with the present results and the results reported from  $^{57}Fe$  Mössbauer spectroscopic studies. Presence of an additional  $Fe^{3+}$  site, apart from the tetrahedral and octahedral sites, in some spinel-type ferrite nanoparticles

have been reported. This contribution from an additional site has been assigned to the surface contribution [59,60] or a second octahedrally coordinated site due to the displacement of some ions from the tetrahedral sites to the octahedral sites [61], resulting in a difference in the local environments. Even though  $\text{ZnFe}_2\text{O}_4$  is a normal spinel and therefore, only paramagnetic at room temperature due to the  $\text{Fe}^{3+}$  ions located in the octahedral sites, nanoparticles of  $\text{ZnFe}_2\text{O}_4$  have been shown to exhibit enhanced magnetization and ferrimagnetic nature due to presence of  $\text{Fe}^{3+}$  ions in the tetrahedral sites. The present NMR results on  $\text{ZnAl}_2\text{O}_4$  directly support this observation. Large number of Al ions are located in the tetrahedral sites when the particles sizes are very small. The present results on  $^{27}\text{Al}$  MAS NMR ions in on  $\text{MgAl}_2\text{O}_4$  and  $\text{ZnAl}_2\text{O}_4$  indicate that both types of contributions, five-coordinated surface contribution (also 3-fold coordination) and the second octahedral contribution due to local structural distortion, are possible. Resonance peaks corresponding to the different coordination geometries are directly visible in the NMR spectra. Thus, the solid state NMR studies on  $\text{MgAl}_2\text{O}_4$  and  $\text{ZnAl}_2\text{O}_4$  give direct evidence for the changes in the coordination environments when the particle size of the material is reduced to nanometer range, due to the enhanced contributions from the surface of the nanoparticles.

---

**References**

- 1 Goldman, A. *Modern Ferrite Technology*; Van Nostrand Reinhold: New York, **1990**.
- 2 West, A. R. *Solid State Chemistry and its Applications*; John Wiley & Sons: Singapore, **2003**
- 3 Schreyeck, L.; Wlosik, A.; Fuzellier, H. *J. Mater. Chem.* **2001**, 11, 483
- 4 Tang, Z. X.; Sorensen, C. M.; Klabunde, K. J.; Hadjipanayis, G. C. *Phys. Rev. Lett.* **1991**, 67, 3602
- 5 Kodama, R. H.; Berkowitz, A. E.; McNiff, E. J., Jr.; Foner, S. *Phys. Rev. Lett.* **1996**, 77, 394
- 6 Liu, C.; Zou, B.; Rondinone, A. J.; Zhang, Z. J. *J. Am. Chem. Soc.* **2000**, 122, 6263
- 7 Zhang, H. E.; Zhang, B. F.; Wang, G. F.; Dong, X. H.; Gao, Y. *J. Magn. Magn. Mater.* **2007**, 312, 126
- 8 Bulte, J. W. M.; Kraitchman, D. L. *NMR Biomed.* **2004**, 17, 484
- 9 Hiergeist, R.; Andra, W.; Buske, N.; Hergt, R.; Hilger, I.; Richter, U.; Kaiser, W. *J. Magn. Magn. Mater.* **1999**, 201, 420
- 10 Son, S. J.; Reichel, J.; He, B.; Schuchman, M.; Lee, S. B. *J. Am. Chem. Soc.* **2005**, 127, 7316
- 11 Basak, J.; Hardia, N.; Saxena, S.; Dixit, R.; Dwivedi, R.; Bhadauria, S.; Prasad, R. *Ind. Eng. Chem. Res.* **2007**, 46, 7039
- 12 Berkowitz, A. E.; Kodama, R. H.; Makhlof, S. A.; Parker, F. T.; Spada, F. E.; McNiff, E. J. Jr.; Foner, S. *J. Magn. Magn. Mater.* **1999**, 196–197, 591
- 13 Nathani, H.; Misra, R. D. K. *Mater. Sci. Eng. B.* **2004**, 113, 228
- 14 Hoffmann, M.; Campbell, S. J.; Ehrhardt, H.; Feyerherm, R. *J. Mater. Sci.* **2004**, 39, 5057
- 15 Nakashima, S.; Fujita, K.; Tanaka, K.; Hirao, K. *J. Phys.: Condens. Matter* **2005**, 17, 137
- 16 Chen, J. P.; Sorensen, C. M.; Klabunde, K. J.; Hadjipanayis, G. C.; Delvin, E.; Kostikas, A. *Phys. Rev. B* **1996**, 54, 9288

- 
- 17 Chinnasamy, C. N.; Narayanasamy, A.; Ponpandian, N.; Joseyphus, R. J.; Jeyadevan, B.; Tohji, K.; Chattopadhyay, K. *J. Magn. Magn. Mater.* **2002**, 238, 281
  - 18 Ponpandian, N.; Narayanasamy, A.; Chinnasamy, C. N.; Sivakumar, N.; Greneche, J.-M.; Chattopadhyay, K.; Shinoda, K.; Jeyadevan, B.; Tohji, K. *Appl. Phys. Lett.* **2005**, 86,192510.1
  - 19 Sepelak, V.; Indris, S.; Heitjans, P.; Becker, K. *D. J. Alloys Compd.* **2007**, 434, 776
  - 20 Chinnasamy, C. N.; Narayanasamy, A.; Ponpandian, N.; Chattopadhyay, K.; Shinoda, K.; Jeyadevan, B.; Tohji, K.; Nakatsuka, K.; Furubayashi, T.; Nakatani, I. *Phys. Rev. B.* **2001**, 63,184108.1
  - 21 Soler, M. A. G.; da Silva, S. W.; Garg, V. K.; Oliveira, A. C.; Azevedo, R. B.; Pimenta, A. C. M.; Lima, E. C. D.; Morais, P. C. *Surf. Sci.* **2005**, 575, 12
  - 22 Gobbi, G. C.; Christoffersen, R.; Otten, M. T.; Milner, B.; Buseck, P. R.; Kennedy, G. J.; Fyfe, C. A. *Chem. Lett.* **1985**, 14, 771
  - 23 Morey, O.; Goeuriot, P. *J. Euro. Ceram. Soc.* **2005**, 25, 501
  - 24 Lee, S. J.; Lee, S. *New J. Phys.* **2006**, 8, 98.1
  - 25 Shim, J. H.; Lee, S.; Park, J. H.; Han, S. J.; Jeong, Y. H.; Cho, Y. W. *Phys. Rev. B.* **2006**, 73,064404.1
  - 26 Wood, B. J.; Kirkpatrick, R. J.; Montez, B. *Am. Mineral.* **1986**, 71, 999
  - 27 Maekawa, H.; Kato, S.; Kawamura, K.; Yokokawa, T. *Am. Mineral.* **1997**, 82, 1125
  - 28 Millard, R. L.; Peterson, R. C.; Hunter, B. K. *Am. Mineral.* **1992**, 77, 44
  - 29 Andreozzi, G. B.; Princivalle, F.; Skogby, H.; Giusta, A. D. *Am. Mineral.* **2000**, 85, 1164
  - 30 Peterson, R. C.; Lager, G. A.; Hitterman, R. L. *Am. Mineral.* **1991**, 76, 1455
  - 31 Schmocker, U.; Boesch, H. R.; Waldner, F. *Phys. Lett. A* **1972**, 40, 237
  - 32 Weeks, R. A.; Sonder, E. *J. Am. Ceram. Soc.* **1980**, 63, 92
  - 33 Montouillout, V.; Massiot, D.; Douy, A.; Coutures, J. P. *J. Am. Ceram. Soc.* **1999**, 82, 3299
  - 34 Pellerin, N.; Dodane-Thiriet, C.; Montouillout, V.; Beauvy, M.; Massiot, D. *J. Phys. Chem. B* **2007**, 111, 12707-12714

- 
- 35 Chick, L. A.; Pederson, L. R.; Maupin, G. D.; Bates, J. L.; Thomas, L. E.; Exarhos, G. J. *Mater. Lett.* **1990**, 10, 6
- 36 Xue, H.; Li, Z.; Wang, X.; Fu, X. *Mater. Lett.* **2007**, 61, 347
- 37 The software is freely available from <http://www.ccp14.ac.uk>.
- 38 Verma, S.; Joy, P. A.; Khollam, Y. B.; Potdar, H. S.; Deshpande, S. B. *Mater. Lett.* **2004**, 58, 1092
- 39 Deka, S.; Joy, P. A. *Mater. Chem. Phys.* **2006**, 100, 98
- 40 Cullity, B. D. *Elements of X-ray Diffraction*, 2nd ed.; Addison-Wesley: Reading, PA, **1978**
- 41 The software is freely available from <http://www.ccp14.ac.uk>.
- 42 Sepelak, V.; Indris, S.; Bergmann, I.; Feldhoff, A.; Becker, K. D.; Heitjans, P. *Solid State Ionics* **2006**, 177, 2487
- 43 Alemany, L. B.; Kirker, G. W. *J. Am. Chem. Soc.* **1986**, 108, 6158-6162
- 44 Schmucker, M.; Schneider, H.; MacKenzie, K. J. D.; Okuno, M. *J. Eur. Ceram. Soc.* **1999**, 19, 99
- 45 Cruickshank, M. C.; Dent Glasser, L. S.; Barri, S. A. I.; Poplett, I. J. F. *J. Chem. Soc., Chem. Commun.* **1986**, 23
- 46 Schmucker, M.; Schneider, H.; MacKenzie, K. J. D. *J. Non-Cryst. Solids* **1998**, 226, 99
- 47 Neuville, D. R.; Cormier, L.; Massiot, D. *Geochim. Cosmochim. Acta* **2004**, 68, 5071
- 48 Massiot, D.; Fayon, F.; Capron, M.; King, I.; Calve, S. L.; Alonso, B.; Durand, J. O.; Bujoli, B.; Gan, Z.; Hoatson, G. *Magn. Reson. Chem.* **2002**, 40, 70
- 49 Alba, M.D.; Castro, M.A.; Naranjo, M.; Perdigon, A.C.; *Phys Chem Minerals*, 2004, 31, 195
- 50 van Bokhoven, J. A.; van der Eerden, A. M. J.; Koningsberger, D. C. *J. Am. Chem. Soc.* **2003**, 125, 7435
- 51 Kashii, N.; Maekawa, H.; Hinatsu, Y. *J. Am. Ceram. Soc.*, **1999**, 82, 1844
- 52 van der Laag, N. J.; Snel, M. D.; Magusin, M. M.; de With, G. *J. Eur. Ceram. Soc.* **2004**, 24, 2417
- 53 Pugnet, V.; Maury, S.; Coupard, V.; Dandeu, A.; Quoineaud, A.; Bonneau, J.; Tichit, D. *Appl. Catal. A: Gen.* **2010**, 374, 71

- 
- 54 Wrzyszczyk, J.; Zawadzki, M.; Trawczyński, J.; Grabowska, H.; Miśta. *Appl. Catal. A: Gen.* **2001**, 210, 263
- 55 Ballarini, A D.; Bocanegra, S A.; Castro, A A.; de Miguel, S R.; Scelza, O A. *Catal Lett* . **2009**, 129, 293
- 56 Sampath, S S.; Cordaro, J F. *J. Am. Ceram. Soc.* 1998, 81, 649
- 57 Mathur, S.; Veith, M.; Haas, M.; Shen, H.; Lecerf, N.; Huch, V.; Hüfner, S.; Haberkorn, R.; Horst P. Beck Jilavi, M. *J. Am. Ceram. Soc.* 2001, 84, 1921
- 58 Alison A. Da Silva, Agnaldo de Souza Gonc, alves Marian R. Davolos, *J Sol-Gel Sci Technol* . 2009, 49, 101
- 59 Chinnasamy, C. N.; Narayanasamy, A.; Ponpandian, N.; Chattopadhyay, K.; Shinoda, K.; Jeyadevan, B.; Tohji, K.; Nakatsuka, K.; Furubayashi, T.; Nakatani, I., *Phys. Rev. B.* **2001**, 63184108.1
- 60 Oliver, S. A.; Hamdeh, H. H.; Ho, J. C. *Phys. Rev. B.* **1999**, 60, 3400
- 61 Nath, B. K.; Chakrabarti, P. K.; Das, S.; Kumar, U.; Mukhopadhyay, P. K.; Das, D., *Eur. Phys. J. B*, **2004**, 39, 417

## CHAPTER 7

### CONCLUSIONS AND FUTURE PROSPECTS

During the recent years, significant progress has been made in the synthesis and study of the structural and magnetic properties of iron oxide nanoparticles. New knowledge with respect to the properties of iron oxide nanoparticles lead to many industrial as well as biomedical applications. There are still myriad issues to address in the area of synthesis of iron oxide nanoparticles, a largely unexplored research area in the field of nanoscience. Though it is imperative to work out immediate large-scale solutions for these problems, the unimaginable technologies about to emerge in the next 100 years will lead on the fundamental research and innovative strategies developed today.

We have addressed some of these issues in the present thesis and the major accomplishments are summarized here. Magnetite nanoparticles have been synthesized using the reverse coprecipitation method. The crystallite and average particle size of the  $\text{Fe}_3\text{O}_4$  nanoparticles depend on mode of addition of Fe stock solution to ammonia solution. It was found that faster addition leads to smaller particle size but with wider particle size distribution and the reproducibility is very poor. On the other hand, slower addition is found to give highly reproducible results. This new cooking parameters can be used in producing  $\text{Fe}_3\text{O}_4$  nanoparticles with desired particle size and distribution. The magnetic properties of the nanoparticles synthesized by different addition methods have been compared by detailed field cooled, zero field cooled and field dependent magnetization studies. The iron oxide nanoparticles of size less than 10 nm do not show magnetic hysteresis at room temperature, which is usually considered as superparamagnetic characteristics. These nanoparticles are useful for biomedical applications

Dextran and ascorbic acid are biocompatible molecules. Dextran coated and ascorbic acid coated magnetite nanoparticles are successfully synthesized by coprecipitation method. Although there are many studies reported on the synthesis of dextran coated magnetite nanoparticles, detailed studies on the difference in the magnetic properties of uncoated and coated particles are lacking in the literature. Moreover, this is the first study on the coating of magnetite with ascorbic acid. The

magnetic characteristics of the uncoated and coated nanoparticles of magnetite ( $\text{Fe}_3\text{O}_4$ ) are studied to understand the effect of inter-particle magnetic interactions on the magnetic properties of the uncoated and coated samples. IR spectroscopic and magnetic studies gave evidence for the effective coating of the magnetite nanoparticles by dextran and ascorbic acid. Interesting changes in the magnetic properties have been observed after coating the nanoparticles. The results have been explained in terms of the reduced inter-particle magnetic interactions. Some memory experiments have been carried out to understand the effect of coating on the magnetic relaxation processes. Similarly, some preliminary studies have been made on the application of the ascorbic coated magnetite nanoparticles for MRI applications and the results are found to be promising.

Decreasing the size of the particles to nanometer size will increase the surface-to-volume ratio and this will strongly influence the physical and chemical properties of these materials. For magnetic nanoparticles, the exchange interactions at the surface of a particle will be different from those inside due to changes in the coordination behavior at the surface. Therefore, studying and understanding the coordination and distribution behavior of the different metal ions in the nanoparticles of spinel-type oxides is very important. Solid state NMR is a useful and important technique to obtain information on local structural variations. The degree of the distribution of the  $\text{Al}^{3+}$  ions in the tetrahedral and octahedral sites in the nanoparticles of the nonmagnetic spinel  $\text{MgAl}_2\text{O}_4$  and  $\text{ZnAl}_2\text{O}_4$  having different particle sizes has been determined by  $^{27}\text{Al}$  magic-angle spinning (MAS) NMR spectroscopy. It has been observed that the inversion parameter decreases with increasing particle size. Apart from the usual tetrahedral and octahedral coordinations present in the bulk material, the presence of five- and three-coordinated Al has been observed in nanoparticles and a second octahedral coordination is observed for nanoparticles of larger sizes. Thus, the solid state NMR studies on  $\text{MgAl}_2\text{O}_4$  and  $\text{ZnAl}_2\text{O}_4$  give direct evidence for the changes in the coordination environments when the particle size of the material is reduced to nanometer range, due to the enhanced contributions from the surface of the nanoparticles.

The results presented in this thesis are believed to be useful for the development of functionalised iron oxide nanoparticles with biocompatible molecules

and to tune the magnetic properties according to the applications. More detailed investigations in terms of biomedical applications may shed more light on the importance of these investigations, especially for the ascorbic acid coated nanoparticles..

Future research on iron oxide nanoparticles will be focused on developing alternative synthesis pathways to yield smaller size particles. Although nanoparticle cores such as iron-oxide with biocompatible molecules naturally lend themselves to dual-imaging and therapeutic applications, the combination of imaging and other functionalities using other nanoparticle cores can be challenging. An alternative strategy to consolidate multiple functionalities onto a single particle is to use core-shell architecture. In this case, an outer shell with one functionality such as targeting may be unveiled to reveal an inner core that performs a secondary function such as drug release. However, to custom-design multifunctional iron oxide nanoparticles with desirable magnetic properties, it is important to develop large scale production of these nanoparticles which can help to the future applications.

## LIST OF PUBLICATIONS

- (1) Magnetic Properties of Maghemite Nanoparticles Synthesized by Microwave Hydrothermal Method  
**V. Sreeja** and P.A.Joy, *Matrerial Research Bulletin*, 42 (2007) 1570–1576
- (2) Size dependent coordination behavior of MgAl<sub>2</sub>O<sub>4</sub> nanoparticles from <sup>27</sup>Al solid state NMR studies  
**V. Sreeja**, T. S. Smitha, Deepak Nand, P.K.Madhu and T.G.Ajithkumar and P. A. Joy, *J. Phys. Chem. C*, 112 (38), (2008) 14737–14744
- (3) Magnetic and Mössbauer spectroscopic studies of NiZn ferrite nanoparticles synthesized by a combustion method  
**V. Sreeja**, S. Vijayanand, S. Deka and P. A. Joy, *Hyperfine Interactions* 183, (2008) 99–107
- (4) Effect of interparticle interaction on the magnetic properties of magnetite nanoparticles after coating with Dextran  
**V. Sreeja**, H.S. Potdar and P. A. Joy, *International Journal of Nanotechnology* 2009, (Revised and Submitted)